2022

Thermo-Hydro-Mechanical analysis of rock formations subject to low temperature CO_2 sequestration

Nikolaos Reppas

School of Engineering,

Newcastle University

Submitted in fulfilment of the requirement for the degree of Doctor of Philosophy

April 2023

Abstract

In May 2019, the UK Committee on Climate Change, recommended that the UK should aim to be net zero by 2050. To help achieve this goal, a promising approach is Carbon Capture and Storage (CCS). Potential CCS schemes include injecting liquid carbon dioxide (CO_2) from ships into subsea formations for permanent storage. CO_2 is stored onboard these ships at sub-zero temperatures and usually heated up to higher than 4.5°C prior to injection. Lower injection temperatures have been suggested as these reduce energy spend. However, these temperatures could lead to damage and fracture of the rock surrounding the wellbore, which is a key component of the integrity of the storage site.

In this thesis, a fully coupled Thermo-Hydro-Mechanical (THM) model considering elastoplastic behaviour of rock with continuum damage effects is presented describing the behaviour of sandstone adjacent to the wellbore wall during CO_2 injection. Sandstone was selected because it is found in sub-sea basins around the UK, it has high porosity and is a likely storage medium for CCS. A macroscopic approach was adopted based on the effective stress concept, the equations of static equilibrium, the conservation of mass, momentum, and heat transfer in the fractured medium. The constitutive model was implemented using Finite Element Method coded in MATLAB and its validity was verified through comparison with thermo-hydro-mechanical models from existing literature.

For elastoplastic considerations, a bounding surface model, based on critical state mechanics adopting a hardening rule, was created. Uniaxial and triaxial experimental tests were undertaken to determine the thermal effects on the mechanical properties of sandstone, while critical state parameters were estimated from a parametric study. It was identified that lower temperature increased the strength of the rock due to ice formation but decreased Poisson's ratio, making the rock more vulnerable to fracture and damage.

The full numerical model was used to investigate several representative injection scenarios and to estimate the influence of cold CO_2 on the rock surrounding the wellbore. Results indicate that sub-zero injection temperatures decrease pore and fissure pressure, while increasing the radial effective stress leading to potential damage. Limitations on injection pressures and temperatures are suggested based on these results.

Publications

Reppas, Nikolaos, Gui, Yilin, Wetenhall, Ben, Davie, Colin, & Ma, Jianjun (2021) Wellbore stability analysis during CO2 injection considering elastoplastic and continuous damage effects. In 11th Asian Rock Mechanics Symposium (ARMS 11).
Wellbore stability analysis during CO2 injection considering elastoplastic and continuous damage effects. - IOPscience

Reppas, N., Gui, Y., Wetenhall, B., Davie, C., Ma, J. (2020), 'Elasto-Plastic Behavior of Rock during Temperature Drop', World Academy of Science, Engineering and Technology, Open Science Index 163, International Journal of Geotechnical and Geological Engineering, 14(7), 177 - 184.
https://publications.waset.org/10011341/elasto-plastic-behavior-of-rock-during-temperature-drop

Reppas, N., Gui, Y. L., & Wetenhall, B. (2019, August 28). A General Review on Rock Stability Due to CO2 Injection. American Rock Mechanics Association.
https://www.onepetro.org/conference-paper/ARMA-2019-1593?sort=&start=0&q=A+general+review+on+rock+stability&from_year=&peer_reviewed=&published_between=&fromSearchResults=true&to_year=&rows=25

Reppas, N., Davie, C., Wetenhall, B., Gui, Y. L., & Ma, J. (2022). Numerical simulation of triaxial experimental results on Sandstone using critical state mechanics. In 55th US Rock Mechanics/Geomechanics Symposium. One Petro.
Link not yet available.

Reppas, N., Davie, C., Wetenhall, B., Gui, Y. L., & Graham, S. (2022). Experimental determination of the effects of cooling on fine-grained sandstone in relation to wellbore injection of carbon dioxide

Submitted to Journal of Rock Mechanics and Rock Engineering.

Contribution to the work

All authors contributed to the study, conception, and design of the papers. Analysis of the results was performed by Nikolaos Reppas. For the journal submitted experimental paper, Dr. Samuel Graham contributed to the microscopic analysis of the sandstone, presented also in Chapter 4 and Dr. Colin Davie helped on the preparation and data collection.

<<Ιθάκη>>

Πάντα στον νου σου να ‘χεις την Ιθάκη.
Το φθάσιμον εκεί είν’ ο προορισμός σου.
Αλλά μη βιάζεις το ταξίδι διόλου.
Καλύτερα χρόνια πολλά να διαρκέσει·
και γέρος πια ν’ αράξεις στο νησί,
πλούσιος με όσα κέρδισες στον δρόμο,
μη προσδοκώντας πλούτη να σε δώσει η Ιθάκη.
Η Ιθάκη σ’ έδωσε τ’ ωραίο ταξίδι.
Χωρίς αυτήν δεν θα ‘βγαινες στον δρόμο.
Άλλα δεν έχει να σε δώσει πια.
Κι αν πτωχική την βρεις, η Ιθάκη δεν σε γέλασε.
Έτσι σοφός που έγινες, με τόση πείρα,
ήδη θα το κατάλαβες οι Ιθάκες τι σημαίνουν.

«Κωσταντίνος Καβάφης

<<Ithaka>>

Keep Ithaka always in your mind.
Arriving there is what you are destined for.
But do not hurry the journey at all.
Better if it lasts for years,
so you are old by the time you reach the island,
wealthy with all you have gained on the way,
not expecting Ithaka to make you rich.
Ithaka gave you the marvellous journey.
Without her you would not have set out.
She has nothing left to give you now.
And if you find her poor, Ithaka won't have fooled you.
Wise as you will have become, so full of experience,
you will have understood by then what these Ithakas mean.

"Kavafis, Konstantinos"

ACKNOWLEDGEMENTS

I am extremely grateful to my supervisors Dr. Yilin Gui, Dr. Ben Wetenhall and Dr. Colin Davie, for their invaluable guidance, continuous support, and constant encouragement throughout my PhD studies. I have been inspired greatly by their knowledge, passion, and commitment to research. Additionally, this endeavour would not have been possible without the tuition fee support from the Engineering and Physical Sciences Research Council (EPSRC).

I would like to extend my sincere thanks to Dr. Jianjun Ma for his assistance and invaluable suggestions on coding using Finite Element Modelling. I would also like to thank Professor David Manning and Dr. Mohamed Rouania for their help and suggestions. Additionally, I would like also to express my deepest appreciation to Professor Nasser Khalili, who is one of the first academics worked on thermo-hydro-mechanical models and all my research is based on his investigations.

Special acknowledgements should be also given to the laboratory technicians: Stuart Patterson, Graham Ewart, Gareth Wear and Michael Finley for their help and support during the experimental work.

I would like also to express my sincere appreciation to the internal examiner Dr. Mark Ireland and to the external examiner Dr. Zhongwei Chen for their comments and proposed suggestions.

Words cannot express the feeling I have for my mother Eirini and my father Konstantinos for their unconditional love and support. Their belief in me has kept my spirits and motivation high during this process. Special thanks also to my friends and people that were around me during this stressful period for their continuous support.

Lastly, but most importantly, I would like to thank God, who has given me strength and encouragement throughout all the challenging moments of completing this PhD thesis. I am truly grateful for the unconditional and endless love, mercy, and grace.

DEDICATION

This thesis is dedicated to my beloved parents and to my grandfather and grandmother who have taught me the joy of knowledge.

Table of Contents

List of Figures

Chapter 1. Introduction

Chapter 2. Literature review

Chapter 3. Theoretical constitutive thermo-hydro-mechanical and elastoplastic damage model

Chapter 4. Analysis of experimental testing of Stainton Sandstone

Chapter 5. Finite Element Modelling implementation, Critical State mechanics parameter determination and validation of the THM model.

Chapter 6. Representative scenarios and parametric studies

List of Tables

Chapter 4. Analysis of experimental testing of Stainton Sandstone

Chapter 5. Finite Element Modelling implementation, Critical State mechanics parameter determination and validation of the THM model.

Chapter 6. Representative scenarios and parametric studies

List of Symbols

Latin symbols

$a = 1\,,2$	This symbol represents the porous and fissure network
$A,\, A_D$	The total and damaged area of a specific domain
C_T	Thermal expansion coefficient of the solid
C_{Ts}	Volumetric thermal expansion of the solid skeleton
C_{Tw}	Thermal expansion coefficient of the saline water in porous and fissure network
C_f	Compressibility of the fractured domain
C_p	Compressibility of the porous domain
C_s	Compressibility of the solid skeleton
C_{fl}	Fluid compressibility
C_{pa}	Heat capacity of the fluid at constant pressure at the porous and fissure domain
C_{ps}	Heat capacity of the solid
D	Damage variable
d_{sw}	Density of saline water
E	Young's modulus
e	Void ratio
f	Yield function at loading surface
$G^{el}(D,T)$	Damage shear modulus including thermal effects
g	Plastic potential
H	Total hardening modulus
H_a	Enthalpy per unit mass of water in the fracture $(a = 1\,,2)$
$H_Y, H_{\sigma_{eq}}$	Damage rate parameters
h	Hardening modulus
h_b	Hardening modulus at the bounding surface

h_f	Arbitrary modulus ore additive hardening modulus at the bounding surface
$h_\gamma, h_{\sigma_{eq}}$	Material constants controls damage rate
J_2, J_3	Second and third invariants of the deviatoric stress vectors
$K_{bulk}^{el}(D,T)$	Damage bulk modulus including thermal effects
k_s	Thermal conductivity of the solid domain
k_a	Thermal conductivity of the saline water inside the pores and fissures $(a = 1\,, 2)$
k_m	The material constant that determines the increase in the rate of damage evolution and influences the bounding surface model
$k_{\sigma_{eq}}$	Material constant controls damage threshold
M_{cs}	Slope of critical state line
M	The parameter controls the shape of the bounding surface
N	Shape function
p_1, p_2	Saline water pressures of porous and fissure network
p'	Mean effective stress
p^*	Crushing pressure of grains
p'_{ch}	Maximum hydrostatic compressive historic pressure or pre-consolidated pressure
p'_c	Effective pressure controlling the size of the yield surface
p'_{conf}	Confining pressure influences the damage and grain crushing
q	Deviatoric stress
R	Material parameter in bounding surface
s	Entropy per unit volume of the fractured porous medium
T_a	Temperature of the fluid in the porous and fissure domain $(a = 1\,, 2)$
T_s	Temperature of the solid
t	Time
v	Specific volume
V_{tot}	Total volume of fracture porous media element

V_{phase}	Volume of phase ($a = 1\,, 2$)
x_D	Coupling parameter between damage evolution and plastic flow
Y_D	Threshold of damage strain energy release rate
Y_{D0}	The initial value for the threshold of damage strain energy release rate

Greek symbols

β_1, β_2	The effective stress parameters for the porous and fissure domain, respectively
$\beta_{11}^e, \beta_{22}^e$	The elastic coefficients relating to the pores and fissure volumetric deformations
$\beta_{12}^e, \beta_{21}^e$	The coupling terms describing the changes in pores and fissure's fluid pressures
β_{11}, β_{22}	Apparent compressibility coefficients of porous and fissure domain
β_{12}, β_{21}	Apparent coupling terms relating to changes in pores and fissure's fluid pressures
β	Finite difference interpolation parameter/ represents the type of approximation applied to time integration
γ	Leakage parameter for flow model
γ_{pl}	Plastic hardening variable
Γ	Specific volume on the critical state line at the mean effective stress of 1 MPa
Γ_s	Energy transfer
η	Stress ratio determines the relation between deviatoric and hydrostatic stresses
κ	Slope of the elastic unloading-reloading line in $v - lnp'$domain
κ_D	Slope of the elastic including damage unloading-reloading line in $v - lnp'$domain
λ	Slope of the isotropic compression line in $v - lnp'$domain
$\dot{\lambda}$	Plastic multiplier
μ_f	Dynamic viscosity of the fluid
N_0	Specific volume on the isotropic compression line at the mean effective stress of 1 MPa

ν	Poisson's ratio
ρ^s	The apparent density of the solid
ρ_s	Intrinsic density of the material
ρ_f	Density of the fluid
φ_a	Porosity in porous or fissure ($a = 1\,, 2$)
φ_s	Porosity of the solid
Θ	Thermo-osmosis coefficient coupling fluid flux to the temperature gradient
Υ_a	Isothermal heat flow coefficient ($a = 1\,, 2$)
Ξ_a	Leakage term between the two phases ($a = 1\,, 2$)
ω_{1s}, ω_{2s}	Coefficient of heat exchange between the solid medium and porous network and solid medium and fissure network.

Matrix and Vectors

$[\boldsymbol{C}]$	Coupling matrix
$\boldsymbol{\delta}$	Identity vector
$\boldsymbol{\varepsilon}$	Strain vector
$\boldsymbol{\varepsilon_p}, \boldsymbol{\varepsilon_q}$	Volumetric strain and Triaxial shear strain
$\boldsymbol{\varepsilon_a}, \boldsymbol{\varepsilon_c}$	Axial and circumferential strain
$[\boldsymbol{H}]_{\boldsymbol{1p}}, [\boldsymbol{H}]_{\boldsymbol{2p}}$	Material property matrices corresponding to the permeabilities of pore and fissure networks
$[\boldsymbol{H}]_{\boldsymbol{Ts}}$	Material property matrix corresponding to the permeability of solid
$[\boldsymbol{K}]$	Element stiffness matrix
$\boldsymbol{k}_a$	Permeability tensor of the domain ($a = 1\,, 2$)
$[\boldsymbol{M}]$	Mass matrix
$\{\boldsymbol{p_1}\}, \{\boldsymbol{p_2}\}$	Vector of nodal pore and fissure saline water pressure
$\{\boldsymbol{q_1}\}, \{\boldsymbol{q_2}\}$	Vector of nodal fluxes of pore and fissure fluid flow
$\{\boldsymbol{r_s}\}$	Vector of nodal heat flux
$[\boldsymbol{S^e(T)}]$	Elastic stiffness matrix for undamaged material considering thermal effects

$\left[S^{epl}(T)\right]$	Elastoplastic stiffness matrix for undamaged material considering thermal effects
$[S^{e}(D,T)]$	Elastic stiffness matrix for damaged material considering thermal effects
$\left[S^{epl}(D,T)\right]$	Elastoplastic stiffness matrix for damaged material considering thermal effects
$\{\dot{Traction}\}$	Vector of nodal traction force
$\{T_s\}$	Vector of nodal temperature of the solid
v_a, v_s	The absolute fluid velocity, the velocity of the solid structure.
σ	Apparent stress
σ'	Effective stress vector
g	Vector of the gravitational acceleration
$\{u^e\}$	Vector of the nodal values of the solid matrix elastic displacements
$\{u_d\}$	Vector of nodal displacements including damage
x	Unit direction of plastic flow
n	Unit vector normal to the loading/bounding surface
$\{W_d\}$	Vector of nodal forces
$\{W_1\},\{W_2\}$	Vector of nodal fluxes of pore and fissure fluid flow
$\{R_s\}$	Vector of nodal heat flux on the solid mediu

Chapter 1. Introduction

1.1 Context

Since the beginning of the industrial revolution, a 45% increase in atmospheric carbon dioxide (CO_2) has been identified (Bachu and Stewart, 2002). As a greenhouse gas, CO_2 is one cause of global warming (Celia et al., 2015). Carbon Capture Utilisation and Storage (CCUS) is a viable technology to mitigate carbon emissions from industrial and power generation facilities and is part of the UK's strategy for meeting its net-zero target by 2050 (Pye et al., 2017; Martin-Roberts et al., 2021; Dixon et al., 2022). CCUS procedure briefly entails three major steps. Firstly, separation of CO_2 from other gases produced at facilities such as coal and natural gas power plants, oil and gas refineries, cement plants and steel mills. The second step is the transportation of CO_2, after capture and separation. CO_2 is compressed to a denser phase or liquified and transported by pipelines or ships to injection sites. Finally, as a last step CO_2 is injected in the storage site in deep underground formations for permanent storage (Herzog and Golomb, 2004; Metz et al., 2005). A schematic representation of a CCUS project can be found in Figure 1.1

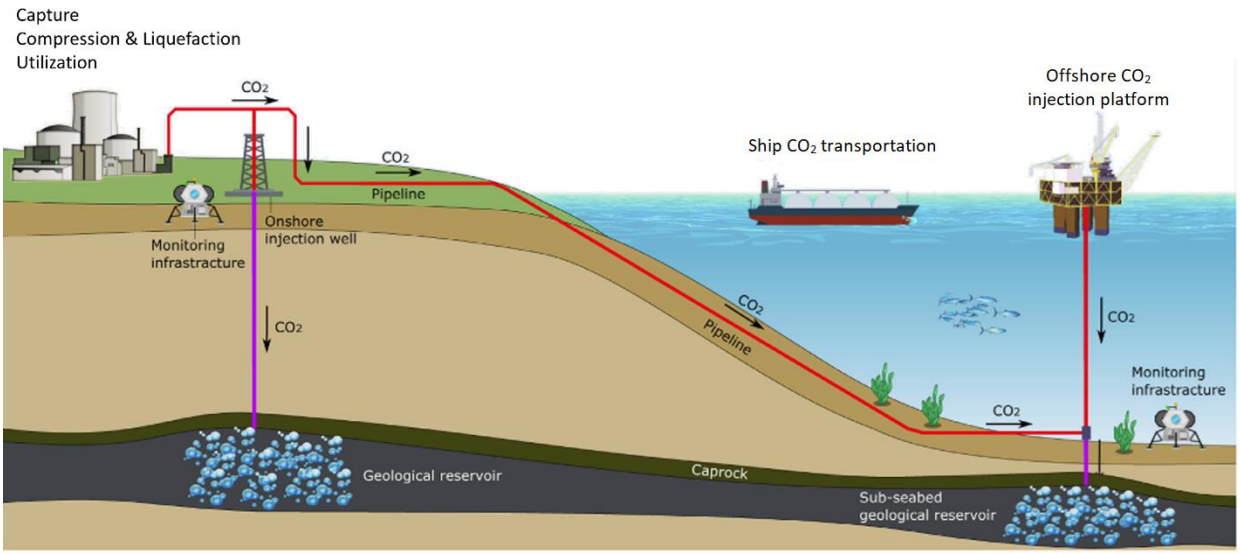

Figure 1. 1 Key processes in offshore CCUS (Li, 2022)

Wellbore integrity is a critical component of the long-term security of carbon dioxide storage and needs to be investigated (Roy et al., 2018). Pipelines are the most common method for transporting large quantities of CO_2 in gaseous and dense liquid phases over long distances (Zhang et al., 2006;

Parfomak et al., 2007). CO_2 in pipelines exist as liquid at ambient temperature and high pressure or subcooled liquid conditions at around 15-20°C in case of onshore pipeline transportation or 6-7°C for offshore pipeline transportation (Lindeberg, 2011). Compressor stations are located at the injection sites, while booster compressors are also used along the pipeline to address pressure drop issues in order to avoid potential phase change of the CO_2 (Parfomak et al., 2007; Roussanaly et al., 2013; Luo et al., 2014). The CO_2 that is transported by pipeline can impose some variations in injection due to daily and seasonal fluctuations in flow rate and also pressure drop along the pipeline (Fernandez et al., 2016). However, the flow of CO_2 transported by ships can lead to an intermittent flow of CO_2 into the storage site as injection stops when CO_2 unloading finishes. This means that direct injection from a ship can induce extreme temperature fluctuation during and post the flow, which can lead to a reduction in effective stresses in the rock and bringing the stress state closer to failure (Segall and Fitzgerald, 1998; Luo and Bryant, 2011; Krogh et al., 2012; Goodarzi et al., 2015; Khurshid and Fujii, 2021). CO_2 on a ship is stored under temperature and pressure conditions close to the triple point (around -52°C and 0.7 MPa) in order to keep containment in near-liquid form (Barrio et al., 2005). Injected CO_2 from a ship will have a much lower temperature than the rock nearby the wellbore (De Andrade et al., 2014). During CO_2 injection, the internal pressure of the wellbore and the temperature difference between the injected CO_2 and the rock formation nearby the wellbore, may result in stress variations that can induce damage (Segall and Fitzgerald, 1998). This could create faults and leakage pathways to the overlying strata. Well-barrier materials such as casing and cement, are usually used to increase the stability and hydraulic sealing to prevent fluid migration (Roy et al., 2018).

Considering the potential thermal and mechanical loadings, studying the deformation, the hydraulic effects and the thermal expansion or shrinkage of the rock at the vicinity of the wellbore, during CO_2 storage, is essential for the wellbore stability. Coupled thermo-hydro-mechanical (THM) models were developed for this reason to numerically simulate these effects (Bai, 2016). As most rocks in nature contain fractures, the presence of fractures in addition to the pore network, indicate the importance of studying a “dual porosity” medium (Khalili-Naghadeh and Valliappan, 1991). Specifically, it is essential to study the physical processes occurring in an individual network but also the interaction between the fractures and pores considering different hydraulic, thermal, and mechanical properties. Elastoplastic damage constitutive modelling is also essential to capture the brittle-ductile behaviour of rock under different confining pressures (Hu et al., 2018).

Throughout the literature, there is a shortage of models describing elastoplastic damage and hydromechanical effects on flow-thermal-deformation models, and this is essential to be investigated to describe the rock nearby the wellbore.

As far as it concerns experimental tests, throughout the literature, there are numerous of studies concerning CO_2 injection in different types of rocks (Matter et al., 2007; Assayag et al., 2009; Hangx et al., 2013; Al-Ameri et al., 2016). However, these experimental studies are limited to high-temperature conditions (range from 25℃ to 800℃) to describe geothermal energy applications and the behaviour of rock under true subsurface conditions. (Rao et al., 2007; Wu et al., 2013; Kong et al., 2016; Zhu et al., 2016; Yang et al., 2017; Yang et al., 2021). Uniaxial (UCS), Brazilian, three-point bending, and triaxial tests are routinely conducted to describe the behaviour of rock under high temperature and pressure effects (Yang et al., 2017). Results showed that rock properties vary as a function of temperature (Sun et al., 2020; Yang et al., 2021) . However, applications like CCS, need information about the mechanical behaviour of rock at low temperatures ($T < 0^oC$), especially in the case of CO_2 ship injection at a lower temperature than the formation, to reduce energy spend for heating operations. Limited research on frozen rock has been undertaken and is only constrained to UCS and indirect tensile stress (Kodama et al., 2013).

In this research, the severity of mechanical and thermal stresses, produced by the internal wellbore pressure and temperature during CO_2 injection are investigated. The behaviour of sandstone at different temperatures and pressures is examined by analysing results of UCS and triaxial tests. Focus is given to sub-zero conditions to simulate scenarios of ship CO_2 liquid injection in order to examine the possibility of reducing energy spend for heating operations prior to injection. Finally, the constructed constitutive model is numerically implemented using FEM, adopting plasticity and continuum damage and hardening effects theory and different injection case scenarios are simulated and analysed.

1.1 Aims and Objectives

The project's main aim is to develop a THM coupling double porous elastoplastic model with continuum damage effects that can describe the influence of injected CO_2 on the rock near the wellbore wall.

This PhD work focuses on the following challenges:

- To address the gap in the literature of a robust THM elastoplastic double porous model that considers continuum damage effects and can describe the rock nearby the wellbore for applications like CCS.
- To develop a robust elastoplastic damage constitutive model that can reproduce UCS and triaxial tests, using critical state mechanics. Mechanical and critical state mechanical parameters are estimated using experimental data and numerical simulations. Additionally, their variation with sub-zero and positive temperatures is presented. A boundary yield surface is proposed after validating its efficiency to rock material, using literature data.
- To numerically implement the fully coupled THM constitutive model using the Finite Element Method (FEM) in MATLAB and calibrate the model using the results of UCS and triaxial tests. The calibrated numerical method considered various wellbore injection cases to seek the optimised conditions for the CO_2 injection procedure, to avoid reducing effective stress to a critical value and potentially create fracturing or damage of the wellbore wall. Different curves at specific time steps of the simulation are plotted such as: deviatoric stress versus axial strain, pore-fissure pressures versus radial distance from the wellbore for different depths and different temperature conditions, and damage evolution versus radial distance from the wellbore wall for different depths and injected temperatures.

1.2 Thesis structure

The thesis comprises of seven chapters and detail contents of each chapter is illustrated below.

CHAPTER 2: LITERATURE REVIEW

This chapter focuses on review of the following aspects associated with CCS and wellbore stability:

- Injection rates, temperatures and pressures of CO_2 during carbon storage procedure needed as input to the THM model.
- The challenges of injecting CO_2 at a lower temperature than that of the wellbore wall
- Different constitutive theoretical models describing the behaviour of rock under different loadings. These models analyse the changes of the rock properties due to temperature drop or freezing, the movement of the water inside the fracture and porous network and mechanical changes due to different confining pressures.
- Elastoplastic design, plastic hardening, damage evolution and permeability evolution.
- Experimental tests on rock such as UCS, triaxial, permeability tests and other related to CO_2 injection.
- Numerical analysis of the THM effects on rock throughout the literature is discussed. TOUGH-FLAC procedure or FEM coded seems to be well performed and can be used to couple thermal and pressure effects.

CHAPTER 3: THEORETICAL CONSTITUTIVE THERMO-HYDRO-MECHANICAL AND ELASTOPLASTIC DAMAGE MODEL

A fully coupled THM model for double porous medium representing the rock nearby an existing wellbore is presented. The mathematical equations describing the model are introduced. The adopted failure criterion, which is a boundary yield surface model, is presented. Damage evolution is discussed based on damage strain energy release rate and on the tensile principle stress. The concept of the critical state line is introduced including plasticity and damage hardening effects.

CHAPTER 4: ANALYSIS OF EXPERIMENTAL RESULTS ON STAINTON SANDSTONE

Uniaxial and triaxial tests are presented for Stainton sandstone at different temperatures (15°C, -5°C, -10°C) and different confining pressures representing different depths of the wellbore. In this way, the effect of a temperature drop on Young's modulus, Poisson's ratio, and shear and bulk

modulus is estimated. The slope of the critical state line is also presented, as well as its change with temperature. A microscopic analysis is included to investigate the reason why the over the limit Poisson's ratios are obtained.

CHAPTER 5: FINITE ELEMENT MODELLING IMPLEMENTATION, CRITICAL STATE MECHANICS PARAMETER DETERMINATION AND VALIDATION OF THE THM MODEL.

Numerical implementation of the fully coupled THM model is presented in this chapter. A finite element formulation of the governing equations using the modified Euler algorithm is described. Correction of the yield surface drift is proposed and validation of the model using the experimental results of Chapter 4 is performed. Additionally, critical state parameters are also proposed.

CHAPTER 6: REPRESENTATTIVE SCENARIOS AND PARAMERIC STUDIES

Different case scenarios are presented using Stainton sandstone, and the influence of material parameters are explored.

CHAPTER 7: CONCLUSSIONS

The objectives of this PhD study and discussions about the experimental tests, the reproduction of them and the different simulated wellbore scenarios are outlined in this chapter. Recommendations for further research are also presented

Chapter 2. Literature review

2.1 Motivation for the study

2.1.1 The importance of CO_2 storage

In CCUS schemes, CO_2 is captured from large-scale industrial emitters and transported to either be used (e.g., algae cultivation) or stored permanently in geological sites, where it is injected into a geological rock formation. (Haszeldine, 2009). CO_2 may be stored permanently in depleted oil and gas fields, deep saline aquifers, or coal seams (Jin et al., 2012). However, to date, only a limited number of projects have been undertaken at scale (Martin-Roberts et al., 2021), for example Sleipner in the North Sea, In Salah in Algeria, Snøhvit in the Barents Sea and the Ordos in China (Chadwick et al., 2004; Armitage et al., 2011; Eiken et al., 2011; Hansen et al., 2013; Jiang et al., 2014). The UK's first decarbonised industrial cluster will be the Net Zero Teesside in the Southern North Sea, where CO_2 will be stored in Triassic Bunter Sandstone (Page et al., 2020; Sutherland et al., 2020; Nevicato, 2022). Net Zero Teesside is a collaboration between local industry and partners in the Oil and Gas Climate Initiative: BP, ENI, Equinor, Occidental Petroleum, Shell and Total (Quirk et al., 2022). However, commerciality is hard to evaluate given the intricacies of carbon pricing, and mixture of public and private funding (Sovacool et al., 2023).

The mechanical properties of the overburden sequence control not only the amount of CO_2 that can be stored, but also the maximum allowable well-bottom pressure, and therefore the rate of injection (Eshiet and Sheng, 2014; Andersen and Nilsen, 2018). To ensure successful injection and the stability of long-term storage, reliable geomechanical characterisation of the wellbore, reservoir and sealing formation rock is required in order to understand the capabilities of potential storage sites and to minimise leakage risk (Mathias et al., 2009; Rutqvist, 2012). The CO_2 delivery method, usually either by pipeline or pumping from ships, will determine the temperature and pressure of the CO2 in the wellbore and reservoir. This study assumes ship transportation and storage in the central and southern North Sea, as this region has a capacity of more than 40 Gt for CO_2 storage.

2.1.2 Challenges during CO_2 storage.

A challenge of CCUS is to prevent the injected CO_2 from finding leakage pathways out of the reservoir back to the atmosphere or contaminating the nearby environment (Oldenburg, 2007; Ziabakhsh-Ganji and Kooi, 2014; Wang et al., 2019c). CO_2 that is transported by pipeline can impose some variations in injection due to daily and seasonal fluctuations in flow rate or suffer from pressure drops along the transportation route, but generally provides steady state continuous flow (Svensson et al., 2004; Fernandez et al., 2016). However, the flow of CO_2 transported by ships to the injection site, stops when CO_2 unloading ceases. This means that direct injection from a ship can cause intermittent flow of CO_2 into the storage site, and thermo-mechanical cycling loading on the wellbore wall (Roy et al., 2018). For this reason, fluid pressures and effective stresses needs to be estimated (Gor and Prévost, 2013).

Another main challenge is that CO_2 injection wells are often subjected to thermal loading due to temperature difference between the injected CO_2 and the surrounding rock (Mukherjee and Brill, 1999; Paterson et al., 2010). If CO_2 is colder than the wellbore rock formation, this can cause thermal contraction and induce stresses, which can induce rock fracturing and damage. In pipeline CO_2 transportation, temperature difference can be extremely high due to the injection of high pressurised CO_2 into a low pressurised wellbore, causing CO_2 expansion and temperature drop due to the Joule-Thomson effect. (Oldenburg, 2007; Ziabakhsh-Ganji and Kooi, 2014; Wang et al., 2019c). For CO_2 transportation offshore and injection by ships, the CO_2 is stored in the ship under temperature and pressure conditions close to the triple point in order to keep containment of the CO_2 mixture in near-liquid form (Barrio et al., 2005), as seen in Figure 2.1. Injection pressures in excess of 4.2 MPa are usually employed in order that the CO_2 remains in the liquid or supercritical phase (Vilarrasa et al., 2013). Rock formation temperature at the seabed level, is typically around 4°C, according to Aursand et al. (2017), increasing with depth. The CO_2 is heated up to the wellbore head formation temperature before injection to avoid thermal loading. However, heating up the CO_2 before injection, can be financially, and energetically burdensome and low pressurised - low temperature CO_2 can be promising if fracturing or damage is prevented.

2.1.3 Injection conditions and wellbore integrity

Injection temperatures and pressures are influenced by the injection flow rate, formation depth and reservoir characteristics. The phase diagram of the CO_2 can be seen in Figure 2.1.

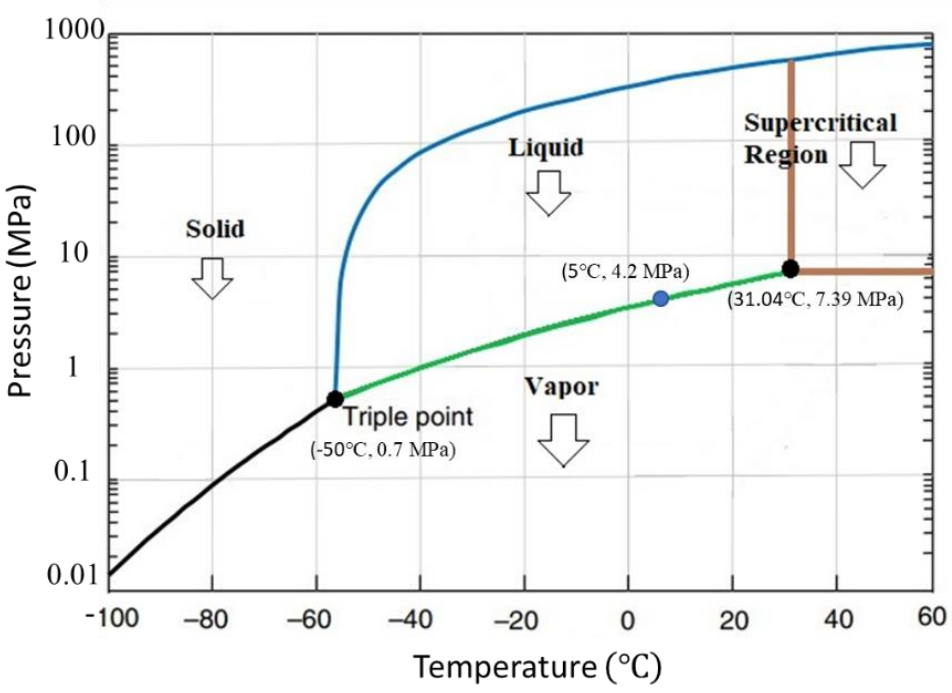

Figure 2. 1 Phase diagram of CO_2 (Li and Zhang, 2018)

Injecting the CO_2 at a temperature equal to the wellhead formation or at supercritical conditions requires pressures greater than 7.39 MPa and temperatures bigger than 31.04°C (Vilarrasa et al., 2010). This may not be the best option, since it would require significant power for throttling and heating operations (Pruess and Garcia, 2002; Bachu and Adams, 2003). Liquid CO_2 is denser and more viscous than in the supercritical phase, and less pressure is required for the injection. Smaller compressibility of the liquid CO_2 demands less compression work at the wellhead, less spent energy and may improve caprock mechanical stability (Vilarrasa et al., 2013).

Studies have been undertaken throughout the literature on injecting CO_2 at lower temperature than that of the wellhead (Rayward-Smith and Woods, 2011; Silva et al., 2011). Vilarrasa et al. (2013) examined a temperature range of injection based on a pilot injection site named "Hontomin" in Spain (Carrera et al., 2011), varying from -20°C for liquid phase injection to 40°C for supercritical phase injection. The studied pressures varied from 4.2 to 8 MPa. Additionally, Silva (2015) gave an example of the temperature range of injection and it can be from -10°C to 40°C, and the pressure of injection can be from 4 MPa to nearly 10 MPa based on the injection model. Finally, Li et al. (2015) also indicated low-temperature conditions at the wellhead in order to study the effects of shut-in and start-up operations.

Wellbore integrity can be achieved by the study of fractures to prevent leakage of CO_2 during injection or afterwards due to reactivation of pre-existed fractures. Segall and Fitzgerald (1998) highlighted that shear-slip of pre-existing fracture might occur due to temperature fluctuation. All these fractures, stresses, different pressures, and temperature fluctuations during CO_2 injection could compromise the storage capacity of the storage site. Appropriate constitutive theoretical models that can predict the behaviour of rock under certain loadings and relevant experimental work and numerical simulations with the aim of optimising the parameters used in the constitutive models for CO_2 storage are essential.

To prevent migration of CO_2 and maintain isolation of geological formations, hydro-mechanical effects on the wellbore have been extensively investigated concerning geological storage of CO_2 (Rutqvist et al., 2007; Rutqvist et al., 2009; Ferronato et al., 2010; Vilarrasa et al., 2010; Rutqvist, 2012). However, limited work has been done as far it concerns thermal loading due to low-temperature injected CO_2. Lower injection temperatures are energetically more efficient and should be considered. However, these injection temperatures can cause problems due to induced thermal stresses and phase changes in the injection tubing or formation. If the temperature inside the wellbore at any depth is different from the temperature of the rock nearby the wellbore wall, this will result in thermal stresses which can potentially induce damage (Vilarrasa and Rutqvist, 2017). These thermal stresses tend to bring the stress state closer to failure as effective radial stresses are reduced (Segall and Fitzgerald, 1998). One example of effective stress reduction can be seen in Figure 2.2, with Mohr's circle reaching the yield surface after colder CO_2 injection for a period of 5 years. One disadvantage of injecting at lower temperatures than the formation is that liquid CO_2 can induce a combination of hydro-mechanical and thermo-mechanical effects that could cause wellbore damage due to tensile stresses (Vilarrasa et al., 2013).

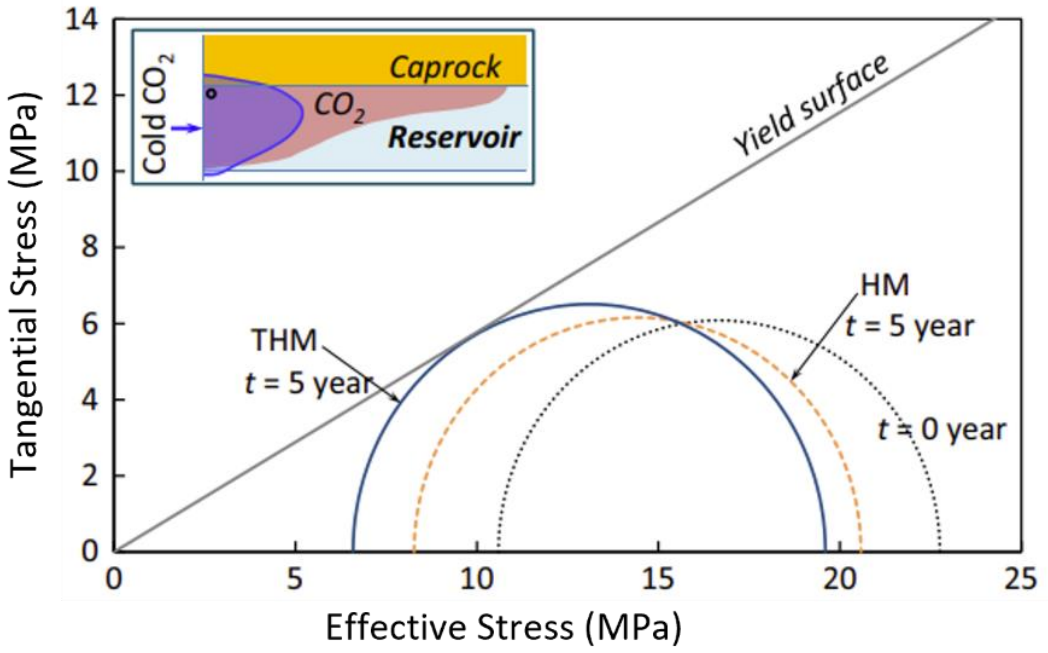

Figure 2. 2 Mohr-circles in a strike slip stress regime prior to injection of CO_2 (t=0 year), after 5 years of CO_2 injection in thermal equilibrium with the formation (HM) and after 5 years of cold CO_2 injection at 20℃ in a 55 ℃ reservoir (Vilarrasa, 2016).

In this PhD study, for the numerical simulations, the injected pressure of CO_2 for the simulations range from 2 to 6 MPa and the injected temperatures vary from -15℃ to 5℃, based on the research of Vilarrasa et al. (2013). In this way the injected CO_2 would remain in the liquid phase. The low temperatures scenarios, compared to the formation temperature injection, would suggest the possibility of reducing the cost and the energy spent for heating up the liquid CO_2, before injection from the ship, by ensuring the wellbore stability.

2.1.4 Reservoir and wellbore formations in the North Sea

In order to apply the double-porous fractured medium concept and estimate the THM effects on the wellbore wall, a specific type of rock with certain characteristics needs to be investigated. The North sea is a semi-enclosed, epi-continental large marine ecosystem in northern Europe (Ducrotoy et al., 2000). Previous oil and gas exploration, and the plentiful availability of the saline aquifers on the sea bed, indicate that the North Sea is geologically stable enough to store carbon dioxide under pressure (Hills et al., 2016). According to the Earth's geological history, Triassic is the thickest and most geographically extensive of the Mesozoic systems in the central and northern North Sea (Lervik et al., 1989). It is followed by the Jurassic and Cretaceous periods. Upper

Jurassic Shales, Middle Jurassic coaly sourced marine sandstones, fluvial sandstones, mudstones, evaporites, and volcanic are the main rocks that exist in the North Sea (Heinemann et al., 2012; Taylor et al., 2015; Petersen and Hertle, 2018) and fine-grained rocks like Carboniferous coal-measures sandstones are common reservoir rocks throughout the North Sea basin (Hawkins, 1978; Hangx et al., 2013).

Throughout the literature, sandstone is considered as one of the best rock formations for CO_2 storage due to its petrophysical and mineralogical properties (Gholami and Raza, 2022). Sandstones existing in the North Sea are mainly composed of well sorted and rounded to sub-rounded quartz, feldspar and rock fragment grains (Brook et al., 2003). Apart from quartz, silicates like clays and zeolites may exist and carbonates like dolomite and calcite, which possibly have different reaction kinetics with CO_2 (Hangx et al., 2013; Gholami and Raza, 2022). The advantage of sandstones for CO_2 storage, is the presence of sufficient quartz and diagenesis of the sandstone at high depths, causing grain-to-grain contact and thus low influence of CO_2 on the mechanical properties of the reservoir (Hangx et al., 2013). Another advantage of using sandstone as a reservoir is increased storage capacity due to mineral and capillary trapping (Gholami and Raza, 2022). According to Taylor et al. (2015), there is adequate porosity and permeability to support commercial hydrocarbon production in the Central Graben area of the North Sea, parted of sandstone, and consequently this type of rock needs to be examined further. Examples of sandstone porosity in the North Sea are: Jurassic Fulmar sandstones range from 21 to 33%, Triassic Skagerrak sandstones ranges from 16 to 27%, Rotliegend sandstones in the southern North Sea vary from 13 to 18% and Bunter's sandstone's average porosity, calculated from 603 core plugs, was 18.7% (Brook et al., 2003; Taylor et al., 2015).

The capacity of the southern North Sea Bunter sandstone saline aquifer for CO_2 storage is 7.8 Gt, while the total CO_2 storage potential of the UK sector of the southern North Sea, including closed structures, is 14.3 Gt (Heinemann et al., 2012). A specific example is the commercialised Northern Endurance project with a reservoir consisting of Bunter sandstone and potential capacity of around 450 Mt (Brook et al., 2003; Gluyas and Bagudu, 2020; Page et al., 2020). However, the central North Sea, with a maximum capacity of 40Gt, has greater storage capacity and mainly consists of Forties Sandstone, a fine to coarse sandstone interbedded with medium to dark grey siltstone and mudstone (Bentham et al., 2014). Another example of an injection site located offshore in the North Sea is the Goldeneye depleted gas field with up to 20 Mt of storage capacity (Marshall et

al., 2016). It is mainly parted of poorly consolidated, carbonate and quartz-cemented Captain Sandstone (Hangx et al., 2013). Additionally, primary reservoirs based on Taylor et al. (2015) are parted of shallow marine sandstones of the Middle Jurassic Fulmar Formation and fluvial sandstones of the Triassic Skagerrak Formation.

It can be said that fine-grained rocks exist in the North Sea's potential CO_2 storage sites which must be thoroughly analysed mechanically and thermally (Heinemann et al., 2012; Noy et al., 2012; Agada et al., 2017). Numerous challenges, however, can arise from the choice of injection temperature and pressure of CO_2. For all the above reasons the selected studied rock for this project is fine-grained sandstone.

2.2 Constitutive modelling

To set up the constitutive model, research must be firstly conducted on the parts that make up the model. In this section, the reason for representing rock as a double porous medium and models available in the literature are carefully reviewed. Additionally, plasticity models, damage models, thermal-mechanical effects, and permeability evolution theories are presented. These components form the final THM model, consisting of the equations describing the deformation, flow and heat transfer.

2.2.1 Porous media, multi porosity and flow model.

A porous medium can be defined as collection of solid bodies, with sufficient open space within the solids to enable fluid to pass. It is a percentage of space occupied by heterogeneous or multiphase matter (Khalili and Valliappan, 1996). Rock is the most common geological medium, referred to as porous medium that may also contain fractures. Early models of single porosity were only applicable to homogeneous rocks without fractures. The drawbacks of the single porosity models are outlined in many studies, with the main disadvantages being the representation of the fracture and porous distribution by an oversimplified average single pore domain in a represented block (Wilson and Aifantis, 1982; Khalili and Valliappan, 1996). However, in some geological rock formations fractures are important to be included in THM analyses especially for those associated with CO_2 sequestration (Bear and Corapcioglu, 1981; Ma and Zhao, 2018). Therefore, double-porosity models are the most appropriate for these applications. They are characterised by two flow areas, the porous rock matrix and fractures between rock blocks. There is mass and

energy exchange between these two porosities due to the flow of liquids and gases. The decomposition of a double porous medium into two overlapping single porous media can be seen in Figure 2.2.

The first double porosity models were possibly proposed by Barenblatt et al. (1960) and Warren and Root (1963). The theory of double porosity models was firstly extended to deformable porous media by Duguid and Lee (1977). Afterwards, Aifantis (1980) proposed a coupled double porous media flow model to describe fractured porous media. Based on the model of Aifantis (1980), other investigations were also undertaken to modify Aifantis's formulation (Wilson and Aifantis, 1982; Khaled et al., 1984; Khalili-Naghadeh and Valliappan, 1991; Bai et al., 1999). The most accurate coupling formulation was proposed by Khalili and Valliappan (1996). Their model contained three phases: one fluid, two porosities and a solid skeleton. Ma and Zhao (2018) extended this study to rock formations and considered plastic and continuous damage effects. However, they neglected thermal effects both on the deformation of the fractured media and on the fluid pressures. Gelet's et al. (2012) introduced the thermal effects on the double phased medium but considered only the elastic response of the material. Therefore, it can be outlined that there is need, for applications like CCS, for a robust THM elastoplastic double porous model that considers continuum damage effects and can describe the rock nearby the wellbore.

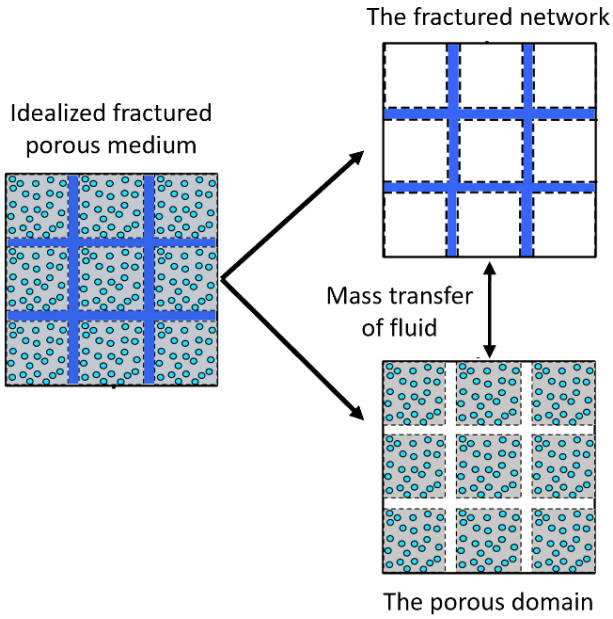

Figure 2. 3 Decomposition of the fractured porous network in two coexisting systems. Mass transfer or leakage between the fractured and porous domain (Gelet, 2011)

2.2.2 Plasticity Models and Yield surface

Conventional plasticity theory usually assumes a yield surface. Inside the yield surface, the material behaves elastically. Plastic flow can be only achieved when the stress state reaches the yield curve. The change in the shape of the yield surface "yield evolution", is mainly controlled by strain hardening or softening (Lemaitre, 1985a; Dafalias and Herrmann, 1986). Generally, the main features of conventional plasticity are isotropic hardening, associated with a flow rule and pure elasticity inside the yield surface (Khalili-Naghadeh and Valliappan, 1991).

Several elastoplastic models have been proposed in the literature, to manage the corner regions of Mohr-Coulomb failure and replace them by smooth yield curve to avoid difficulties during implementation of numerical codes. Some of the most widely used are: the modified Cap model, which is applied to quasi-brittle rocks with low and medium porosity (Fossum and Fredrich, 2000; Khoei et al., 2004; Dolarevic and Ibrahimbegovic, 2007), the Cam-Clay model applied to soft rock with high porosities (Shah, 1997; Bigoni and Piccolroaz, 2004; Carter and Liu, 2005) the double surface failure model, which is a general constitutive model for soft rocks in their saturated state (Zhou and Zhu, 2010), the hierarchical model for frictional materials (Mortara, 2009), the Drucker-Prager model for concrete or rock formations (Arslan, 2007; Alejano and Bobet, 2012; ZHANG et al., 2013) and the bounding surface model (Guo and Wan, 1998; Lü et al., 2004). Most of these models are usually applied to specific rock types or other materials, assume an elastic regime inside the yield surface, which may cause a sharp transition from the elastic to the elastoplastic domain.

The bounding surface plasticity was firstly proposed for metal materials by Dafalias and Popov (1975). Afterwards, the theory was applied to soil mechanics for sands or granular material under monotonic and cyclic loading (Dafalias and Herrmann, 1986; Wang et al., 1990; Khalili et al., 2005). For concrete material, the first study to apply the bounding surface concept was Fardis et al. (1983) followed by many investigations (Han and Chen, 1985; Fardis and Chen, 1986; Voyiadjis and Abu-Lebdeh, 1993). The bounding surface plasticity extends the conventional theory by defining that the elastic behaviour disappears within the yield envelope (Habte, 2006). This indicates there is no transition from the elastic to the elastoplastic behaviour but they both occur at any stress level.

For rock materials, the application of the bounding surface plasticity model can be found in the work of Guo and Wan (1998), Masoumi et al. (2016), Ma (2016), Kang and Liao (2019) and Huang

et al. (2022). The fundamental elements of the bounding surface model, as also seen in Figure 2.3, according to Dafalias and Herrmann (1986) and Khalili et al. (2005), are:

- The model defines the acceptable and rejected states of stress
- A loading surface in which the current stress lies
- A plastic potential to simulate the magnitudes of plastic deformation
- Hardening rules that can control the bounding surface evolution determine the distance between the current stress state σ' and the stress state $\breve{\sigma}'$ at the bounding surface, with the direction being defined by a normal vector n.

As the mechanical behaviour of rock, especially sandstone shows some similarities to that of soil and concrete, it is reasonable to consider the bounding surface theory works satisfactorily with those materials (Cuss et al., 2003).

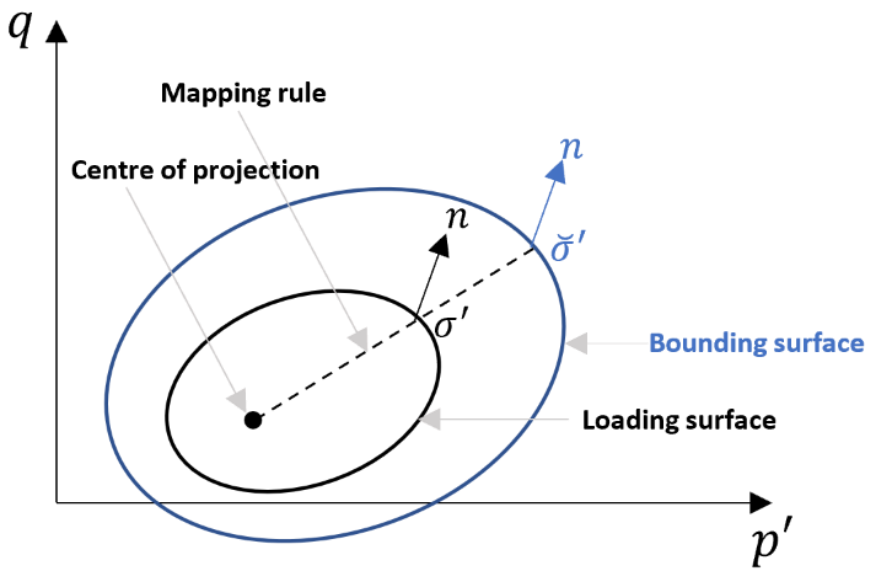

Figure 2. 4 Schematic illustrations of the principles of bounding surface plasticity (Khalili et al., 2005)

2.2.3 Continuum Damage Models

2.2.3.1 Macroscopic approach using average microscopic inputs

Kachanov (1980) was the first to propose a continuum damage model. Afterwards, Lemaitre (1985a) studied dissipation and low cyclic fatigue in metals using continuum damage considerations. Continuum Damage Mechanics (CDM) was firstly introduced to study brittle

material by Dougill (1976) and Krajcinovic (1989). They developed thermodynamic theories of anisotropic damage and detailed the damage evolution for brittle and ductile materials.

There are two main classes of damage models: micro-mechanics and macro-mechanics models. In the micromechanics models, the propagation of crack density or the growth of a single crack is analysed and then related to a macroscopic level. One of the basic techniques is the "homogenisation technique" or "micro-to-macro transition", which is applied to homogenise the heterogeneity of a rock created by micro-cracks and average it into an equivalent continuum macroscopic representative volume element (Charlez, 1997; Pensee and Kondo, 2003; Yuan and Harrison, 2006). Some models based on micro-mechanics have been proposed as follows: the frictional sliding of the micro-cracks model (Brignoli and Sartori, 1993), the micro-crack closure model (Pensee and Kondo, 2003), the anisotropic damage model (Brignoli and Sartori, 1993; Pensee and Kondo, 2003), and the modified model considering the density and direction of the micro-fissures (Shao and Rudnicki, 2000) as well as many others. However, the difficulty in estimating the microscopic properties of faults makes these models impractical, and the "homogenisation techniques" are empirically based on fitting curves to experimental data and do not consider deformation mechanisms (Chen et al., 2010; Ma, 2014b). Confining pressures and porosity evolution cannot also be captured, setting limits to the estimation of brittle-ductile transition and failure. Some alternate approaches have been proposed considering confining pressure degradation index (Fang and Harrison, 2002a; Fang and Harrison, 2002b), but these models lack sufficient mechanistic validation. However, at the macroscopic level, the focus is based on the change of the mechanical properties such as stiffness and strength due to damage evolution (Charlez, 1997; Yuan and Harrison, 2006). Some macro-mechanics models are: the rigorous continuum damage model of Lemaitre (1971) based on the framework of thermodynamics, the continuum damage model (Yazdchi et al., 1996; Guo and Wan, 1998), the bounding surface plasticity-damage model that influences the strength of brittle and semi-brittle materials under low to medium confining pressure (Shao et al., 2006b; Chen et al., 2010; Ma, 2014b).

2.2.3.2 Damage evolution and fractures

To describe damage evolution in a rock formation, a damage variable is considered, defined as the ratio between the damaged part to the whole rock material (Voyiadjis and Kattan, 2005). This

damage variable quantifies the effects of fissures on the total strength of the rock, fracture propagation, pore collapse and other failure modes. The assumption of isotropic damage is usually sufficient to give a robust prediction (Lemaitre, 1985a; Yazdchi et al., 1996; Burlion et al., 2000). Usually, in the literature, the damage energy release rate and damage threshold value are presented (Wohua and Valliappan, 1998; Shao et al., 2006a). The damage strain energy release rate expresses the general resistance to damage growth and depends on the damage variable (Wohua and Valliappan, 1998). The damage evolution threshold can be found as a function of stress-strain and damage percentage as in the research of Shao et al. (2006a), Guo and Wan (1998), Chen et al. (2010) and Salari et al. (2004). If the damage strain energy rate is bigger than the damage threshold value, the damage variable increases (Wohua and Valliappan, 1998). A constant value of damage is also experimentally investigated in the research of Lemaitre (1985a) , Yazdchi et al. (1996) and Fahrenthold (1991).

Two main damage hypotheses can be identified throughout the literature:

1. Strain equivalence (Lemaitre and Chaboche, 1975)
2. Complementary energy (Valliappan et al., 1990)

The strain equivalence hypothesis indicates that strain associated with a damage state under applied stress is equivalent to the strain linked with the undamaged condition under effective stress loading. It is only, however, applicable to isotropic damage materials (Yazdchi et al., 1996). The complementary energy hypothesis indicates that the complementary energy of a damaged state is equal to that of the undamaged, under effective stress loading (Zhang et al., 1990b; Han, 2003).

As far as it concerns the damage evolution law, three different approaches are used in the literature. The first is the explicitly defined damage evolution law approach, which relates the parameters to the material's mechanical properties, gives accurate predictions, and the parameters used have physical meaning and can be experimentally calibrated (Fahrenthold, 1991; Yazdchi et al., 1996; Guo and Wan, 1998; Chen et al., 2006). The other two approaches are the damage consistency approach (Shao et al., 2006a; Chen et al., 2010; Zhou and Zhu, 2010) and the energy dissipation potential approach (Lemaitre, 1985a; Wohua and Valliappan, 1998; Mohamad-Hussein and Shao, 2007). Both do not consider the macroscopic behaviour of rock, which is in contrast with the constitutive model principles. However, these two approaches are widely used (Lemaitre, 1985a; Salari et al., 2004; Shao et al., 2006a)

2.2.4 Permeability evolution model

One aspect which has gained much attention in CO_2 sequestration is the evolution of permeability of the rock formation due to different loadings. The change in the permeability can influence the strength of the material (Figueiredo et al., 2015; Zhao et al., 2019). Many theoretical investigations were undertaken to ascertain the evolution of permeability with damage (Zhu and Wong, 1997; Morris et al., 2003). Morris et al. (2003) developed a simple, but robust constitutive model, where the complex behaviour noticed in experiments was simulated by combining the effects of dilation (creation of new pores) and compaction (crushing of incipient pores). These two effects were modelled as competing processes, with the predominant one indicating whether the material dilated or compacted. Morris et al. (2003) used macroscopic variables for damage evolution, and their theoretical constitutive permeability model was in good agreement with the experimental work of Zhu and Wong (1997). However, significant differences between the model and the experimental work occur at low effective stresses due to the assumption that the damage at low and high effective stress has the same type of influence upon the porosity and permeability influence (Morris et al., 2003).

Additionally, many other models were also proposed to predict the permeability evolution of the fracture network based on different loading conditions. Some of them are fracture network models (Zhu and Wong, 1996; Zhu and Wong, 1999; Bernabé et al., 2010), the discrete model of Pan et al. (2010) and different constitutive models (Rudnicki 2001; Yale, 2002; Gessner, 2009), etc. Nevertheless, most of these models are oversimplified or too complicated, making them unfeasible for application. The most widely accepted constitutive model is the generalised power law, which is defined in the permeability porosity space (Zhu et al., 2007; Morris et al., 2003; Bernabé at al., 2003). However, most of these models were empirical and based on curve-fitting sets without considering damage-induced pore collapse and the creation of new fractures. Generally, there is a lack of constitutive models that can address the permeability evolution caused when various loading paths, confining pressures, and hydro-mechanical damage processes are applied together (Ma and Zhao, 2018).

2.2.5 Thermal considerations

2.2.5.1 Heat transfer type and thermo-elasticity

Heat transportation in a fractured porous medium can be achieved by conduction, convection, and radiation. In THM models conduction is the most dominant heat transfer mode. Earth's crust modelling forced convection is normally implemented in large fissure networks but free convection is used in soil modelling (Gelet, 2011). Bear and Corapcioglu (1981) introduced the effect of convection in the energy balance equation describing the effects of temperature in the thermoelastic aquifer when hot water injection or field pumping took place. Nair et al. (2004) considered both convective and conductive effects in the FEM of their THM model. However, their energy equation did not couple with the mass conservation equations for the fluids. Finally, Pao et al. (2001), in a three-phase non-isothermal model, found that convection influenced pressure and temperature distribution significantly.

Throughout the literature, elastic temperature effects in the porous fractured media can be divided into two categories. The first is the effect of the temperature on the fundamental parameters of the porous medium (Youssef, 1961; Laguros, 1969), and the second one is the influence of temperature on the volume change of the medium (Delage et al., 2000; Tao and Ghassemi, 2010). The primary focus of this research is on the latter. When a rock is parted of the solid medium and fully saturated pores and fissures, the temperature fluctuation will cause the solid and fluid volumes to change and therefore influence the stress and pore-fissure pressure distribution (Tao and Ghassemi, 2010). There is a considerable amount of work in the literature extending the isothermal theory to the solid and porous domain (Schiffmann, 1971; Bear and Corapcioglu, 1981; McTigue, 1986; Savvidou and Booker, 1989; Zimmerman, 2000; Khalili and Selvadurai, 2003b; Gelet et al., 2012a; Bai, 2016b).

Rock plasticity effects due to thermal loading, can be considered only for elevated temperatures, while ignored for lower than 30°C temperatures (Hueckel and Borsetto, 1990; Hassanzadegan et al., 2012; Gajo and Bigoni, 2015b). Even though reservoir temperatures may be bigger than 30°C, thermo-elasticity will be assumed in this research for simplicity. Free convection and radiation are also neglected in this study.

2.2.5.2 Isothermal and non-isothermal models

McTigue (1986) is one of the most cited research articles that considers local thermal equilibrium in rock and provides analytical results for the thermo-elastic behaviour of saturated porous rock with single porosity. It outlines the importance of fluid flow in the heating process. The thermo-mechanical behaviour is based on Biot's (1941) poro-elasticity theory and on the isothermal theory of Rice and Cleary (1976). The characteristics of McTigue's model is that the thermal expansion of the porous medium is controlled by the solid skeleton only, the constitutive diffusion equations are based on Darcy's and Fourier's laws and a reduced form of the energy balance equation are presented as convective transport. Thermo-elastic couplings are neglected. Masters et al. (2000), assumed local thermal equilibrium among all phases and only one temperature is considered. Both convection and conduction are included, and Masters et al. (2000) validated their model with a double porosity isothermal problem and one non-isothermal single porosity example.

For non-isothermal conditions, much work is presented in double porous media throughout the literature. Bowen and Garcia (1970) introduce a thermo-mechanical theory of a mixture, in which each phase has its own temperature, considering non-linear elasticity, non-linear heat conduction, non-linear viscosity, and diffusion. Aifantis (1980) and Aifantis and Beskos (1980) were among the first to attempt non-isothermal models in fractured media, based on the assumption that the flow mechanism is convective in the fractures and conductive in the porous phase. Heat transfer between the phases is considered, whereas the variation of internal energy of the fluid with respect to pressure changes is neglected. De La Cruz and Spanos (1989) coupled temperature variation and mechanical motion by considering separate temperature and heat transfer parameters for each phase of the saturated porous medium.

Gajo (2002), following the work of Pecker and Deresiewicz (1973), created a model in which each phase has its own temperature, validated against a hot fluid scenario and investigated the effects of convection, the volume change of each phase and their coupled interaction. Gelet et al. (2012b) presented a robust model for fractured rock saturated with a single fluid. They considered a separate energy balance equation for each phase, and inter-phase energy transfer was included in addition to mass transfer. The leakage of fluid between the phases was also investigated.

It can be suggested that non-isothermal conditions exist in double porous media during thermal loading, due to different thermal diffusivity of the fluid in the pores and fissure and of the solid

grains. However, adopting a non-isothermal model raise two issues: the correct determination of the work conjugate variables that describe the constitutive couple laws and the heat transfer parameters at each phase (Gelet et al. 2012). For the current research and for simplicity, the assumption that pores and fissures have the same temperature at each time step is adopted, i.e., the phases are in thermal equilibrium, based on Gelet et al. (2012). One energy balance equation is written for the entire system, and the thermal interaction between the liquid of the porous and fracture domain is not captured. However, leakage between the phases is considered.

2.2.6 Fully coupled Thermo-Hydro-Mechanical (THM) constitutive models

Coupling mechanical, hydraulic and thermal effects on fractured porous medium is important to describe efficiently the rock behaviour at different conditions. The first fully coupled flow-deformation analysis for elastic responses of saturated single porous media was considered in Biot (1941). The model has been widely adopted to describe pore pressure and effective stress distribution in saturated porous media (Detournay and Cheng, 1988; Cheng et al., 1993). Throughout the literature, the most basic principles of THM modelling can be considered by Terzaghi's consolidation theory (von Terzaghi, 1923), Biot's theory of elasticity (Biot, 1941) and mixture theory (Goodman and Cowin, 1972; Bowen, 1982).

In recent years, more advanced models have been developed, for example models that consider plasticity effects (Guo and Wan, 1998; Mortara, 2009; Sinha et al., 2010; Zhou and Zhu, 2010; Xu et al., 2012; Huang et al., 2015; Zang et al., 2016; Ma et al., 2016). Furthermore, a new pattern that was adopted in the constitutive modelling of rock is coupling elastoplastic models with micromechanics and continuum damage models. In the coupled plasticity-damage models, strain softening and changes in elastic stiffness can be captured by the damage model, while irrecoverable strain and the residual state are simulated by plasticity theory (Nguyen, 2005). This coupling is essential, as pure continuum damage models cannot reproduce permanent deformations (Ma and Zhao, 2018), and this becomes even more complicated when the unloading-reloading cycle is applied.

According to Lemaitre (1985a) and Lemaitre (1992), two approaches can be used in the coupling between damage and plasticity theories, which are the direct state coupling and indirect kinetic coupling. In the direct state coupling, the deterioration of material strength is achieved by setting the elastic stiffness as a decreasing function of the damage fluctuation, while the damage criterion

and yield function are determined using effective or latent stress (Zhou and Zhu, 2010; Salari et al., 2004; Chen et al., 2010). However, this coupling does not consider the actual interaction between damage and plasticity, as plastic strain and damage are mainly independent (Nguyen, 2005). On the other hand, the indirect kinetic coupling can be a combined function of damage energy dissipation and plasticity strain, or two separate damage and plasticity functions (Wohua and Valliappan, 1998; Mashayekhi et al., 2005). Even though a combined function is more straightforward, it introduces high difficulty in identification of model parameters, which restricts the model application. Two separated functions have the advantage that an increase in damage can be prescribed by a damage evolution law, while the plastic strain can be established by a flow theory coupled with plastic parameters (Chen et al., 2010; Shao et al., 2006).

Apart from mechanical and flow-deformation models, one other parameter affecting the behaviour of rock is temperature fluctuation, as mentioned in Section 2.3.5. Rock can be damaged by the freeze-thaw of fluids contained within it (Liu and Yu, 2011). Liu and Yu (2011) recommended a coupled THM model to describe the behaviour of unsaturated porous media during freezing. Their model was based on thermodynamics and fluid mechanics. It took into consideration elastoplastic design and the change of volumetric heat capacity and ice content during freezing. Following the same framework, Nishimura et al. (2009) recommended a fully coupled THM model with an elastoplastic constitutive relation, including pore ice water pressure. Khalili and Selvadurai (2003), proposed a fully coupled THM model for fully saturated elastic dual porous media, assuming local thermal non-equilibrium. Thermal convection is accounted between the phases, and three balance energy equations are proposed for the solid, porous and fracture domains (Khalili and Selvadurai, 2003b). Furthermore, the constitutive equations proposed by the THM model of Gelet et al. (2012) can be used to identify the possible failure of a borehole exposed to both temperature and pressure gradients. Tan et al. (2011) set up a coupled thermo-hydraulic model describing the heat transfer and temperature distribution as well as the water migration. They suggested a fully THM combined with a damage theory model, which could analyse the freeze-thaw stability of a tunnel under severe conditions. Huang et al. (2018) did a validation of the THM laboratory test conducted by Neaupane and Yamabe (1999) by comparing it to a theoretical THM model, which was also numerically analysed, and found a good prediction of heat and frost energy dissipation. Their validation demonstrated that all the critical parameters, including pore ice pressure, permeability, and thermal

energy, were linked to the unfrozen water content. However, their test was limited to homogeneous and isotropic rock in which thermal transmission was the same in every direction during freezing.

In this PhD thesis the theoretical formulations of Khalili's and Selvadurai (2003) and Gelet's et al. (2012) are adopted, considering also elastoplastic and continuum damage effects based on Ma (2014). A schematic representation of linking THM to plasticity, damage and hardening effects is also presented in Figure 2.5.

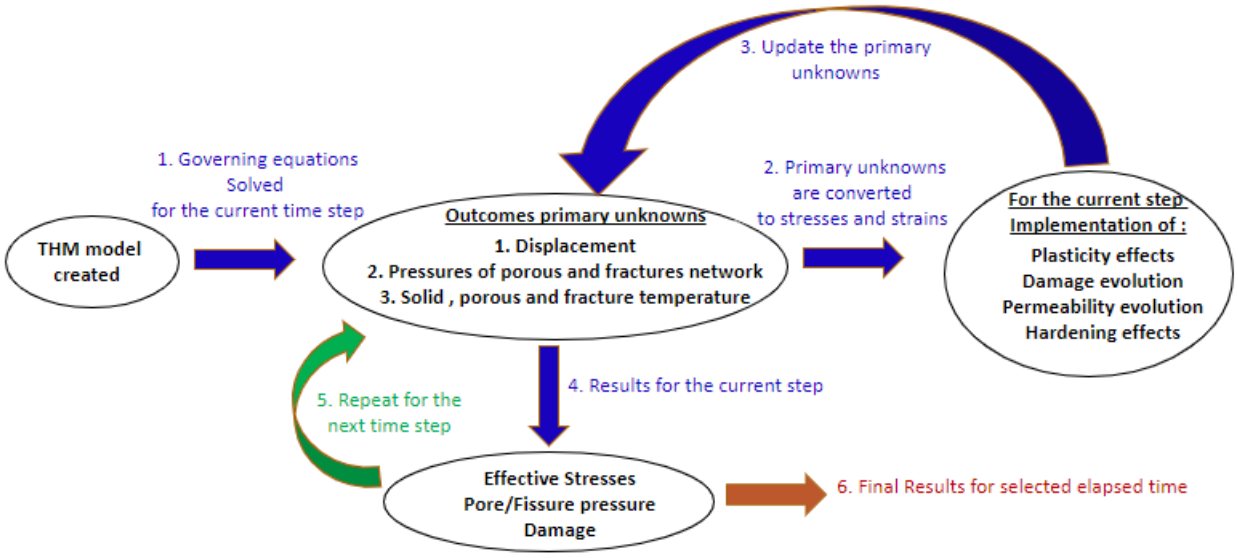

Figure 2. 5 THM link to damage theory, plastic deformation, and hardening effects

2.3 Experimental Investigations

2.3.1 Uniaxial (UCS) and Triaxial tests

Apart from theoretical models, the rock being used for CO_2 sequestration can be experimentally investigated using triaxial apparatuses and the mechanical properties of rock can be estimated. In this way THM models, like in Section 2.3.6, can be validated, or improved, and the wellbore breakout pressure under various conditions can be found. One of the first experimental works on fracture and flow in rocks that introduced the use of a True Triaxial Test (TTT apparatus) was undertaken by Mogi (1971) and is illustrated in Figure 2.6. They suggested that yielding or fracture of a region occurs when the distortional strain energy stored in the area reaches a critical value that can be increased with the effective mean pressure. Mogi (1971) also suggested that in deep formations, fracturing is higher than expected in a convention triaxial compression experiment due

to potential sudden energy release or earthquake, as high principal stress σ_1 values cause the decline in ductility. From the results of Mogi (1971), fracture and flow properties of rock were also deduced. After the development of the Mogi-type apparatus, many apparatuses were created which imitated and improved Mogi's experimental setup (Spetzler et al., 1981; Xu et al., 1990; Haimson and Chang, 2000).

UCS and triaxial tests have been used to characterise the mechanical properties of different rocks at temperatures, range from 30℃ to 1200℃ (Rao et al., 2007; Wu et al., 2013; Kong et al., 2016; Zhu et al., 2016; Yang et al., 2017; Yang et al., 2021). They help predict the behaviour of rocks under true subsurface conditions at depths of engineering interest. Results of UCS and triaxial tests showed that rock mechanical properties were highly reliant on temperature (Yang et al., 2017; Xiao et al., 2021). For sandstone, the Elastic modulus E shows almost a linear decrease when increasing the temperature from 30℃ to 1000℃, while when the confinement increases, the elastic modulus is slightly changing (Wu et al., 2013; Yang et al., 2017). Whilst high-temperature characterisations are beneficial for geothermal energy applications and conventional CO_2 injection, the mechanical properties of rocks and specifically sandstones at low temperatures ($T<0^oC$) are poorly investigated in the literature. Although, there have been several studies on clay and sand at low temperatures (Bragg and Andersland, 1981; Painter and Karra, 2014; Yugui et al., 2016; Watanabe and Osada, 2017) there are limited UCS and triaxial tests on frozen rock. It is important to study the mechanical behaviour of frozen rock, as freezing can be achieved due to Joule-Thompson effect or due to sub-zero ship CO_2 injection (Torsæter et al., 2017). Some of the experimental tests considering low temperature effects are: the UCS and indirect tensile tests of Kodama et al. (2013), which investigated the variation in strength and failure process of frozen rocks; the UCS and triaxial tests of Wang et al. (2019a), which indicated increase in tensile and compressive strength of sandstone due to temperature drop from 20℃ to -4℃ while further freezing had no mechanical impact; and the freeze-thaw cycles study of Liping et al. (2019), which indicated increase in porosity and microfractures in rocks.

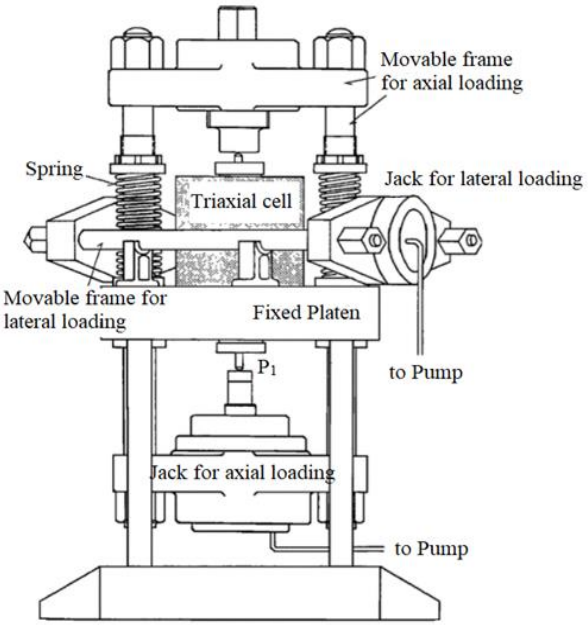

Figure 2. 6 Schematic diagram of triaxial compression apparatus (Mogi, 1971)

2.3.1.1 Failure mechanisms of rock under different confining pressures

Rock failure on a micro-scale is a process of micro defects initiation, propagation, nucleation, further extension and final failure (Wohua and Valliappan, 1998). In macro-scale response, it is characterised as elastic and plastic deformation, including the decrease of the strength or load-bearing capacity (Ofoegbu and Curran, 1991). Moving from low to high confining pressure, the peak strength of the rock increases and there is an apparent transition from brittle failure to ductile failure at a certain confining pressure (Sheorey, 1997; Wong et al., 1997b). However, transition from brittle behaviour to ductile is not only due to confinement, but depends also on physical parameters such as geothermal gradient, strain rate and activation energy (Dragoni, 1993). Sedimentary rocks like those exist in the North Sea and influenced by CCS procedures, change their properties by increasing the burial depth (Bjørlykke and Høeg, 1997). It should be also mentioned that depth increases cementation and consequently the strength of the rock, while lateral stress and temperature will tend to reduce brittleness (Goodman, 1989; Bjørlykke and Høeg, 1997; Ishii et al., 2011; Meng et al., 2021). At certain low confining pressures, depending on the type of rock, usually less than 30 MPa for sandstones, the rock experiences a quick fracture at the start of dilatancy, followed by brittle failure. (Fredrich et al., 1989; Baud et al., 2000; Shimada, 2000; Ma, 2014b). In contrast, for high confining pressure, usually larger than 50 MPa for sandstones, only

ductile failure occurs (Khan et al., 1991; Baud et al., 2000; Shimada, 2000; Ma, 2014b).It should also be mentioned that the rocks under high confining pressure show higher strength, as it is more difficult for faults or micro-cracks to propagate (Chen et al., 2006). Additionally, plastic flow and damage evolution are highly dependent on the confining pressure applied (Mohamad-Hussein and Shao, 2007).

2.3.2 Permeability tests

With regards to permeability, experimental tests throughout the literature were the main way to examine its evolution on a rock due to hydro-mechanical damage. One of the first experimental investigations on permeability evolution is the research of Zoback and Byerlee (1975) on granite, under increased axial stress at several confining pressures. Shi and Wang (1986), following the experimental permeability results under confining pressure and shear stress of Morrow et al. (1984), suggested that effective stress-permeability relationship follows a power law and that permeability and porosity are dependent not only on the current applied load but also on the stress history (David et al., 1994). Several triaxial compression, extension, and hybrid tests, based on the theoretical models described previously, were conducted to analyse the effects of hydrostatic and deviatoric stress as well as the damage on rock mass (David et al., 1994; Zhu et al., 2007). Experimental results revealed that the mechanical behaviour and permeability expansion under different loading paths were remarkably similar. Both porosity and permeability decreased when the mean effective stress increased, with the most exceptional reductions being developed after the commencement of grain crushing and pore collapse, while permeability increased with increasing pore pressure (Zhu et al., 2007; Jasinge et al., 2011).

Moreover, fractures and faults can create high permeability fluid flow pathways through the surrounding caprock (Tenma et al., 2008). Mitchell and Faulkner (2008) presented experimental data on the continuous evolution of permeability pore volume of crystalline rock under increasing differential stress, by using the pore pressure oscillation technique and triaxial tests. It was found that initially pore volume and permeability decrease with loading followed by permeability increase up to sample failure. This was explained by initial axial crack opening and transverse crack closure (Mitchell and Faulkner, 2008). Walker et al. (2013) did a combination of field, microstructural and experimental permeability tests to determine the fault permeability structure evolution in basalts. Effective pressure enhanced permeability due to cracking was identified.

Frash et al. (2017) investigated the influence of stress on rock permeability due to fracturing by using an X-ray compatible triaxial direct-shear apparatus, which was developed by Carey et al. (2015) and modified by Frash et al. (2016). The main adjustment Frash et al. (2016) made was the introduction of thrust collars to limit specimen rotation, allowing higher confining stresses and improving the certainty of permeability measurements. Frash et al. (2017) suggested that permeability induced by fracturing is significantly reliant on the stresses at which the fractures are being created, the magnitude of shearing displacement and the duration of the flow. The highest permeability difference that observed was between specimens that fractured at low and high stresses. For future studies, different material tests, the study of more extensive fractures and different directions of fluid flow inside the caprock was proposed (Frash et al., 2017). Zhu et al. (2021) did dynamic compression tests to study the mechanical behaviour and permeability evolution of sandstone after dynamic loading under realistic in-situ stress. Their results indicated permeability increased due to crack propagation and rock damage and fracture dependency on the absorbed energy. Finally, Cappa et al. (2022) did fault permeability evolution experiments, by injecting fluid in fractured limestone and suggested that transient evolution of fault permeability significantly influences fault stability during fluid flow and that permeability is linked to effective normal stress and slip.

2.3.3 Other thermal and CO_2 related experiments

Experimental work was also undertaken to determine the temperature fluctuation in rock formations. Neaupane et al. (1999), based on a theoretical formulation that accommodated linear stress-strain constitutive relationship with elastic considerations, undertook experimental tests on freeze-thaw of rock. Measurements investigated temperature and strain along different directions. The variation of temperature used was -20℃ to +20℃, and both the freezing and thawing phases had durations of 72 hours. The material used for the test was a sandstone collected from Sirahama district in Japan (Neaupane et al., 1999). It was found out that the freeze-thaw rock model had a satisfactory prediction of the temperature transfer and deformation behaviour obtained from experimental tests if the materials did not fail. However, Neaupane et al. (1999) considered only elastic effects during their research and as a result they proposed future studies to focus on irreversible and plastic effects, due to non-linearity of rock formations.

Further freeze-thaw experiments were undertaken throughout the literature by Fang et al. (2018), Fan et al. (2020) and Hou et al. (2022). Park et al. (2004) examined the thermal characteristics of granite and sandstone using an environmental chamber and thermal expansion techniques for a temperature range between -160℃ and 40℃. They found that thermal conductivity increased slightly with temperature drop, while specific heat and thermal expansion coefficient decreased.

Furthermore, an alternating water gas (WAG) core flooding study was performed by Mohamed and Nasr-El-Din (2012) under different temperatures and CO_2 injection rates. The results showed that for higher temperature and injection percentages, the permeability of cores increased due to CO_2 injection. Based on those experiments, Azin et al. (2015) did an experimental study examining different temperatures and pressures through a batch laboratory test. They investigated the mineralogical and chemical changes due to rock-brine-CO_2 interactions. Figure 2.7 shows the experimental setup of Azin et al. (2015) that can be used for future research to determine the relationship between temperature and pressure during CO_2 injection.

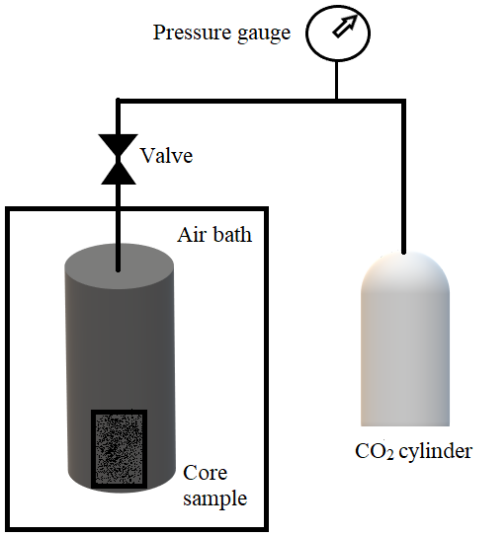

Figure 2. 7 Schematic of brine-CO_2-rock interaction experiment (Azin et al., 2015)

2.4 Numerical Analysis

Most available laboratory-scale experiments were restricted to low injection pressures and high-temperature conditions and, currently, have restraints on their applicability to real field situations (Rathnaweera et al., 2017). Thus, the importance of validating and developing appropriate laboratory-scale models using numerical packages is of extreme importance for wellbore stability

in carbon sequestration and the further exploration of reservoirs at high depths (Leary, 1991; Cui et al., 1997; Benson and Surles, 2006; Zang et al., 2017).

Several approaches have been used throughout the literature for the determination of coupled hydrologic, thermal, and mechanical stresses on a rock that can be used to address the behaviour of the material under CO_2 injection conditions. One of them was ROCMAS II, a finite element program with hydro-mechanical coupling for fractured porous media that assumes the fractures to be linear (Noorishad et al., 1992). Following the same idea, Swenson (1994) set up a code (GEOCRACK) that coupled hydro-mechanical features by also incorporating thermal fluctuations. This model used a discrete fracture network and ignored fluid depository in the rock matrix. Additionally, DECOVALEX (DEvelopment of COupled models and their VALidation against EXperiments) was an international cooperative study of coupled THM models in hard rocks, where numerical results were compared (Jing et al., 1995). However, all these models considered single porosity capability (Jing et al., 1995). For this reason, double porosity models started to appear to simulate fracture fluid flow. FEHM was a finite element method that could simulate rock behaviour by computing heat and fluid mass transfer (Bower and Zyvoloski, 1997). Bower and Zyvoloski (1997) modified a double porosity finite element code (FEHM) to couple hydrologic, thermal, and mechanical changes in a fractured storage area by permitting the permeability to change as the effective normal stress varied across the fracture. The modified FEHM code performed well compared to analytic results for the occasion of fracture flow increase due to a fissure opening under fluid pressure (Bower and Zyvoloski, 1997).

More recently, the TOUGH-FLAC simulator was developed (Rutqvist et al., 2002). TOUGH-FLAC is a numerical finite-volume multiphase flow code (TOUGH2-Pruess et al. (1999)) and finite-difference geomechanical code (FLAC^{3D} – Itasca, 2006). Cappa and Rutqvist (2011) used TOUGH-FLAC to investigate the coupled hydro-mechanical processes during fault reactivation. In the analysis of coupled thermo-hydro mechanical problems, TOUGH2 and FLAC^{3D} are performed on adaptable numerical grids and linked together as presented schematically in Figure 2.8. TOUGH-to-FLAC procedure is transferring information of updated temperature, pressures, saturation, and pore-pressure from the TOUGH2 simulation to FLAC^{3D}. There, thermal expansion and effective stresses are determined. Generally, the FLAC^{3D} computer code is used to determine a rock's geomechanical behaviour, while the TOUGH2 code used as a reservoir simulation

describing multiphase fluid and heat transportation. A separate batch program is used to control the coupling of TOUGH2 and FLAC^{3D}.

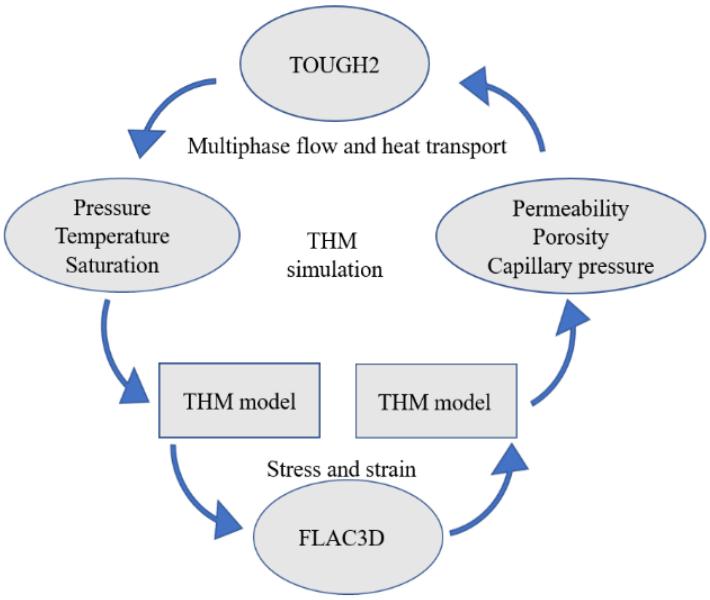

Figure 2. 8 Schematic linking of TOUGH2 and FLAC^{3D} for coupled thermo-hydro-mechanical simulations (Cappa and Rutqvist, 2011).

In addition to these numerical codes, Chen et al. (2010) set up governing equations for a coupled thermo-hydro-mechanical model of unsaturated porous media. They used a finite element method based on the Galerkin formulation to simulate their theoretical model. Numerical results indicated that the model was able to reproduce the main features of mechanical behaviour of shales. However, as the formulation did not consider a mass transfer equation, Chen et al. (2010) suggested that future studies should focus on investigating gaseous flows. Moreover, Ma and Zhao (2018) created a dual-porosity finite element model for the stability analysis of boreholes drilled in fractured porous media with the consideration of elastoplastic deformation and continuum damage. This analysis adopted the theoretical model of Ma (2016) and gave an approximate solution to the governing differential equations by using FEM. They found out that a more deformable geoformation may be followed by more damage being developed in the vicinity of the wellbore. This indicates that the pure elastic model underestimates effective stresses and overestimates the fluid pressure response and that plasticity consideration is important. Ma and Zhao (2018), following the work of Ma (2016), suggested a numerical model that can predict essential aspects of boreholes in fractured porous media but they did not consider any possible thermal effects that can be used as a complete guide for the setup of a fully coupled THM model.

However, the dimensional distributions for isothermal conditions of effective stresses and fluid pressures determined at different distances from the wellbore in the Ma and Zhao (2018) study, are in agreement with the numerical model of Gelet et al. (2012a). Additionally, the model of Ma and Zhao (2018) satisfactorily reproduced the plumbing test of Kazemi (1969) and the hydraulic fracturing test of Papanastasiou (1997). This indicates that the Ma's and Zhao (2018) research can be used as a guide for hydro-mechanical coupling effects.

Concerning CO_2 injection, Jie et al. (2016) made a comparison between analytical and numerical methods for an isothermal hydro-mechanical model of CO_2 geological sequestration based on Xu et al. (2012). They used a finite element solution based on an open-source solver 'Elmer' which was designed to simulate the entire period of carbon dioxide injection. Jie et al. (2016) suggested that the analytical method could be used to quantitatively calculate the problem of sequestration which is the thermo-hydro-mechanical effects, while the finite element model can offer more optimised results. Based on the numerical results, a shear-slip failure zone was determined, indicating the capability of estimating the maximum injection rate and temperature. Jie et al. (2016) neglected thermal stresses on pressure evolution and assumed a simplified temperature distribution in the aquifer. Despite this, the displacement on the top surface after ten years was in good agreement with the analytical and numerical simulation, showing only a 9% reduction of vertical displacement near the injection well. Jie et al. (2016) also proposed future studies to include more precise thermal effects to achieve more accurate results for deformation and fracturing evolution.

Vilarrasa and Laloui (2016) simulated cold CO_2 injection in deep saline rock formations and investigated the thermal expansion effects between the reservoir and cap rock, considering elastoplastic deformation for inelastic strains. For the setup of the THM coupled problem, they used the finite element numerical code CODE_BRIGH (Olivella et al., 1994) extended for CO_2 injection by Vilarrasa et al. (2013). Vilarrasa and Laloui (2016) concluded that irrevocable stresses took place within the cooled region of the reservoir, but that fracture instability did not expand into the caprock. However, some damage could be identified in the caprock in the cooled region, when the thermal expansion was greater compared to the reservoir.

Jen et al. (2017) investigated the performance of the reservoir under various injection pressures (1.3, 1.5 and 1.7 times the initial pressure) based on numerical simulations. The simulations in

their study used TOUGH2- MP/ECO2N (Zhang et al., 2008). They concluded that the injected CO_2 mass was proportional to the applied injection pressure and found that the percentage of aqueous CO_2 changed from 10% at the end of the 50-year injection period to 40% after a few hundred years. After 50 years post-injection, the over-pressurisation effects associated with the injection in the system were decreasing, and the pressure returned to its original condition (Jen et al., 2017).

Summarising, until 1995, most of the existing numerical models took into consideration single porosity of rock. FEHM was then introduced, by Bower and Zyvoloski (1997), taking into consideration double porosity and THM effects on fracture evolution. Later on, TOUGH-FLAC simulation appeared (Rutqvist, 2011), a well-performed approach to link fluid flow and heat transport with stress and strain effects. Afterwards, Chen et al. (2010) set up a THM finite element model with a focus on heat exchange. Chen et al. (2010) did not consider a mass transfer, while Jie et al. (2016) on a try to reflect THM effects on the rock during CO_2 injection assumed isothermal effects in the aquifer and disregarded thermal effects on pressure evolution. It can be outlined that there is a lack of a precise THM numerical model for carbon sequestration and sub-zero temperatures. It is suggested for future studies that THM models should be considered in CO_2 or other fluids injection cases. TOUGH-FLAC procedure or FEM code seems to be well-performed and can be updated to couple precise thermal effects (e.g. cold CO_2 injection) and different injection pressures, according to Jen et al. (2017) and Vilarrasa et al. (2010).

2.5 Literature review outcomes

From the above literature review some principal knowledge gaps are identified. Firstly, there is a lack of experimental results on rock at low temperatures that can be used as input in numerical studies to describe scenarios such as Joule-Thompson effect or ship injection at sub-zero conditions. As far as concerns elastoplastic damage behaviour of rock, most investigations ignored brittle-ductile behaviour under different confining pressures. It should be also mentioned that damage models in the literature are complex enough to investigate fracturing or crack reopening or closure. Finally, the major scientific gap is a fully coupled THM rock model that considers elastoplastic continuum damage effects and can describe the rock nearby an existing wellbore.

Furthermore, in the literature review, different research studies on THM effects on the rock due to CO_2 injection or different fluid flow are presented. It should be outlined that proper site

characterisation and site-specific THM modelling are necessary to conduct safe CO_2 storage projects. Moreover, double porosity models represent better the flow-deformation changes, as rock formations are heterogeneous and consist of fractures. Additionally, elastoplastic design is more reliable due to the non-linearity of rock formations.

To sum up, taking into consideration a fully coupled hydro-mechanical model with elastoplastic considerations of Ma and Zhao (2018), thermal influence will be developed. Initial pore pressure will be present, simulating the internal pressure due to CO_2 injection. Gelet's (2012) THM numerical model describing thermo-hydro-mechanical effects on a wellbore will be expanded to include elastoplastic considerations with continuum damage effects and used to simulate further scenarios. Experimental work was also undertaken at Newcastle University, UCS and Triaxial tests, to outline the change of the rock's mechanical properties due to temperature change.

Chapter 3. Theoretical constitutive thermo-hydro-mechanical and elastoplastic damage model

3.1 Introduction

This chapter describes a robust and complete coupled thermal, hydraulic and mechanical model for fractured porous media during the injection of CO_2, exposed to elastoplastic continuum damage effects. The double porosity model from Khalili (2008) and Ma and Zhao (2018) is extended to include heat transfer to describe the thermal fluctuation of the rock near the wellbore during the CO_2 injection. Governing equations were developed based on the effective stress concept, equations of static equilibrium, the conservation of mass and momentum, elastoplastic deformations, continuum damage and thermal effects. The main variables of this study are the injected CO_2 pressures which change the effective stresses applied to the rock nearby the wellbore wall, the deformation of the rock formation, the water pressure in the porous and fracture domain, the temperatures of the solid, porous and fracture network and the damage evolution due to applied pressures. This model is validated in Chapter 5 using the results of Gelet et al. (2012) and Ma and Zhao (2018). The elastoplastic bounding surface model is validated using the experimental results in Chapter 4. The constituent parts are valid along the entire length of the wellbore and in Chapter 6 certain depths of the wellbore are simulated as case scenarios.

3.1.1 Phases of fractured porous media

According to the flow deformation theory of fully saturated fractured porous media proposed by Khalili and Valliappan (1996) and Ma and Zhao (2018) a more rigorous and complete model is presented. A Representative Elementary Volume (REV) of fractured rock with a certain volume (V_{tot}) is parted of three mediums. These three mediums are the solid, the porous and fractured medium (Figure 3.1). The rock studied was fully saturated. In this study, (V_p) represents the volume of the pores and (V_f) the fissure network volume. The two phases can be determined independently using their kinematic, thermodynamic, mass and momentum equations. As water exists both in pores and fractures, two types of pressure are identified, the pore water pressure (p_p) and the fissure water pressure (p_f). The solid and fluid phases are slightly compressible. The

fissure network is assumed as a continuum. The formation of new fractures due to mechanical, hydraulic and thermal loading is considered in the elastoplastic damage model of Chapter 5.

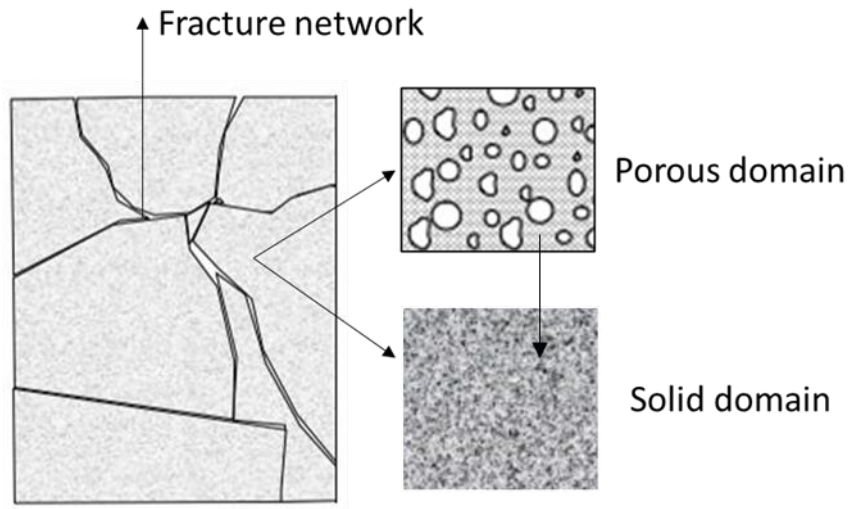

Figure 3. 1 Fractured porous medium (Khalili, 2008)

The total volume (V_{tot}) and the total mass (M_{tot}) are given respectively as:

$$M_{tot} = M_s + M_{wp} + M_{wf} \tag{3.1}$$

$$V_{tot} = V_s + V_{wp} + V_{wf} \tag{3.2}$$

For each phase, the volume fraction (φ_{phase}) can be expressed as:

$$\varphi_{phase} = {V_{phase}}/{V_{total}} \tag{3.3}$$

The following constraint can be satisfied by the volumetric fractions:

$$\varphi_s + \varphi_{wp} + \varphi_{wf} = 1 \tag{3.4}$$

The internal mass density of each phase can be expressed as:

$$\rho_{phase} = {M_{phase}}/{V_{phase}} \tag{3.5}$$

The apparent mass density:

$$\rho^{phase} = {M_{phase}}/{V_{total}} \tag{3.6}$$

The two densities are related as follows:

$$\rho^{phase} = \varphi_{phase}\rho_{phase} \tag{3.7}$$

where subscripts *s*, *wp* and *wf* representing the solid, pore water and fissure water phases, respectively. To simplify the notation, the solid phase was represented by 's' and the pore water and fissure water domain by '1' and '2', respectively.

3.1.2 Effective stress

The effective stress theory describes the pore fluid pressure effect on the stress of the solid skeleton. It can be used to set up constitutive relationships for the solid skeleton and to link the solid skeleton's deformation to the volumetric distribution of the liquids in the double porosity domain. According to Khalili and Valliappan (1996) and Voigt's notation, the incremental form of the effective stress for saturated double porous media can be given as:

$$\dot{\boldsymbol{\sigma}}' = \dot{\boldsymbol{\sigma}} + \beta_1 \dot{p_1}\boldsymbol{\delta} + \beta_2 \dot{p_2}\boldsymbol{\delta} \tag{3.8}$$

$\dot{\boldsymbol{\sigma}}$ is the incremental total stress, $\boldsymbol{\delta}$ is the Kronecker's delta $\dot{p_1}$ and $\dot{p_2}$ are the increments of pore and fissure fluid pressures, respectively.

where $\beta_1 = {C_p}/{C_f} - {C_s}/{C_f}$ and $\beta_2 = 1 - {C_p}/{C_f}$ are the effective stress parameter, in which C_p, C_f and C_s represent the drained tangent elastic compressibilities of the porous medium, the fracture porous domain and the solid skeleton. The compressibility of solid grains C_s is assumed to be negligible according to Khalili and Valliappan (1996), $\beta_1 + \beta_2 = 1$. In the case of zero fissure volume $C_p = C_f$ thus, $\beta_1 = 1$ and $\beta_2 = 0$.

3.1.3 Damage variable and stress connection

Damage variable *(D)* is an internal variable that describes the micro-cracks effect in the continuum thermodynamics scheme. It can give an estimation of the isotropic damage and describe anisotropic growth. Stress (σ) for undamaged material is the internal force acting on a unit area of

the solid part, while for the damaged material and for isotropic deformation is the force acting on a unit area of the damaged domain.

Considering complementary energy compatibility, the equivalent latent stress (σ^l) under an undamaged state can be associated with the damage variable to the stress (σ) in the damaged condition using the following equation:

$$\sigma^l = {}^{\sigma}/_{(1-D)} \tag{3.9}$$

The primary value of the damage for the tested material can be determined by the ratio of the fractured area to the total area of the rock, prior to any injection of CO_2. Drilling a borehole can increase the damage near the wellbore wall due to existing tectonic stresses at each depth of the rock formation. For the specific study, where the wellbore already exists, this increase is taken as initial damage D_{init}. Injection of the CO_2 will create stresses at the wellbore wall due to the injection pressure and temperature. According to the current phase of the injected CO_2, pressure and temperature at the wellbore wall will increase by depth. This pressure and temperature increase, enhance the pore and fissure pressure nearby the wellbore wall and the existing effective stresses, resulting in damage evolution. Degradation of the rock occurs as damage expands, which increases with the aggregation of micro-cracks.

3.2 Sign Convention and Notation

Following the continuum mechanics convention, compressive stresses and strains are negative, while tensile stresses are positive. The water pressure is positive for compression and negative for tension and suction. The mean normal stress is expressed as $p = -(\sigma_1 + \sigma_2 + \sigma_3)/3$, the volumetric strain as $tr(\varepsilon) = \varepsilon_v = -(\varepsilon_1 + \varepsilon_2 + \varepsilon_3)$, the deviatoric strain as $\varepsilon_q = \sqrt{\frac{2}{3}\left(\boldsymbol{\varepsilon} - \boldsymbol{\delta}\frac{\varepsilon_v}{3}\right):\left(\boldsymbol{\varepsilon} - \boldsymbol{\delta}\frac{\varepsilon_v}{3}\right)}$, the deviator stress $q = \sqrt{3J_2}$ and the stress ratio $\eta = \frac{q}{p'}$ for which the second invariant of deviatoric stress is $J_2 = \frac{1}{2}(\boldsymbol{S}:\boldsymbol{S}) = \frac{1}{2}S_{ij}S_{ji}$. In the thesis, bold symbols and letters represent matrices and vectors. The deviatoric stress tensor is $\boldsymbol{S} = \boldsymbol{\sigma}' - \boldsymbol{\delta}tr(p)$. The spatial gradient is expressed as $\nabla(\blacksquare) = \partial(\blacksquare)/\partial(x)$ while the divergence operator is $div(\blacksquare) = \nabla(\blacksquare)$.The identity vector is defined as $\delta = \{1\ 1\ 1\ 0\ 0\ 0\}^T$

3.3 Governing equations

The proposed governing equations followed the fully coupled model for fractured porous media with the elastoplastic damage design of Ma and Zhao (2018) by adding thermal parts that described the effect of the CO_2 injection. The deformation model was established based on the theory of thermo-elasticity by also using an elastoplastic damage model. Stress concept, equations of static equilibrium and the conservation of mass and momentum, accounting also elastoplastic deformation, continuum damage effects and thermal changes, were determined by setting up differential governing equations. The connection between the deformation and the energy distribution is settled through thermal growth coefficients.

The flow system described by Darcy's law, is extended to consider temperature changes, the conservation of mass and momentum and the theory of elastoplasticity. Saline water flow is studied both for the porous and fracture media. The rate of the fluid transfer due to applied pressure at the wellbore wall is expected to depend on the pressure difference between the two domains and on each permeability value.

The coupling between the deformation, the flow and the temperature model is outlined in Section 3.3.

3.3.1 Deformation model and momentum balance equation

Selecting a REV of fractured porous medium, the element is fully saturated with a slightly compressive fluid representative of the fluid found in the North Sea (Ma, 2014b). Assuming no internal acting forces, the linear momentum equation for the whole element can be expressed as:

$$\boldsymbol{div\sigma} + \boldsymbol{F} = 0 \tag{3.10}$$

Where $\boldsymbol{\sigma}$ is the total external stress and $\boldsymbol{F}$ represents the body force per unit volume.

In the Cartesian coordination system, the divergence for the total external stress can be expressed as:

$$div\boldsymbol{\sigma} = \nabla\boldsymbol{\sigma} = \left(\frac{\partial}{\partial x}, \frac{\partial}{\partial y}, \frac{\partial}{\partial z}\right)(\boldsymbol{\sigma}_x, \boldsymbol{\sigma}_y, \boldsymbol{\sigma}_z) \tag{3.11}$$

The incremental stress-strain relationship can be indicated as:

$$\dot{\boldsymbol{\sigma}}' = [\boldsymbol{S}(D,T)]\dot{\boldsymbol{\varepsilon}} \tag{3.12}$$

where $\boldsymbol{S}(D,T)$ is the tangential drained stiffness of the solid matrix of the damaged material including any elastic thermal effects and $\dot{\boldsymbol{\varepsilon}}$ is the strain increment of the solid skeleton.

For small deformations, the total strain can be expressed as:

$$\boldsymbol{\varepsilon} = \frac{1}{2}(\nabla \boldsymbol{u} + \boldsymbol{u}\nabla) \tag{3.13}$$

where $\boldsymbol{u}$ is the displacement vector of the solid phase.

Thermal dissipation should also be considered. Because the injected CO_2 is at a different temperature from the rock formation nearby the wellbore wall, temperature fluctuation will occur, and thermal stresses will exist due to temperature differences. These stresses will influence the model's deformation due to shrinkage or expansion of the matrix as well as the pore and fracture pressure. For this study the existing casing and cement is not considered for simplicity.

Based on Khalili et al. (2010) research, the volumetric thermal expansion coefficient of a whole porous medium is fully determined and equal to the thermal expansion of the solid skeleton. This outcome allows the thermal expansion of the medium to be determined as $\frac{C_{Ts}}{C_f}$ (Bai, 2016a). Specifically, it will be the ratio between the solid's volumetric thermal expansion and the fracture domain's compressibility, respectively. The effective stress for a thermo-elastic medium expanding Equation (3.12) and assuming insignificant deformations is given as follows:

$$\dot{\boldsymbol{\sigma}}' = \frac{1}{2}[\boldsymbol{S}(D,T)](\nabla \dot{\boldsymbol{u}} + \dot{\boldsymbol{u}}\nabla) - \frac{C_{Ts}}{C_f}\dot{T}_s\boldsymbol{\delta} \tag{3.14}$$

Using Equations (3.10) - (3.14) the partial differential equation for the deformation model of a thermo-elastic double porous medium is described as follows:

$$div\left(\frac{1}{2}[\boldsymbol{S}(D,T)](\nabla \dot{\boldsymbol{u}} + \dot{\boldsymbol{u}}\nabla) - \beta_1\dot{p}_1\boldsymbol{\delta} - \beta_2\dot{p}_2\boldsymbol{\delta} - \frac{C_{Ts}}{C_f}\dot{T}_s\boldsymbol{\delta}\right) + \dot{\boldsymbol{F}} = 0 \tag{3.15}$$

where C_f according to Khalili et al. (2008) is the compressibility of the fractured medium and can be expressed in terms of Young's modulus (E), and Poisson's ratio (ν) as:

$$\begin{cases} C_f = \dfrac{(1-2\nu)(1+\nu)}{(1-\nu)E}, & for\ 1D\ strain\ conditions \\ C_f = \dfrac{2(1-2\nu)(1+\nu)}{E}, & for\ 2D\ strain\ conditions \\ C_f = \dfrac{3(1-2\nu)}{E}, & for\ 3D\ strain\ conditions \end{cases} \tag{3.16}$$

3.3.2 Flow model and mass balance equation

The flow in fractured rock is determined by linking Darcy's law with the fluid and temperature gradient mass balance equation. Disregarding any internal and viscous effects, considering isotropic porous medium, the Darcy's law mathematic equation is as follows:

$$\boldsymbol{v}_a^r = -\frac{\boldsymbol{k}_a}{\mu_f}\left(\nabla p_a + \rho_f \boldsymbol{g}\right) - \varphi_a \Theta \nabla T,\ a = 1\,,2 \tag{3.17}$$

where $a = 1\,,2$ represents the porous and fractured network, respectively, $\boldsymbol{v}_a^r$ is the relative velocity of the fluid, $\boldsymbol{k}_a$ is the average permeability, ∇p_a is the fluid pressure gradient, ρ_f is the density of the fluid, μ_f is the dynamic viscosity of the fluid and $\boldsymbol{g}$ is the vector of the gravitational acceleration, Θ is the thermo-osmosis coefficient coupling fluid flux to the temperature gradient.

The relative velocity of the fluid can be also expressed as:

$$\boldsymbol{v}_a^r = \varphi_a(\boldsymbol{v}_a - \boldsymbol{v}_s) \tag{3.18}$$

where φ_a is the porosity of the porous or fracture network, $\boldsymbol{v}_a$ is the absolute fluid velocity and $\boldsymbol{v}_s$ is the velocity of the solid structure.

The two absolute velocities can be expressed as:

$$\boldsymbol{v}_a = \frac{\partial \boldsymbol{u_a}}{\partial t},\ \boldsymbol{v}_s = \frac{\partial \boldsymbol{u}}{\partial t} \tag{3.19}$$

in which $\boldsymbol{u}_a$and $\boldsymbol{u}$ are the displacement vectors of fluid and solid skeleton, respectively.

According to the conservation of mass theory, the mass that enters a system must either leave or accumulate within the system. Ma et al. (2016) and Bai (2016a) suggested that considering the

mass exchange between the porous medium and fissure network, the mass balance equation for a double porosity system can be given as:

$$div(\varphi_a \rho_f \boldsymbol{v}_a) + \left[\frac{\partial}{\partial t}(\varphi_a \rho_f) + (-1)^a \Xi\right] = 0 \tag{3.20}$$

Where Ξ is the leakage term and describes the flow rate from pores to fracture network and from fracture media to porous domain.

$$\Xi = \gamma(p_1 - p_2) \tag{3.21}$$

Where γ is the leakage parameter.

Implementing the relative velocity expressed by Equation (3.18) inside Equation (3.20) turn out:

$$-div(\varphi_a \rho_f \boldsymbol{v}_s) - div(\rho_f \boldsymbol{v}_a^r) = \frac{\partial}{\partial t}(\varphi_a \rho_f) + (-1)^a \Xi \tag{3.22}$$

The Lagrangian total derivative concept describes the time rate of change of some physical quantity. This can be used to describe the moving solid and fluid inside the fractured porous medium as below. The identity vector is also presented below.

$$\begin{cases} \dfrac{d_s(\blacksquare)}{d_t} = \dfrac{\partial(\blacksquare)}{\partial t} + \nabla(\blacksquare)\cdot \boldsymbol{v}_s\,, & \text{moving solid} \\ \dfrac{d_a(\blacksquare)}{d_t} = \dfrac{\partial(\blacksquare)}{\partial t} + \nabla(\blacksquare)\cdot \boldsymbol{v}_a\,, & \text{moving fluid} \\ div[(\blacksquare)\cdot \boldsymbol{v}_a] = (\blacksquare) div(\boldsymbol{v}_a) + \nabla(\blacksquare)\cdot \boldsymbol{v}_a, & \text{identity vector} \end{cases} \tag{3.23}$$

Equation (3.22) can be represented after applying (3.23) as follows:

$$-\rho_f div(\boldsymbol{v}_a^r) = \varphi_a \frac{d_a \rho_f}{dt} + \rho_f \frac{d_s \varphi_a}{dt} + \varphi_a \rho_f div(\boldsymbol{v}_s) + (-1)^{a+1}\Xi \tag{3.24}$$

Also, considering the coefficient of fluid compressibility (C_{fl}) and thermal expansion coefficient of the fluid (C_T) based on Khalili et al. (2008), the term $\frac{d_a \rho_f}{dt}$ of Equation (3.24) can be expressed as:

$$\frac{d_a \rho_f}{dt} = C_{fl} \rho_f \frac{d_a p_a}{dt} - \rho_f C_T \frac{d_a T_a}{dt} \tag{3.25}$$

where T_a is the saline water temperature in the porous and fractured domain.

The porosity can be defined as:

$$\varphi_a = {}^{V_a}/_{V_{total}} \tag{3.26}$$

Where V_a and V_{total} denotes the volume of pores ($a = 1$) and fissures ($a = 2$) and the total volume of the fractured porous medium, respectively.

Term $\frac{d_s \varphi_a}{dt}$ from Equation (3.24) can be also expressed as:

$$\frac{d_s \varphi_a}{dt} = \frac{1}{V_{total}} \left(\frac{d_s V_a}{dt} - \varphi_a \frac{d_s V_{total}}{dt} \right) \tag{3.27}$$

According to Ma et al. (2016) :

$$div(\boldsymbol{v}_s) = \frac{1}{V_{total}} \frac{d_s V_{total}}{dt} \tag{3.28}$$

Equations (3.17), (3.24), (3.25) and (3.27) can be combined into a final general equation that describes the fluid flow through the fully saturated rock.

Flow in the porous medium:

$$div \left[\frac{\boldsymbol{k}_1}{\mu_1} \left(\nabla p_1 + \rho_f \boldsymbol{g} \right) + \varphi_1 \Theta \nabla T \right] = \varphi_1 C_{fl} \frac{d_1 p_1}{dt} - \varphi_1 C_T \frac{d_1 T_1}{dt} + \frac{1}{V_{total}} \frac{d_s V_1}{dt} + \Xi \tag{3.29}$$

Flow in the fractured network:

$$div \left[\frac{\boldsymbol{k}_2}{\mu_2} \left(\nabla p_2 + \rho_f \boldsymbol{g} \right) + \varphi_2 \Theta \nabla T \right] = \varphi_2 C_{fl} \frac{d_2 p_2}{dt} - \varphi_2 C_T \frac{d_2 T_2}{dt} + \frac{1}{V_{total}} \frac{d_s V_2}{dt} - \Xi \tag{3.30}$$

3.3.3 Stress-Strain Relationship

Constitutive equations are used to compile the flow, deformation, and temperature effects. In this problem, elastic and elastoplastic damage deformation model is considered. Stress-strain response of the solid skeleton and stress variable-volumetric deformation of pores and fissures is proposed.

According to Ma et al. (2016) and Voyiadjis et al. (2004) the irrecoverable energy dissipation ψ consists of two parts, the damage elastic part ψ_e and the damage plastic part ψ_p. In isothermal conditions, the irrecoverable energy dissipation ψ can be expressed as:

$$\psi = \psi_e + \psi_p = \frac{1}{2}[\boldsymbol{\varepsilon}^e]^T[\boldsymbol{S}^e(D,T)][\boldsymbol{\varepsilon}^e] + \psi_p \tag{3.31}$$

where $\boldsymbol{\varepsilon}^e$ is the elastic strain and $\boldsymbol{S}^e(D,T)$ is the elastic stiffness for the damaged material including elastic thermal effects. In the elastic strain thermal influence is included.

The effective stress is presented as the derivative of the energy dissipation to the derivative of the elastic strain:

$$\boldsymbol{\sigma}' = \frac{\partial \psi}{\partial \boldsymbol{\varepsilon}^e} = [\boldsymbol{S}^e(D,T)][\boldsymbol{\varepsilon}^e] \tag{3.32}$$

By differentiating Equation (3.32) the stress rate is determined:

$$\dot{\boldsymbol{\sigma}}' = \frac{\partial[\boldsymbol{S}^e(D)]}{\partial D} : (\boldsymbol{\varepsilon}^e)\dot{D} + \boldsymbol{S}^e(D,T) : \boldsymbol{\varepsilon}^e \tag{3.33}$$

Taking into consideration the damage hypothesis for complementary energy equivalence, the elastic stiffness matrix for the deformed material can be expressed as:

$$\boldsymbol{S}^e(D,T) = (1-D)^2\boldsymbol{S}^e(T) \tag{3.34}$$

where $\boldsymbol{S}^e(T)$ is the elastic stiffness of undamaged material influenced only be the temperature.

Substituting Equation (3.33) into Equation (3.32) then the stress rate is reproduced as:

$$\dot{\boldsymbol{\sigma}}' = -\frac{2\dot{D}}{1-D}[\boldsymbol{S}^e(D,T)] : \boldsymbol{\varepsilon}^e + [\boldsymbol{S}^e(D,T)] : [\dot{\boldsymbol{\varepsilon}}^e] \tag{3.35}$$

Equation (3.35) can be rearranged as:

$$\dot{\boldsymbol{\sigma}}' = [\boldsymbol{S}^e(D,T)]: \dot{\boldsymbol{\varepsilon}}^e_{dam} \tag{3.36}$$

in which

$$\dot{\boldsymbol{\varepsilon}}^e_{dam} = \dot{\boldsymbol{\varepsilon}}^e - \frac{2\dot{D}}{1-D}\boldsymbol{\varepsilon}^e \tag{3.37}$$

According to Khalili and Valliappan (1996) and Ma and Zhao (2018), the elastic constitutive equation for fully saturated fractured porous media can be achieved using the Maxwell-Betti reciprocal work theorem. Applying Betti's theorem and considering Equations (3.8), (3.36) and (3.37), the elastic strain components ($\dot{\boldsymbol{\varepsilon}}^e$, $\frac{1}{V_{total}}\frac{d_s V_a}{dt} = \frac{\dot{V}_a}{V_{total}}$) are related to the stress components ($\dot{\sigma}, \dot{p}_a$).

$$\begin{aligned}\dot{\boldsymbol{\varepsilon}}^e &= \dot{\boldsymbol{\varepsilon}}^e_{dam} + \frac{2\dot{D}}{1-D}\boldsymbol{\varepsilon}^e + \dot{\boldsymbol{\varepsilon}}_T \\ &= \frac{1}{[\boldsymbol{S}^e(D,T)]}(\dot{\boldsymbol{\sigma}} - \beta_1\dot{p}_1\boldsymbol{\delta} - \beta_2\dot{p}_2\boldsymbol{\delta}) + \frac{2\dot{D}}{1-D}\boldsymbol{\varepsilon}^e - \frac{C_{Ts}}{C_f}\dot{T}_s\end{aligned} \tag{3.38}$$

The change in the pore and fissure volume, included in Equations (3.29) and (3.30), over the current volume of the porous domain with respect to the moving solid is expressed based on Khalili et al. (2008); Bai (2016b) as:

$$\frac{1}{V_{total}}\frac{d_s V_1}{dt} = -\beta_1(\dot{\boldsymbol{\varepsilon}}^e_v - \dot{\boldsymbol{\varepsilon}}_T) + \beta^e_{11}\dot{p}_1 - \beta^e_{12}(\dot{p}_2 - \dot{p}_1) + \varphi_1\frac{C_{Ts}}{C_f}\dot{T}_s \tag{3.39}$$

$$\frac{1}{V_{total}}\frac{d_s V_2}{dt} = -\beta_2(\dot{\boldsymbol{\varepsilon}}^e_v - \dot{\boldsymbol{\varepsilon}}_T) + \beta^e_{22}\dot{p}_2 - \beta^e_{21}(\dot{p}_1 - \dot{p}_2) + \varphi_2\frac{C_{Ts}}{C_f}\dot{T}_s \tag{3.40}$$

Equations (3.39) and (3.40) will help to solve Equations (3.29) and (3.30).

Where $\beta^e_{11}, \beta^e_{22}, \beta^e_{21}, \beta^e_{12}$ are the elastic coefficients relating to the porous volumetric deformations and changes of the porous fluid pressures and $\dot{\varepsilon}_T = \frac{C_{Ts}}{C_f}\dot{T}_s$.

The elastic coefficients can be obtained by:

$$\beta_{11}^{e} = \varphi_1 C_f + \beta_{12}^{e} \tag{3.41}$$

$$\beta_{22}^{e} = \varphi_2 C_f + \beta_{21}^{e} \tag{3.42}$$

$$\beta_{12}^{e} = \beta_{21}^{e} = \left(\beta_1 \beta_2 - \frac{\varphi_1 \varphi_2}{\varphi_1 + \varphi_2} \right) C_f \tag{3.43}$$

For the undamaged material Equation (3.38) can be rearranged as follows:

$$\dot{\boldsymbol{\varepsilon}}^{e} = \boldsymbol{\varepsilon}^{e} + \dot{\boldsymbol{\varepsilon}}_T = \frac{1}{[\boldsymbol{S}^{e}(T)]} (\dot{\boldsymbol{\sigma}} - \beta_1 \dot{p_1} \boldsymbol{\delta} - \beta_2 \dot{p_2} \boldsymbol{\delta}) - \frac{C_{Ts}}{C_f} \dot{T}_s \tag{3.44}$$

3.3.4 Plastic variable implementation

According to Khalili et al. (2008) the plasticity is fully undertaken by the solid skeleton and the water in porous and fissure domain is linear compressible barotropic fluid. For the current elastoplastic damage model, the yield surface is determined as a function of plastic volumetric strain and damage parameter. The incremental effective stress is related to the elastic strain as:

$$\dot{\boldsymbol{\sigma}}' = \frac{\partial [\boldsymbol{S}^{e}(D,T)]}{\partial D} : (\boldsymbol{\varepsilon}^{e}) \dot{D} + [\boldsymbol{S}^{e}(D,T)] : \dot{\boldsymbol{\varepsilon}}^{e} \tag{3.45}$$

The total increment strain of the solid skeleton and the fluid volume rate change is parted of elastic and plastic parts. The plastic parts are presented using the superscript 'p'.

$$\dot{\boldsymbol{\varepsilon}} = \dot{\boldsymbol{\varepsilon}}^{e} + \dot{\boldsymbol{\varepsilon}}^{p} \tag{3.46}$$

$$\frac{\dot{V}_a}{V_{total}} = \frac{\dot{V}_a^{e}}{V_{total}} + \frac{\dot{V}_a^{p}}{V_{total}} \tag{3.47}$$

Following the general plasticity approach and the definition of the effective stress concept, the incremental strain rate and the incremental fluid in fracture or porous volume rate can be expressed as:

$$\dot{\boldsymbol{\varepsilon}}^p = \dot{\lambda}\frac{\partial g}{\partial \boldsymbol{\sigma}'} \tag{3.48}$$

$$\frac{\dot{V}_a^p}{V_{total}} = \dot{\lambda}\frac{\partial g}{\partial p_a} = \dot{\lambda}\frac{\partial g}{\partial \boldsymbol{\sigma}'}\frac{\partial \boldsymbol{\sigma}'}{\partial p_a} = -a_a\dot{\lambda}\boldsymbol{\delta}^T\frac{\partial g}{\partial \boldsymbol{\sigma}'} \tag{3.49}$$

In which $\dot{\lambda}$ and $g\,(\boldsymbol{\sigma}')$ are the plastic multipliers and plastic potential as expressed by Khalili et al. (2008), respectively.

As a result, the deformation of water in porous and fissure domain due to plastic change of the solid matrix can be expressed as:

$$\frac{\dot{V}_1^p}{V_{total}} = -\beta_1\dot{\boldsymbol{\varepsilon}}_v^p \tag{3.50}$$

$$\frac{\dot{V}_2^p}{V_{total}} = -\beta_2\dot{\boldsymbol{\varepsilon}}_v^p \tag{3.51}$$

The thermal effects are considered only for the incremental elastic strain. In this study, low temperatures will be studied ($-5℃$ and $-10℃$), and elastic deformations will be assumed. For high temperatures, more than 100℃, according to Gajo and Bigoni (2015), plasticity damage should be considered separately for the temperature fluctuation.

Furthermore, the plastic hardening parameter can be determined as a function of the plastic volumetric strain and damage. The yield function can be settled in terms of effective stress and plastic hardening parameter as follows:

$$f\left(\boldsymbol{\sigma}', p_c'\left(\varepsilon_v^p, D\right)\right) = 0 \tag{3.52}$$

p_c' is a function of the plastic volumetric strain and damage, and it controls the size of the yield surface.

The consistency condition for the yield surface according to Ma and Zhao (2018) is presented as follows:

$$\dot{f} = \left(\frac{\partial f}{\partial \boldsymbol{\sigma}'}\right)^T \boldsymbol{\sigma}' + \frac{\partial f}{\partial p_c'}\left(\frac{\partial p_c'}{\partial \varepsilon_v^p}\dot{\boldsymbol{\varepsilon}}_v^p + \frac{\partial p_c'}{\partial D}\dot{D}\right) \tag{3.53}$$

The consistency condition for yield surface can be rearranged by substituting Equation (3.53) into Equation (3.52).

$$\dot{f} = \left(\frac{\partial f}{\partial \boldsymbol{\sigma}'}\right)^T \boldsymbol{\sigma}' - \dot{\lambda} h_p = 0 \tag{3.54}$$

where h_p is the plastic hardening modulus, and the plastic multiplier $\dot{\lambda}$ for the damaged material is achieved by substituting Equations (3.45) -(3.48) into Equation (3.53) as:

$$\dot{\lambda} = \frac{1}{H}\left(\frac{\partial f}{\partial \boldsymbol{\sigma}'}\right)^T [\boldsymbol{S}^e(D,T)](\dot{\boldsymbol{\varepsilon}}_{dam}) \tag{3.55}$$

in which

$$\dot{\boldsymbol{\varepsilon}}_{dam} = \dot{\boldsymbol{\varepsilon}} - \frac{2\dot{D}}{1-D}\boldsymbol{\varepsilon}^e \tag{3.56}$$

The total hardening modulus $H = H(D)$ can be defined as:

$$H = h_p + \left(\frac{\partial f}{\partial \boldsymbol{\sigma}'}\right)^T [\boldsymbol{S}^e(D,T)]\left(\frac{\partial g}{\partial \boldsymbol{\sigma}'}\right) \tag{3.57}$$

The plastic hardening parameter is determined as:

$$h_p = -\frac{\partial f}{\partial p_c'}\frac{\partial g}{\partial p'}\left(\frac{\partial p_c'}{\partial \varepsilon_v^p} + \frac{\partial p_c'}{\partial D}\frac{\dot{D}}{\dot{\varepsilon}_v^p}\right) \tag{3.58}$$

The elastoplastic damage constitutive equation for the solid skeleton deformation is outlined by substituting Equations (3.38) - (3.43) and (3.52) as follows:

$$\dot{\boldsymbol{\sigma}}' = \boldsymbol{S}^{epl}(D,T)\dot{\boldsymbol{\varepsilon}}_{dam} \tag{3.59}$$

Ma and Zhao (2018) and Ma et al. (2022) suggested that the stiffness $\boldsymbol{S}^{epl}(D,T)$ of the double-porosity system is then drained elastoplastic stiffness matrix of the damaged material. $\boldsymbol{S}^{epl}(D,T)$

depends on the stress and damage and can be obtained by the elastoplastic constitutive equation proposed by Ma et al. (2016) as:

$$\boldsymbol{S}^{epl}(D,T) = \left([\boldsymbol{S}^{e}(D,T)] - \frac{1}{H} [\boldsymbol{S}^{e}(D,T)] \left(\frac{\partial f}{\partial \boldsymbol{\sigma}'} \right)^{T} \left(\frac{\partial g}{\partial \boldsymbol{\sigma}'} \right) [\boldsymbol{S}^{e}(D,T)] \right) \tag{3.60}$$

The elastoplastic stress-rate equation also including temperature effects is presented as:

$$\dot{\boldsymbol{\sigma}} = \boldsymbol{S}^{epl}(D,T)\dot{\boldsymbol{\varepsilon}}_{dam} - \beta_1 \dot{p_1}\boldsymbol{\delta} - \beta_2 \dot{p_2}\boldsymbol{\delta} - \frac{C_{Ts}}{C_f}\dot{T}_s\boldsymbol{\delta} \tag{3.61}$$

For the undamaged material, the drained elastoplastic stiffness matrix is defined as $\boldsymbol{Sep}$, and the elastoplastic constitutive equation for the solid skeleton is written as:

$$\dot{\boldsymbol{\sigma}}' = \boldsymbol{S}^{epl}(T)\dot{\boldsymbol{\varepsilon}} = \left(\boldsymbol{S}^{e}(T) - \frac{1}{H}\boldsymbol{S}^{e} \left(\frac{\partial f}{\partial \boldsymbol{\sigma}'} \right)^{T} \left(\frac{\partial g}{\partial \boldsymbol{\sigma}'} \right) \boldsymbol{S}^{e} \right) \dot{\boldsymbol{\varepsilon}} \tag{3.62}$$

The modulus H and the plastic hardening parameter h_p are reduced to:

$$H = h_p + \left(\frac{\partial f}{\partial \boldsymbol{\sigma}'} \right)^{T} [\boldsymbol{S}^{epl}(D,T)] \left(\frac{\partial g}{\partial \boldsymbol{\sigma}'} \right) \tag{3.63}$$

$$h_p = -\frac{\partial f}{\partial z_c'} \frac{\partial g}{\partial p'} \frac{\partial z_c'}{\partial \varepsilon_v^p} \tag{3.64}$$

The elastoplastic rate equation for solid skeleton in undamaged material, including temperature effects, is formed as follows:

$$\dot{\boldsymbol{\sigma}} = \boldsymbol{S}^{epl}(T)\dot{\boldsymbol{\varepsilon}} - \beta_1 \dot{p_1}\boldsymbol{\delta} - \beta_2 \dot{p_2}\boldsymbol{\delta} - \frac{C_{Ts}}{C_f}\dot{T}_s\boldsymbol{\delta} \tag{3.65}$$

Combining Equations (3.45) and (3.49), the total volume change of fluid in pores and fissures is presented respectively as:

$$\frac{\dot{V}_1}{V_{total}} = -\beta_1(\dot{\boldsymbol{\varepsilon}} - \dot{\boldsymbol{\varepsilon}}_T) + (-\beta_{11}^{e} - \beta_{12}^{e})\dot{p_1} + \beta_{12}^{e}\dot{p_2} + \varphi_1 C_T \dot{T}_s \tag{3.66}$$

$$\frac{\dot{V}_2}{V_{total}} = -\beta_2(\dot{\boldsymbol{\varepsilon}} - \dot{\boldsymbol{\varepsilon}}_T) - \beta_{21}^e \dot{p_1} + (\beta_{22}^e + \beta_{21}^e)\dot{p_2} - \varphi_2 C_T \dot{T_s} \tag{3.67}$$

3.3.5 Entropy of the fractured porous media

Entropy is crucial in determining the free energy of a system. For the fully saturated fractured porous media the entropy of the solid, porous and fractured media should be calculated. The entropy of a solid phase is expressed in terms of total volumetric strain, fluid pressure and solid temperature according to Bai (2016a) as follows:

$$\dot{s}_{solid} = A_1 \dot{\varepsilon} + A_2 \dot{p_1} + A_3 \dot{p_2} + A_4 \dot{T_s} \tag{3.68}$$

where s is the entropy per unit volume of the fractured porous medium and the coefficients $A_1, A_2, A_3, and\ A_4$ are comparing changes in the total strain and fluid volume parts to the solid temperature. This coefficients in a reversible system must satisfy symmetry and can be expressed following Bai (2016b) as:

$$\begin{cases} A_1 = \dfrac{C_{Ts}}{C_f} \\ A_2 = -(\beta_1 - \varphi_1)C_{Ts} \\ A_3 = -(\beta_2 - \varphi_2)C_{Ts} \\ A_4 = \dfrac{\rho_s C_{ps}}{T_s} \end{cases} \tag{3.69}$$

$$\dot{s}_{solid} = \frac{C_{Ts}}{C_f}\dot{\varepsilon} - (\beta_1 - \varphi_1)C_{Ts}\dot{p_1} - (\beta_2 - \varphi_2)C_{Ts}\dot{p_2} + \frac{\rho^s C_{ps}}{T_s}\dot{T_s} \tag{3.70}$$

Where C_{ps} is the possible heat capacity of the solid ($^{J}/_{m^3 K}$) and ρ^s is the apparent density of the solid ($^{kg}/_{m^3}$), which is equal to the porosity of the solid (φ_s) multiplied by the intrinsic density of it (ρ_s).

It should be mentioned that the density of the thermo-barotropic fluid can vary according to the pressure and temperature as follows:

$$\rho_w \dot{\rho}_w = C_{fl}\dot{p}_a - C_{Tw}\dot{T_s}\ , a = 1{,}2 \tag{3.71}$$

where ρ_w is the density of the saline water, C_{Tw} is the thermal expansion coefficient of the saline water.

As the rock is fully saturated, according to Bai (2016a) for a single fluid, which in the current project is saline water, the entropy may be expressed in terms of the pressure and temperature as presented:

$$\dot{s} = -C_{Tw} V_{sp} \dot{p} + \frac{C_p}{T} \dot{T} \tag{3.72}$$

V_{sp} is the specific volume which is the complementary of the intrinsic density and C_p is the heat capacity at a constant pressure of the fluid.

To determine the local thermal non-equilibrium for saline water in porous and fissure medium, Equation (3.72) can be modified as follows:

$$\dot{s}_a = -\frac{\varphi_a C_{Ta}}{p_a} \dot{p}_a + \frac{C_{pa}}{T_a} \dot{T}_a \tag{3.73}$$

Where C_{Ta} is the volumetric thermal expansion coefficient of the fluid, C_{pa} is the heat capacity of the fluid, which is saline water at constant pressure at the porous and fractured medium ($^{J}/_{m^3 K}$).

3.3.6 Energy exchange equations

3.3.6.1 Energy exchange for solid material

The energy model is determined by assuming local thermal non-equilibrium, enabling the description of heat transfer between the phases. According to Bai (2016a) the energy balance equation for the solid phase can be presented as:

$$\dot{h}_s + \Xi_s = -div \boldsymbol{q}_s \tag{3.74}$$

Where h_s is the enthalpy per unit volume of the domain for the solid medium, $\boldsymbol{q}_s$ is the conductive heat flux, and Ξ_s is the energy transfer term for the solid phase.

The change in enthalpy can be related to the change in entropy as follows:

$$\dot{h}_s = T_s \dot{s}_{solid} \tag{3.75}$$

The heat transfer is due to the temperature gradient only and can be described by Fourier's law multi-dimensional extension as:

$$\boldsymbol{q}_s = -\varphi_s k_s \nabla T_s \tag{3.76}$$

in which φ_s is the porosity of the solid and k_s is the thermal conductivity of the solid.

Substituting Equation (3.76) into Equation (3.74), the energy balance equation for the solid phase can be expressed as:

$$div(\varphi_s k_s \nabla T_s) = T_s \dot{s}_{solid} + \Gamma_s \tag{3.77}$$

The energy transfer Γ_s to the solid phase can be determined as:

$$\Gamma_s = -\omega_{1s}(T_1 - T_s) - \omega_{2s}(T_2 - T_s) \tag{3.78}$$

Where ω_{1s} and ω_{2s} are the coefficients of heat exchange between the solid medium and porous network and solid medium and fissure domain, respectively.

3.3.6.2 Energy exchange for fractured and porous domain

Taking into consideration Equation (3.74) and the balanced equation for a typical thermodynamic system according to Majid Hassanizadeh (1986), the basic form of the energy balance equations for wet porous and fracture network are:

$$\frac{\partial(\varphi_a p_a H_a)}{\partial t} + div(\varphi_a p_a H_a \boldsymbol{v_a}) - \Gamma_a = -div\boldsymbol{q}_a \tag{3.79}$$

Where $a = 1, 2$ represents the porous and fractured network respectively, H_a is the enthalpy per unit mass of the water in the fracture, and porous media and $\boldsymbol{v}_a$ is the mean velocity vector for the water.

According to Bai (2016a), heat can proliferate because of the presence of hydraulic gradient in the porous and fissure domain. According to Equation (3.74), which describes the conductive heat flux of the solid medium, Equation (3.76) can be modified to describe the flow heat flux in the two phases as follows:

$$q_a = -\varphi_a T_a \Upsilon_a \nabla p_a - \varphi_a k_a \nabla T_a \tag{3.80}$$

Where $a = 1, 2$ represents the porous and fractured network, respectively, Υ_a is the isothermal heat flow coefficient, and k_a is the thermal conductivity of the fluid in the porous and fissure network.

Enthalpy consists of entropy and chemical potential. The deviation of density for a compressible fluid can be indicated as a function of pressure and temperature fluctuation as follows:

$$\frac{\dot{\rho}_a}{\rho_a} = C_f \dot{p}_a - C_{Ta} \dot{T}_a \tag{3.81}$$

Integrating Equation (3.81) the fluid density in porous media or fissure network can be written as:

$$\rho_a = \rho_a^0 \exp\left(C_a(p_a - p_a^0) - C_{Ta}(T_a - T_a^0)\right) \tag{3.82}$$

The differential of fluid entropy can be presented in terms of density and temperature as follows:

$$\dot{s}_a = -\frac{C_{Ta}}{\rho_a^2 C_f} \dot{p}_a + \frac{C_{va}}{T_a} \dot{T}_a \tag{3.83}$$

The difference between Equation (3.73) and Equation (3.83) is that the heat capacity C_{va} in Equation (3.83) is expressed at constant volume($J/kg/K$). Integrating Equation (3.83) with the superscript '0' denoting the initial state yields:

$$s_a - s_a^0 = \frac{C_{Ta}}{C_f}\left(\frac{1}{\rho_a} - \frac{1}{\rho_a^0}\right) + C_{va}\left(ln\frac{T_a}{T_a^0}\right) \tag{3.84}$$

At that point, *R* is introduced, which according to Bai (2016a), is a function of fluid pressure and temperature:

$$\dot{R}_a = \frac{\dot{p}_a}{\rho_a} - s_a \dot{T}_a \tag{3.85}$$

Integrating Equation (3.85) leads to:

$$R_a - R_a^0 = \frac{1}{\rho_a^2 C_a}(\rho_a - \rho_a^0) + \left(C_{va} - s_a^0 + \frac{C_{Ta}}{C_a \rho_a}\right)(T_a - T_a^0) - C_{va} T_a (ln \frac{T_a}{T_a^0}) \tag{3.86}$$

The fluid enthalpy, according to Bai (2016a), can be determined in the energy balance equations as follows:

$$H_a = R_a + T_a s_a \tag{3.87}$$

Using Equation (3.72) which describes the rate of entropy for fluid phase Equation (3.79) can be rearranged as:

$$\varphi_a p_a \left(\frac{-C_{Ta} T_a}{p_a}\dot{p}_a + C_{pa}\dot{T}_a\right) + H_a \varphi_a \dot{p}_a + \varphi_a p_a (\boldsymbol{v}^a - \boldsymbol{v}^s) div H_a + H_a div(\varphi_a p_a \boldsymbol{v}^a) + \Xi_a = div \boldsymbol{q}_a \tag{3.88}$$

The energy transfer Γ_a for the porous and fracture fluid is defined similarly as for the solid:

$$\Gamma_1 = -\omega_{1s}(T_s - T_1) - \omega_{12}(T_2 - T_1) \tag{3.89}$$

ω_{1s} and ω_{12} are the coefficients of heat exchange between the solid medium and porous network and porous and fissure domain, respectively.

$$\Gamma_2 = -\omega_{2s}(T_s - T_2) - \omega_{21}(T_1 - T_2) \tag{3.90}$$

ω_{2s} and ω_{21} are the coefficients of heat exchange between the fissure medium and solid part and fissure and porous domain, respectively.

3.3.7 Leakage parameter

The leakage parameter fully controls the fluid flow between the porous block and the fissure network (Warren and Root, 1963). In the case of thermo-mechanical loading at the wellbore wall due to the injected CO_2,the leakage parameter would be equal to the one proposed by (Ma, 2014b) and could be expressed as:

$$leak^{iso} = (-1)^{a+1}\frac{1}{\rho_f}\Xi \tag{3.91}$$

For non iso-thermal conditions as the one used at the specific study based on Bai (2016b) the leakage parameter can be expressed as:

$$leak^{non-iso} = sign(\propto)\frac{\Psi_a}{\rho_a} \tag{3.92}$$

Where $\propto$ is the thermal diffusivity and for each phase Ψ_a can be expressed as:

$$\Psi_1 = {\rho_1}^2\frac{k_1}{\mu_1}\gamma(\{R_2\} - \{R_1\}) \tag{3.93}$$

$$\Psi_2 = {\rho_2}^2\frac{k_2}{\mu_2}\gamma(\{R_1\} - \{R_2\}) \tag{3.94}$$

Where R_1 and R_2 are the chemical potentials per unit mass of the constituent and calculated based on Equation (3.86). However, in this research, the leakage parameter by Warren and Root (1963) is adopted as the temperature of the solid, pores, and fissure is the same, and no heat exchange is considered. Specifically:

$$\Xi_1 = \gamma(p_1 - p_2) \tag{3.95}$$

$$\Xi_2 = \gamma(p_2 - p_1) \tag{3.96}$$

where γ is the shape aperture factor for quasi-steady-state condition and is expressed according to Warren and Root (1963) as:

$$\gamma = \frac{4\omega(\omega + 2)}{l^2} \tag{3.97}$$

where ω is the number of the total sets of fractures and l is expressed as follows:

$$l = \begin{cases} \dfrac{3d_1d_2d_3}{(d_1d_2 + d_2d_3 + d_1d_3)} & ,\omega = 3 \\ \dfrac{2d_1d_2}{(d_1+d_2)} & ,\omega = 2 \\ d_1 & ,\omega = 1 \end{cases} \tag{3.98}$$

3.4 Fully coupled equations

All the partial differential equations describing the deformation due to injection pressures, the fluid flow of the water inside pores and fractures, and the heat transfer both at the solid and at the two phases for a fully saturated double porous medium are summarised below.

For the **deformation model**, the balance of momentum equation is:

$$div\left(\frac{1}{2}[\boldsymbol{S}^{ep}(D,T)](\nabla \dot{\boldsymbol{u}}_{\boldsymbol{d}} + \dot{\boldsymbol{u}}_{\boldsymbol{d}}\nabla) - \beta_1\dot{p_1}\boldsymbol{\delta} - \beta_2\dot{p_2}\boldsymbol{\delta} - \frac{C_{Ts}}{C_f}\dot{T}_s\boldsymbol{\delta}\right) + \dot{\boldsymbol{F}} = 0 \tag{3.99}$$

For the flow of the water inside the pores and fracture network, the two equations are based on Equations (3.29-3.31) and on the non-isothermal leakage parameter of Equations (3.95-3.96) are presented respectively as follows:

$$div\left(\frac{\boldsymbol{k}_1}{\mu_f}\left(\nabla p_1 + \rho_f \boldsymbol{g}\right) + \varphi_1\Theta_1\nabla T\right) = \varphi_1 C_{fl}\dot{p_1} - \varphi_1 C_T\dot{T}_1 + \frac{\dot{V}_1}{V_{total}} + \Xi_1 \tag{3.100}$$

$$div\left(\frac{\boldsymbol{k}_2}{\mu_f}\left(\nabla p_2 + \rho_f \boldsymbol{g}\right) + \varphi_2\Theta_2\nabla T\right) = \varphi_2 C_{fl}\dot{p_2} - \varphi_2 C_T\dot{T}_2 + \frac{\dot{V}_2}{V_{total}} + \Xi_2 \tag{3.101}$$

The effective stress parameters based on Equations (3.41) and (3.43) are:

$$\beta_{12} = \beta_{21} = \left(\beta_1\beta_2 - \varphi_1\varphi_2\frac{\beta_1+\beta_2}{\varphi_1+\varphi_2}\right)C_f \tag{3.102}$$

$$\beta_{11} = \varphi_1 C_{fl} + (\beta_1 - \varphi_1)C_s + \beta_{12} \tag{3.103}$$

$$\beta_{22} = \varphi_2 C_{fl} + (\beta_2 - \varphi_2)C_s + \beta_{21} \tag{3.104}$$

The volumetric strain can be expressed to calculate the displacement vector as follows:

$$\varepsilon_v = -\boldsymbol{\delta}^T(\dot{\boldsymbol{\varepsilon}} - \dot{\boldsymbol{\varepsilon}}_T) = -div\boldsymbol{u} \tag{3.105}$$

Considering the effective stress parameters and the displacement vector **the flow equations** for the porous and fracture network, respectively, are:

$$div\left(\frac{\boldsymbol{k}_1}{\mu_f}\left(\nabla p_1 + \rho_f \boldsymbol{g}\right) + \varphi_1\Theta_1\nabla T\right) = \beta_1 div\dot{\boldsymbol{u}} + \beta_{11}\dot{p}_1 - \beta_{12}\dot{p}_2 - \varphi_1 C_T\dot{T}_1 - (\beta_1 - \varphi_1)C_{TS}\dot{T}_s + \Xi_1 \tag{3.106}$$

$$div\left(\frac{\boldsymbol{k}_2}{\mu_f}\left(\nabla p_2 + \rho_f \boldsymbol{g}\right) + \varphi_2\Theta_2\nabla T\right) = \beta_2 div\dot{\boldsymbol{u}} + \beta_{22}\dot{p}_2 - \beta_{21}\dot{p}_1 - \varphi_2 C_T\dot{T}_2 - (\beta_2 - \varphi_2)C_s\cdot\dot{T}_s + \Xi_2 \tag{3.107}$$

The **energy balance equation for the solid** based on Equations (3.77-3.78) is:

$$div(\varphi_s k_s\nabla T_s) = T_s\frac{C_s}{C_{fr}}div(\dot{u}) - T_s(\beta_1 - \varphi_1)C_s\dot{p}_1 - T_s(\beta_2 - \varphi_2)C_s\dot{p}_2 + \varphi_s C_{ps}\dot{T}_s - \omega_{s1}(T_1 - T_s) - \omega_{s2}(T_2 - T_s) \tag{3.108}$$

The energy balance equation for the energy exchange between the porous and fracture network and fracture and porous domain, respectively, based on Equations (3.79-3.90), are:

$$-\varphi_1 C_{T1}T_1\dot{p}_1 + \varphi_1 C_{p1}\rho_1\dot{T}_1 + \varphi_1(1 - C_{T1}T_1)(\boldsymbol{v}^1 - \boldsymbol{v}^s)divp_1 + C_{p1}M_1 divT_1 - H_1 sign(\propto)\Psi_1 - \omega_{1s}(T_s - T_1) - \omega_{2s}(T_2 - T_1) = div(\varphi_1 T_1\Upsilon_1\nabla p_1 + \varphi_1 k_1\nabla T_1) \tag{3.109}$$

$$-\varphi_2 C_{T2}T_2\dot{p}_2 + \varphi_2 C_{p2}\rho_2\dot{T}_2 + \varphi_2(1 - C_{T2}T_2)(\boldsymbol{v}^2 - \boldsymbol{v}^s)divp_2 + C_{p2}M_2 divT_2 - H_2 sign(\propto)\Psi_2 - \omega_{2s}(T_s - T_2) - \omega_{2s}(T_1 - T_2) = div(\varphi_2 T_2\Upsilon_2\nabla p_2 + \varphi_2 k_2\nabla T_2) \tag{3.110}$$

where Υ_a is the isothermal heat flow coefficient and k_a is the thermal conductivity of the fluid in the porous and fissure network, $\propto$ thermal diffusivity and Ψ is the element boundary or leakage term. M_1 and M_2 are expressed as follows:

$$M_a = \varphi_a \rho_a (\boldsymbol{v}^a - \boldsymbol{v}) \tag{3.111}$$

where $\boldsymbol{v}$ is the velocity vector and, as previously $mentioned, a = 1, 2$ represents the porous and fractured network, respectively.

It should be mentioned that Equations (3.109) and (3.110) will not be used as it is assumed that all the domains will have the same temperature in the solid and the two phases at each point for any time step.

3.4.1 Parameter identification of the fully coupled model

The coefficients included in the six equations (Equations (3.99–3.105 and 3.108-3.110)) presented in Section 3.4 can be divided into two categories: laboratory-based or empirically measured geological parameters and analytically calculated parameters.

Lab-based or empirically estimated geological parameters are:

- The permeabilities of the two phases, k_1 and k_2 with a unit of m^2. They can be calculated using experimental tests, such as direct permeability measurements (Gelet, 2011). Permeability of existing sandstones in the North Sea can range from 10^{-8} to 10^{-15} m^2 according to Fisher et al. (1999). The range of values for porous blocks and fissure network is provided in the research of Kazemi (1969), Khalili and Selvadurai (2003a) and Gelet et al. (2012a).
- The drained elastoplastic stiffness of the material $\boldsymbol{S}^{ep}(D, T)$ used for the deformation model and the calculation of the stress and displacement vector at any selected point, is based on the damage proposed model. It is parted of the Shear and Bulk modulus, which can be estimated after UCS and triaxial tests.
- The coefficients for the heat capacity for the solid C_{ps} and for the saline water in porous and fracture domain C_{p1} and C_{p2}, respectively. Their units are J/kgK. Microscopic analysis needs to be done to identify the minerals and their specific heat capacity and then estimate the heat capacity of the solid and liquid. For sandstones, heat capacity can vary from 775 to 920 J/kgK (Waples and Waples, 2004; Gelet, 2011). For water the specific heat capacity fluctuates with temperature, and it has an average value of 4.2 J/kgK.

- k_s, k_1, k_2 are the thermal conductivity parameters of the solid medium and the saline water inside the porous and fractures domain. Usually, thermal conductivity can be estimated in the laboratory using a guarded parallel-plate apparatus, which consists of a high-pressure chamber, a thermal-conductivity measuring cell, an air thermostat, a high precision temperature regulator, and a high-pressure liquid and gas compressors. The thermal conductivity is estimated by measurement of the heat flux and temperature gradient in the sample placed between heating and cooling plates (Abdulagatova et al., 2009). Thermal conductivity of North Sea can also be estimated using a Needle Probe. For sandstone it varies from 1.7 to 3.4 $\mathrm{W/m℃}$ (Robertson, 1988).

Analytically estimated parameters:

- The effective stress parameters are dimensionless quantities and used for tuning. They relate the changes in saline water pressure to the change in the effective stress, influencing the deformation of the matrix. These are: $\beta_1$and β_2 representing the pore and fracture domain, respectively and the coupling effective stress parameters $\beta_{11},\ \beta_{22}, \beta_{12},\ \beta_{21}$ which are used in Equations (3.102-3.104).
- The compressibility coefficient$s\ c_p, c_f$ and c_s can be estimated analytically and are mentioned in Section 3.4.3. These coefficients have units of Pa^{-1}
- The volumetric thermal expansion coefficient of the fractured porous medium, saline water and the porous and fracture domain are C_T, C_{T1} and C_{T2}, respectively. The volumetric thermal expansion coefficient can be calculated as the change in volume divided by the product of temperature's change and initial volume. If the exact composition of the sandstone is known the thermal expansion coefficient can be estimated using the research of Horseman and McEwen (1996).
- The viscosity of the saline water can be found in the literature, for example work of Qasem et al. (2021) and Li et al. (2013). The average viscosity of the saline water of the North Sea is approximately 1.02 $\mathrm{MPa \cdot s}$ (Couling and Hein, 2019).It can be measured in the lab using a viscometer or a rheometer.
- The aperture factor or leakage parameter is gathered in Section 3.3.7. It can be estimated using a one-dimensional analysis by assuming a normal set of fissures according to Warren

and Root (1963). In the literature, the leakage parameter can vary from $5.3\times 10^{-10}\ 1/\mathrm{P_a s}$ according to Kazemi (1969) to $10^{-7}\ 1/\mathrm{P_a s}$ according to Khalili et al., (1999).

It should be noted here that as the only liquid used in the porous and fracture network is saline water one coefficient can be used for the heat capacity and thermal expansion of the liquid inside the pores and fractures.

3.4.2 Permeability Parameter

Permeability is the ability of a medium to allow the passage of fluid. Ma and Wang (2016) proposed a permeability evolution model for fissured porous sandstones under a wider range of confining pressures. The relationship between permeability and the overall porosity can better estimate the permeability evolution.

$$k = k_0 \left(\frac{\varphi}{\varphi_0}\right)^{\Psi} \left(\frac{1}{\tau}\right)^{\varsigma} \tag{3.113}$$

k, k_0 are the current and reference permeabilities, φ is the current porosity and φ_0 is the reference porosity, Ψ and ς are the parameters of the permeability and permeability resistance.

where $\left(\frac{\varphi}{\varphi_0}\right)^{\Psi}$ is the conventional permeability-porosity approach, which includes the effect of the total porosity on permeability. The $\left(\frac{1}{\tau}\right)^{\varsigma}$ expresses the effects of fissure closure and tortuosity on permeability evolution.

The permeability resistance factor can be expressed as:

$$\tau = \tau_{compaction} + \tau_{tortuosity} \tag{3.114}$$

where

$$\tau_{compaction} = \alpha \left(\frac{\sigma_0'}{\sigma_{oi}'}\right)^{x} \tag{3.115}$$

in which α is the permeability resistance parameter for fissures closure, x is the mean effective stress parameter and σ_{oi}', σ_0' are the initial effective stress and current effective stress, respectively.

The tortuosity resistance factor can be taken as:

$$\tau_{tortuosity} = \beta(\varepsilon_q)^{\xi} \tag{3.116}$$

where β is the permeability resistance parameter, ε_q is the total shear strain and ξ is the shear strain parameter constant for certain materials.

The reference porosity $\varphi_0 = \frac{e}{1+e_0}$, according to Ma and Wang (2016), is obtained through some physical testing methods, and the current porosity can be calculated based on volumetric strain $\varepsilon_v = \varepsilon_1 + 2\varepsilon_3$ in the triaxial test, which can be given from the bounding surface of the presented model. According to Ma and Wang (2016), the whole fractured matrix solids are not deformable, and the volumetric change mainly comes from the change in pore space.

$$\varphi = \frac{e_0 - (1+e_0)\varepsilon_v}{1 + (e_0 - (1+e_0)\varepsilon_v)} \tag{3.117}$$

Thus, in further study, a large set of experimental data is required to investigate the influence of each model parameter on the behaviour of the model for specific loading conditions.

3.4.3 Compressibility coefficients

The compressibility of the fractured porous medium C_f is equal to the inverse drained bulk modulus(K_d) of the material and can be expressed as:

$$C_f = \frac{1}{K_d} \tag{3.118}$$

$$K_d = K_{bulk}^{el}(D) = \frac{vp'}{K_d} \tag{3.119}$$

where $v = 1 + e$ is the specific volume, the void ratio is expressed as: $e = (\varphi_1 + \varphi_2)v$

and $\kappa(D)$ is the slope of the unloading- reloading line (URL) in a $v - lnp'$ space, including also damage effects.

3.5 Damage evolution model for fractures porous media

The hydro-mechanical behaviour of rocks is complicated as the stress-strain response is mostly controlled by porosity, confining pressure, permeability, fracture density and stress-induced

damage. Throughout the literature, most elastoplastic damage models cannot describe the brittle-ductile behaviour of rocks under different confining pressures. This section presents an extensive and unified elastoplastic damage model that could capture macro-scale responses such as brittle, brittle-ductile behaviour, micro-cracks and closure and reopening of existing cracks, based on the framework of Ma and Zhao (2018),

For a certain Representative Elementary Volume (REV) that is quite small to be noticed but big enough to contain several discrete micro-cracks, a plane normal to the direction vector ($\boldsymbol{n}_s$), which has an area (A) and is parted of damaged area (A_D) and undamaged area (A_u) is considered. (D) is the damage variable which is a scalar for the isotropic damage and anisotropic operations. Applying now the normal force (F) on this plane, the stress can be defined as:

$$\sigma = \frac{F}{A} \tag{3.120}$$

The damage variable linked to the vector ($\boldsymbol{n}_s$) is determined as:

$$D = \frac{A_D}{A} \tag{3.121}$$

For the undamaged area, the stress is called latent stress (σ^l), and it is equal to:

$$\sigma^l = \frac{F}{A - A_D} = \frac{F}{A(1 - D)} = \frac{\sigma}{(1 - D)} \tag{3.122}$$

3.5.1 Damage variable

As the damage expands, rock may become anisotropic. Nevertheless, the application of damage scalar according to Ma and Zhao (2018) and Lemaitre (1984), has adequately satisfactory results in damaged materials. Consequently, isotropic damage with some anisotropic extensions is adopted in this study.

During the enlargement of micro-cracks, new free surfaces are generated, and as a result the specific quantity of energy is used up. According to Ma and Zhao (2018) and Lemaitre (1984), energy dissipation consists of two parts, the damaged elastic part ψ_e and the damaged plastic part ψ_p. According to Shao et al. (2006b), ψ_p is the 'locked plastic energy for plastic hardening of

damaged material'. Considering isothermal conditions, the free energy ψ is determined as thermodynamic potential:

$$\psi = \psi_e + \psi_p = \frac{1}{2}[\boldsymbol{\varepsilon} - \boldsymbol{\varepsilon}^p]^T[\boldsymbol{S}^e(D,T)][\boldsymbol{\varepsilon} - \boldsymbol{\varepsilon}^p] + \psi_p(\gamma_{pl}, D, T) \tag{3.123}$$

Where $\boldsymbol{\varepsilon}$ is the total strain and $\boldsymbol{\varepsilon^p}$ is the plastic strain, D is the fourth-order tensor damage variable, $\boldsymbol{S}^e(D,T)$ is the elastic stress matrix of the damaged material, which also contains any expansion of the material due to thermal changes and γ_{pl} is the internal variable for the plastic hardening.

The equation for stress and damage strain release rate are as presented based on (3.123) as follows:

$$\sigma = \frac{\partial \psi}{\partial \boldsymbol{\varepsilon}^e} = [\boldsymbol{S}^e(D,T)][\boldsymbol{\varepsilon} - \boldsymbol{\varepsilon}^p] \tag{3.124}$$

$$Y = -\frac{\partial \psi}{\partial D} = -\frac{1}{2}[\boldsymbol{\varepsilon} - \boldsymbol{\varepsilon}^p]^T[\boldsymbol{S}^e(D,T)]'[\boldsymbol{\varepsilon} - \boldsymbol{\varepsilon}^p] - \frac{\partial \psi_p}{\partial D} \tag{3.125}$$

$[\boldsymbol{S}^e(D,T)]'$ is the derivative of the elastic stiffness tensor at any temperature condition towards the damage variable D. Additionally, based on the second law of thermodynamics, the system will produce energy after the damage, and as a result, the strain damage energy should be bigger or equal to zero.

$$Y\dot{D} \geq 0 \tag{3.126}$$

The stress rate is calculated as follows:

$$\dot{\boldsymbol{\sigma}}' = [\boldsymbol{S}^e(D,T)]'\dot{D}[\boldsymbol{\varepsilon} - \boldsymbol{\varepsilon}^p] + [\boldsymbol{S}^e(D,T)][\dot{\boldsymbol{\varepsilon}} - \dot{\boldsymbol{\varepsilon}}^p] \tag{3.127}$$

3.5.2 Damage characterisation

There are two main hypotheses for the behaviour of the damaged material (Wohua and Valliappan, 1998). The first one is the strain equivalence according to Lemaitre and Chaboche (1975), which mentions that the strain linked with a damaged state under applied stress is similar to the strain associated with its undamaged condition under effective stress. The second one is the complementary energy equivalence. This theory determines that the complementary energy of the damaged state is assumed to be equal to that of the undamaged state when effective stress is applied

(Valliappan et al., 1990). It provides a satisfactory approach for the damage states of both isotropic and anisotropic rock materials.

For this reason, this model applied the complementary energy equivalence hypothesis. The elastic modulus and shear modulus of isotropic damage material is reduced by $(1-D)^2$ from the undamaged value and by a parameter (j) which is the variable accounting for the thermal change. (j) is the percentage of reduced or increased materials stiffness due to temperature change. To determine (j), experimental work needs to be done on the studied rock. Consequently, for isotropic damage:

$$\boldsymbol{S}^e(D,T) = (1-D)^2 j\, \boldsymbol{S}^e \tag{3.128}$$

The Poisson's ratio can be determined according to the International Society for Rock Mechanics and Rock Engineering (ISRM) as "the ratio of the shortening in the transverse direction to the elongation in the direction of applied force in a body under tension below the proportional limit" will also be influenced by the temperature and can be calculated after experimental tests (Dong et al., 2021). It is expressed as:

$$\nu(D,T) = \nu_{temp} \tag{3.129}$$

For anisotropic damage to the three main principal directions $i, r = 1,2,3$, the stress matrix and the Poisson's ratio are presented:

$$\boldsymbol{S^e}_i(D,T) = (1-D_i)^2\, j\boldsymbol{S}_i^e \tag{3.130}$$

$$\nu_{ir}(D,T) = \frac{1-D_i}{1-D_r}\nu_{irtemp} \tag{3.131}$$

The elastic stress rate for isotropic material based on Equations (3.127) and (3.129) can be expressed now as:

$$\dot{\boldsymbol{\sigma}}' = -2(1-D)(\boldsymbol{S}^e(T))\dot{D}[\boldsymbol{\varepsilon}^{el}] + [\boldsymbol{S}^e(D,T)][\dot{\boldsymbol{\varepsilon}}^{el}] \tag{3.132}$$

According to Shao et al. (2006b), as the damaging force Y depends on the plastic strain, the damage criterion is linked to the plastic flow. For isotropic damage and in the case of a non-viscous flow, the damage criterion can be expressed according to Shao et al. (2006b) as follows:

$$f_D(Y, D) = Y - Y_D = 0 \tag{3.133}$$

where Y_D is the damage energy release threshold for the elastoplastic damage behaviour.

Introducing a damage multiplier $\dot{\lambda}_D$ as a positive scalar, the damage evolution rate can be determined as:

$$\dot{D} = \dot{\lambda}_D \frac{\partial f_D}{\partial Y_D} = \dot{\lambda}_D \tag{3.134}$$

The damage multiplier $\dot{\lambda}_D$ is expressed according to Kuhn-Tucker's loading-unloading relations as follows (Kiefer et al., 2017):

$$f_D(Y, D, T) \leq 0, \;\; \dot{\lambda}_D \geq 0, \;\; \dot{\lambda}_D f_D(Y, D, T) = 0 \tag{3.135}$$

where $\dot{\lambda}_D$ can be determined by setting $f_D(Y, D, T) = 0$ and this condition according to Ju (1989) is called consistency condition.

Shao et al. (2006b) proposed a linear function for the damage energy release threshold Y_D for simplicity. According to Ma et al. (2016) this linear equation was only valid for brittle materials under low to medium confining pressures. Consequently, the threshold of damage strain energy release was expressed considering the effects of plastic hardening and hydrostatic pressure, according to Ma et al. (2016), as a kinematic function of hydrostatic stress state (p') , damage variable (D) and plastic hardening modulus (h_p). In addition, according to Ju (1989) scalar damage is appropriate for isotropic damage processes and a fourth-order tensor for anisotropic damage effects.

$$Y_D = Y_{D0} + k_m D \ln(p') exp\left(\frac{1}{h_p}\right) \tag{3.136}$$

where Y_{D0} is the initial value of the damage evolution, and k_m is the material constant that determines the increase in the rate of damage evolution.

For anisotropic damage in one specific direction, Equation (3.136) can be rearranged as:

$$Y_{Di} = Y_{D0i} + k_m D_i \ln(p') exp\left(\frac{1}{h_p}\right) \tag{3.137}$$

According to Lemaitre (1984), Voyiadjis and Kattan (2005) and Ma et al. (2016) a critical damage variable D_{crit} is introduced. This damage variable can describe large–scale brittle rupture. According to Lemaitre (1984) it is suggested that:

$$0.2 \leq D_{crit} \leq 0.8 \tag{3.138}$$

As far as it concerns fractured porous media, according to Ma et al. (2016), (D_{crit}) can link any internal crack development to macroscopic fracture when a brittle fracture occurs in the rock sample. Reaching D_{crit} can induce the collapse of brittle materials with low confining pressure.

According to Ma et al. (2016), the damage consistency condition can be written as:

$$\dot{f}_D = \dot{Y} - \dot{Y}_D = 0 \tag{3.139}$$

3.5.3 Damage Evolution

Two different evolution laws, depending on the material type, have been proposed for fractured porous media. For brittle materials, the model is based on damage strain energy release rate, and for ductile materials, it is developed based on tensile principal stress.

3.5.3.1 Damage Strain Energy Release Rate

The free energy contains elastic (ψ_e) and plastic (ψ_p) parts. The elastic complementary energy release rate is characterised as the rate of energy dissipation of micro-cracks. Stiffness before and after the micro-cracks can determine this release rate. According to Lemaitre (1985b) and Ma et al. (2016) the function of the complementary elastic energy can be given as:

$$\psi_e = \frac{1}{2}[\sigma']^T [\boldsymbol{S}^e(D,T)]^{-1}[\sigma'] \tag{3.140}$$

The plastic function $\psi_p(\gamma_{pl}, D)$ will be parted only from the plastic energy for plastic hardening of damaged material as the temperature is assumed to influence only the elastic part. The plastic deformation due to temperature fluctuation can occur only at elevated temperatures. According to

Shao et al. (2006b) the plastic function can be expressed as a reduction of the plastic function rate to account for the damage evolution.

$$\psi_p(\gamma_{pl}, D) = (1 - x_D D)\psi_{pin}(\gamma_{pl}) \tag{3.141}$$

where $x_D \in [0,1]$ is imported for the coupling between damage evolution and plastic flow. According to Shao et al. (2006b), $x_D = 0$ when there is no coupling between plastic flow and damage. Additionally, assuming that p^* is the crushing pressure of the grains when triaxial conditions are applied, and p'_{conf} is the confining pressure that influences damage, the plastic hardening energy for the undamaged material $\psi_{pin}(\gamma_{pl})$ can be expressed in Equation (3.142). Following the function of plastic hardening energy by Shao et al. (2006b) designed to describe the behaviour of argillite and some modifications by Ma (2014a) in order to extend for a different types of rocks, $\psi_{pin}(\gamma_{pl})$ is suggested as:

$$\psi_{pin}(\gamma_{pl}) = p^*\gamma_{pl} - \mathrm{H}(p^* - p'_{conf})ln\left(\frac{H + \gamma_{pl}}{H}\right) \tag{3.142}$$

where H is the hardening rate parameter and γ_{pl} is the plastic hardening variable, and the rate of each can be defined as the equivalent plastic deviatoric strain:

$$\dot{\gamma_{pl}} = \sqrt{\frac{2}{3}\left(\dot{\boldsymbol{\varepsilon}}^p - \boldsymbol{\delta}\frac{tr(\dot{\boldsymbol{\varepsilon}}^p)}{3}\right) : \left(\dot{\boldsymbol{\varepsilon}}^p - \boldsymbol{\delta}\frac{tr(\dot{\boldsymbol{\varepsilon}}^p)}{3}\right)} \tag{3.143}$$

Substituting Equations (3.141) and (3.142) into Equation (3.125) the damage strain energy release rate is extended to:

$$Y = -\frac{\partial\psi}{\partial D} = -\frac{1}{2}[\boldsymbol{\varepsilon} - \boldsymbol{\varepsilon}^p]^T[\boldsymbol{S}^e(D,T)]'[\boldsymbol{\varepsilon} - \boldsymbol{\varepsilon}^p] + x_D\psi_{pin}(\gamma_{pl}) \tag{3.144}$$

Based on the damage evolution using the power of law for brittle materials according to Yazdchi et al. (1996) , the damage model of Lemaitre (1985b) for ductile fracturing and the research of Ma et al. (2016) ,the damage evolution can be then expressed as:

$$\dot{D} = \begin{cases} \mathrm{H}_Y(Y)^{1/m} & ,Y > Y_D \\ 0 & ,Y \leq Y_D \end{cases} \tag{3.145}$$

For anisotropic damage the subscript index *i* will be included in Equation (3.146):

$$\dot{D}_i = \begin{cases} \mathrm{H}_{Yi}(Y_i)^{1/m} & ,Y_i > Y_{Di} \\ 0 & ,Y_i \leq Y_{Di} \end{cases} \tag{3.146}$$

Where $m > 1$ is the material constant and can be determined by experimental results, H_Y and Y_D are not constant and are the damage evolution rate parameter and the threshold value of damage energy release rate, respectively.

The stress ratio $\eta = \frac{q}{p'}$ can be used to determine the relation between deviatoric and hydrostatic stresses. This is important as, generally, hydrostatic stress can be responsible for the closure of micro-cracks, and we need to discover the propagation of the micro-cracks. Taking into consideration the confining pressure p'_{conf} and the slope of the critical state line M_{cs}, the rate parameter H_Y can be expressed according to Ma (2014a) as follows:

$$H_Y = h_\gamma |lnz| \left| ln\left(\frac{M_{cs} + \eta}{2M_{cs}}\right)\right| \tag{3.147}$$

Rocks generally undergo cracking in tension and crushing in compression., where $z = {p'_o}/{\left(p'_{conf} + 1\right)}$, with the p'_o being the maximum hydrostatic compressive pressure or the historic consolidated pressure and h_γ is a material constant determined by fitting the experimental results.

For anisotropic damage, the damage evolution rate parameter is expressed for a specific loading direction as follows:

$$H_{Yi} = h_{\gamma i} |lnz| \left| ln\left(\frac{M_{cs} + \eta}{2M_{cs}}\right)\right| \tag{3.148}$$

3.5.3.2 Damage evolution based on Von-Mises criterion or tensile principal stress

A damage kinematic equation based on tensile principal stress that could describe the stress and damage evolution for ductile materials was proposed by Kachanov (1980). Yazdchi et al. (1996) adopted this evolution and used it for brittle materials. Both estimated well the brittle and ductile

material behaviour. Considering the experimental data describing the mechanical behaviour of Baud et al. (2000) and Wong and Baud (1999), the damage evolution mainly depends on confining pressure, strain rate, porosity and stress ratio.

In fracture mechanics, fracture takes place when the current principal tensile stress exceeds the tensile strength in the stress domain. Rock materials are exposed both to hydrostatic and deviatoric stress. Consequently, the equivalent stress or Von-Mises criterion is applied. Von-Mises criterion is applicable for the analysis of plastic deformation for ductile materials. The yielding of the ductile material begins when the second invariant of deviatoric stress J_2 reaches a critical value. The equivalent stress is equal to the deviatoric stress as mentioned previously ($\sigma_{eq} = \sqrt{3J_2}$). According to Yazdchi et al. (1996), Lemaitre (1985b), Kachanov (1980) and Ma (2014a), a more accurate evolution law for ductile material is proposed.

The damage evolution law based on the Von-Mises criterion is:

$$\dot{D} = \begin{cases} \mathrm{H}_{\sigma_{eq}} \left(\sigma_{eq}\right)^{1/m} & , \sigma_{eq} > \sigma_{eqt} \\ 0 & , \sigma_{eq} \leq \sigma_{eqt} \end{cases} \tag{3.149}$$

For anisotropic damage in certain principal stress directions, the damage evolution can be expressed as:

$$\dot{D}_{\iota} = \begin{cases} \mathrm{H}_{\sigma_{eqi}} \left(\sigma_{eqi}\right)^{1/m} & , \sigma_{eqi} > \sigma_{eqti} \\ 0 & , \sigma_{eqi} \leq \sigma_{eqti} \end{cases} \tag{3.150}$$

where the $H_{\sigma_{eq}}$ is the damage evolution rate and depends on the stress state (confining pressure and stress ratio).

$$H_{\sigma_{eq}} = h_{\sigma_{eq}} |lnz| \left| ln\left(\frac{M_{cs} + \eta}{2M_{cs}}\right) \right| \tag{3.151}$$

For anisotropic damage in certain principal stress directions:

$$H_{\sigma_{eqi}} = h_{\sigma_{eqi}} |lnz| \left| ln\left(\frac{M_{cs} + \eta}{2M_{cs}}\right) \right| \tag{3.152}$$

The hydrostatic stress (p') is responsible for the development of micro-cracks, the damage variable (D) describes the degradation in material stiffness and the plastic hardening or softening of the rock is determined by the plastic hardening energy (h). $h_{\sigma_{eq}}$ is the material constant that may be determined by fitting experimental results. Based on those, the threshold of the damage equivalent stress σ_{eqt} can be expressed as (Ma, 2014b):

$$\sigma_{eqt} = \sigma_{eqt0} + \frac{k_{\sigma_{eq}} p' \exp(1/h)}{(1-D)} \tag{3.153}$$

For anisotropic damage in a specific principal stress direction:

$$\sigma_{eqti} = \sigma_{eqt0i} + \frac{k_{\sigma_{eqi}} p' \exp(1/h)}{(1-D_i)} \tag{3.154}$$

During grain crushing, when the maximum hydrostatic stress is applied, the values of damage evolution rate get closer to zero as plasticity influences the deformation and there is extremely low damage propagation. Additionally, the threshold damage energy release rate, i.e., Equation (3.134), and threshold damage equivalent stress, i.e., Equation (3.151), are both considering the hydrostatic stress (p'). This can be explained as during the rise of pore water pressure, cracks may regenerate, while when the pore water pressure decreases, the open cracks and fractures may disappear due to the increase in effective mean stress p'. As a result, when the pore water pressure decreases, the threshold value of damage would increase, and higher demand on pressure would be needed for further damage evolution.

3.6 Plasticity Model

3.6.1 Critical State Mechanics considerations

The critical state line (CSL) separates the brittle and ductile deformation in the $p' - q$ graph. Based on the Mohr-Coulomb model and introducing the frictional angle at the critical state (ϕ'_{cs}) the slope of CSL (M_{cs}) can be expressed according to Wood (1991) as follows:

$$M_{cs} = \frac{6sin\phi'_{cs}}{\pm 3 - sin\phi'_{cs}} \tag{3.155}$$

The $(\pm)$ is used to represent the compressive loading by using the positive symbol and the extension by using the minus. According to Wood (1991) the friction angle is the same in compression and tension, but the value of (M_{cs}) is different.

The slope of the critical state line (M_{cs}) as a function of the lode angle (ϑ) can be expressed as :

$$\vartheta = sin^{-1}\left[-\frac{3\sqrt{3}}{2}\frac{J_3}{\sqrt{J_2}}\right] \tag{3.156}$$

where $J_3 = det\boldsymbol{S} = \frac{1}{3}S_{ij}S_{jk}S_{ki}$ is the third invariant of the deviatoric stress vector.

The Lode angle can vary from $+\frac{\pi}{6}$ for the maximum critical state line slope (M_{csmax}) during a compressive triaxial test to $-\frac{\pi}{6}$ for the minimum critical state line slope (M_{csmin}) during extensive triaxial test (Khalili et al. 2008). The slope of the critical state line can be expressed in terms of Lode angle as below (Sheng et al., 2000; Khalili et al., 2008):

$$M_{cs}(\vartheta) = M_{csmax}\left(\frac{2\Delta^4}{1+\Delta^4-(1-\Delta^4)sin3\vartheta}\right)^{\frac{1}{4}} \tag{3.157}$$

In Equation (3.157) if $\Delta = 1$ then the yield surface represents the Von-Mises Circle. The Mohr-Coulomb hexagon in the deviatoric plane can be represented if $\Delta = \Delta_M$ with Δ_M being equal to:

$$\Delta_M = \frac{M_{csmin}}{M_{csmax}} = \frac{3-sin\phi'_{cs}}{3+sin\phi'_{cs}} \tag{3.158}$$

The failure surface described by the Equation (3.157) is differentiable for all stress states and is convex if $\Delta \geq 0.6$, i.e. $\phi'_{cs} = 48.59℃$ or Mcs≤2.

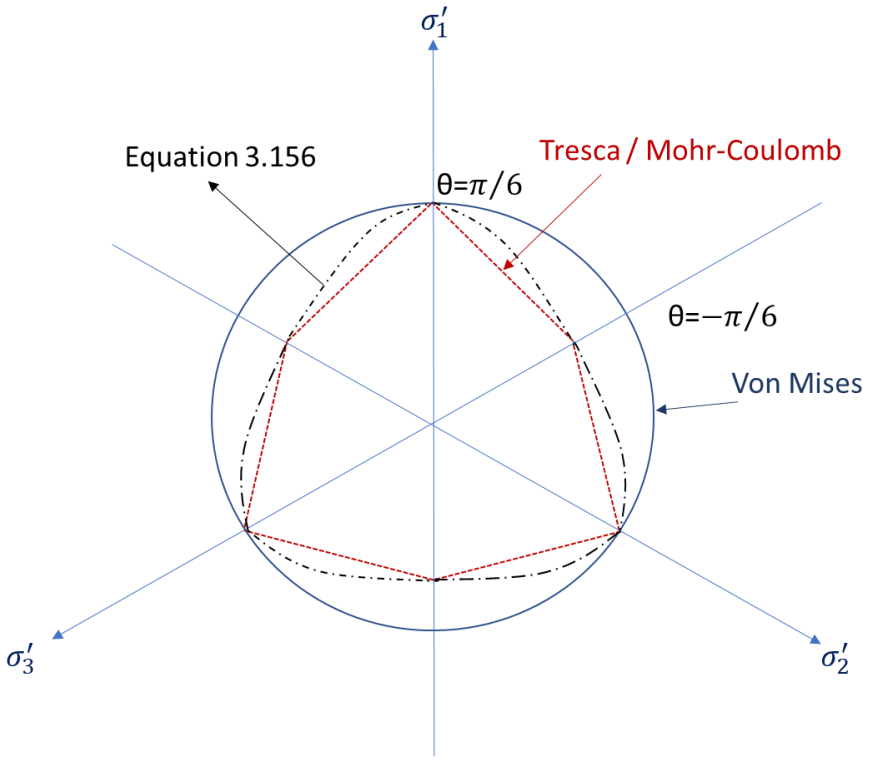

Figure 3. 2 Shape of the failure surface compared to Von-Mises and Tresca criterion

For critical state models, the elastic bulk modulus $\left(K_{bulk}^{el}\right)$and elastic shear modulus (G^{el}) can be expressed considering that the loading-unloading line occurs along a κ line in the $v - lnp'$ plane as follows:

$$K_{bulk}^{el} = \frac{vp'}{\kappa} \tag{3.159}$$

$$G^{el} = \frac{3(1-2v)}{2(1+v)}\frac{vp'}{\kappa} \tag{3.160}$$

where $v = 1 + e$ is the specific volume; κ is the slope of the unloading- reloading line (URL) in a $v - lnp'$ diagram. The schematic illustration of the isotropic compression line (ICL), critical state line (CSL), of the unloading-reloading line (URL) in the $v - lnp'$domain based on Wood (1991) is presented in Figure 3.3.

Where λ is the is the gradient of the isotropic compression line, N_0 and Γ are the values of the specific volume for ICL and CSL, respectively at $p' =$

$1\ KPa\ or\ 1\ MPa$ and p'_{ch} is the historic consolidated pressure (pre-consolidation pressure). The ICL is the loosest possible state that the rock can achieve for a specific mean effective stress.

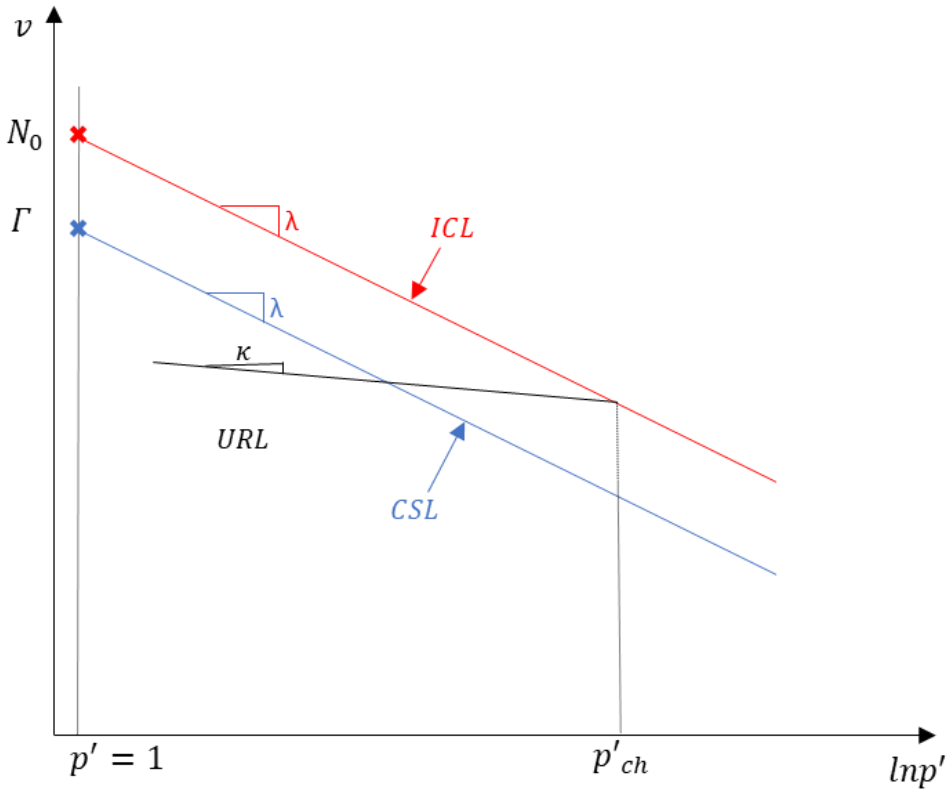

Figure 3. 3 Full representation of ICL, URL, and CSL in the v − lnp′ space based on CSSM.

If the rock is exposed to plastic damage, the lines in Figure 3.3 will be affected by the damage evolution. Experimental data by Baud et al. (2000), Cuss et al. (2003), Zhang et al. (1990b), Zhang et al. (1990a) , and David et al. (1994) indicated that despite the fact that the slope of the *CSL* in the $q - p'$ space is the same, in the $v - lnp'$ domain the ICL and URL are becoming steeper during damage increase, compared to the lines presented in Figure 3.3 where the damage does not exist. After comparing these different experimental results, Ma (2014a) suggested that the ICL and CSL moved downwards by increasing damage while the URL line shift upwards. A representation of this can be seen in Figure 3.4.

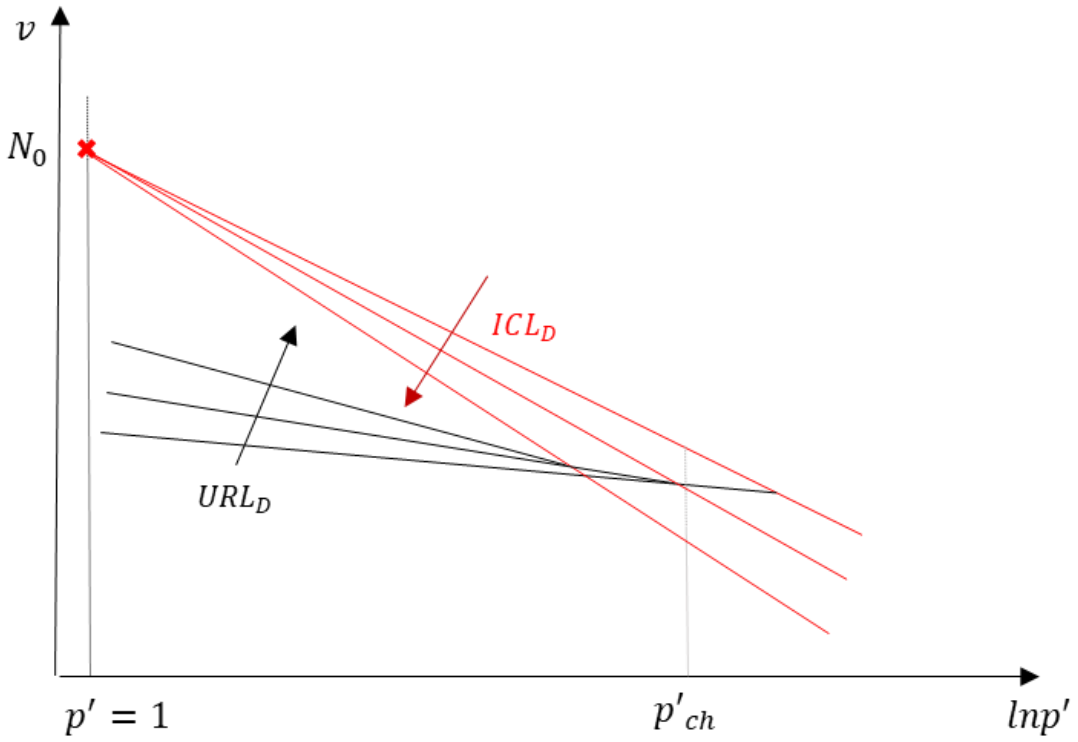

Figure 3. 4 Damage influence on the gradients of ICL and URL line. Arrows indicate an increase in damage.

According to Zhang et al. (1990b) and David et al. (1994), it can be assumed that the CSL and the ICL are parallel to each other in the $v - lnp'$ space. In order to consider the damage evolution, the lines shown at Figure 3.3 will be renamed as ICL_D, CSL_D and URL_D. The gradient of the line and the values of the specific volume will also be presented according to damage: N_D, Γ_D, κ_D, with λ not being influenced by the damage.

According to Khalili et al. (2005), certain aspects of the model are associated to a state parameter (ξ), which is a dimensionless parameter defined as the vertical distance between the current state and specific effective stress and the critical state line in the $v - lnp'$ domain, as shown in Figure 3.5. ξ is positive on the loose side and negative on the dense side of the critical state line.

The damaged bulk modulus considering the present acting hydrostatic pressure (p') and damage variable (D) can be expressed as:

$$K_{bulk}^{el}(D) = \frac{vp'}{\kappa_D} \tag{3.161}$$

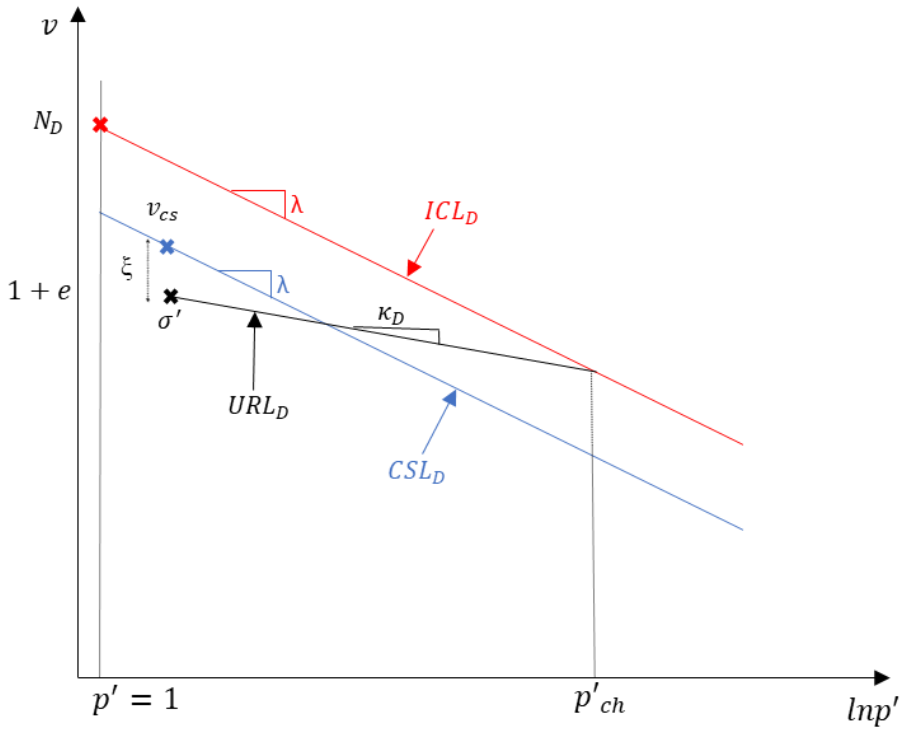

Figure 3. 5 Full representation of ICL_D,URL_D, CSL_D in the $v - lnp'$ space based on CSSM including damage

Using Equation (3.161) it can be said that increasing the damage to the material (generate new fractures or microcracks), the slope of the unloading-reloading line κ_D increases and consequently, the bulk modulus decreases.

In addition to the damage influence, thermal change-induced volume change of the material due to the injection of CO_2 should be considered. Based on the formation of Equation (3.128), the elastic damage bulk modulus can be related to the undamaged bulk modulus by multiplying the undamaged part by $(1-D)^2$ as well as by a parameter j which is the variable accounting for the thermal expansion. The $(1-D)^2$ was created by decreasing the specific volume by $(1-D)$ and by increasing the gradient of the URL line by the same amount.

$$K_{bulk}^{el}(D,T) = (1-D)^2 \frac{vp'^{new}}{\kappa} j \tag{3.162}$$

The damaged elastic bulk modulus will be expressed on behalf of a new different hydrostatic pressure p'^{new}, which will be lower compared to the hydrostatic pressure in the undamaged material, as the rock will lose elastic stiffness according to Equation (3.128).

Elastic shear damage modulus $G^{el}(D)$ and gradient of URL_D line are presented as follows:

$$G^{el}(D,T) = \frac{3(1-2\nu)}{2(1+\nu)} K^{el}_{bulk}(D,T) \tag{3.163}$$

$$\kappa_D = \frac{\kappa}{(1-D)} \tag{3.164}$$

3.6.2 Elastoplastic behaviour coupled with damage effects.

According to Ofoegbu and Curran (1991), elastic deformation is linked to the compression and extension of the uncracked rock. On the other hand, plastic deformation is associated with two aspects: reopening-closure of the existing microcracks or generating new ones (brittle behaviour under low pressure), grain crushing and microcrack surface sliding results in ductile behaviour under high pressure. In most rocks, the two aspects contribute to plastic behaviour simultaneously. Therefore, the coupling of the two behaviours could give a robust model describing the rock.

According to Ofoegbu and Curran (1991) and Ma (2014a), plastic behaviour can be quantified by damage evolution and plastic flow. The damage evolution creates more cracked areas for sliding or crushing and as a result, the plastic flow depends on the damage evolution and the stress rate. Therefore, the effect of damage evolution is considered for developing the plastic hardening function (Ma 2014)

The strain rate consists of elastic, including also the thermal-induced elastic component, and plastic parts as follows:

$$\dot{\boldsymbol{\varepsilon}} = \dot{\boldsymbol{\varepsilon}}^{el} + \dot{\boldsymbol{\varepsilon}}^{p} + \dot{\boldsymbol{\varepsilon}}^{T} \tag{3.165}$$

Where $\dot{\boldsymbol{\varepsilon}}^{el}$ is the elastic strain increment, $\dot{\boldsymbol{\varepsilon}}^{p}$ is the plastic strain increment, $\dot{\boldsymbol{\varepsilon}}^{T}$ is the thermal induced elastic strain as it is assumed that the temperature change leads to isotropic elastic expansion with $\dot{\boldsymbol{\varepsilon}}^{T} = \frac{C_{Ts}}{C_f}\delta\dot{T}$

The elastic incremental stress rate can be expressed by integrating Equation (3.124) and also considering the damage and thermal expansion variable. The derivative of the elastic stress matrix will be multiplied by the damage evolution variable plus the rate of expansion due to thermal change.

$$\dot{\boldsymbol{\sigma}}' = [\boldsymbol{S}^e(D,T)]\left(\left(-\frac{2\dot{D}}{(1-D)}\right)\left(\boldsymbol{\varepsilon}^{el} - \frac{C_{Ts}}{C_f}\Delta T\right) + \left(\dot{\boldsymbol{\varepsilon}} - \frac{C_{Ts}}{C_f}\delta\dot{T}\right)\right) \tag{3.166}$$

Where $\Delta T = T - T_0$, which is the reference gap between the initial (T_0) and current state (T).

The damaged elastic modulus can be expressed as:

$$\boldsymbol{S}^e(D,T) = \begin{bmatrix} K_{bulk}^{el}(D,T) & 0 \\ 0 & 3G^{el}(D,T) \end{bmatrix} \tag{3.167}$$

According to Khalili et al. (2005), for plasticity, the incremental plastic stress-strain relationship is presented as:

$$\dot{\boldsymbol{\varepsilon}}^p = \frac{1}{h}\boldsymbol{x}\boldsymbol{n}^T\dot{\boldsymbol{\sigma}}' = \dot{\lambda}\boldsymbol{x} \tag{3.168}$$

Where $\boldsymbol{n} = [n_p \quad n_q]^T$ is the unit vector normal to the loading surface at the current stress state $\boldsymbol{\sigma}'$ and $\boldsymbol{x} = [x_p \quad x_q]^T$ is the unit direction of the plastic flow at $\boldsymbol{\sigma}'$; h is the hardening modulus and $\dot{\lambda}$ is the plastic multiplier.

Combining Equations (3.161), (3.162), (3.165) and (3.166), the increments of stress-strain can be determined as:

$$\dot{\boldsymbol{\sigma}}' = \left(\dot{\boldsymbol{\varepsilon}} - \frac{C_{Ts}}{C_f}\boldsymbol{\delta}\dot{T} - \left(\frac{2\dot{D}}{(1-D)}\right)\left(\boldsymbol{\varepsilon}^{el} - \frac{C_{Ts}}{C_f}\boldsymbol{\delta}\Delta T\right)\right)\left(\frac{\boldsymbol{S}^e(D,T)h}{h + \boldsymbol{x}\boldsymbol{n}^T\boldsymbol{S}^e(D,T)}\right) \tag{3.169}$$

3.6.3 Bounding Surface Model

Elastic behaviour takes place when the current stress state σ' lies inside the loading surface. The first yield occurs when σ' cross the loading surface. Plastic straining occurs when the stress state σ' is on or within the bounding surface. The key elements of bounding surface plasticity according to Khalili et al. (2005) are:

- The bounding surface that divides the allowed and unacceptable states of stress,
- The loading surface where the current stress state exists,
- The plastic potential characterising the mode and basic magnitude of plastic change and

- Hardening rules controlling the size and position of the loading and bounding surface as well as the progression of the current state by using an image point to the bounding surface.

The hardening modulus expressed in Equation (3.168) can be determined according to the bounding surface based on Khalili et al. (2005) as a decreasing function of the distance between the current state σ' and an "image point" on the bounding surface $\breve{\sigma}'$. The "image point" is based on a mapping rule such that the unit normal vectors to the loading and bounding surface are the same. Stress states at the bounding surface are expressed by using a breve bar.

The key elements of the bounding surface and the unit normal vectors are presented in Figure 3.6.

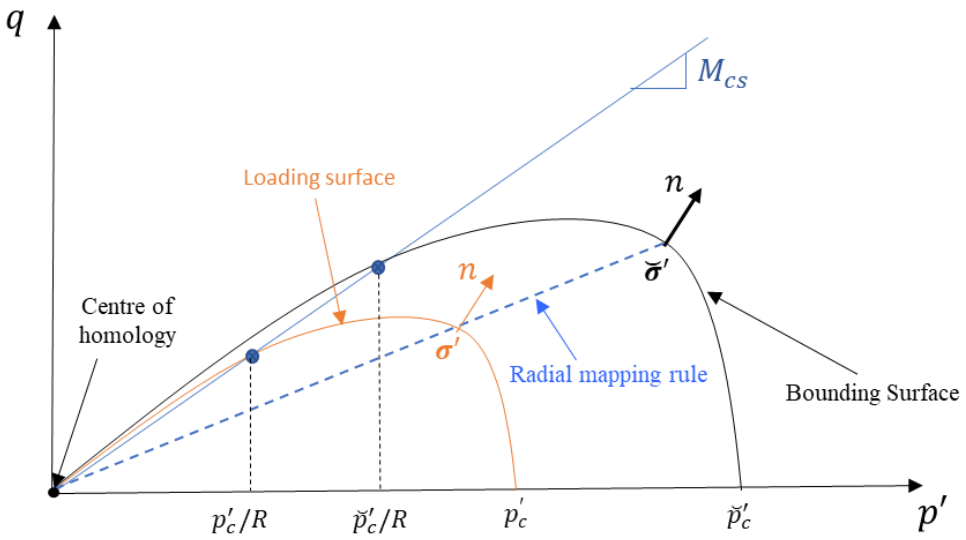

Figure 3. 6 Bounding surface, Loading surface and mapping rule for compression of rock.

The unit normal vector $\boldsymbol{n}$ at the at the stress state $\boldsymbol{\sigma}'$, as seen in Figure 3.6, defines the direction of loading and can be determined by the general equations of Khalili et al. (2005) as follows:

$$\boldsymbol{n} = \pm \frac{\partial L/\partial \boldsymbol{\sigma}'}{\|\partial L/\partial \boldsymbol{\sigma}'\|} = \pm \frac{\partial f/\partial \boldsymbol{\sigma}'}{\|\partial f/\partial \boldsymbol{\sigma}'\|} \tag{3.170}$$

The components of $\boldsymbol{n} = [n_p \quad n_q]^T$ at $\boldsymbol{\sigma}'$ can be expressed as:

$$n_p = \pm \frac{-\breve{q}/(\breve{p}'[1 - 1/(Mln(\breve{p}'_c/\breve{p}'))])}{\sqrt[+]{\{-\breve{q}/(\breve{p}'[1 - 1/(Mln(\breve{p}'_c/\breve{p}'))])\}^2 + 1}} \tag{3.171}$$

$$n_q = \pm \frac{1}{\sqrt[+]{\{-\breve{q}/(\breve{p}'[1-1/(Mln(\breve{p}_c'/\breve{p}'))])\}^2+1}} \tag{3.172}$$

Khalili et al. (2005) theory was adopted in this study. The equation describing the bounding surface presented in Figure 3.6, for a different type of porous rock, can be determined as:

$$f(\breve{p}', \breve{q}, \breve{p}_c') = \frac{\breve{q}}{M_{cs}\breve{p}'} - \left(\frac{ln(\breve{p}_c'/\breve{p}')}{lnR}\right)^{1/M} = 0 \tag{3.173}$$

Where $\breve{p}'$ represents the current effective stress on the yield surface, $\breve{p}_c'$ controls the size of the bounding surface and is a function of the damage variable D and the plastic volumetric strain ε_v^p; M is a calibrating parameter that controls the shape of the bounding surface and according to Yu (1998) for soils it range between 1 to 5. For the value of 1 the yield function is reduced to the original Cam-Clay model; R is a material constant that represents the ratio between $\breve{p}_c'$ and the value of $\breve{p}'$ at the crossing point of the yield function f with the CSL_D in the $q-p'$ domain as shown in Figure 3.7. For sandstone, according to Ma (2014b), M can take values from 1.75 to 2.5 and R from 2 to 2.45.

The loading and the bounding surface are assumed to be of the same shape and homologous about the origin in the $q-p'$ space. So, the loading function can be expressed as follows:

$$L(p', q, p_c') = \frac{q}{M_{cs}p'} - \left(\frac{ln(p_c'/p')}{lnR}\right)^{1/M} = 0 \tag{3.174}$$

p_c' is an isotropic hardening parameter controlling the size of the loading surface. The effective stress σ' is always located on the loading surface.

For unloading and reloading (cyclic loading) the centre of homology, presented in Figure 3.7, moves to the last point of stress in the loading surface (Khalili et al. (2005)). Now the maximum loading surface becomes the bounding surface for the unloading-reloading procedure. The new stress is facing opposite to the previous one, and the loading surfaces that will be created following the kinematic hardening are tangent to the local bounding surface.

The shape of the bounding surface is created by plotting the yield points in the $q-p'$space for different materials. To validate Equation (3.173), the yielding points were plotted for different

types of sandstones based on the experimental research of Wong et al. (1997a), as seen in Figure 3.7.

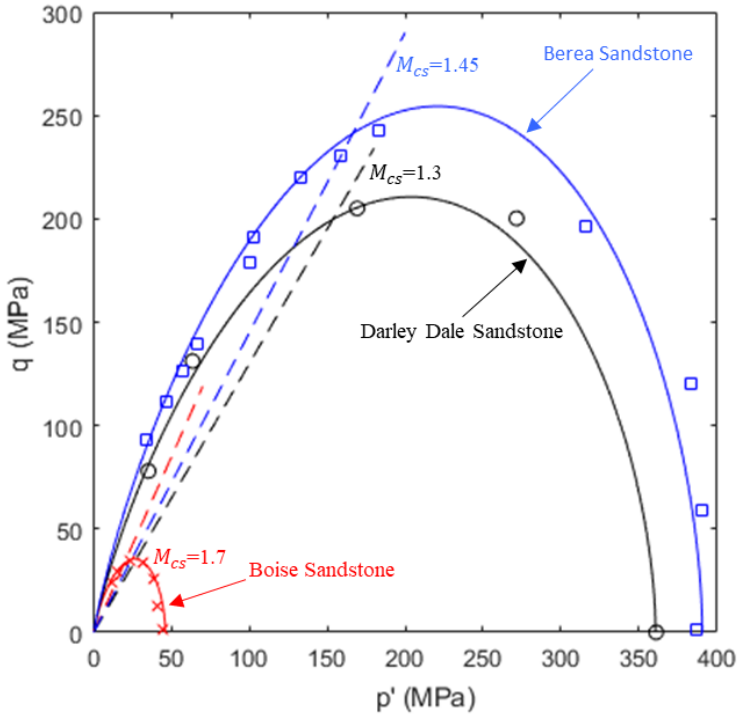

Figure 3. 7 Yield points for three different types of rock (Boise Sandstone, Darley Dale Sandstone and Berea Sandstone) from experimental data (Wong et al., 1997a) and fitted yield curves using the modified Cam-Clay model bounding surface based on Khalili et al. (2005)

3.6.4 Plastic damage hardening

If damage takes place at the rock, the dilatancy-induced plastic strain can be accommodated by the plastic potential ($g = 0$), which is a factor of stress state, and by the dilatancy factor (d). The plastic damage hardening expresses the ratio between the incremental plastic volumetric strain and the incremental plastic shear strain. The dilatancy factor is positive for the opening or regeneration of micro-cracks and negative for the closure. The forces acting during the procedure are the deviatoric stress and the hydrostatic stress. Gajo and Wood (1999) adopted the stress dilatancy relationship of Rowe and Taylor (1962), which is a widely used flow rule, and Khalili et al. (2005) suggested for the plastic dilatancy the follow equation:

$$d = \frac{\dot{\varepsilon}_p^p}{\dot{\varepsilon}_q^p} = \frac{\partial g/\partial p'}{\partial g/\partial q} = M_d - \frac{q}{p'} \tag{3.175}$$

where $M_d = (1 + k_d\xi)M_{cs}$, and k_d is a material constant. M_d is used instead of M_{cs} to capture the change of the shape of the critical state line due to damage hardening (Rowe and Taylor, 1962).

For porous rock, the plastic potential of Khalili et al. (2005) was adopted:

$$g(p', q, p_0) = q + (1 + k_d\xi)M_{cs}p' ln\frac{p'}{p'_o} \tag{3.176}$$

Where p'_o is a dummy variable controlling the size of the plastic potential according to Ma (2014a).

According to Khalili et al. (2005) and Khalili (2008), at any stress point $\boldsymbol{\sigma}'$ of a typical shape of plastic potential, two vectors of plastic flow are identified, one for compressive and one for extensive loading. The compressive vector, which will be used in this research, can be seen in Figure 3.8.

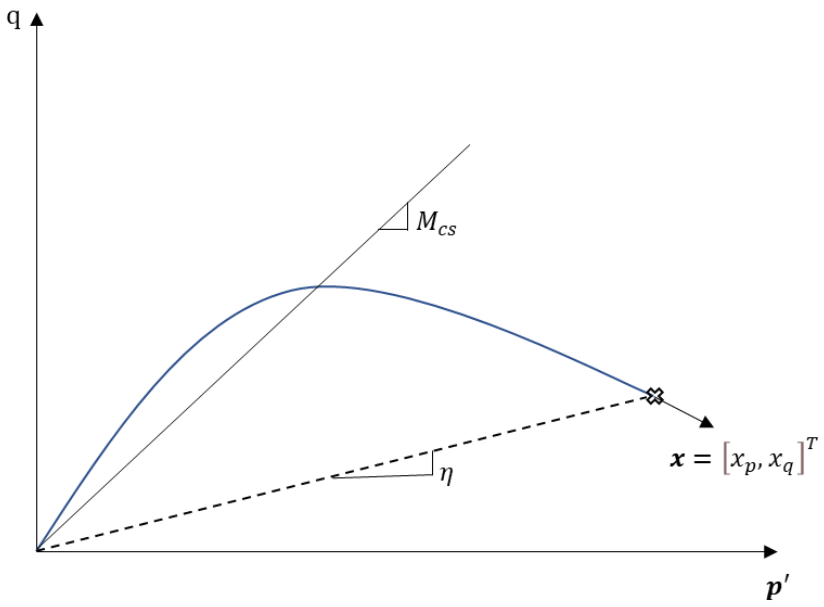

Figure 3. 8 Flow plasticity model based on Khalili et al. (2005)

The components of $\boldsymbol{x} = [x_p, x_q]^T$ at $\boldsymbol{\sigma}'$ can be determined in a general form as:

$$x_p = \pm\frac{\partial g/\partial\boldsymbol{\sigma}'}{\|\partial g/\partial\boldsymbol{\sigma}'\|} = \pm\frac{d}{\sqrt[+]{1 + d^2}} \tag{3.177}$$

$$x_q = \pm\frac{\partial g/\partial \mathrm{q}}{\|\partial g/\partial\boldsymbol{\sigma}'\|} = \pm\frac{1}{\sqrt[+]{1 + d^2}} \tag{3.178}$$

It should be noted that the positive or negative direction is based on the sign of deviatoric stress at bounding surface rather than at the loading surface.

Regarding the plastic hardening of the rock, Ma (2014a) suggested that the damage would reduce the yield surface expansion under the same plastic volumetric change. The hardening rule for the coupled plasticity damage can be achieved considering fluctuation of the ICL_D for an arbitrary loading path IF as indicated in Figure 3.9.

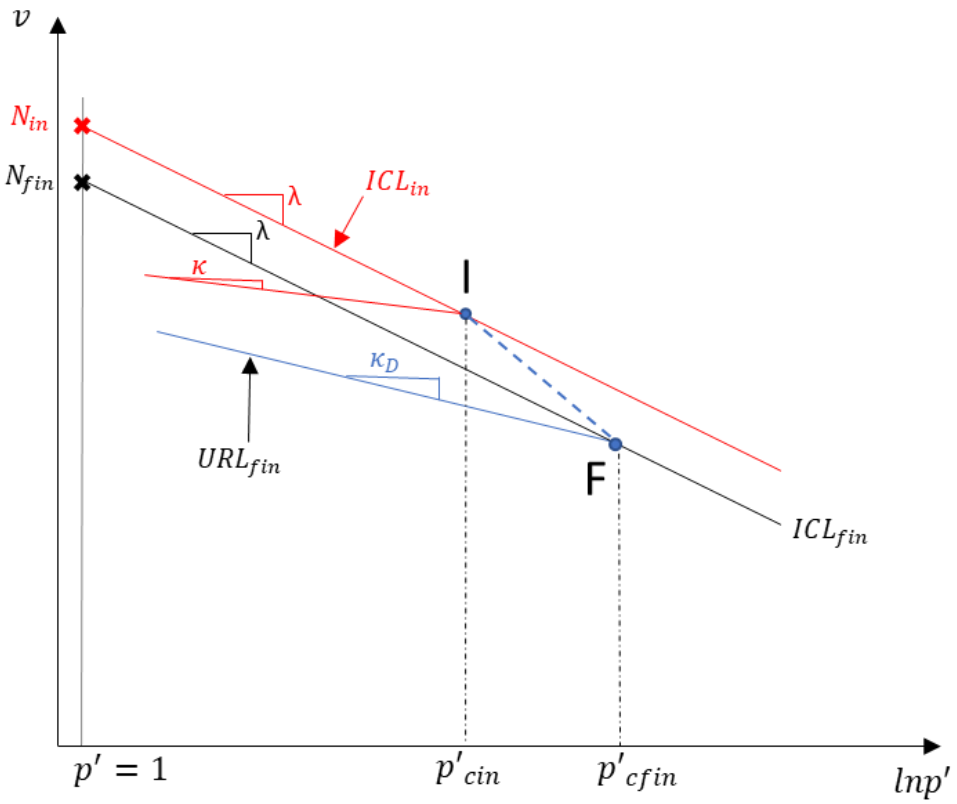

Figure 3. 9 Initial and final damage state representation for Isotropic Compression Line (ICL_{in}, ICL_{fin}) and Unloading-Reloading Line ((URL_{in}, URL_{fin})

The plastic volumetric change from points I to F as shown in Figure 3.9 is:

$$\Delta v^p = \Delta v_{IF} - \Delta v^e = [N_{in} - \lambda \ln(p'_{cin})] - [N_{fin} - \lambda \ln(p'_{cfin})] - \kappa_D ln\left(\frac{p'_{cfin}}{p'_{cin}}\right) \quad (3.179)$$

p'_{cin} and p'_{cfin} are equivalent to the hardening parameters at the initial and final states of damaged materials. As the volume at the initial damage state (point I) is v_{in}, the plastic strain is written as $\Delta\varepsilon_p^p = {\Delta v^p}/{v_{in}}$.

After rearranging Equation (3.179) a new equation can be determined as follows:

$$\breve{p}'_{cfin} = \breve{p}'_{cin} exp\left(\frac{N_{fin} - N_{in}}{\lambda - \kappa_D}\right) exp\left(\frac{v_{in}\Delta\varepsilon_p^p}{\lambda - \kappa_D}\right) \tag{3.180}$$

Following the usual approach in the bounding surface plasticity, the hardening modulus h is separated in two components, the plastic modulus h_b at stress point $\boldsymbol{\sigma}'$ and the arbitrary modulus h_f (the distance between the $\boldsymbol{\sigma}'$ and $\breve{\boldsymbol{\sigma}}'$), as:

$$h = h_b + h_f \tag{3.181}$$

Applying the plastic consistency condition at the bounding surface according to Khalili et al. (2008) and assuming that isotropic hardening of the bounding surface is connected with isotropic damage and plastic compressive volumetric strain, h_b can be expressed as:

$$h_b = -\frac{\partial f}{\partial \breve{p}'_c}\left(\frac{\partial \breve{p}'_c}{\partial \varepsilon_p^p} + \frac{\partial \breve{p}'_c}{\partial D}\frac{\dot{D}}{\dot{\varepsilon}_p^p}\right)\frac{x_p}{\|\partial f/\partial \breve{\boldsymbol{\sigma}}'\|} \tag{3.182}$$

The arbitrary modulus h_f can be expressed based on the formulation proposed by Khalili et al. (2008) for sand and soil materials as:

$$h_f = \pm\left(\frac{\partial \breve{p}'_c}{\partial \varepsilon_p^p} + \frac{\partial \breve{p}'_c}{\partial D}\frac{\dot{D}}{\dot{\varepsilon}_p^p}\right)\frac{p'}{\breve{p}'_c}\left(\frac{\breve{p}'_c}{p'_c} - 1\right)m_p(\eta_p - \eta) \tag{3.183}$$

where $\breve{p}'_c$ and p'_c control the size of the bounding surface and the loading surface, respectively, m_p being a material parameter and $\eta = \frac{q}{p'}$ and $\eta_p = (1 - k_d\xi)M_{cs}$, with k being a material parameter. According to Khalili et al. (2005) h_f is zero at the bounding surface and infinite at the stress reversal point.

3.6.5 Parameters identification of the bounding surface model

Two major damage evolution laws have been proposed for fractured porous media. The damage strain energy release rate and the Von-Mises criterion or tensile principal stress. The parameters define the damage model are presented as follows and can be separated into tuning or lab/analytically estimated geological parameters.

Lab-based or analytically estimated parameters are:

- H the hardening rate parameter, which is obtained by isotropic compressive test.
- $\breve{p}_c'$ is a material parameter controls the size of the bounding surface and it is obtained by hydrostatic compressive test.
- $k_{\sigma_{eq}}$ controls the increase rate for the damage evolution threshold values and
- Y_{D0i} and σ_{eqt0} are the initial thresholds of the damage evolution and only depend on the damage and current stress, respectively.

Tuning parameters:

- x_D is the coupling parameter for damage plasticity. For fully coupled analysis it is equal to 1 and 0 for uncoupled.
- m_p is the material constant related to hardening modulus
- h_γ and $h_{\sigma_{eq}}$ are material constants that determine the damage evolution
- rate m is the material parameter for the damage evolution rate and it varies according to the material.
- k_d is used to define the peark strength line
- R and M are model parameters that define the shape of the bounding surface and can be determined by studying the failure bounding surface under high pressure.

Chapter 4. Analysis of experimental testing of Stainton Sandstone

4.1 Introduction

This Chapter presents uniaxial and triaxial laboratory tests conducted on sandstone to explore how the mechanical properties evolve under freezing conditions over a range of confining pressures relevant to the near-wellbore region during subsurface storage and injection of CO_2.

As mentioned in Section 2.1.2, the injected CO_2 can be heated up to wellbore head formation temperature, to avoid large thermal fluctuations inside the wellbore. However, these heating operations are financially, and energetically burdensome and colder temperatures could be more advantageous. Several previous studies have considered CO_2 injection temperatures lower than that of the rock formation nearby the wellbore (Vilarrasa et al., 2013; Aursand et al., 2017; Roy et al., 2018). Cold CO_2 injection (at temperatures lower than the wellbore-head temperature, usually < 4.5°C) can result in a large thermal contrast between the wellbore wall and surrounding rock leading to a reduction in effective stresses, which can bring the stress state closer to failure (Segall and Fitzgerald, 1998). The uniaxial and triaxial freezing tests on sandstone are essential as the mechanical properties of specific rock at low temperatures ($T < 0^oC$) are rarely reported in the literature.

The average seabed depths for the current CCS projects in the North Sea, such as Teesside endurance saline aquifer is 80 m according to Sündermann and Pohlmann (2011), corresponding to a hydrostatic pressure of 0.8 MPa. The fully saturated formation is subjected to vertical gradients of in situ stresses range from 23 to 25 kPa/m (Kazemi, 1969; Zoback and Zoback, 2002; Ma and Zhao, 2018)In this research, the assumed vertical gradient of in situ stresses is 24 kPa/m andthat the mechanical properties for rock at the seabed are represent by UCS tests. For experimental convenience, triaxial tests are conducted at 12.5 MPa and 24 MPa confining pressure, which are representative of conditions at around550 m depth and 1000 m depth in a wellbore, respectively, as seen in Figure 4.1. Experiments are conducted at 15°C, -5°C and -10°C to compare the properties of rock at positive and sub-zero temperatures and with the aim of using the mechanical results as input for CO_2 injection scenarios. These depths are representative of injection depths in currently active CO_2 storage projects in the North Sea basin such as in the Sleipner field of 700m

(Eiken et al., 2011), and wellbore conditions in prospective North Sea storage sites such as the Endurance field (Gluyas and Bagudu, 2020). Young's modulus (E), Poisson's ratio (ν), bulk modulus (K) and shear modulus (G) are considered, to characterise the rock, its strength, and the development of damage. The critical state slope is also estimated, which will be used for numerical parametric analysis in later chapters.

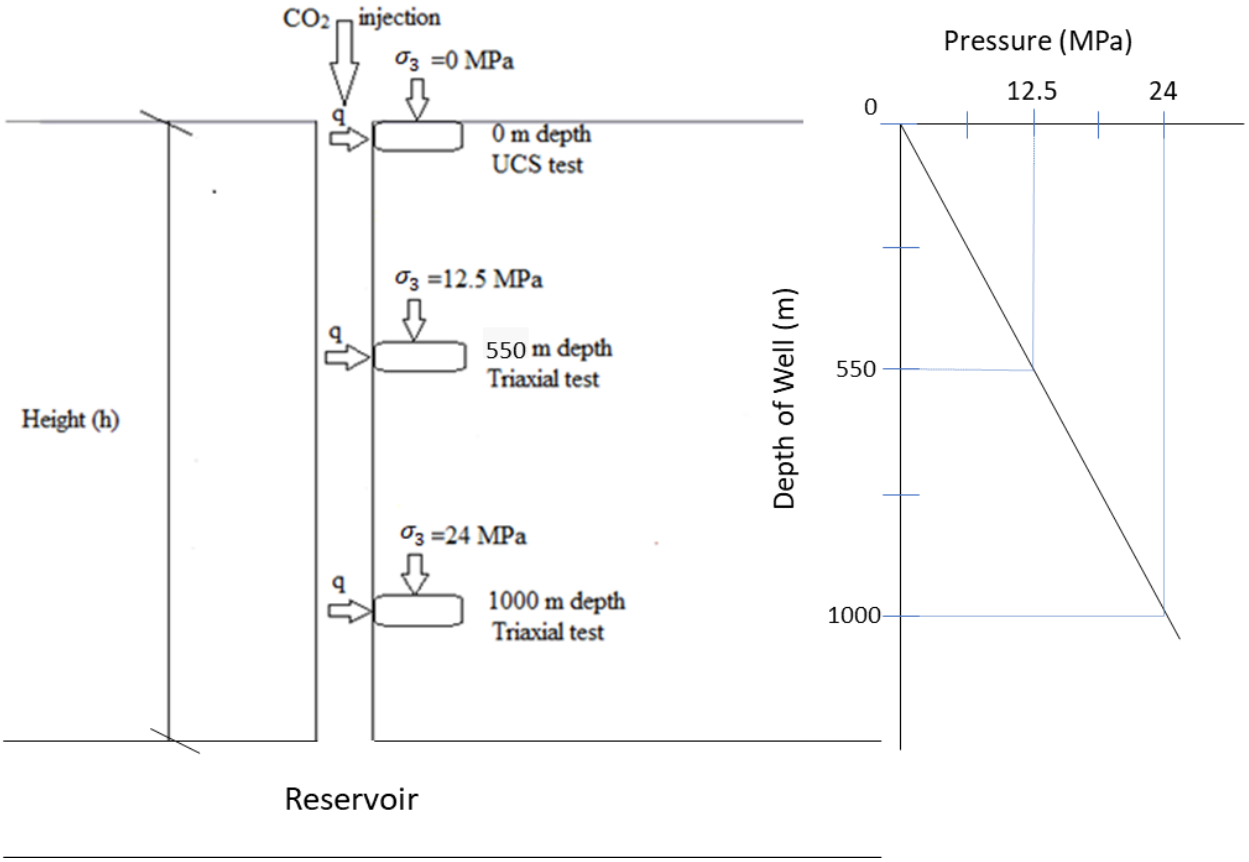

Figure 4. 1 Representative conditions of the test

4.2 Experimental setup and methodology

4.2.1 Macro and microstructural details of the testing material

In the presented experiments, samples of Carboniferous coal-measures sandstone from onshore UK (Stainton Quarry, UK) are used. This sandstone was selected because carboniferous coal-measures sandstones can be reservoir rocks throughout the North Sea basin (Hawkins, 1978; Heinemann et al., 2012; Hangx et al., 2013; Agada et al., 2017). It should be mentioned that this type of rock is different from the Bunter sandstone exist at the Endurance storage development

plan as mentioned by Gluyas and Bagudu (2020). However, it can provide a good analogue material for understanding how low temperatures may influence the mechanical behaviour of the near wellbore region in practical scenarios.

The rock sample can be described according to British Standards and BS5930 (2015), as a strong medium bedded, buff coloured with fine brown speckle, medium grained, clastic SANDSTONE. The rock was extracted from a 10.5 m face below 3.6 m of overburden. The location of the quarry from where the rock was collected is 2 miles east of Barnard Castle, UK. The calculated porosity of the rock isin agreement to the technical data sheet of the quarry and is approximately 17%. The dry density of the rock was calculated to be 2.3 g/cm^3.

To understand the origins of the mechanical behaviours observed during the deformation experiments, a microstructural characterisation of the sandstone was undertaken. This allowed assessment of the influence of the primary rock fabric on the deformation behaviour. The sample largely comprises quartz, present as well-sorted sub-angular to subrounded grains between 100 and 150 microns in size (Figure 4.2). Based on the research of Schultz et al. (2010), for a porosity of 17% and a grain size of 0.15 mm, the pre-consolidation pressure is estimated to be 240 MPa and the estimated maximum burial depth is around 10 km. Occasional lithic fragments (Figure 4.2a) and ribbons of muscovite mica are present throughout the sample (Figure 4.2b). Iron oxide coatings are ubiquitous throughout, forming dusty rims to quartz grains, and is locally pore filling (Figure 4.2a). Syntaxial quartz cements are also present, generally confined to pore throats, and only developed where ferric coatings are absent. This implies coexistence of clay minerals with the ferric oxides. These are likely illite-smectite which are well-known to act as inhibitors to authigenic quartz growth (Fisher et al., 1999; Worden and Burley, 2003; Busch et al., 2017).

Thin sections reveal a tightly packed microstructure. Under purely mechanical compaction (estimated depth 1000 m and pressures around 20 MPa), well sorted sandstones can be expected to reach porosities of 26% (Worden and Burley, 2003). The low recorded porosity of 17% suggests additional chemically enhanced compaction of the sample or porosity reduction by diagenetic pore filling material. The first one is evidenced by quartz grain boundaries, which display irregular grain contact geometries (Figure 4.2b). This is indicative of pressure solution at grain contacts during burial. The irregular contacts promote geometric interlocking of grains and increased contact area between grains. There is also local evidence of grain suturing (Figure 4.2a), evidenced

by an abrupt change in interference colour within a single grain. This reflects the differing orientations of the two parent grains that have become fused because of intense chemically enhanced compaction. It is likely that the enhanced intergrain contacts and local because of pressure solution, would contribute to the overall frictional strength characteristics of the material and may act as a major control on material strength in comparison to the comparatively poorly developed syntaxial quartz cements and very localized grain suturing. The clay-mineral + ferric oxide coats and pore filling cements would not be expected to contribute significantly to the overall material strength (Fisher et al., 1999).

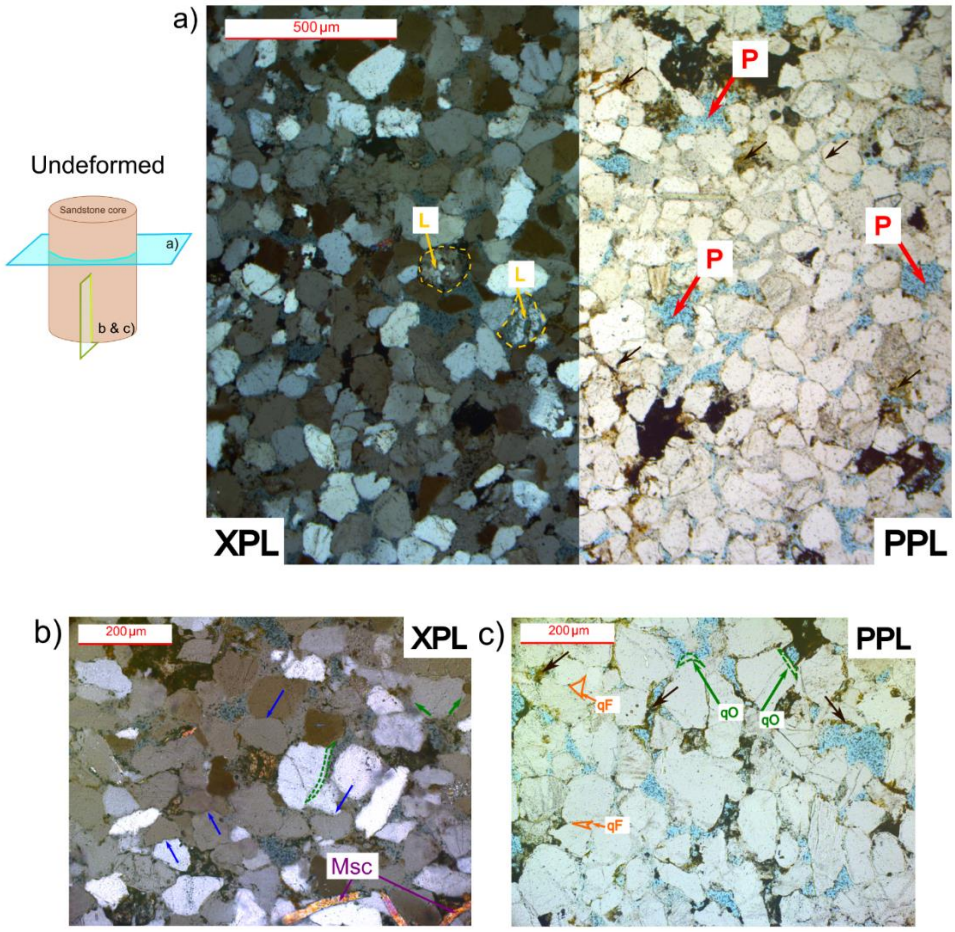

Figure 4. 2 Optical microscopy images of the undeformed sample taken under plane and crossed polarised light conditions. a) Low magnification (x100) showing representative microstructure in plane (PPL) and crossed-polarised (XPL) light. b) High magnification (x400) Crossed-polarised. L = lithic fragments, P = pore space, qO = syntaxial quartz overgrowths (green), qF = quartz fills (orange). Msc = muscovite mica. FeO – iron oxide grain coatings. These likely also contain clay-minerals.

In total, twenty-seven samples were tested, as listed in Table 4.1. The samples were cylindrical with a height to diameter ratio of 2:1, as recommended by ISRM (Ulusay, 2014). The samples were cored from two rock blocks extracted from the same depth and the dimensions and weight of them can be seen in Table 4.1. Strain gauges were attached and "Araldite rapid epoxy" was used to waterproof them. Each sample was then saturated in a water bath under vacuum for approximately 24 h in a NaCl solution with a molar concentration of 0.6 $mol \cdot L^{-1}$ to represent North Sea conditions(Greenwood et al., 2010).

To achieve the target temperatures, the saturated samples were placed in a freezer for 35 minutes to achieve -5°C, and 44 minutes to achieve -10°C. The freezer's temperature was -20°C and the calculated time to achieve these temperatures was estimated by using a thermometer attached, after drilling a hole, at the centre of the saturated samples. After freezing, the whole 38 mm diameter Hoek cell, with the saturated sample inside, was placed inside an Instron environmental chamber and set to test temperature for 30 minutes, before the start of the test. The temperature was maintained at a constant value during testing. This is not fully representative of the in-situ injection conditions, as initially temperature will fluctuate until equilibrium is achieved. However, results can give a good estimation of the change in mechanical properties due to thermal and mechanical loading. For each triaxial test, the confining pressure was increased at a constant rate of 1 MPa/min up to the maximum before axial stress was applied. Both uniaxial and triaxial compression tests were performed under axial strain-control with an axial displacement rate of 0.1 mm/min. A characteristic sample, the Hoek cell and the environmental chamber can be seen in Figure 4.3.

Table 4. 1 Characteristics of the test samples

Temperature	Samples	Diameter (mm)	Length (mm)	Dry Mass (g)	Wet Mass (g)	Water Content %
UCS Tests Dry sandstones						
15 ℃	A’	59.3	129.31			
	B’	59.3	129.32			
	C’	59.3	130.22			
UCS Tests Saturated sandstones						
15 ℃	A	37.62	83.37	199.44	215.20	7.32
	B	37.61	84.65	202.46	217.13	6.76
	C	37.61	82.85	198.21	214.30	7.51
	D	37.89	81.39	206.95	226.90	8.79
-5 ℃	E	37.83	77.88	197.88	210.33	5.92
	F	37.81	81.16	202.56	217.25	6.76
	G	37.82	84.18	212.56	225.72	5.83
-10 ℃	H	37.80	80.14	199.08	213.73	6.85
	I	38.12	84.24	210.14	224.87	6.55
Triaxial Tests 12.5 MPa Saturated Sandstones						
15 ℃	1	37.65	82.45	208.11	221.12	5.88
	2	37.60	83.14	199.18	214.22	7.02
	3	37.40	80.76	191.13	208.55	8.35
	4	37.79	79.31	201.60	214.50	6.01
-5 ℃	5	37.81	83.06	209.27	223.91	6.54
	6	37.91	81.74	203.68	218.80	6.91
	7	37.92	80.91	204.30	218.31	6.42
-10 ℃	8	37.81	79.29	199.98	212.94	6.09
	9	37.79	79.49	200.57	215.17	6.79
Triaxial Tests 24 MPa Saturated Sandstones						
15 ℃	I	37.42	84.40	200.80	213.22	5.82
	II	37.58	82.86	196.65	213.71	7.98
	III	37.80	83.25	208.4	221.32	5.84
	IV	37.79	83.30	208.91	221.10	5.51
-5 ℃	V	37.82	84.87	213.10	227.50	6.33
	VI	37.78	83.24	209.21	223.14	6.24
	VII	37.88	80.35	202.01	216.57	6.72
-10 ℃	VIII	38.01	83.76	212.57	226.45	6.13
	IX	37.94	82.25	207.65	222.02	6.47

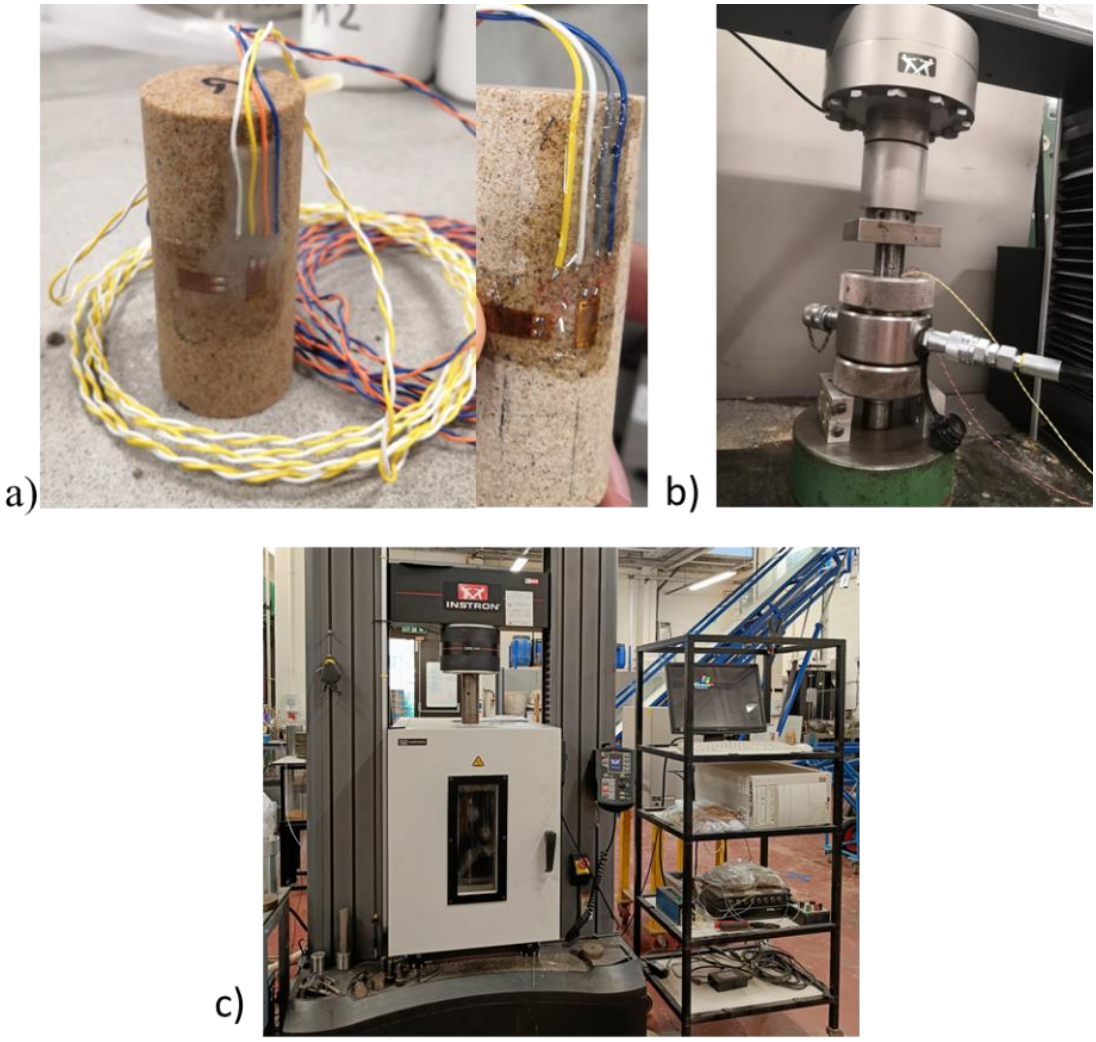

Figure 4. 3 a) Example sample with strain gauges attached, b) Hoek cell equipment, c) Environmental chamber with Hoek cell inside

4.2.2 Methods used for the analysis of the experimental results

According to Małkowski et al. (2018), during uniaxial tests five different phases can be identified. The first phase (I) is compaction, where pre-existing fractures, cracks, joints and any grain pores close during the application of the axial loading. The second phase (II) is the elastic deformation part where the stress-strain curve is linear followed by the third phase (III) where crack propagation starts. The fourth part (IV) is where the shear surface forms and the volume of the rock increases rapidly. During this phase the stress-strain curves are non-linear and the phase ends when the rock reaches its peak strength. The fifth (V) and final stage is when slip failure occurs. All the phases can be seen in Figure 4.4.

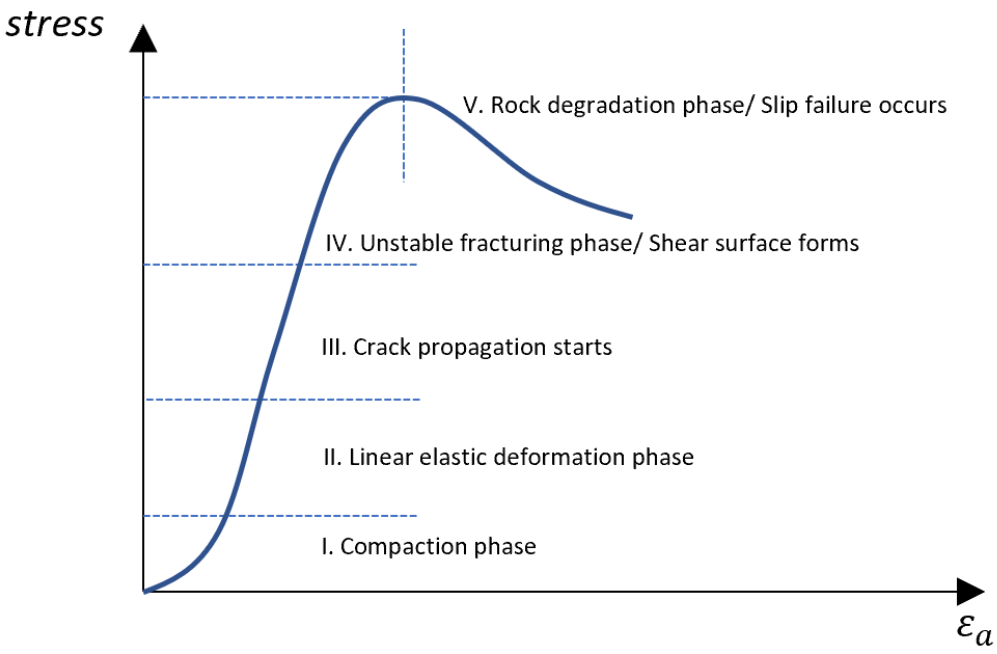

Figure 4. 4 The five different phases of a typical stress-strain graph for rock during UCS test

According to the ISRM the rock's Young's modulus (E) can be determined using three standard methods based on the stress-strain curve stages, which can be seen in Figure 4.5 (Małkowski et al., 2018). The method are as follows:

- Tangent Young's modulus (E_{tan}) at fixed percentage of ultimate stress. This is defined as the slope of the stress-strain curve at a fixed percentage of the ultimate strength.
- The average Young's modulus (E_{ave}) using the straight-line part of the stress-strain curve
- The secant Young's modulus (E_{sec}). It is usually defined as the slope of the line from the origin to a certain percentage of the peak strength of the rock.

Poisson's ratio is defined according to the ISRM as "the ratio of the shortening in the transverse direction to the elongation in the direction of applied force in a body under tension below the proportional limit" (Dong et al., 2021). Poisson's ratio in most projects is determined as a fixed constant that can take values smaller than 0.5, which is the representative of a fully elastic behaviour. Poisson's ratio, ν, can be expressed as $\frac{Lateral\ strain}{Longidutinal\ strain}$ or where a tangent modulus E_{tan} is used by comparison of the slopes of the curves:

$$\nu = \frac{Young's\ modulus\ (E)}{slope\ of\ lateral\ stress - strain\ curve} \tag{4.1}$$

In this study, tangent and secant Young's modulus were used for the determination of the tangent and secant Poisson's ratio, respectively, as seen in Figure 4.5. For the UCS tests, the tangent Poisson's ratio is calculated at the centre point of the stress interval with a span of around $\pm 20\%$, to remain on the linear part of the stress-strain curve. This range in the selected span of the stress interval can differ but its effect is negligible on the Young's modulus and consequently on Poisson's ratio (Dong et al., 2021). The secant Poisson's ratio is estimated from the slope of the axial-volumetric strain curve (see Figure 4.5) corresponding to the span from the beginning to 50% of the uniaxial compressive strength.

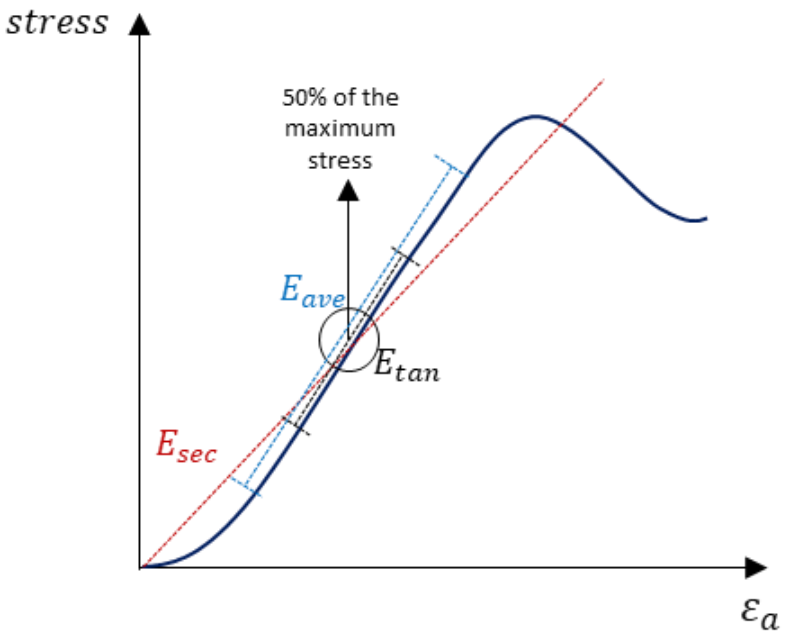

Figure 4. 5 Tangent, average and secant representative spans based on Małkowski et al. (2018)

The bulk and shear moduli can be calculated using the following formulae:

$$K = \frac{E}{3(1-2\nu)} \tag{4.2}$$

$$G = \frac{E}{2(1+\nu)} \tag{4.3}$$

Apart from the ISRM method used for UCS tests, many geomechanical models for sandstones are built from the concepts of critical state soil mechanics (Gerogiannopoulos and Brown, 1978; Cuss et al., 2003; Singh et al., 2005; Shen et al., 2018). Wood (1990) expanded the critical state soil

mechanics theory to describe brittle rock or work-softening materials. The material moduli (E, ν, K and G) can be calculated from the slope of the different plots presented in Figure 4.6. Wood's (1990) method was used as the ISRM approach is only applicable to UCS tests.

According to Wood (1991), Poisson's ratio can be expressed as the ratio between the volumetric strain increment $d\varepsilon_p$ and the triaxial shear strain increment $d\varepsilon_q$. The deviatoric stress q, the volumetric strain increment and the shear strain increment can be presented as follows:

$$q = \sigma_1 - \sigma_3 \tag{4.4}$$

$$d\boldsymbol{\varepsilon_p} = d\boldsymbol{\varepsilon_a} + 2d\boldsymbol{\varepsilon_c} \tag{4.5}$$

$$d\boldsymbol{\varepsilon_q} = 2(d\boldsymbol{\varepsilon_a} - d\boldsymbol{\varepsilon_c})/3 \tag{4.6}$$

where σ_1 and σ_3 are the axial and radial stress or confining stress, $d\boldsymbol{\varepsilon_a}$ and $d\boldsymbol{\varepsilon_c}$ are the axial and circumferential strain increments.

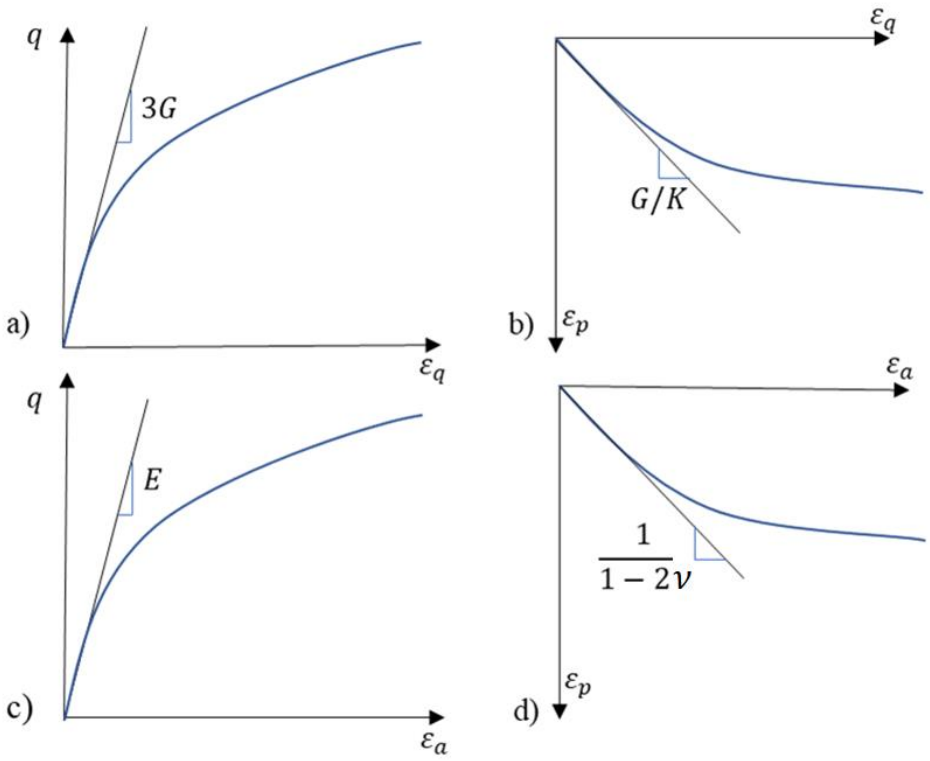

Figure 4. 6 Drained triaxial test a) shear modulus slope, b) bulk modulus calculation, c)Young's modulus slope d) Poisson's ratio calculation (Wood, 1991)

4.3 Experimental Results

4.3.1 UCS Results

Results from the UCS tests for dry oven dried samples (Figure 4.7) and fully saturated samples (Figures 4.8 to 4.10) are presented in this section. From the results in dry conditions the rock can be classified according to BS EN ISO 14689-1 as strong sandstone (Hawkins, 1998). Comparing the dry and saturated UCS tests it can be seen that the peak strength is higher in the dry one by approximately 40%, which is in agreement with the testing results presented by Romana and Vásárhelyi (2007). The saline water decreases the strength of the material in room temperature conditions. For the lower temperatures: -5℃ and -10℃, the maximum deviatoric stress increases due to ice formation inside the pores and fissures of the sandstone. For the saturated samples, it can be determined that when moving from 15℃ to -5℃, where ice forms, the strength of the material increases by more than 35%. However, when moving the temperature from -5℃ to -10℃ the peak strength remains approximately constant (Figures 4.8 to 4.10). This indicates that the ice has already formed at -5℃ and a further temperature drop does not influence the strength of the rock significantly. Additionally, lower temperatures decrease the ductility and deformability of the sandstones. The post-failure phase indicates this ductility decrease effect, as seen by comparing figures (Figures 4.8-4.10). Specifically, in the 15℃ UCS test, the ductility of the material can be seen at the post-failure phase (see Figure 4.8), while at freezing temperatures, the rock mostly fails once it reaches the peak strength (Figure 4.9-4.10). Masri et al. (2014) outlined this trend but for temperatures greater than sub-zero using a range from 20℃ to 250℃.

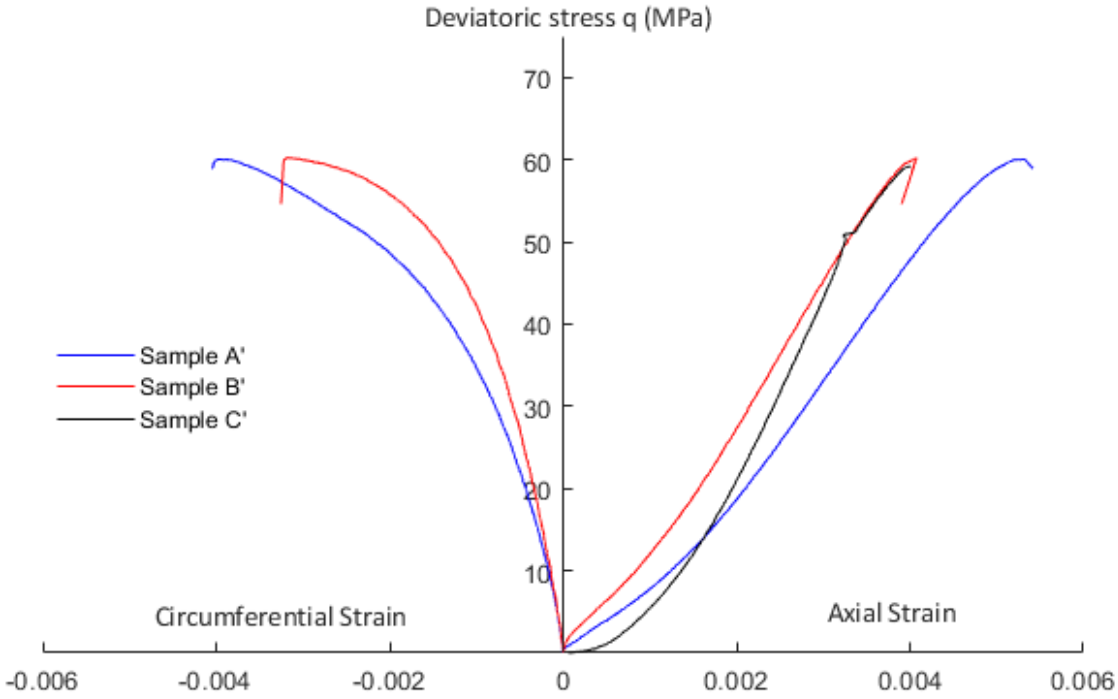

Figure 4. 7 UCS test - Dry sandstone at 15°C

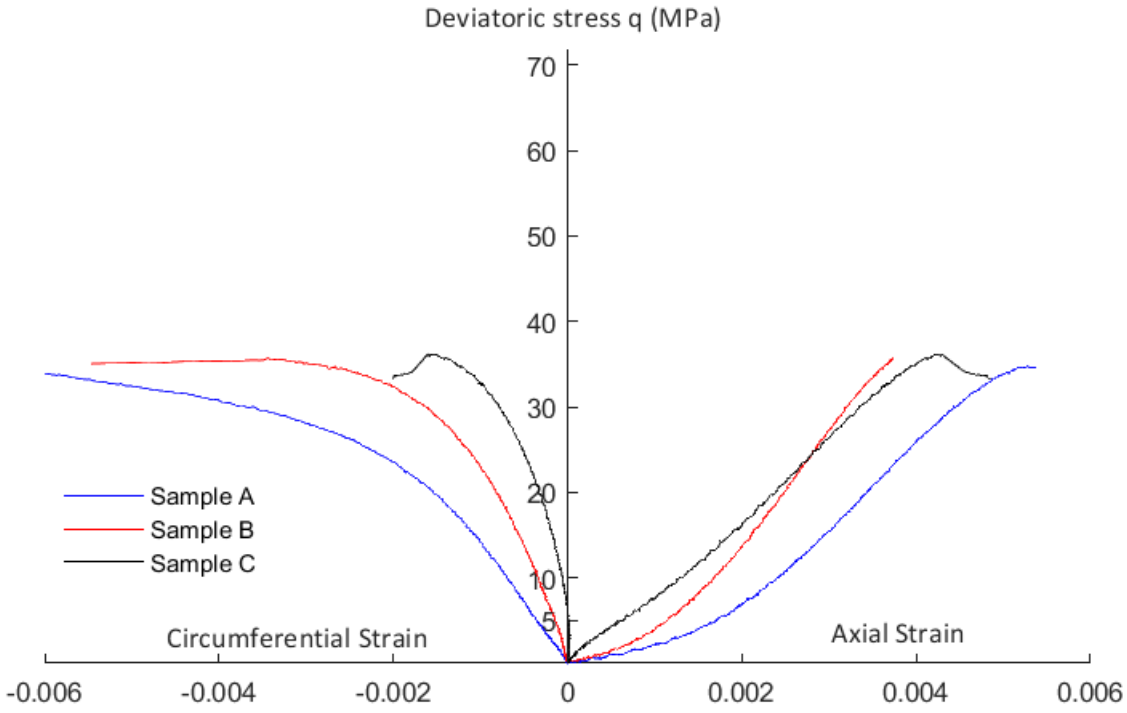

Figure 4. 8 UCS test - Saturated sandstone at 15 °C

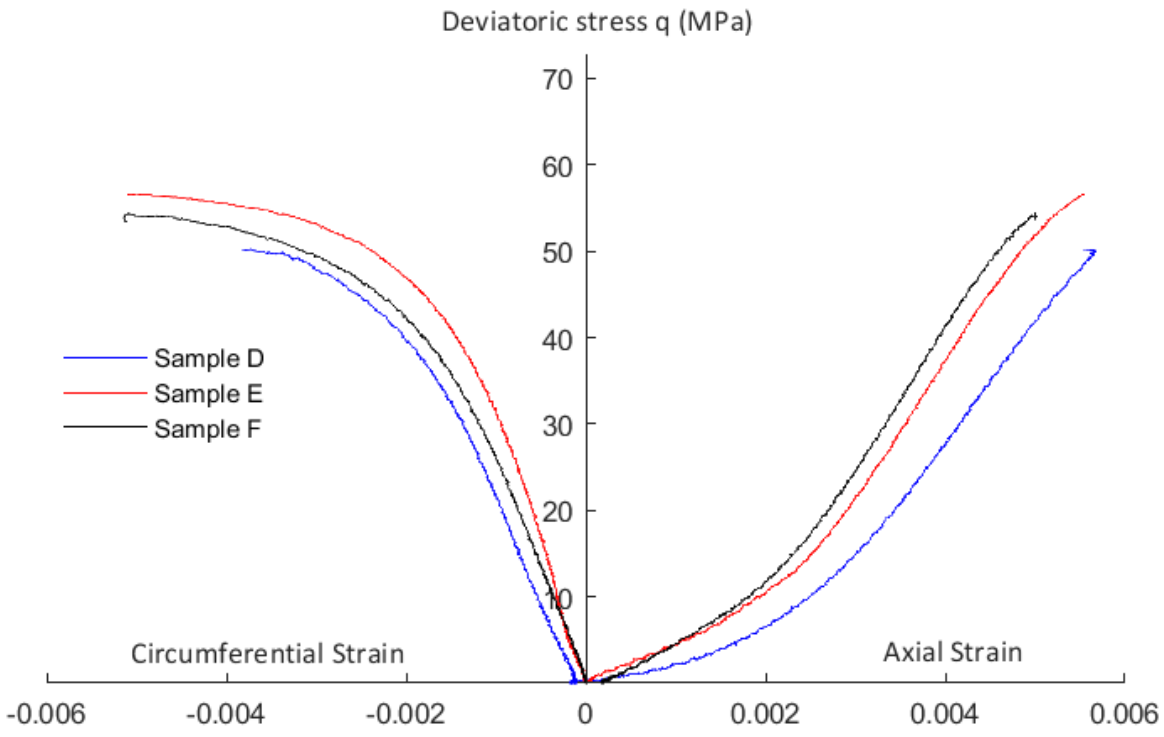

Figure 4. 9 UCS test - Saturated sandstone at -5 °C

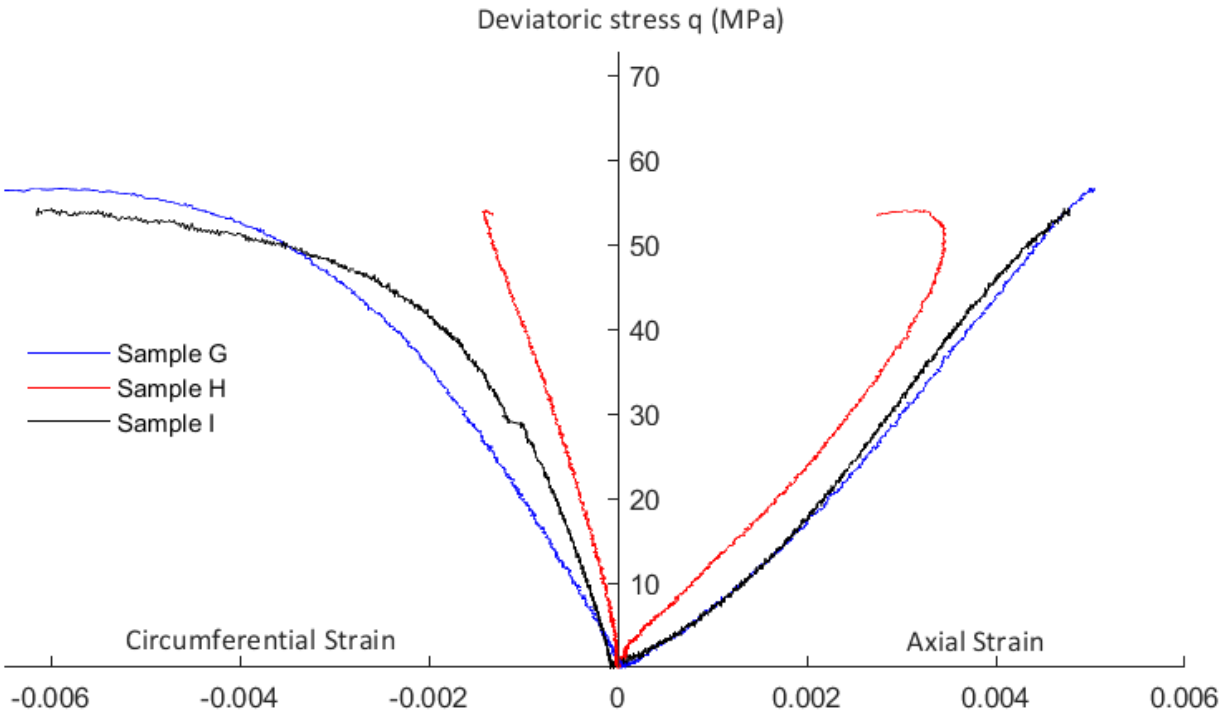

Figure 4. 10 UCS test - Saturated sandstone at -10 °C

In Figure 4.11 the tested samples are presented showing the different types of failure. From Figure 4.11a, it can be seen that the sandstones at 15℃ developed clean fractures in either a double shear or shear along a single plain, following the research of Everall and Sanislav (2018). For lower temperatures, some parts of the sandstone were detached, especially for -10℃, as seen in Figure 4.11c. This can be explained by ice formation and a decrease in Poisson's ratio causing multi-fracturing during the test. The post peak behaviour of sample H (see Figure 4.10) can be explained by the ice formation and indicates a collapse of part of the sample, as seen in Figure 4.11c.

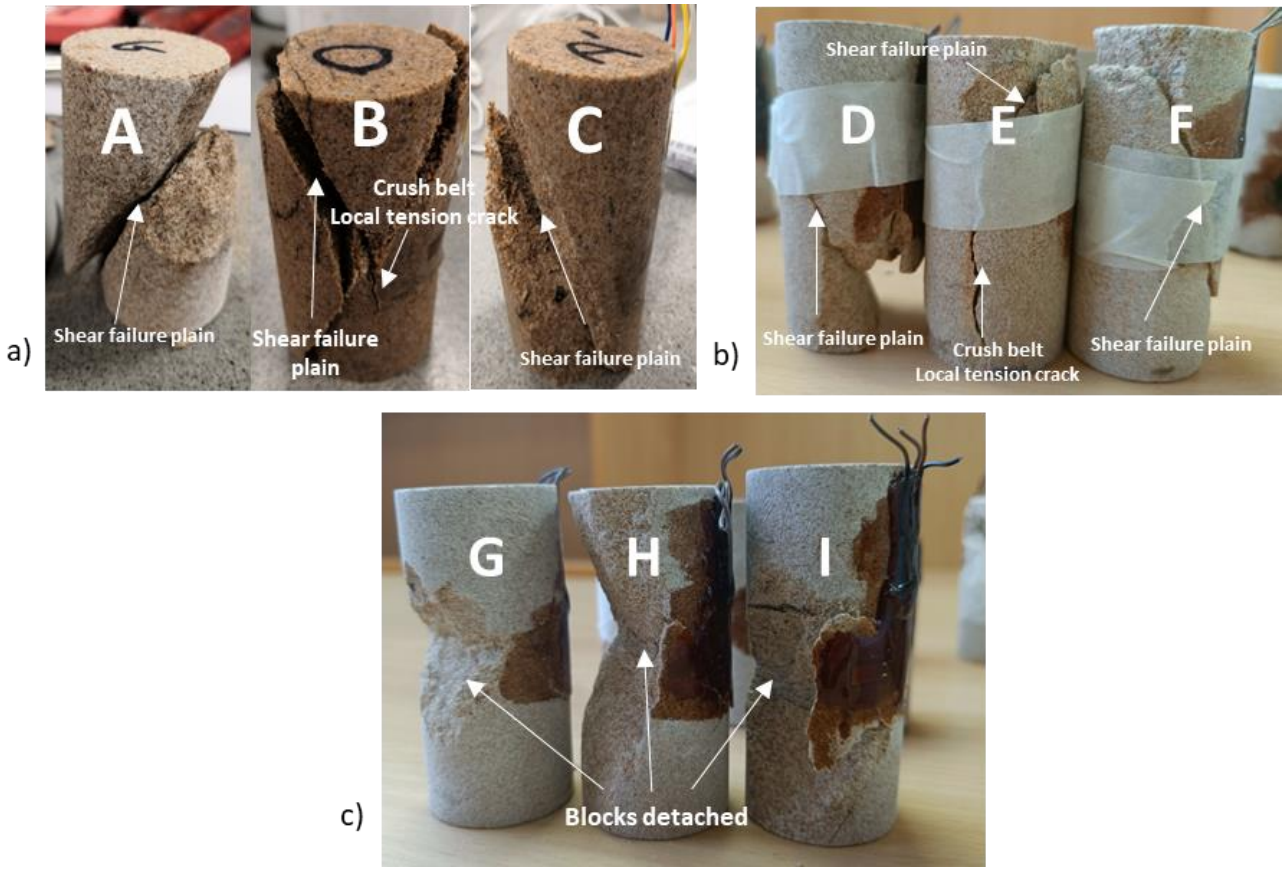

Figure 4. 11 Saturated samples after testing at a)15℃ b)-5℃ c)-10℃

The ISRM method and Wood's method are compared in terms of the Poisson' ratio in Table 4.2. The Young's modulus is also presented. ISRM and Wood's method for both tangent and secant moduli agree with similar results, indicating that the triaxial approach of Wood (1991) can be applied to UCS tests for the estimation of Poisson's ratio. This can permit comparison of the UCS test results to the triaxial outcomes.

Table 4. 2 Tangent and Secant Young's moduli, Tangent and Secant Poisson's ratios and comparison between the ISRM and Wood's methods

Samples	Max UCS Strength MPa	Young modulus (E) GPa		ν ISRM	ν Woods method
Room Temperature Dry Sandstone UCS					
Sample A'	60.0	Tangent	15.0	0.71	0.71
		Secant	10.4	0.27	0.26
Sample B'	60.2	Tangent	17.8	0.52	0.57
		Secant	13.1	0.24	0.24
Sample C'	59.1	Tangent	8.8	0.20	0.19
		Secant	7.7	0.11	0.10
Room Temperature Saturated Sandstone UCS					
Sample A	34.7	Tangent	9.5	0.78	0.78
		Secant	5.2	0.35	0.35
Sample B	35.6	Tangent	13.0	0.64	0.62
		Secant	7.5	0.28	0.27
Sample C	36.1	Tangent	10.1	0.54	0.53
		Secant	7.7	0.17	0.14
Freezing -5 ℃ Saturated Sandstone UCS					
Sample D	51.2	Tangent	16.6	0.68	0.68
		Secant	6.5	0.27	0.27
Sample E	56.5	Tangent	16.4	0.64	0.62
		Secant	7.3	0.22	0.22
Sample F	54.3	Tangent	16.1	0.76	0.75
		Secant	7.8	0.30	0.30
Freezing -10 ℃ Saturated Sandstone UCS					
Sample G	56.6	Tangent	15.2	0.61	0.60
		Secant	10.4	0.32	0.32
Sample H	54.0	Tangent	12.2	0.33	0.33
		Secant	11.4	0.23	0.22
Sample I	54.2	Tangent	14.1	0.61	0.60
		Secant	7.7	0.30	0.29

To further examine temperature effects on the mechanical behaviour of sandstone, the tangent and secant bulk and shear moduli from the UCS tests, calculated based on the respective tangent and secant Young's modulus (ISRM method) and on the slopes of the curves presented in Figure 4.5 (Wood's (1991) method), are presented in Figures 4.12 to 4.15.

Error bars show the maximum and minimum value of each test with the box representing the average value of the modulus. Full results from Sample C, Sample C' and Sample H are not shown since Sample C had a Poisson's ratio significantly lower than the other two tests, for Sample C' the circumferential strain gauge failed, possibly due to crushing of the cable and for Sample H there was a crack at the attachment point to the strain gauge.

Selecting the linear part of the UCS stress-strain curve with approximate $\pm 20\%$ span up and down from the middle point to calculate the tangent modulus, the Poisson's ratio is larger than 0.5 for both the dry and saturated samples, suggesting dilation in the sandstone. According to Dong et al. (2021), despite the fact that the theoretical maximum of Poisson's ratio is 0.5, soft rocks see a quick increase in Poisson's ratio during loading beyond this value. This is due to an increase in volume as grains realign. Due to dilation of the material, the average tangent bulk modulus showed a negative value, as seen in Figure 4.12. Its absolute value for saturated sandstone increased significantly from 11 GPa to nearly 21 GPa moving from 15℃ to -10℃. Dry sandstone, due to higher peak strength, also has a higher absolute value of tangent bulk modulus than the saturated sandstone; nearly 30%. For the secant bulk modulus of the saturated samples, an increase is seen with decreasing temperature, while the value at 15℃ is seen to be lower in the saturated sample compared to the dry sample. Both tangent and secant moduli have the same behaviour, moving from dry to the saturated conditions. However, considering tangent values of the UCS, the shear modulus achieved its peak at -5℃ in contrast to the secant shear modulus, which achieved its maximum at -10℃ and increased gradually for saturated sandstone when the temperature dropped. This indicates that the selected slopes of the curves influence the outcome concerning the properties of the material.

Comparison between the results of Wood's (1990) and ISRM method are presented for the UCS test in Figures 4.12 to 4.15 and Table 4.2. In this way, the robustness of Wood's (1990) method in describing the UCS tests can be assessed. Triaxial test results, where only Wood's (1990) method is applicable due to confinement, can then be compared to UCS outcomes. The assumption made

is that during the UCS test the deviatoric stress is equal to axial stress and the confining pressure is set equal to zero.

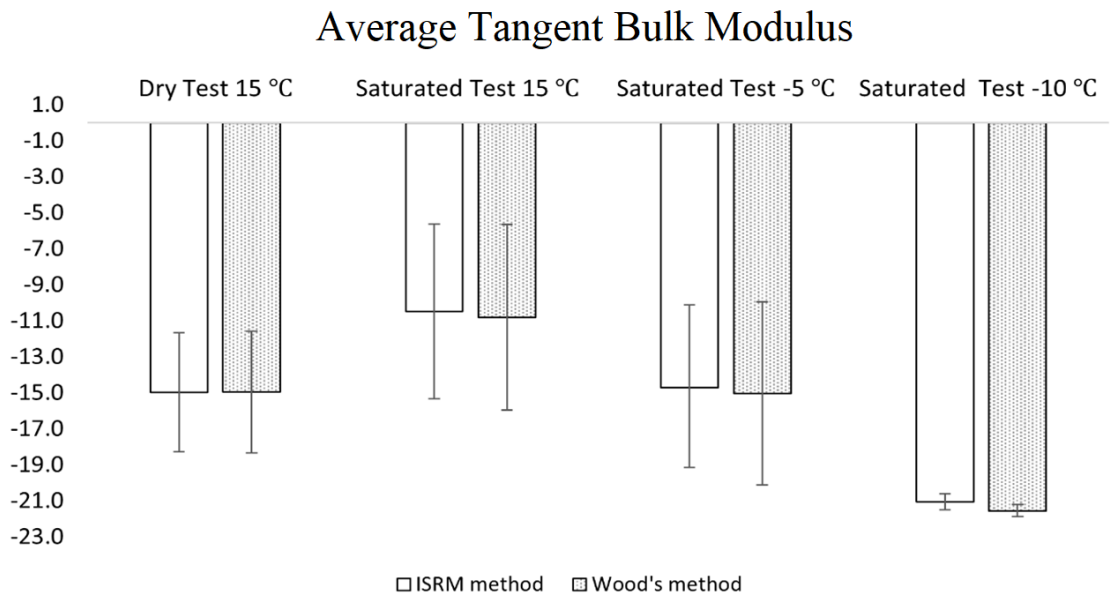

Figure 4. 12 Average tangent bulk modulus, K (GPa), for different temperatures from ISRM and Wood's methods. Error bars indicate the maximum and minimum calculated value.

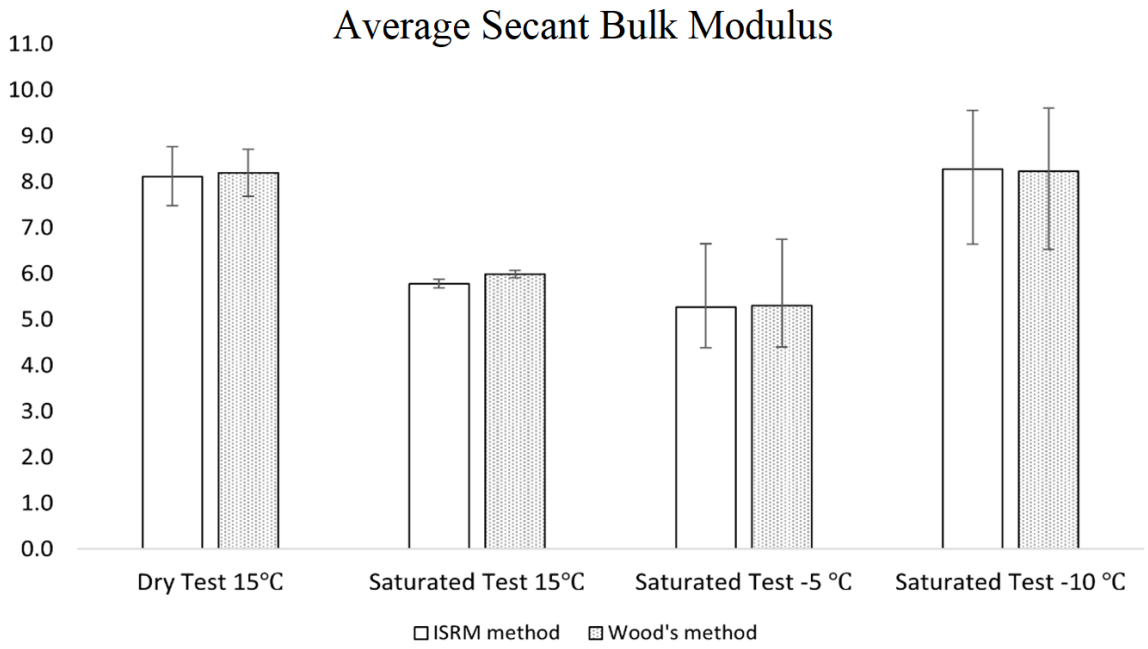

Figure 4. 13 Average secant bulk modulus, K (GPa), for different temperatures from ISRM and Wood's methods. Error bars indicate the maximum and minimum calculated value.

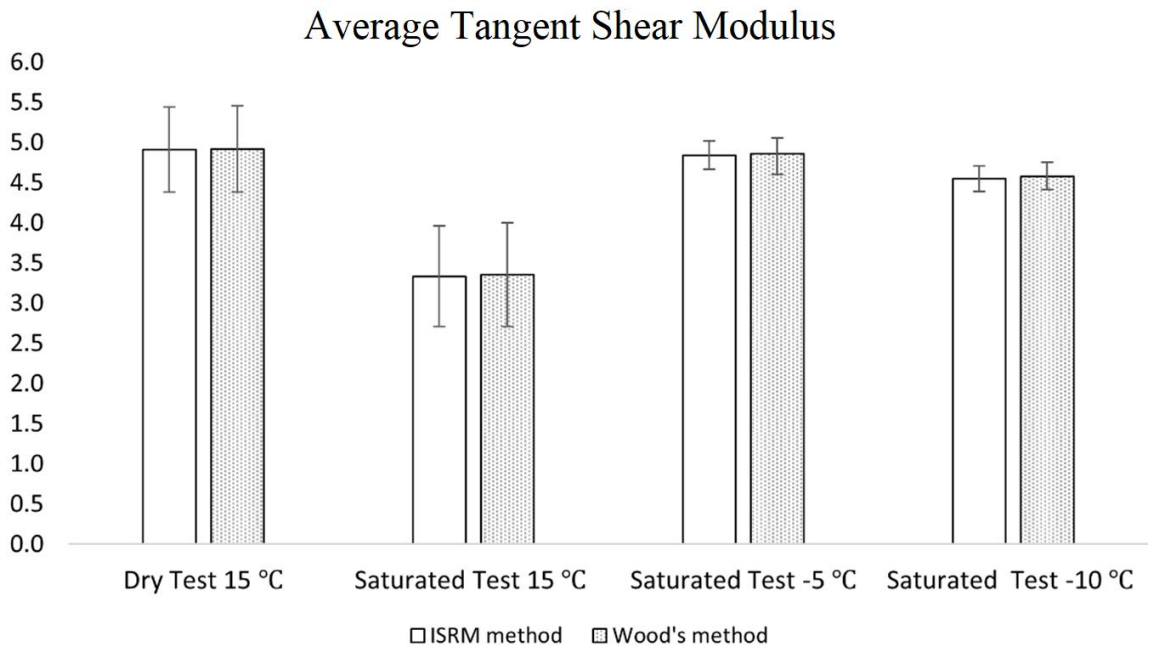

Figure 4. 14 Average tangent shear modulus, G (GPa), for different temperatures from ISRM and Wood's methods. Error bars indicate the maximum and minimum calculated value.

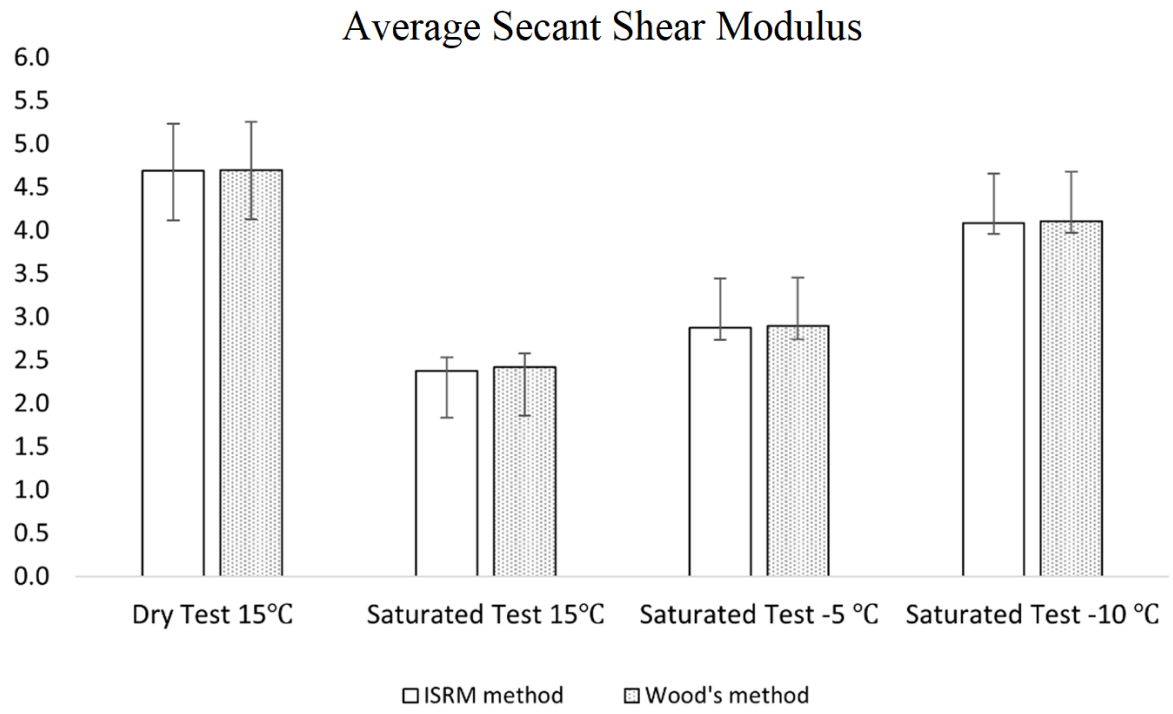

Figure 4. 15 Average secant shear modulus, G (GPa), for different temperatures from ISRM and Wood's methods. Error bars indicate the maximum and minimum calculated value.

4.3.2 Triaxial Results

Results from the triaxial tests for the saturated samples are presented in this section in Figures 4.16 to 4.21. The different calculated moduli using the Wood's (1991) method are presented for 12.5 MPa and 24 MPa confinement in Table 4.3 and Table 4.4, respectively. Shear failure was the usual type of failure mechanism. In contrast to the UCS tests, all the results were in good agreement to each other as an increase in volume during grain crushing was not permitted because of the confinement.

It can be seen from Figures 4.16 to 4.21 that moving in from 15℃ to sub-zero temperatures (-5℃ and -10℃), the strength of the sandstone samples increases with higher confining pressures, in agreement with Zhang et al. (2019). According to the 12.5 MPa triaxial results, an increase in the peak deviatoric stress with temperature drop from 15℃ to -5℃ of approximately 20%, is seen. Analysing the 24 MPa triaxial results, the deviatoric stress increased almost 10% for the same decrease in temperature. For both confining pressures, the maximum deviatoric stress is hardly influenced by further temperature drop from -5℃ to -10℃, as seen in Table 4.3 and Table 4.4.

Comparison was also achieved between 12.5 MPa and 24 MPa tests, concerning the Young's modulus and Poisson's ratio. Young's modulus was higher and the Poisson's ratio lower for the 24 MPa compared to 12.5 MPa triaxial test. For the 12.5 MPa test, moving from 15℃ to -5℃ an average increase in the Young's modulus is identified, while the Poisson's ratio reduced. A further temperature decrease, reaching -10℃, indicated the opposite trend with the Young's modulus reducing and Poisson's ratio increasing. With an increase in the confinement and specifically reaching the 24 MPa confinement, temperature has minimal influence on the mechanical parameters.

Shear and bulk modulus, for the three temperatures, follow the same trend for both confining pressures, where the shear modulus increases with temperature decrease, while the bulk modulus decreases. It is worth mentioning that for 12.5 MPa confinement, the reduction in the bulk modulus is much larger than for 24 MPa, indicating that lower confinement has higher compressibility.

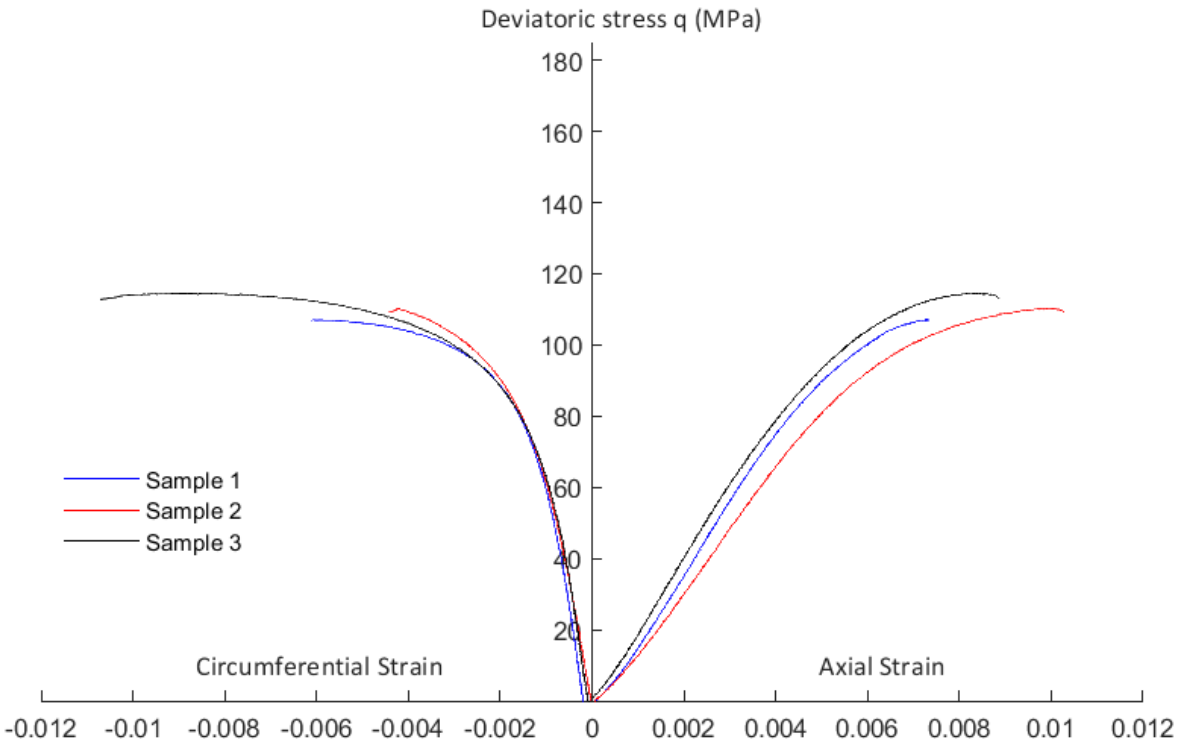

Figure 4. 16 Vertical and circumferential strain versus deviatoric stress for 12.5 MPa confining pressure representing 550m depth in a wellbore. Temperature 15°C.

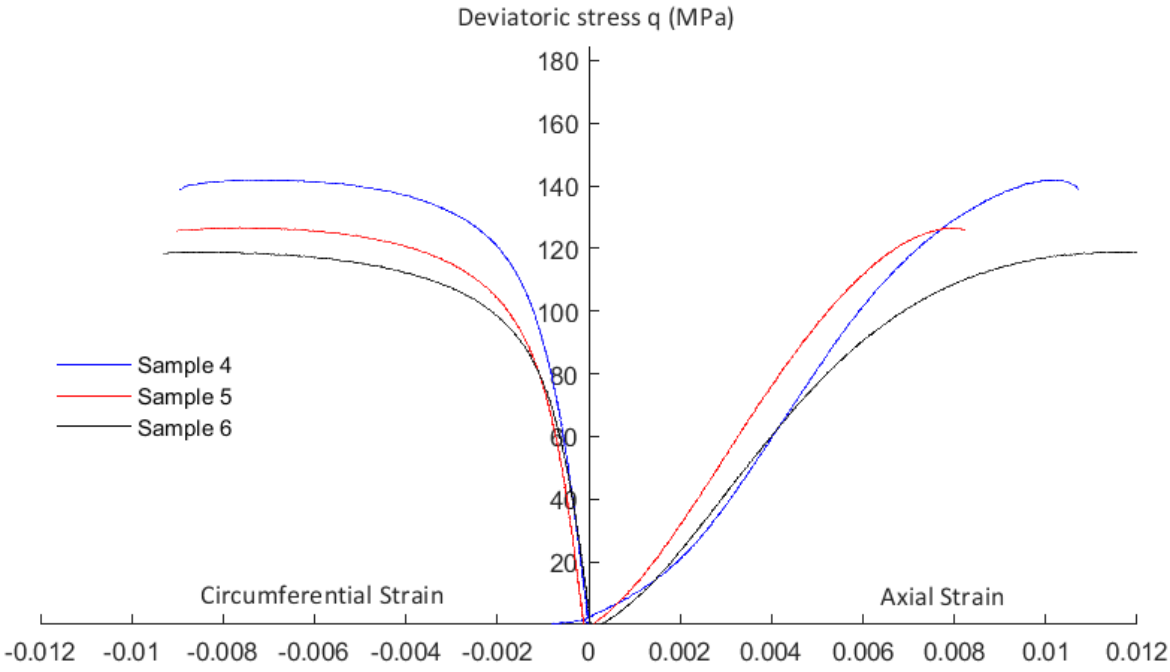

Figure 4. 17 Vertical and circumferential strain versus deviatoric stress for 12.5 MPa confining pressure representing 550m depth in a wellbore. Temperature -5°C.

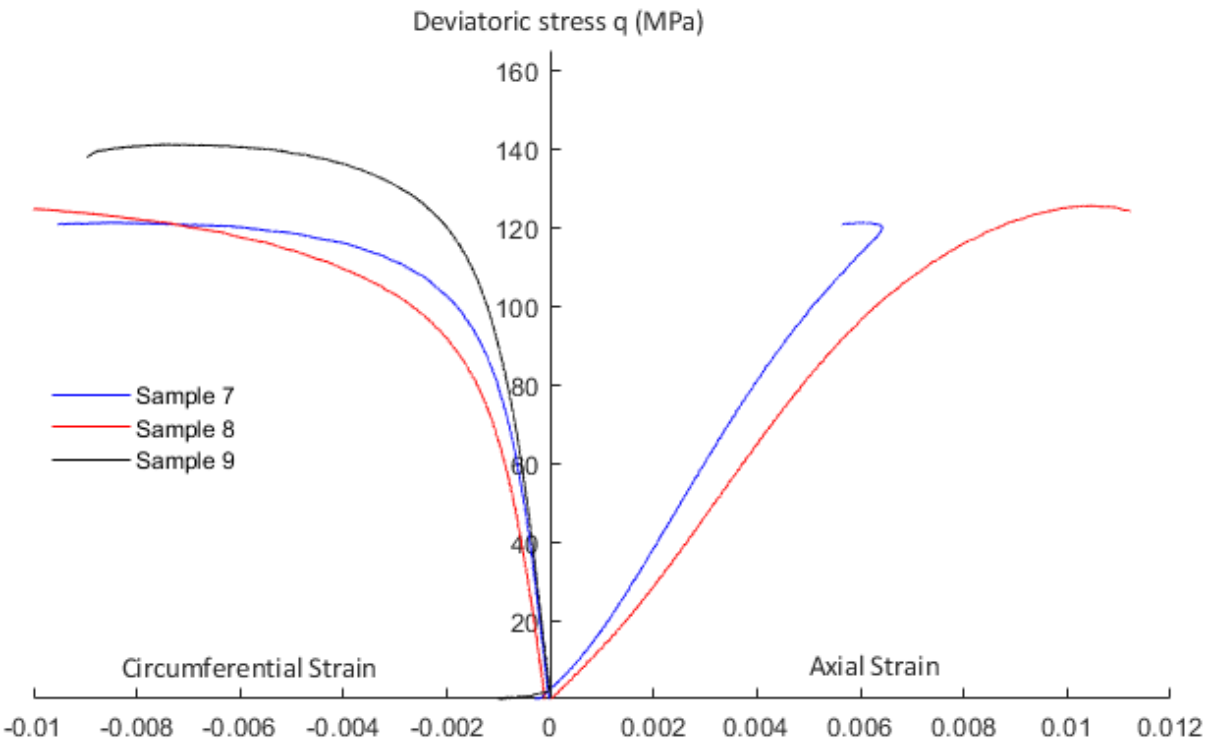

Figure 4. 18 Vertical and circumferential strain versus deviatoric stress for the 12.5 MPa confining pressure representing 550m depth in a wellbore. Temperature -10°C.

Table 4. 3 Calculated mechanical properties for triaxial test with 12.5 MPa confining pressure

Sample ID	Max Deviatoric Strength (MPa)	Young's modulus (GPa)	Poisson's ratio	Shear Modulus (GPa)	Bulk Modulus (GPa)
			15°C Temperature		
Sample 1	107.09	20.67	0.37	7.55	26.35
Sample 2	110.25	17.96	0.36	6.60	21.60
Sample 3	114.51	19.69	0.39	7.10	29.51
			-5°C Temperature		
Sample 4	141.54	21.81	0.25	8.76	14.34
Sample 5	126.72	22.33	0.27	8.74	16.86
Sample 6	118.83	18.04	0.26	7.04	13.48
			-10°C Temperature		
Sample 7	121.18	18.27	0.30	6.99	15.86
Sample 8	125.50	21.73	0.27	8.52	15.49

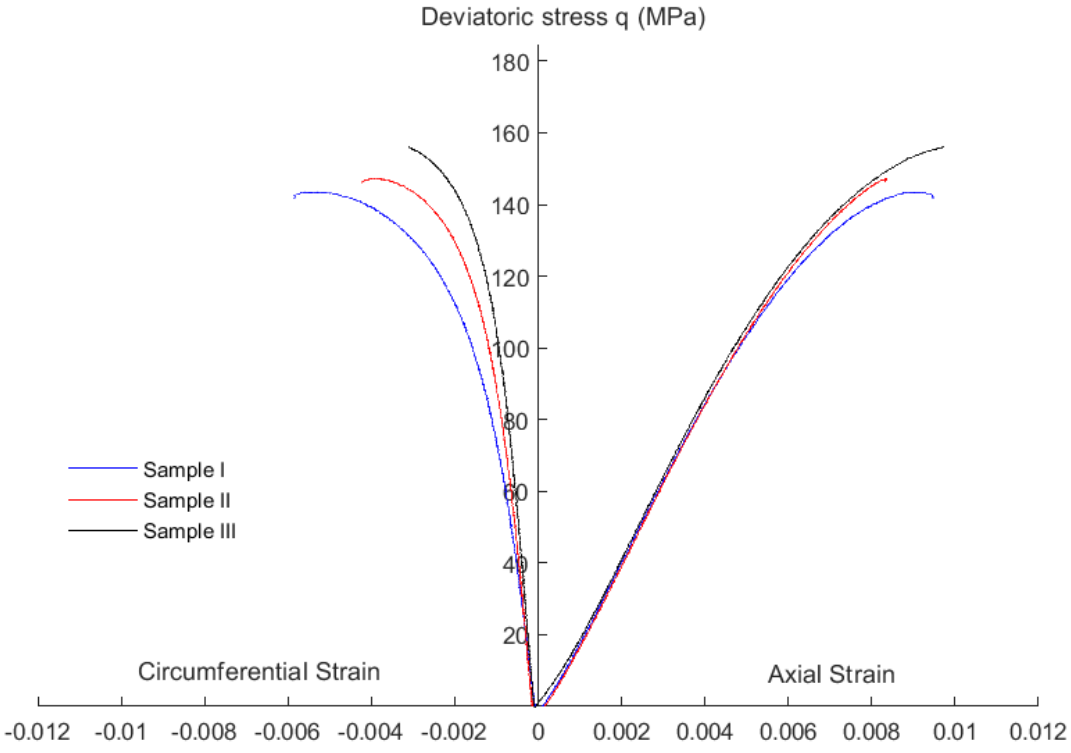

Figure 4. 19 Vertical and circumferential strain versus deviatoric stress for 24 MPa confining pressure representing 1000m depth in a wellbore. Temperature 15°C.

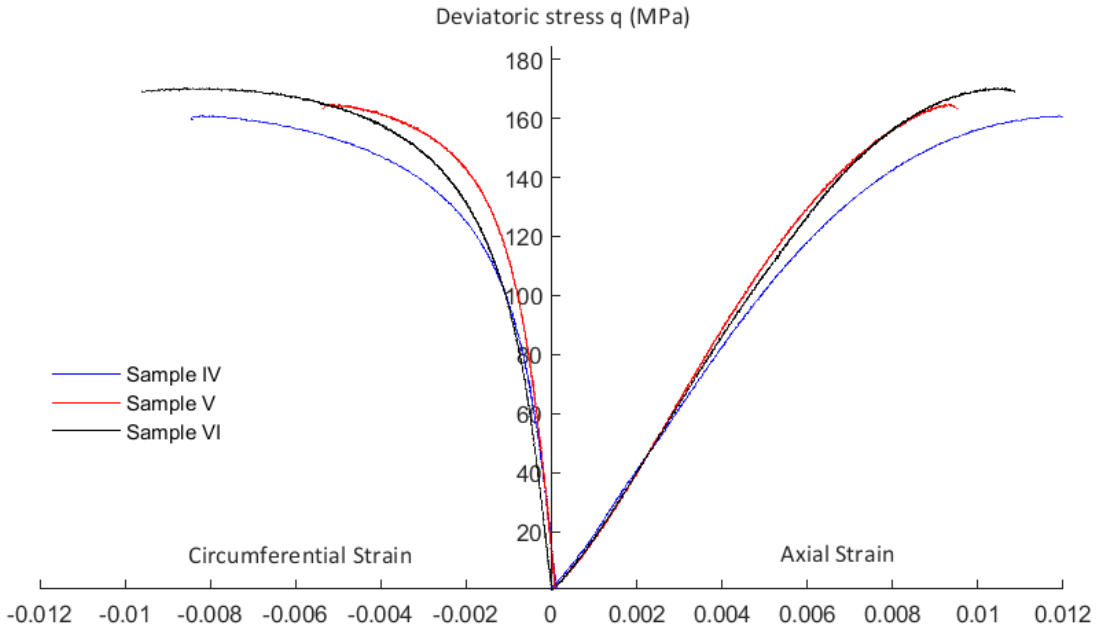

Figure 4. 20 Vertical and lateral strain versus deviatoric stress for 24 MPa confining pressure representing 1000m depth in a wellbore. Temperature -5°C.

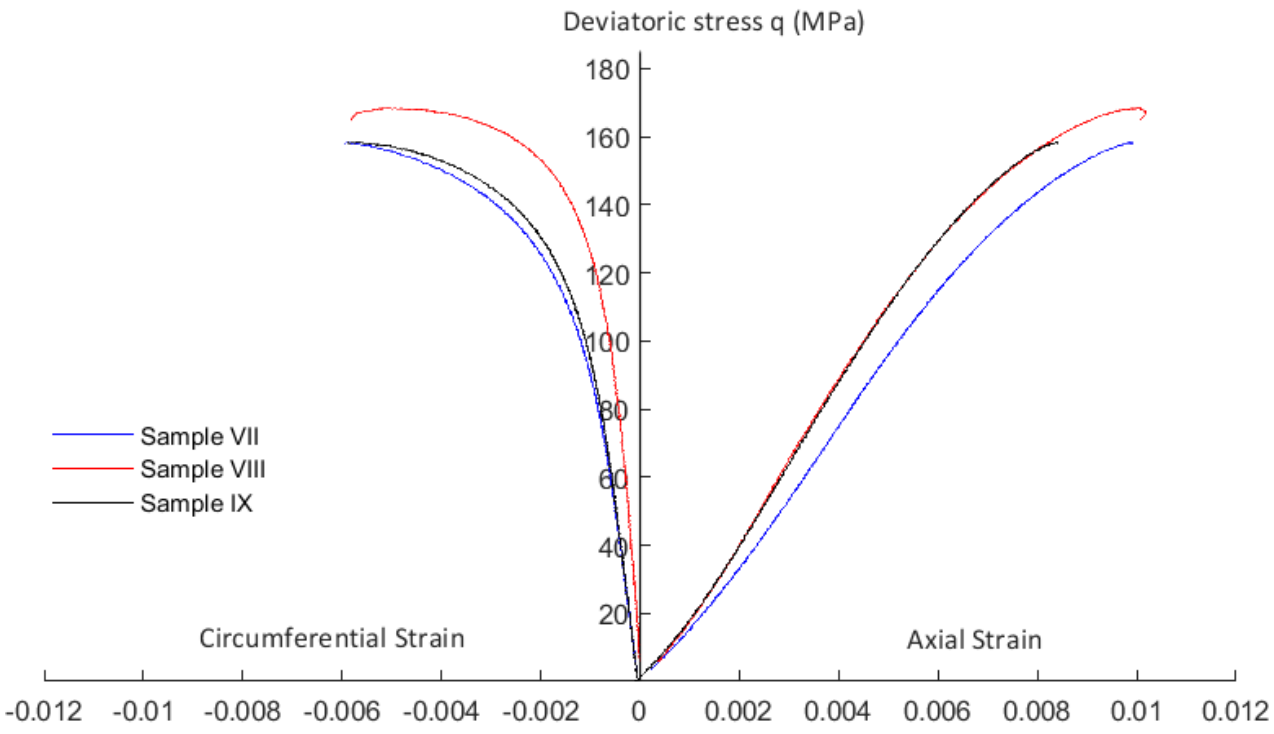

Figure 4. 21 Vertical and circumferential strain versus deviatoric stress for 24 MPa confining pressure representing 1000m depth in a wellbore. Temperature -10℃.

Table 4. 4 Calculated mechanical properties for triaxial test with 24 MPa confining pressure

Sample ID	Max Deviatoric Strength (MPa)	Young's modulus (GPa)	Poisson's ratio	Shear Modulus (GPa)	Bulk Modulus (GPa)
15℃ Temperature					
Sample I	143.48	23.09	0.29	8.97	18.25
Sample II	147.34	22.08	0.26	8.79	15.35
Sample III	156.08	23.02	0.26	9.65	12.70
-5℃ Temperature					
Sample IV	160.89	21.09	0.26	8.36	15.30
Sample V	164.90	24.57	0.22	10.10	14.84
Sample VI	170.29	23.33	0.25	9.32	15.82
-10℃ Temperature					
Sample VII	158.31	21.14	0.23	8.66	14.46
Sample VIII	168.38	23.98	0.19	10.08	13.05
Sample IX	158.37	23.84	0.23	9.69	15.78

It should be noted that, as ice forms, the strength of the rock increases, however the Poisson's ratio decreases, indicating an increase in plasticity and potential damage. In contrast to the UCS, where dilation occurs, the rock does not increase in volume and consequently Poisson's ratio remains under the elastic limit of 0.5. The average shear modulus increases with temperature decrease, while the bulk modulus fluctuates for the -5℃ triaxial condition. This is mainly happening as the calculation varies according to the selected slope and due to differences in the deviatoric stress-vertical strain curves. This dissimilarity may occur due to stretching of the rock caused by the application of confining pressure prior to reaching isotropic conditions.

4.4 Effects of temperature and pressure on Young's modulus and Poisson's ratio

Figures 4.22 and 4.23, show how the tangent Young's modulus and Poisson's ratio vary with temperature for the different tests. Functions fitted to the data points are also presented in the figures. As the data were only limited to three different tests the linear assumption between the points seemed to be reasonable, based on the research of Wang et al. (2019b). For a temperature decrease from 15℃ to -5℃, the tangent Young's modulus calculated at the UCS conditions is 75% higher than the tangent Young's modulus at 12.5 MPa confining conditions, and 96% higher than the tangent Young's modulus at 24 MPa confining conditions. This trend follows the findings of Wang and Zhang (2021) although it is clear that there is a significant change in behaviour between -5℃ and -10℃.

For tangent Poisson's ratio, when moving from 15℃ to -5℃ a slight change is seen for both the UCS and 24 MPa confining test (Figure 4.23). In the 12.5 MPa confining test a decrease of tangent Poisson's ratio is seen. Further temperature reduction indicates a significant reduction, an increase, and a slight decrease in tangent Poisson's ratio for the UCS, 12.5 MPa confinement and 24 MPa confinement cases, respectively. The UCS test seems to be the most sensitive to temperature effects for both Young's modulus and Poisson's ratio.

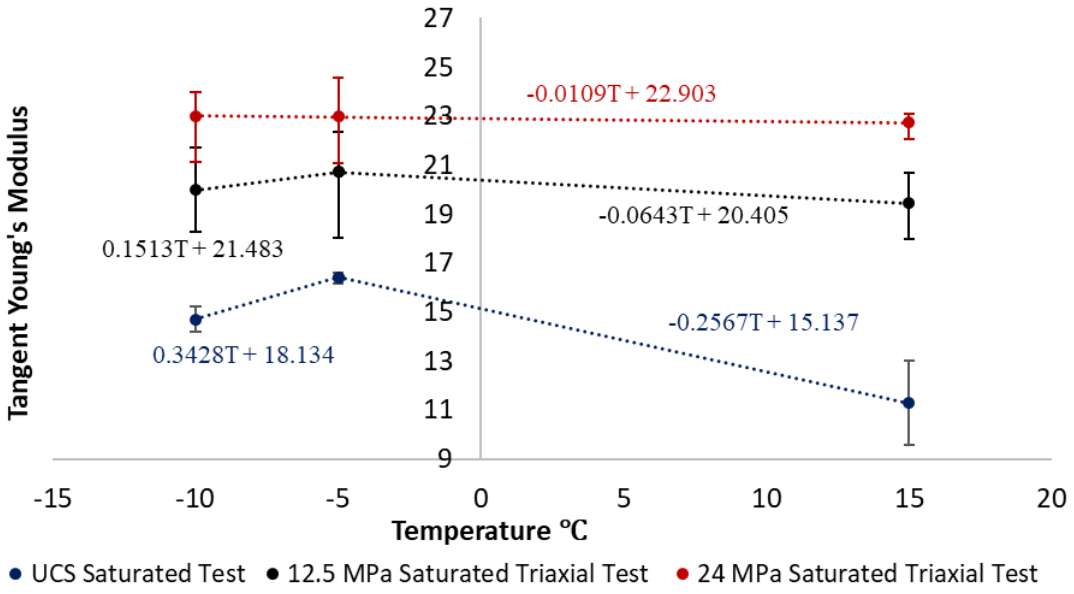

Figure 4. 22 Average values of tangent Young's moduli and error bars at different confining pressures and temperatures.

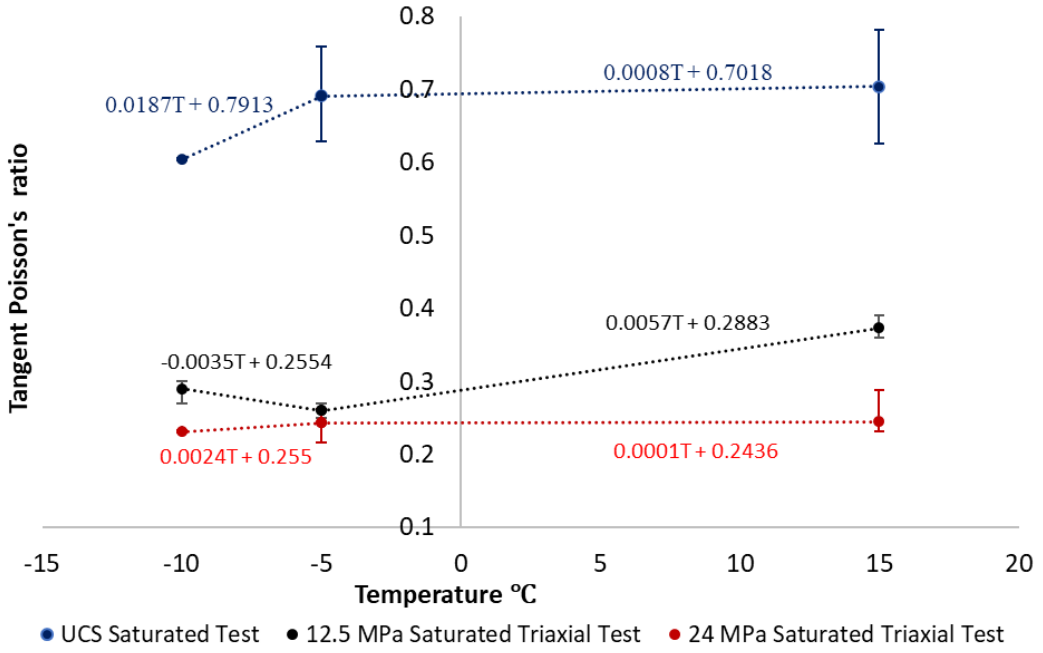

Figure 4. 23 Average values of tangent Poisson's ratios and error bars at different confining pressures and temperatures.

As the tangent calculated Poisson's ratio for the UCS is bigger than 0.5, this value cannot be used as an input parameter for numerical simulations as the bulk modulus will take negative values. For this reason, plots of the distribution of the secant values of the Young's modulus and Poisson's

ratio are presented based on the experiments, in Figures 4.24 and 4.25. It should be mentioned that there is a different trend between the tangent and secant Poisson's ratio for the UCS tests when cooling the sandstone more than -5°C.

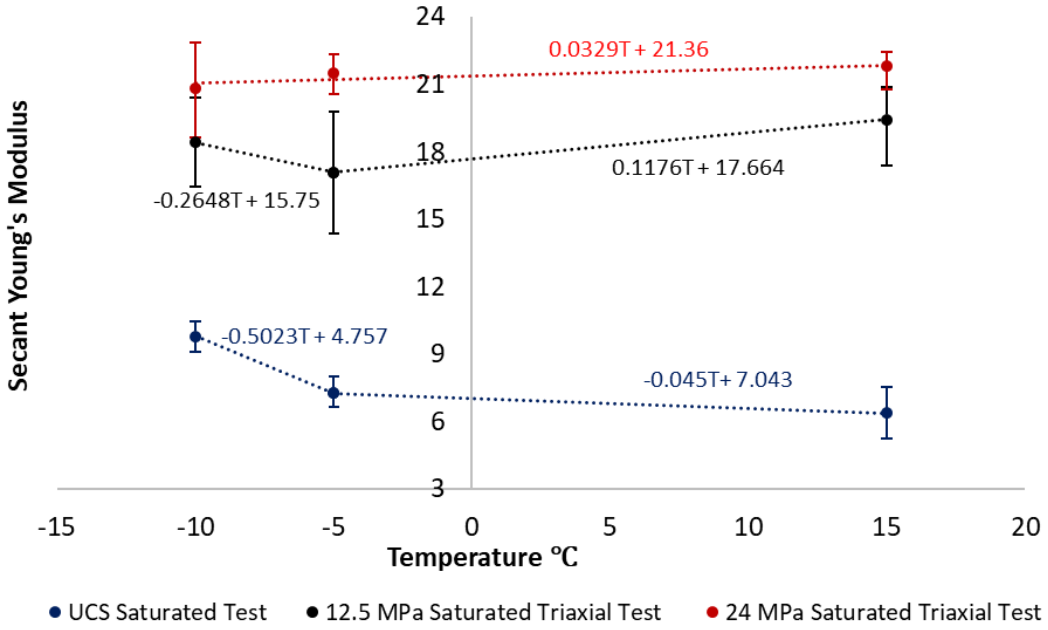

Figure 4. 24 Average values of secant Young's moduli and error bars at different confining pressures and temperatures.

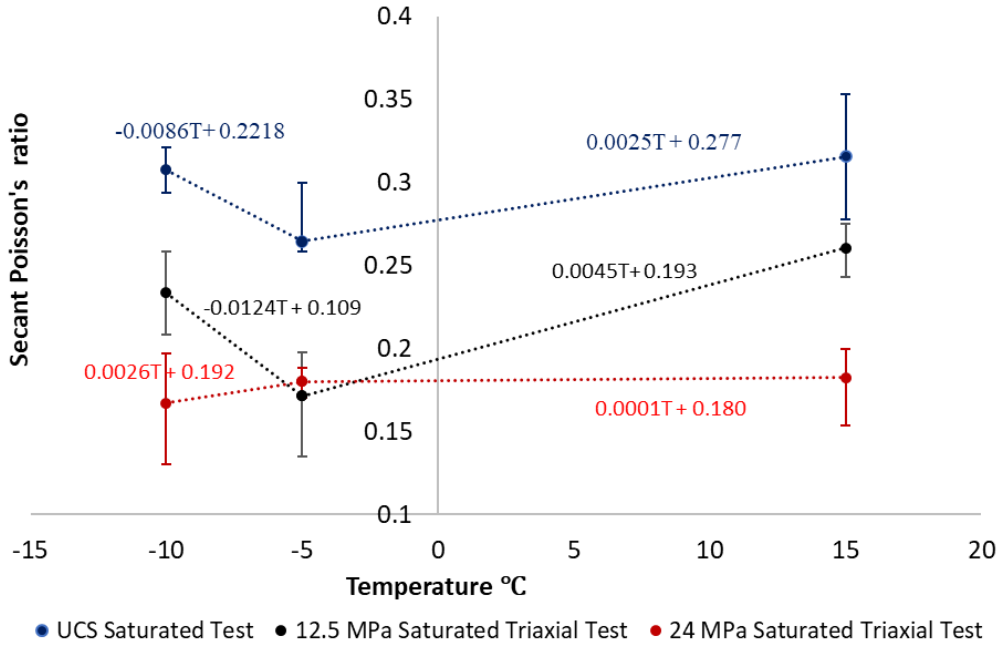

Figure 4. 25 Average values of secant Poisson's ratios and error bars at different confining pressures and temperatures.

4.5 Critical State Mechanics

After calculating the mechanical parameters of the UCS and triaxial tests, the slope of the critical state line is estimated. In this way, numerical models can use the mechanical and critical state mechanics variables to simulate different wellbore stability problems. Studying the temperature influence on the critical state line is important, as it marks the transition between brittle and ductile behaviour in the $q - p'$ domain and can be used as an input in future numerical simulations (Wood, 1991; Shah, 1997). The slope of the critical state line M_{cs} is the slope of the failure line where compactive and dilatant strains are equal (Rutter and Glover, 2012).

The bounding surface of Khalili et al. (2005) is used as presented in Equation (3.170) to plot the yield curve of the Stainton Sandstone.. The influence of M_{cs} and M on the bounding surface can be seen in Figure 4.26. The material constant R is estimated to be equal to 2 as the ratio between the pre-consolidated pressure and the current stress at the intersection of the yield function and the critical state line in the $\mathrm{q} - \mathrm{p}'$ domain.

Figure 4.27 presents the bounding yield surface, the critical state line and the pathways of the loadings inside that yield surface until reaching the maximum stress points. The yielding points or higher stress points should generally lie on the yield surface. M based on the values range of Ma (2014b) and how it affects the bounding surface, as seen in Figure 4.26b, was estimated equal to 1.9. Assuming that M and R are temperature independent and fitting the yield bounding surface curve to the yield data, M_{cs} was estimated. One interesting outcome is that M_{cs} increases with reducing temperature, a logical outcome as the strength of rock increases.

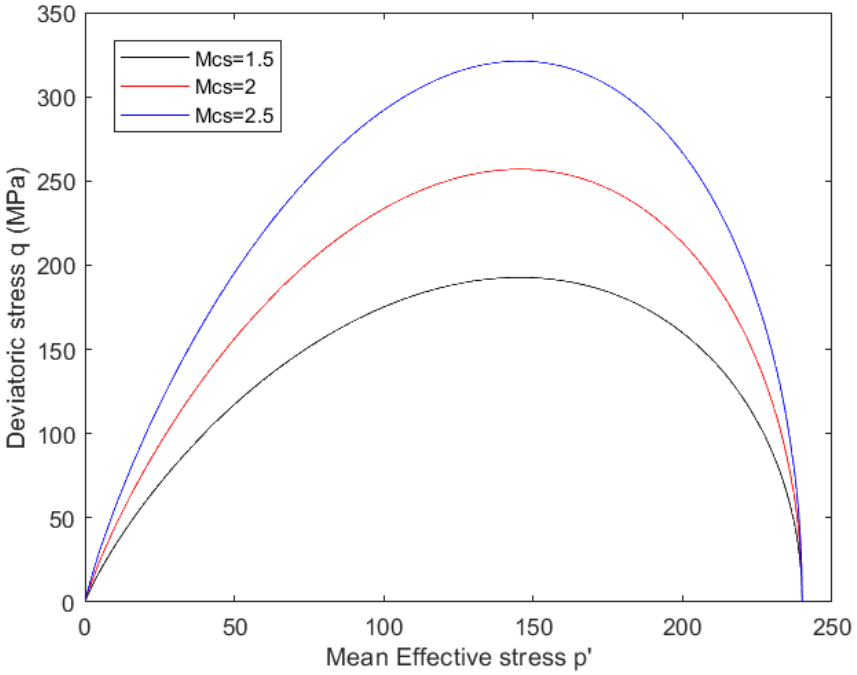

Figure 4.26a

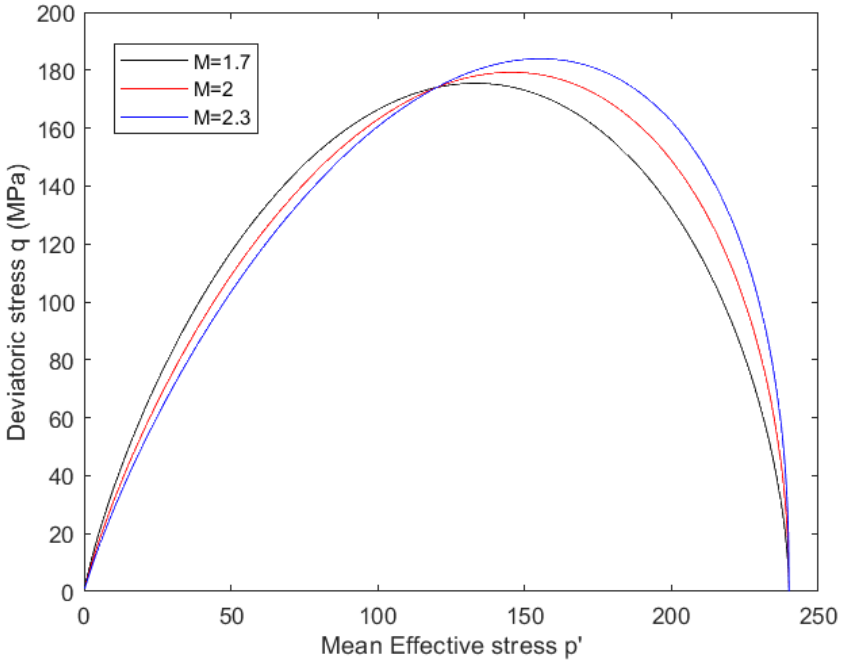

Figure 4. 26 Influence of a) M_{cs} and b) M on the bounding yield surface

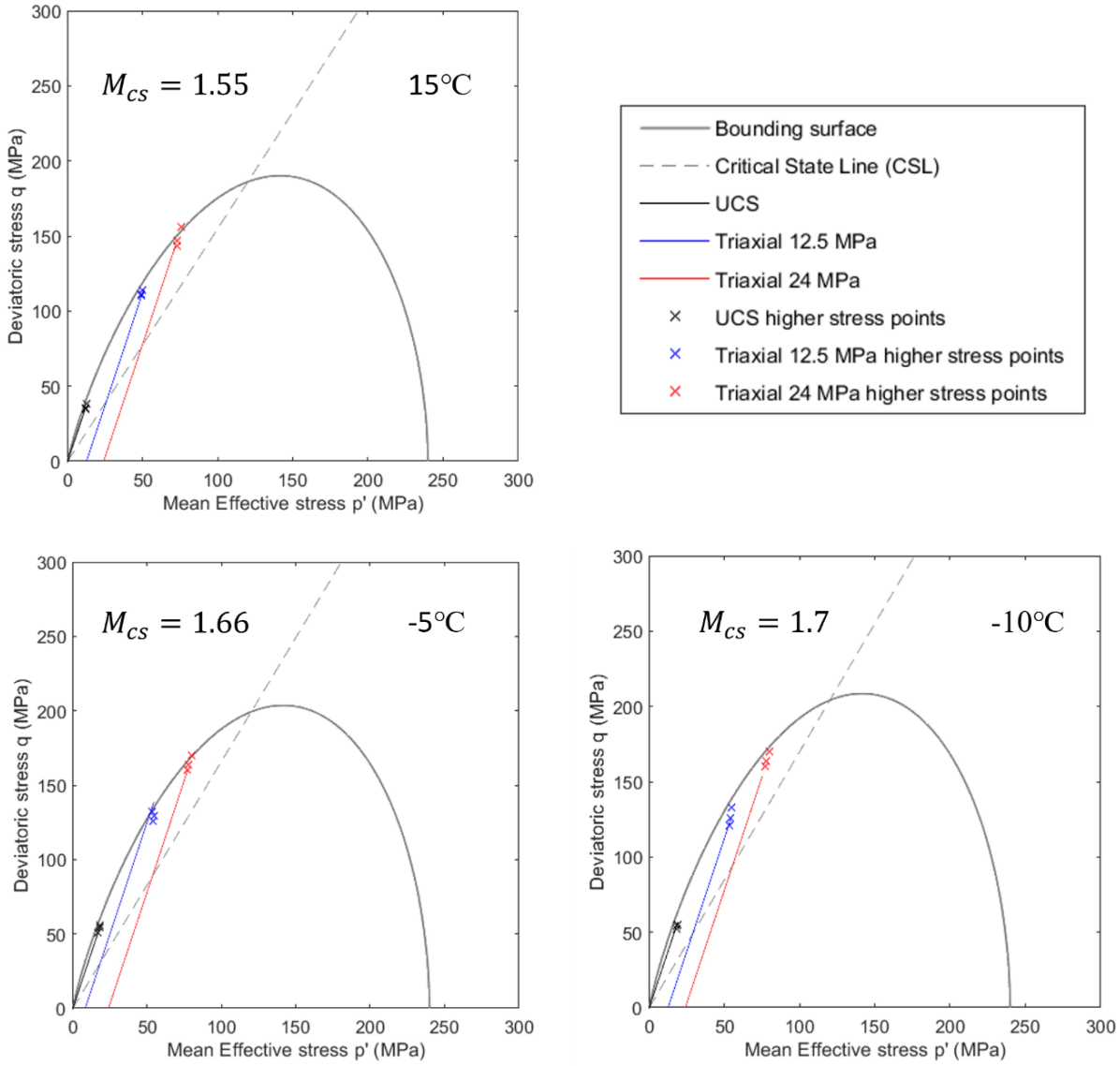

Figure 4. 27 Bounding surface model and slope of Critical State line (M_{cs}) for three different tests

4.6 Microstructural Analysis of tested samples

In this section, microstructural characterisation of the sample in both natural and deformed states is presented. Analysis of the deformation and failure mechanisms allows for a better understanding if the test results and for insights as to how the rock in the near wellbore region may fail during injection operations.

A significant finding noted above was that, under the uniaxial compression tests conducted in this study the Poisson's ratio exceeded the permitted linear value, i.e., it was >0.5. A proposed explanation to this is that the samples underwent significant dilation during deformation. To investigate this, the microstructural development of the samples was studied. To understand the origins of the mechanical behaviours observed during the deformation experiments, a microstructural characterisation of the sandstone was first undertaken on an undeformed core as a control. Similar examinations were then performed on a sample tested to failure under UCS conditions and a sample tested to failure under triaxial conditions with a confining pressure of 12.5 MPa. The thin studied sections that used to obtain the appropriate images from the microscope were made at the department of Earth Sciences in Durham University. The analysis of the images presented in Sections 4.6.1 and 4.62 joint work conducted with Dr. Samuel Graham, Newcastle University.

4.6.1 Microstructural analysis of UCS sample

Microscopy images of the sample tested under UCS conditions show some significant differences and evidence of damage. In the far field (Figure 4.28c), sample porosity remains close to that of the undeformed sample (Figure 4.2a). This contrasts with Figure 4.28a, where porosity near the damage zone appears reduced. Grains showed little internal brittle deformation, with intra-granular microcracks absent. There is some degree of undulous extinction present implying permanent twisting to the crystal lattice during deformation.

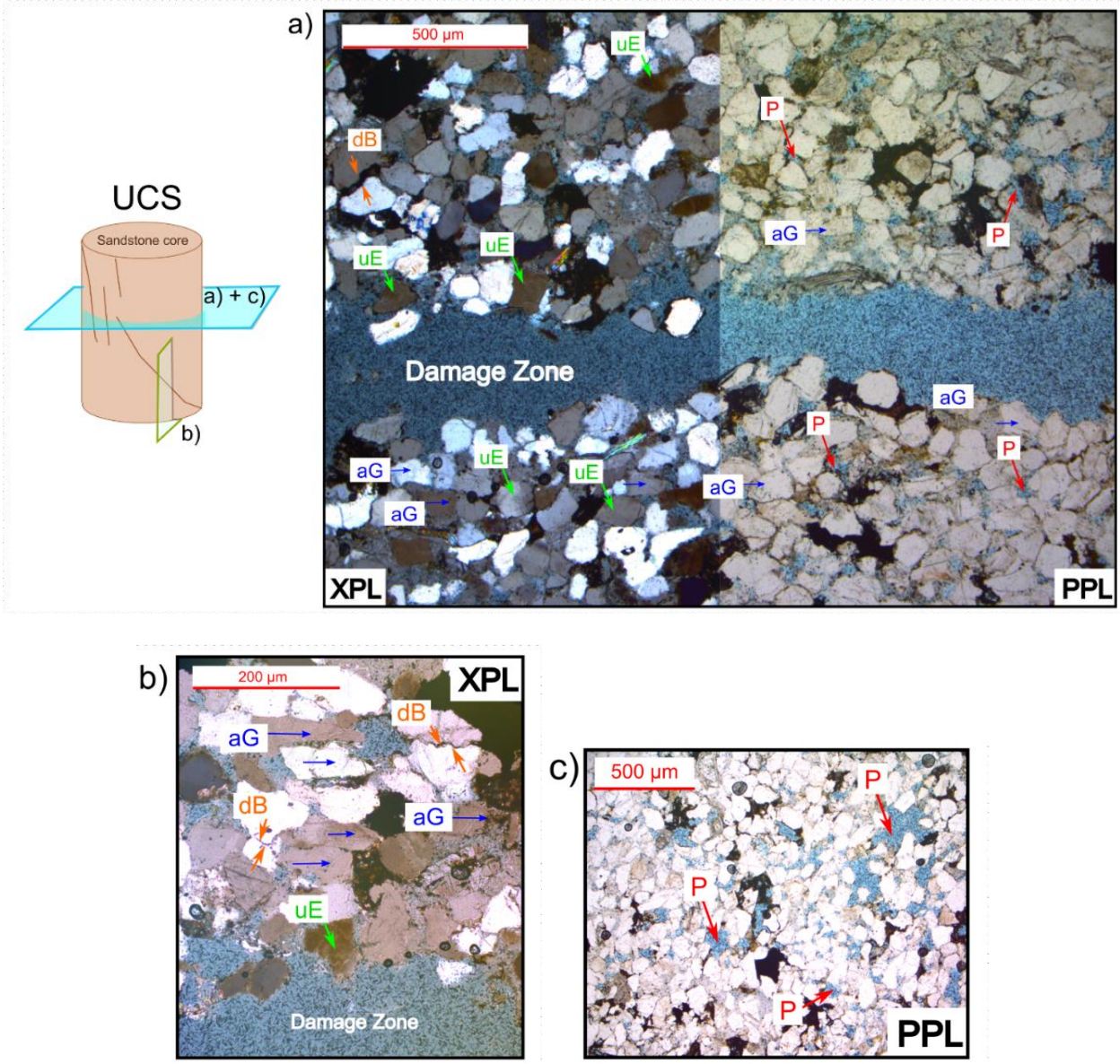

Figure 4. 28 a) Crossed and plane polarised light images of Sample D showing experimental damage zone. b) higher magnification view under crossed polarised light near the damage zone. c) polarised image in a region distant to the experimentally formed damage zone. Symbols in figure are as follows. P = pore space, uE = undulous extinction, dB = dilatant boundary, aG = alignment of grains.

Operation of such crystal-plastic mechanisms acts to promote work hardening, and arrest of microcrack development (Rutter, 1986; Menéndez et al., 1996). This implies that failure during unconfined conditions was primarily accommodated by shearing of quartz cements before sufficient strain was achieved within the grains to initiate internal fracture. Figure 4.28a and b show evidence of parting along grain-to-grain contacts, (marked dB). Note from Figure 4.2a, that the irregular contacts between grains are only rarely fully sutured. Figure 4.28b shows evidence of

particle alignment, with a sub-parallel arrangement of the long axes of elongate quartz grains evident. This is also seen more widely in the rest of the damage zone (Figure 4.28a). Combined, these microstructural observations provide evidence of shear enhanced particle-to-particle sliding and realignment. Such processes contribute a mechanism by which an increase in sample volume can occur after shearing of quartz cements.

4.6.2 Microstructural analysis of the triaxial tested sample

In the uniaxially deformed sample, there is evidence for inter-grain rotation which acts to promote sample dilation after initial shearing of cements. In the triaxially deformed sample, there is prevalent intragranular cracking observed (Figure 4.29a) that is not present in the undeformed material (Figure 4.2a), which is present throughout the sample, but increases in intensity towards the damage zone (Figure 4.29b). This is due to increased contact stresses preventing inter-grain slip (Menéndez et al., 1996). Lack of inter-grain sliding seeks to prevent volumetric dilation of the sample during loading. Although, grain size reduction could also be interpreted as evidence against dilation through pore collapse, this is generally only possible where such mechanisms accompany macroscopically ductile deformation (Rutter, 1986). Instead, the samples deformed under 12.5 MPa confining stress display clear shear localization and macroscopically brittle deformation (Figure 4.29). Therefore, the apparent compaction observed in the fine-grained region likely occurs due to late stage collapse of the sample during shear localization from microcracking (Menéndez et al., 1996) rather than as a controlling deformation mechanism in its own right.

Note that the samples deformed under 24 MPa confining pressure also result in a discrete fracture plane, rather than diffuse internal deformation. This is due to the experimental conditions of these tests resulting in an intersection of the yield surface on the shear side rather than the cap side. Therefore, the deformation mechanisms controlling failure in these samples are expected to be similar, although microcracking would be more intense.

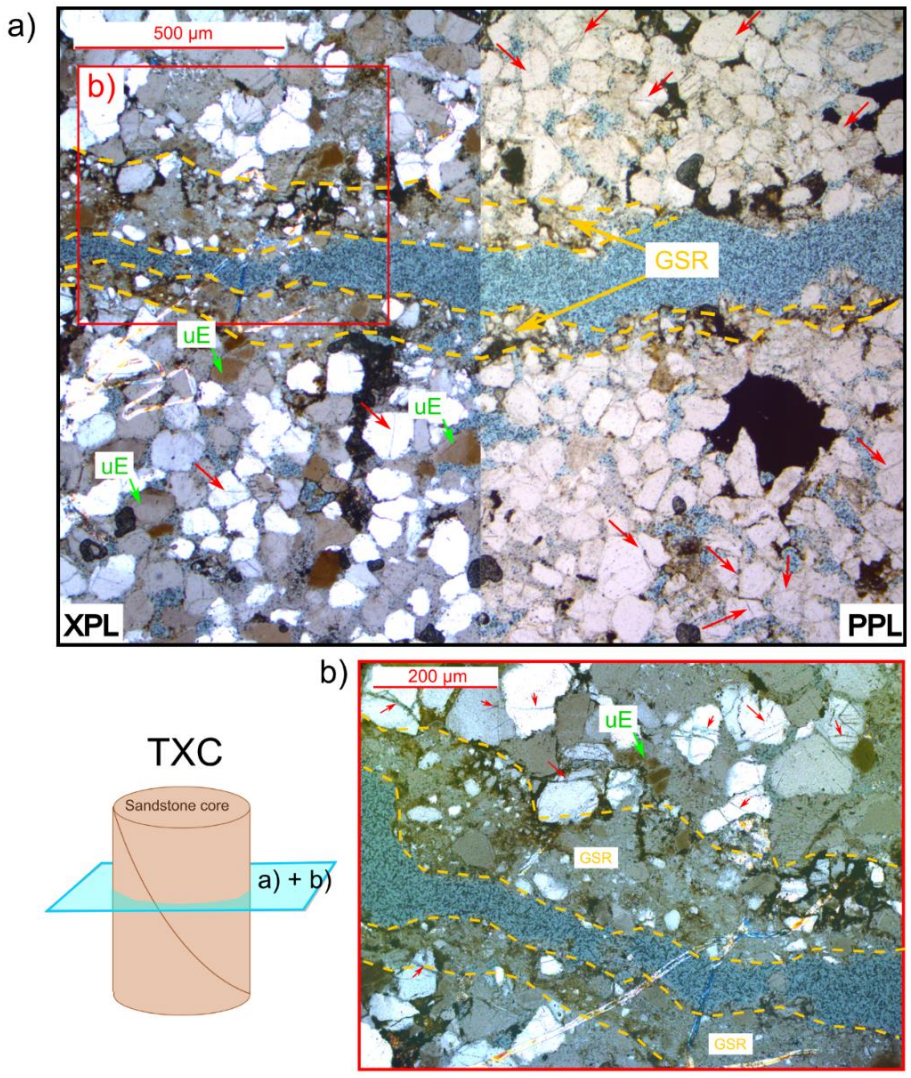

Figure 4. 29 a) Plane (PPL) and crossed (XPL) polarized light view of sample deformed under 12.5 MPa confining stress. b) Higher resolution of damage zone under crossed polarized light.

4.7 Discussions of the experimental results

Three different temperatures (15℃, -5℃ and -10℃) were tested at UCS, 12.5 and 24 MPa confining conditions. ISRM and Wood's (1990) method showed similar results for the mechanical properties of rock. The results confirmed that the sandstone exhibits elastoplastic behaviour and strong dependency on the confining pressure and temperature conditions. An interesting outcome of the experimental tests was the estimated value of the Poisson's ratio, which describes the deformation of the material in a direction perpendicular to the direction of the applied force. Poisson's ratio usually ranges between 0.1 and 0.5, with the upper limit being the fully elastic

limit. However, using certain slope of the deviatoric stress-strain curve, Poisson's ratio was identified greater than 0.5. This outcome results in numerical issues, as the calculated bulk modulus was estimated negative. To explain the unusual Poisson's ratio value a microscopic analysis took place, which indicated dilation and grain realignment. As the sample was axially compacted the circumferential direction expanded further, indicating an increase in volume. It should be also mentioned that -5°C works as a transition point for the behaviour of the mechanical properties (Young's modulus and Poisson's ratio), especially for the 12.5 MPa confining stress and UCS tests. It can be suggested that the decrease of temperature from room conditions (15°C) to sub-zero temperatures enhances the brittle behaviour of rock as the Poisson's ratio drops, which is in agreement with Han et al. (2022) . However, for low confinement, freezing the rock further than -5°C increases the ductility of the material again. Focusing on the UCS and low confinement (12.5 MPa) tests, cooling causes an increase in Young's modulus down to -5°C and a reduction with further decrease of temperature. For higher confining pressure (24 MPa), Young's modulus is not affected by changes in temperature. However, a reduction in Poisson's ratio and a decrease in the dilation of the material is seen with decreasing temperature, while the slope of the critical state line increases.

Finally, it was identified that both an increase in confinement and a reduction in temperature, increased the maximum deviatoric stress of sandstone and the sandstone's strength, which is in agreement with the research of Feng et al. (2017), Liu et al. (2021) and Jia et al. (2022). As strength also increases, the critical state line M_{cs} reduces with temperature drop. However, the Poisson's ratio reduced with a reduction in temperature, especially in the UCS tests, indicating the possibility of brittle failure due to elasticity loss. UCS tests seem to be more sensitive to temperature effects. This is an important outcome as expanding the results to a wellbore stability problem, brittle failure and damage may occur when sub-zero injection temperatures are applied at the wellbore head, where confinement is low. Less influence will be identified at higher depths. Mathematical functions have been determined from these results for use in modelling. Additional testing would help constrain their variability. Relationships linking the temperature to the mechanical parameters will be implemented in robust Thermo-Hydro-Mechanical model to predict the behaviour of the rock in the vicinity of the wellbore during CO_2 injection.

Chapter 5. Finite Element Modelling implementation, Critical State Mechanics parameter determination and validation of the THM model

5.1 Introduction

This chapter presents the application of the finite element method (FEM) to obtain the approximate governing differential equation solution that couples deformation, fluid flow and heat transfer in a double porous medium. Section 5.2 presents the finite element formulation.

The governing differential equations for the coupled THM elastoplastic damage model developed in Chapter 3 are formulated in a finite element formulation scheme to link the primary unknowns to the applied boundary conditions and loadings. The set of the coupled governing equations are non-linear second-order differential equations that contain both spatial and temporal derivatives of the primary variables. The general solutions of these differential equations are achieved by numerical approaches, which give approximate results based on the user specified tolerance. The approximate outcomes are produced after iterations and mesh refinements once the size of the approximation medium becomes small enough (Ma and Zhao, 2018).

The main advantage of a numerical model is that it can solve the complex continuum problem as a linear problem using finite discrete elements (Kwon and Bang, 2018). The solutions produced by this technique for a typical boundary condition problem are formed of both global and local solutions (Duarte and Kim, 2008). For this study, the global solution scheme is used for the primary variable such as nodal displacements, pore-fissure water pressure and temperature of the fractured medium. The integrated constitutive model produces the local solutions, and variables such as stress, strain, plastic hardening, damage, and permeability evolution are determined. The requirements of equilibrium, constitutive law, boundary conditions and robustness, accuracy and efficiency are achieved by calculating the global and local solution schemes.

5.2 Finite Element Method and MATLAB software

FEMs are powerful numerical techniques for determining approximate solutions of partial differential equations. FEM assumes that the approximate solution is calculated after successive iterations, while analytical solutions are estimated by mesh refinements as the size of the approximation domain becomes extremely small (Jagota et al., 2013; Kwon and Bang, 2018). The solution approach is based either on reducing the partial differential equations to linear systems (steady-state problem) or to semi-discrete systems of ordinary differential equations (time-dependent model). The general procedure of the FEM according to Bathe (2006) and Kwon and Bang (2018) is as follows:

1. A complex geometrical domain is replaced by several smaller sub-domains, called finite elements. The primary variables are selected and applied at the nodes of each element. The variation of these primary variables is described in terms of nodal values.
2. The interpolation function is selected to represent the variation of the primary variables over each element. The interpolation function is the shape function of the elements.
3. The governing differential equation is replaced by a more straightforward, approximate algebraic system using variational techniques or weighted residual approaches.
4. The element stiffness matrices and equations are now assembled for the entire system.
5. Boundary conditions are incorporated by applying the known values to the nodal variables.
6. The global equations are solved for the unknown nodal variables using numerical techniques such as iterations.
7. Finally, local solutions are estimated, and secondary variables such as stresses, strains, plastic hardening parameters, damage variable and permeability evolution are determined.

For this study, the nodal values are the displacements, the pore pressures, the fissure pressures, and the temperature of the solid domain. Galerkin's weighted residual approach is adopted based on Kwon and Bang (2018). MATLAB software is to solve the final matrix equation. It is a useful tool for vector and matrix calculation and is very helpful, while applying the Finite Element Method (Kwon and Bang, 2018). The basic structure of the FEM in MATLAB software is as follows:

1. Read input data and create array sizes.
2. Calculation of element matrices and vectors for each element
3. Element matrices and vectors are assembled into the system matrix and vector
4. Solve the matrix equation for the primary nodal variables
5. Compute any secondary variables
6. Plot the desired results

In the next sections the implementation of the problem into MATLAB using FEM is outlined, starting from the nodal and global unknown vectors.

5.2.1 Nodal and global unknown vectors

Five primary unknowns need to be calculated at each node as follows:

- The displacement vector at the two directions $\boldsymbol{u_d} = \begin{bmatrix} \boldsymbol{u_{d-x}} \\ \boldsymbol{u_{d-y}} \end{bmatrix}$
- The porous saline water pressure $\boldsymbol{p_1}$
- The fissure saline water pressure $\boldsymbol{p_2}$
- The temperature of the solid medium $\boldsymbol{T_s}$

5.2.2 Axisymmetric considerations and shape functions.

For an axisymmetric analysis, the Cartesian coordinates are expressed in terms of cylindrical coordinates as follows:

- $\boldsymbol{u_{d-x}} = u_{d-r}$ is the radial displacement, including damage
- $\boldsymbol{u_{d-y}} = u_{d-z}$ is the axial displacement, including damage
- $\boldsymbol{u_{d-z}} = u_{d-\theta}$ is the circumferential displacement, including damage

The circumferential displacement is assumed to be equal to zero and all functions are independent of θ and dependent only on r and z. Two shearing stress components disappear when the problem degenerates from three-dimension to axisymmetry.

The remaining stresses are:

$$\{\boldsymbol{\sigma}\} = \{\boldsymbol{\sigma_r}\ \ \boldsymbol{\sigma_\theta}\ \ \boldsymbol{\sigma_z}\ \ \boldsymbol{\tau_{rz}}\} \tag{5.1}$$

The strains describing an axisymmetric problem are:

$$\{\boldsymbol{\varepsilon}\} = \{\boldsymbol{\varepsilon_r}\ \ \boldsymbol{\varepsilon_\theta}\ \ \boldsymbol{\varepsilon_z}\ \ \boldsymbol{\gamma_{rz}}\} \tag{5.2}$$

The stress-strain relationship including initial strain ε_T due to thermal expansion based on Zienkiewicz et al. (2005) is expressed as :

$$\sigma = [\boldsymbol{S^{ep}}(D,T)](\varepsilon - \varepsilon_T) \tag{5.3}$$

The material property matrix is as follows:

$$[\boldsymbol{S^{ep}}(D,T)] = \frac{E}{(1+\nu)(1-2\nu)}\begin{bmatrix} 1-\nu & \nu & \nu & 0 \\ \nu & 1-\nu & \nu & 0 \\ \nu & \nu & 1-\nu & 0 \\ 0 & 0 & 0 & \frac{1-2\nu}{2} \end{bmatrix} \tag{5.4}$$

Based on Kwon and Bang (2018) and Gelet et al. (2012a) the stresses can be connected to strains as follows:

$$\begin{bmatrix} \boldsymbol{\sigma_r} \\ \boldsymbol{\sigma_\theta} \\ \boldsymbol{\sigma_z} \\ \boldsymbol{\tau_{rz}} \end{bmatrix} = [\boldsymbol{S^{ep}}(D,T)]\begin{bmatrix} \boldsymbol{\varepsilon_r} \\ \boldsymbol{\varepsilon_\theta} \\ \boldsymbol{\varepsilon_z} \\ \boldsymbol{\gamma_{rz}} \end{bmatrix} - [\boldsymbol{S^{ep}}(D,T)]C_{Ts}T\begin{bmatrix} 1 \\ 1 \\ 1 \\ 0 \end{bmatrix} \tag{5.5}$$

The damage evolution will influence Young's modulus based on the dependence shown in equation (3.162). Specifically:

$$E = 3K_{bulk}^{el}(D,T)(1-2\nu) \tag{5.6}$$

5.3 Spatial discretization

In Chapter 3, five constitutive equations are presented describing the deformation model, the flow model in the porous and fracture network, the energy balance equation for the solid and the energy balance equation for the energy exchange between the porous and fracture network and vice versa. For the purposes of simplicity, and as it is hard to estimate the coefficients of heat exchange between the porous and fissure network, the rate of the entropy and enthalpy, it is assumed that the temperature of the solid, porous and fracture domains are equal. Consequently, the governing equations are reduced to four and are as follows:

Deformation governing equation:

$$\operatorname{div}\left(\frac{1}{2}[\boldsymbol{S^{ep}}(D,T)](\nabla\dot{\boldsymbol{u}}_{\boldsymbol{d}}+\dot{\boldsymbol{u}}_{\boldsymbol{d}}\nabla)+\beta_1\dot{p}_1\boldsymbol{\delta}+\beta_2\dot{p}_2\boldsymbol{\delta}-\frac{C_{Ts}}{C_f}\dot{T}_s\boldsymbol{\delta}\right)+\dot{\boldsymbol{F}}=0 \tag{5.7}$$

Flow governing equations:

$$\begin{aligned}\operatorname{div}\left(\frac{\boldsymbol{k}_1}{\mu_f}\left(\nabla p_1+\rho_f\boldsymbol{g}\right)+\varphi_1\Theta_1\nabla T\right)\\ =\ \beta_1 div\dot{\boldsymbol{u}}+\ \beta_{11}\dot{p}_1-\ \beta_{12}\dot{p}_2-\varphi_1C_T\dot{T}_1-(\beta_1-\varphi_1)C_{TS}\dot{T}_s\\ +\Xi_1\end{aligned} \tag{5.8}$$

$$\begin{aligned}\operatorname{div}\left(\frac{\boldsymbol{k}_2}{\mu_f}\left(\nabla p_2+\rho_f\boldsymbol{g}\right)+\varphi_2\Theta_2\nabla T\right)\\ =\ \beta_2 div\dot{\boldsymbol{u}}+\ \beta_{22}\dot{p}_2-\ \beta_{21}\dot{p}_1-\varphi_2C_T\dot{T}_2-(\beta_2-\varphi_2)C_s\dot{T}_s+\Xi_2\end{aligned} \tag{5.9}$$

Energy balance equation for the solid:

$$\begin{aligned}\operatorname{div}(\varphi_s k_s\nabla T_s)=T_s\frac{C_s}{C_{fr}}div(\dot{u})-T_s(\beta_1-\varphi_1)C_s\dot{p}_1-T_s(\beta_2-\varphi_2)C_s\dot{p}_2\\ +\rho^sC_{ps}\dot{T}_s\end{aligned} \tag{5.10}$$

The four equations can be rearranged into a convenient finite element formulation form applying the divergence operator as follows:

$$\begin{aligned}\nabla'^T([\boldsymbol{S^{ep}}(D,T)]\{\nabla(\dot{\boldsymbol{u}}_{\boldsymbol{d}})\})+\beta_1\dot{p}_1\nabla'^T\{\boldsymbol{\delta}\}+\beta_2\dot{p}_2\nabla'^T\{\boldsymbol{\delta}\}-\frac{C_{Ts}}{C_f}\dot{T}_s\nabla'^T\{\boldsymbol{\delta}\}\\ +\{\dot{\boldsymbol{F}}\}=0\end{aligned} \tag{5.11a}$$

$$\begin{aligned}\nabla^T\left[\frac{\boldsymbol{k}_1}{\mu_f}\left(\nabla p_1+\rho_f\{\boldsymbol{g}\}\right)+\varphi_1\Theta_1\nabla T\right]-\ \beta_1\{\delta\}^T\nabla'\{\dot{\boldsymbol{u}}\}-\ \beta_{11}\dot{p}_1+\ \beta_{12}\dot{p}_2\\ +\varphi_1C_T\dot{T}_1+(\beta_1-\varphi_1)C_s\dot{T}_s+\Xi_1=0\end{aligned} \tag{5.11b}$$

$$\nabla^T\left[\frac{\boldsymbol{k}_2}{\mu_f}\left(\nabla p_2+\rho_f\{\boldsymbol{g}\}\right)+\varphi_2\Theta_2\nabla T\right]-\beta_2\{\delta\}^T\nabla'\{\dot{\boldsymbol{u}}\}-\beta_{22}\dot{p}_2+\beta_{21}\dot{p}_1+\varphi_2C_T\dot{T}_2+(\beta_2-\varphi_2)C_s\dot{T}_s+\Xi_2=0 \tag{5.11c}$$

$$\nabla'^T[\varphi_s k_s\nabla T_s]=T_s\frac{C_s}{C_{fr}}\nabla'\{\dot{\boldsymbol{u}}\}-T_s(\beta_1-\varphi_1)C_s\dot{p}_1-T_s(\beta_2-\varphi_2)C_s\dot{p}_2+\rho^sC_{ps}\dot{T}_s \tag{5.11d}$$

The differential operator corresponding to the definition of strains is taken as:

$$\nabla'=\begin{bmatrix}\partial/\partial x & 0 & 0\\ 0 & \partial/\partial y & 0\\ 0 & 0 & \partial/\partial z\\ \partial/\partial y & \partial/\partial x & 0\\ 0 & \partial/\partial z & \partial/\partial y\\ \partial/\partial z & 0 & \partial/\partial x\end{bmatrix}$$

where δ is the identity vector defined as:

$$\delta=\{1\quad 1\quad 1\quad 0\quad 0\quad 0\}^T$$

The vector format of the gradient operator $\nabla^T=\{\partial/\partial x\quad \partial/\partial y\quad \partial/\partial z\}$

Galerkin's weighted residual approach is applied to approximate the solution of equations (5.11) by using the element shape functions as the weighted factors.

$$\int[\boldsymbol{N}]^T\left(\nabla'^T\left([\boldsymbol{S^{ep}}(D,T)]\{\nabla(\dot{\tilde{\boldsymbol{u}}}_{\boldsymbol{d}})\}\right)+\beta_1\dot{\tilde{p}}_1\nabla'^T\{\boldsymbol{\delta}\}+\beta_2\dot{\tilde{p}}_2\nabla'^T\{\boldsymbol{\delta}\}-\frac{C_{Ts}}{C_f}\dot{\tilde{T}}_s\nabla'^T\{\boldsymbol{\delta}\}+\{\dot{\boldsymbol{F}}\}\right)d\Theta=0 \tag{5.12a}$$

$$\int[\boldsymbol{N}]^T\left(\nabla^T\left[\frac{\boldsymbol{k}_1}{\mu_f}\left(\nabla\tilde{p}_1+\rho_f\{\boldsymbol{g}\}\right)+\varphi_1\Theta_1\nabla\tilde{T}_1\right]-\beta_1\{\boldsymbol{\delta}\}^T\nabla'\{\dot{\tilde{\boldsymbol{u}}}\}-\beta_{11}\dot{\tilde{p}}_1+\beta_{12}\dot{\tilde{p}}_2+(\beta_1-\varphi_1)C_s\dot{\tilde{T}}_s+\Xi_1\right)d\Theta=0 \tag{5.12b}$$

$$\int [\boldsymbol{N}]^T \left(\nabla^T \left[\frac{\boldsymbol{k}_2}{\mu_f} \left(\nabla \tilde{p}_2 + \rho_f \{\boldsymbol{g}\} \right) + \varphi_2 \Theta_2 \nabla \tilde{T}_2 \right] - \beta_2 \{\boldsymbol{\delta}\}^T \nabla' \{\dot{\tilde{\boldsymbol{u}}}\} - \beta_{22} \dot{\tilde{p}}_2 + \beta_{21} \dot{\tilde{p}}_1 + (\beta_2 - \varphi_2) C_s \dot{\tilde{T}}_s + \Xi_2 \right) d\Theta = 0 \tag{5.12c}$$

$$\int [\boldsymbol{N}]^T \left(\nabla'^T [\varphi_s k_s \nabla T_s] \right) d\Theta = \int [\boldsymbol{N}]^T \left(T_s \frac{C_s}{C_{fr}} \nabla' \{\dot{\tilde{\boldsymbol{u}}}\} - T_s (\beta_1 - \varphi_1) C_s \dot{\tilde{p}}_1 - T_s (\beta_2 - \varphi_2) C_s \dot{\tilde{p}}_2 + \rho^s C_{ps} \dot{\tilde{T}}_s \right) d\Theta \tag{5.12d}$$

The body force vector is ignored in this study for the sake of simplicity.

where $\tilde{\boldsymbol{u}}_{\boldsymbol{d}}$, $\tilde{p}_1$, $\tilde{p}_2$ and $\tilde{T}_s$ are the approximate solutions, $[\boldsymbol{N}]$ is the shape function and Θ is the element domain. The approximate solutions are computed in terms of the nodal values of the primary values of the primary variable by the element shape functions:

$$\tilde{\boldsymbol{u}}_{\boldsymbol{d}} \cong [\boldsymbol{N}]\{\boldsymbol{u}_{\boldsymbol{d}}\} \tag{5.13a}$$

$$\tilde{p}_1 \cong [\boldsymbol{N}]\{\boldsymbol{p}_{\boldsymbol{1}}\} \tag{5.13b}$$

$$\tilde{p}_2 \cong [\boldsymbol{N}]\{\boldsymbol{p}_{\boldsymbol{2}}\} \tag{5.13c}$$

$$\tilde{T}_s \cong [\boldsymbol{N}]\{\boldsymbol{T}_{\boldsymbol{s}}\} \tag{5.13d}$$

$$\{\boldsymbol{u}_{\boldsymbol{d}}\} = \{\boldsymbol{u}\} - 2\dot{D}\{\boldsymbol{u}^{\boldsymbol{e}}\}/(1 - D) \tag{5.13e}$$

$\{\boldsymbol{u}\}$, $\{\boldsymbol{p}_{\boldsymbol{1}}\}$, $\{\boldsymbol{p}_{\boldsymbol{2}}\}$, $\{\boldsymbol{T}_{\boldsymbol{s}}\}$ are the vectors of the nodal values of the solid matrix displacement, pore saline water and fissure saline water pressure and temperature of the solid, respectively.

$\{\boldsymbol{u}^{\boldsymbol{e}}\}$ is the vector of the nodal values of the solid matrix elastic displacement.

This research uses two-dimensional four-node isoparametric elements to represent the fractured porous medium. The associated shape functions are shown in Figure 5.1, and equal-order interpolation for all the unknowns is selected because of its computational speed.

$$N_u = N_1 = N_2 = N_T = [\boldsymbol{N}] \tag{5.14}$$

$$N_A = \frac{1}{4}(1 - x_1)(1 - y_1)$$

$$N_B = \frac{1}{4}(1 + x_1)(1 - y_1)$$

$$N_C = \frac{1}{4}(1 + x_1)(1 + y_1)$$

$$N_D = \frac{1}{4}(1 - x_1)(1 + y_1)$$

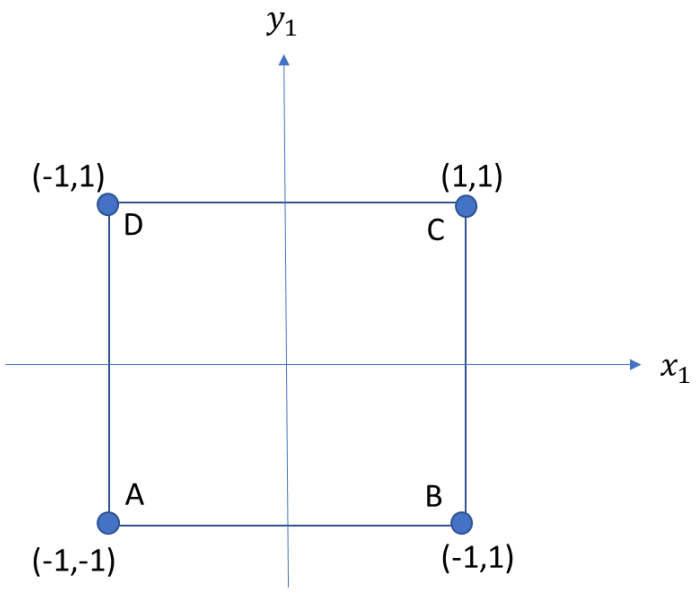

Figure 5. 1 Shape functions associated to a four-node bilinear quadrilateral element.

The Galerkin method involves interpolating the variations $\dot{\boldsymbol{u}}_{\boldsymbol{d}}$, $\dot{\boldsymbol{p}}_{\boldsymbol{1}}$, $\dot{\boldsymbol{p}}_{\boldsymbol{2}}$ and $\dot{\boldsymbol{T}}_{\boldsymbol{s}}$ through the shape functions N. Taking into consideration those shape functions and employing Green's theorem and substituting Equation (5.13) into Equation (5.12) results in:

$$\begin{aligned} &-\int [\nabla' \boldsymbol{N}]^T [\boldsymbol{S^{ep}}(D,T)][\nabla' \boldsymbol{N}]\{\dot{\boldsymbol{u}}_{\boldsymbol{d}}\}\, d\Theta + \int [\boldsymbol{N}]^T [\boldsymbol{S^{ep}}(D,T)][\nabla' \boldsymbol{N}]\{\dot{\boldsymbol{u}}_{\boldsymbol{d}}\}\, d\Gamma \\ &+ \int \beta_1 [\nabla' \boldsymbol{N}]^T \{\boldsymbol{\delta}\}[\boldsymbol{N}]\{\dot{\boldsymbol{p}}_{\boldsymbol{1}}\}\, d\Theta - \int \beta_1 [\boldsymbol{N}]^T \{\boldsymbol{\delta}\}[\boldsymbol{N}]\{\dot{\boldsymbol{p}}_{\boldsymbol{1}}\}\, d\Gamma \\ &+ \int \beta_2 [\nabla' \boldsymbol{N}]^T \{\boldsymbol{\delta}\}[\boldsymbol{N}]\{\dot{\boldsymbol{p}}_{\boldsymbol{2}}\}\, d\Theta - \int \beta_2 [\boldsymbol{N}]^T \{\boldsymbol{\delta}\}[\boldsymbol{N}]\{\dot{\boldsymbol{p}}_{\boldsymbol{2}}\}\, d\Gamma \\ &+ \int \frac{C_{Ts}}{C_f} [\nabla' \boldsymbol{N}]^T \{\boldsymbol{\delta}\}[\boldsymbol{N}]\{\dot{\boldsymbol{T}}_{\boldsymbol{s}}\}\, d\Theta - \int \frac{C_{Ts}}{C_f} [\boldsymbol{N}]^T \{\boldsymbol{\delta}\}[\boldsymbol{N}]\{\dot{\boldsymbol{T}}_{\boldsymbol{s}}\} d\Gamma \\ &+ \int [\boldsymbol{N}]^T \{\dot{\boldsymbol{F}}\}\, d\Theta = 0 \end{aligned} \tag{5.15a}$$

$$-\int \beta_1[\boldsymbol{N}]^T\{\boldsymbol{\delta}\}^T[\nabla'\boldsymbol{N}]\{\dot{\boldsymbol{u}}\}\,d\Theta-\int \beta_{11}[\boldsymbol{N}]^T[\boldsymbol{N}]\{\dot{\boldsymbol{p}}_1\}\,d\Theta$$
$$+\int \beta_{12}[\boldsymbol{N}]^T[\boldsymbol{N}]\{\dot{\boldsymbol{p}}_2\}\,d\Theta+\int(\beta_1-\varphi_1)C_s\,[\boldsymbol{N}]^T[\boldsymbol{N}]\{\dot{\boldsymbol{T}}_s\}d\Theta$$
$$-\int[\nabla\boldsymbol{N}]^T\frac{\boldsymbol{k}_1}{\mu_f}[\nabla\boldsymbol{N}]\{\boldsymbol{p}_1\}\,d\Theta+\int[\boldsymbol{N}]^T\frac{\boldsymbol{k}_1}{\mu_f}[\nabla\boldsymbol{N}]\{\boldsymbol{p}_1\}\,d\Gamma$$
$$-\int[\boldsymbol{N}]^T[\boldsymbol{N}]\gamma\{\boldsymbol{p}_1\}\,d\Theta+\int[\boldsymbol{N}]^T[\boldsymbol{N}]\gamma\{\boldsymbol{p}_2\}\,d\Theta=0 \tag{5.15b}$$

$$-\int \beta_2[\boldsymbol{N}]^T\{\boldsymbol{\delta}\}^T[\nabla'\boldsymbol{N}]\{\dot{\boldsymbol{u}}\}\,d\Theta-\int \beta_{22}[\boldsymbol{N}]^T[\boldsymbol{N}]\{\dot{\boldsymbol{p}}_2\}\,d\Theta$$
$$+\int \beta_{21}[\boldsymbol{N}]^T[\boldsymbol{N}]\{\dot{\boldsymbol{p}}_2\}\,d\Theta+\int(\beta_2-\varphi_2)C_s\,[\boldsymbol{N}]^T[\boldsymbol{N}]\{\dot{\boldsymbol{T}}_s\}d\Theta$$
$$-\int[\nabla\boldsymbol{N}]^T\frac{\boldsymbol{k}_2}{\mu_f}[\nabla\boldsymbol{N}]\{\boldsymbol{p}_2\}\,d\Theta+\int[\boldsymbol{N}]^T\frac{\boldsymbol{k}_2}{\mu_f}[\nabla\boldsymbol{N}]\{\boldsymbol{p}_2\}\,d\Gamma$$
$$-\int[\boldsymbol{N}]^T[\boldsymbol{N}]\gamma\{\boldsymbol{p}_2\}\,d\Theta+\int[\boldsymbol{N}]^T[\boldsymbol{N}]\gamma\{\boldsymbol{p}_1\}\,d\Theta=0 \tag{5.15c}$$

$$-\int[\nabla\boldsymbol{N}]^T\varphi_s k_s[\nabla\boldsymbol{N}]\,\{\boldsymbol{T}_s\}d\Theta+\int[\boldsymbol{N}]^T\varphi_s k_s[\nabla\boldsymbol{N}]\,\{\boldsymbol{T}_s\}d\Gamma$$
$$-\int T_s\frac{C_s}{C_{fr}}[\boldsymbol{N}]^T\{\boldsymbol{\delta}\}^T[\nabla'\boldsymbol{N}]\{\dot{\boldsymbol{u}}\}d\Theta$$
$$+\int T_s(\beta_1-\varphi_1)C_s\,[\boldsymbol{N}]^T[\boldsymbol{N}]\{\dot{\boldsymbol{p}}_1\}d\Theta$$
$$+\int T_s(\beta_2-\varphi_2)C_s[\boldsymbol{N}]^T[\boldsymbol{N}]\{\dot{\boldsymbol{p}}_2\}\,d\Theta$$
$$-\int\rho^s C_{ps}\,[\boldsymbol{N}]^T[\boldsymbol{N}]\{\dot{\boldsymbol{T}}_s\}d\Theta=0 \tag{5.15d}$$

where Γ is the element domain.

Implementing the boundary conditions, Equations (5.15) can be rearranged as:

$$\int [\nabla' \boldsymbol{N}]^T [\boldsymbol{S^{ep}}(D,T)][\nabla' \boldsymbol{N}]\{\dot{\boldsymbol{u}}_{\boldsymbol{d}}\}\, d\Theta + \int \beta_1 [\nabla' \boldsymbol{N}]^T \{\boldsymbol{\delta}\}[\boldsymbol{N}]\{\dot{\boldsymbol{p}}_{\boldsymbol{1}}\}\, d\Theta + \int \beta_2 [\nabla' \boldsymbol{N}]^T \{\boldsymbol{\delta}\}[\boldsymbol{N}]\{\dot{\boldsymbol{p}}_{\boldsymbol{2}}\}\, d\Theta - \int \frac{C_{Ts}}{C_f} [\nabla' \boldsymbol{N}]^T \{\boldsymbol{\delta}\}[\boldsymbol{N}]\{\dot{\boldsymbol{T}}_{\boldsymbol{s}}\}\, d\Theta = \int [\boldsymbol{N}]^T \{\dot{\boldsymbol{F}}\}\, d\Theta + \int [\boldsymbol{N}]^T \{\dot{\boldsymbol{Traction}}\} d\Gamma \tag{5.16a}$$

$$-\int \beta_1 [\boldsymbol{N}]^T \{\boldsymbol{\delta}\}^T [\nabla' \boldsymbol{N}]\{\dot{\boldsymbol{u}}\}\, d\Theta - \int \beta_{11} [\boldsymbol{N}]^T [\boldsymbol{N}]\{\dot{\boldsymbol{p}}_{\boldsymbol{1}}\}\, d\Theta + \int \beta_{12} [\boldsymbol{N}]^T [\boldsymbol{N}]\{\dot{\boldsymbol{p}}_{\boldsymbol{2}}\}\, d\Theta + \int (\beta_1 - \varphi_1) C_s [\boldsymbol{N}]^T [\boldsymbol{N}]\{\dot{\boldsymbol{T}}_{\boldsymbol{s}}\} d\Theta - \int [\nabla \boldsymbol{N}]^T \frac{\boldsymbol{k}_1}{\mu_f} [\nabla \boldsymbol{N}]\{\boldsymbol{p}_{\boldsymbol{1}}\}\, d\Theta - \int [\boldsymbol{N}]^T [\boldsymbol{N}]\, \gamma \{\boldsymbol{p}_{\boldsymbol{1}}\} d\Theta + \int [\boldsymbol{N}]^T [\boldsymbol{N}]\, \gamma \{\boldsymbol{p}_{\boldsymbol{2}}\} d\Theta = \int [\boldsymbol{N}]^T \{\mathbf{q}_{\mathbf{1}}\}\, d\Gamma \tag{5.16b}$$

$$-\int \beta_2 [\boldsymbol{N}]^T \{\boldsymbol{\delta}\}^T [\nabla' \boldsymbol{N}]\{\dot{\boldsymbol{u}}\}\, d\Theta - \int \beta_{22} [\boldsymbol{N}]^T [\boldsymbol{N}]\{\dot{\boldsymbol{p}}_{\boldsymbol{2}}\}\, d\Theta + \int \beta_{21} [\boldsymbol{N}]^T [\boldsymbol{N}]\{\dot{\boldsymbol{p}}_{\boldsymbol{2}}\}\, d\Theta + \int (\beta_2 - \varphi_2) C_s [\boldsymbol{N}]^T [\boldsymbol{N}]\{\dot{\boldsymbol{T}}_{\boldsymbol{s}}\} d\Theta - \int [\nabla \boldsymbol{N}]^T \frac{\boldsymbol{k}_2}{\mu_f} [\nabla \boldsymbol{N}]\{\boldsymbol{p}_{\boldsymbol{2}}\}\, d\Theta - \int [\nabla \boldsymbol{N}]^T \varphi_2 \Theta_2 [\nabla \boldsymbol{N}]\{\boldsymbol{T}_{\boldsymbol{2}}\} d\Theta + \int [\boldsymbol{N}]^T [\boldsymbol{N}]\, \gamma \{\boldsymbol{p}_{\boldsymbol{1}}\} d\Theta - \int [\boldsymbol{N}]^T [\boldsymbol{N}]\, \gamma \{\boldsymbol{p}_{\boldsymbol{2}}\} d\Theta = \int [\boldsymbol{N}]^T \{\mathbf{q}_{\mathbf{2}}\}\, d\Gamma \tag{5.16c}$$

$$-\int [\nabla \boldsymbol{N}]^T \varphi_s k_s [\nabla \boldsymbol{N}]\, \{\boldsymbol{T}_{\boldsymbol{s}}\} d\Theta - \int T_s \frac{C_s}{C_{fr}} [\boldsymbol{N}]^T \{\boldsymbol{\delta}\}^T [\nabla' \boldsymbol{N}]\{\dot{\boldsymbol{u}}\} d\Theta + \int T_s (\beta_1 - \varphi_1) C_s [\boldsymbol{N}]^T [\boldsymbol{N}]\{\dot{\boldsymbol{p}}_{\boldsymbol{1}}\} d\Theta + \int T_s (\beta_2 - \varphi_2) C_s [\boldsymbol{N}]^T [\boldsymbol{N}]\{\dot{\boldsymbol{p}}_{\boldsymbol{2}}\}\, d\Theta - \int \rho^s C_{ps} [\boldsymbol{N}]^T [\boldsymbol{N}]\{\dot{\boldsymbol{T}}_{\boldsymbol{s}}\} d\Theta = -\int [\boldsymbol{N}]^T \{\boldsymbol{r}_{\boldsymbol{s}}\} d\Gamma \tag{5.16d}$$

where $\{\dot{\boldsymbol{Traction}}\}$, $\{\boldsymbol{q_1}\}$, $\{\boldsymbol{q_2}\}$ and$\{\boldsymbol{r_s}\}$ vectors of the nodal traction force, pore and fissure water pressure influx and heat flux respectively and are defined as follows:

$$\{\dot{\boldsymbol{Traction}}\} = [\boldsymbol{Sep}(D)][\nabla' \boldsymbol{N}]\{\dot{\boldsymbol{u}}_{\boldsymbol{d}}\} - \beta_1\{\boldsymbol{\delta}\}[\boldsymbol{N}]\{\dot{\boldsymbol{p}}_{\boldsymbol{1}}\} - \beta_2\{\boldsymbol{\delta}\}[\boldsymbol{N}]\{\dot{\boldsymbol{p}}_{\boldsymbol{2}}\} - \frac{C_{Ts}}{C_f}\{\boldsymbol{\delta}\}[\boldsymbol{N}]\{\dot{\boldsymbol{T}}_{\boldsymbol{s}}\} \tag{5.17a}$$

$$\{\mathbf{q_1}\} = -\frac{\boldsymbol{k}_1}{\mu_f}[\nabla \boldsymbol{N}]\{\boldsymbol{p}_{\boldsymbol{1}}\} \tag{5.17b}$$

$$\{\mathbf{q_2}\} = -\frac{\boldsymbol{k}_2}{\mu_f}[\nabla \boldsymbol{N}]\{\boldsymbol{p}_{\boldsymbol{2}}\} \tag{5.17c}$$

$$\{\boldsymbol{r_s}\} = \varphi_s k_s[\nabla \boldsymbol{N}]\{\boldsymbol{T}_{\boldsymbol{s}}\} \tag{5.17d}$$

Equations (5.16) are implemented in MATLAB and presented in a contracted form as follows:

$$[\mathbf{K}]\{\dot{\boldsymbol{u}}_{\boldsymbol{d}}\} - \beta_1[\mathbf{C}]_{\boldsymbol{p}}\{\dot{\boldsymbol{p}}_{\boldsymbol{1}}\} - \beta_2[\mathbf{C}]_{p}\{\dot{\boldsymbol{p}}_{\boldsymbol{2}}\} - \frac{C_{TS}}{C_f}[\mathbf{C}]_{\boldsymbol{uT}}\{\dot{\boldsymbol{T}}_{\boldsymbol{s}}\} = \{\dot{\boldsymbol{W}}_{d}\} \tag{5.18a}$$

$$-\beta_1[\mathbf{C}]_{\boldsymbol{pT}}\{\dot{\boldsymbol{u}}\} - \beta_{11}[\mathbf{M}]\{\dot{\boldsymbol{p}}_{\boldsymbol{1}}\} + \beta_{12}[\mathbf{M}]\{\dot{\boldsymbol{p}}_{\boldsymbol{2}}\} + (\beta_1 - \varphi_1)C_s[\mathbf{M}]\{\dot{\boldsymbol{T}}_{\boldsymbol{s}}\} - [\mathbf{H}]_{1p}\{\boldsymbol{p}_{\boldsymbol{1}}\} - \gamma[\mathbf{M}]\{\dot{\boldsymbol{p}}_{\boldsymbol{1}} - \dot{\boldsymbol{p}}_{\boldsymbol{2}}\} = \{\dot{\boldsymbol{W}}_1\} \tag{5.18b}$$

$$-\beta_2[\mathbf{C}]_{\boldsymbol{pT}}\{\dot{\boldsymbol{u}}\} - \beta_{22}[\mathbf{M}]\{\dot{\boldsymbol{p}}_{\boldsymbol{2}}\} + \beta_{21}[\mathbf{M}]\{\dot{\boldsymbol{p}}_{\boldsymbol{1}}\} + C_s[\mathbf{M}]\{\dot{\boldsymbol{T}}_{\boldsymbol{s}}\} - [\mathbf{H}]_{2p}\{\boldsymbol{p}_{\boldsymbol{2}}\} - \gamma[\mathbf{M}]\{\dot{\boldsymbol{p}}_{\boldsymbol{2}} - \dot{\boldsymbol{p}}_{\boldsymbol{1}}\} = \{\dot{\boldsymbol{W}}_2\} \tag{5.18c}$$

$$-T_s\frac{C_s}{C_{fr}}[\mathbf{C}]_{\boldsymbol{Tu}}\{\dot{\boldsymbol{u}}\} + T_s(\beta_1 - \varphi_1)C_s[\mathbf{M}]\{\dot{\boldsymbol{p}}_{\boldsymbol{1}}\} + T_s(\beta_2 - \varphi_2)C_s[\mathbf{M}]\{\dot{\boldsymbol{p}}_{\boldsymbol{2}}\} - \rho^s C_{ps}[\mathbf{M}]\{\dot{\boldsymbol{T}}_{\boldsymbol{s}}\} - [\mathbf{H}]_{Ts}\{\boldsymbol{T}_{\boldsymbol{s}}\} = -\{\mathbf{R_s}\} \tag{5.18d}$$

The finite element matrices in equations are listed below:

$$[\mathbf{K}] = \int [\nabla' \boldsymbol{N}]^T [\boldsymbol{S^{ep}}(D,T)][\nabla' \boldsymbol{N}]\, d\Theta \tag{5.19a}$$

$$[\mathbf{C}]_{\boldsymbol{p}} = [\mathbf{C}]_{\boldsymbol{uT}} = \int [\nabla' \boldsymbol{N}]^T \{\boldsymbol{\delta}\} [\boldsymbol{N}] d\Theta \tag{5.19b}$$

$$[\mathbf{C}]_{\boldsymbol{pT}} = [\mathbf{C}]_{\boldsymbol{Tu}} = \int [\boldsymbol{N}]^T \{\boldsymbol{\delta}\}^T [\nabla' \boldsymbol{N}] \, d\Theta \tag{5.19c}$$

where the shape functions are as follows:

$$\mathrm{N} = [N^A \;\; N^B \;\; N^C \; N^D] \tag{5.20}$$

$[\nabla' \boldsymbol{N}]$ is the strain displacement matrix. For axisymmetric case, it can be expressed as follows:

$$[\nabla' \boldsymbol{N}] = \begin{bmatrix} \frac{\partial N^A}{\partial r} & 0 & \frac{\partial N^B}{\partial r} & 0 & \frac{\partial N^C}{\partial r} & 0 & \frac{\partial N^D}{\partial r} & 0 \\ 0 & \frac{\partial N^A}{\partial z} & 0 & \frac{\partial N^B}{\partial z} & 0 & \frac{\partial N^C}{\partial z} & 0 & \frac{\partial N^D}{\partial z} \\ \frac{N^A}{r} & 0 & \frac{N^B}{r} & 0 & \frac{N^C}{r} & 0 & \frac{N^D}{r} & 0 \\ \frac{\partial N^A}{\partial z} & \frac{\partial N^A}{\partial r} & \frac{\partial N^B}{\partial z} & \frac{\partial N^B}{\partial r} & \frac{\partial N^C}{\partial z} & \frac{\partial N^C}{\partial r} & \frac{\partial N^D}{\partial z} & \frac{\partial N^D}{\partial r} \end{bmatrix} \tag{5.21}$$

The matrices for hydraulic conductivity and heat conduction are:

$$[\mathbf{H}]_{1p} = \int [\nabla \boldsymbol{N}]^T \frac{\boldsymbol{k}_1}{\mu_f} [\nabla \boldsymbol{N}] \, d\Theta \tag{5.22a}$$

$$[\mathbf{H}]_{2p} = \int [\nabla \boldsymbol{N}]^T \frac{\boldsymbol{k}_2}{\mu_f} [\nabla \boldsymbol{N}] \, d\Theta \tag{5.22b}$$

$$[\mathbf{H}]_{Ts} = \int [\nabla \boldsymbol{N}]^T \varphi_s k_s [\nabla \boldsymbol{N}] \, d\Theta \tag{5.22c}$$

The mass matrix is:

$$[\mathbf{M}] = \int [\boldsymbol{N}]^T [\boldsymbol{N}] d\Theta \tag{5.23}$$

The matrices of the load vector corresponding to the nodal forces and fluxes are as follows:

$$\{\dot{\boldsymbol{W}}_d\} = \int [\boldsymbol{N}]^T \{\dot{\boldsymbol{F}}\}\, d\Theta + \int [\boldsymbol{N}]^T \{\dot{\boldsymbol{Traction}}\} d\Gamma \tag{5.24a}$$

$$\{\dot{\boldsymbol{W}}_1\} = \int [\boldsymbol{N}]^T \{\mathbf{q_1}\}\, d\Gamma \tag{5.24b}$$

$$\{\dot{\boldsymbol{W}}_2\} = \int [\boldsymbol{N}]^T \{\mathbf{q_2}\}\, d\Gamma \tag{5.24c}$$

$$\{\mathbf{R_s}\} = \int [\boldsymbol{N}]^T \{\boldsymbol{r_s}\} d\Gamma \tag{5.24d}$$

5.4 Temporal discretization

To determine the solution of the coupled problem in time, the rate form of the discretized equation needs to be integrated over time. Specifically, the integration of an arbitrary function y over the interval time Δt is taken as:

$$\int_t^{t+\Delta t} y(t)dt = [(1-\beta)y_t + \beta\, y_{t+\Delta t}]\Delta t = (y_t + \beta \Delta y)\Delta t$$
$$\Delta y = y_{t+\Delta t} - y_t \tag{5.25}$$

where y_t is the value of y at the time t, and β represents the type of approximation applied to the time integration. $\beta = 1$ is used for backward interpolation, $\beta = 0.5$ for central interpolation and $\beta = 0$ for forwarding interpolation.

Applying the spatially discretized function Equation (5.19), the Equations (5.12) will be rearranged as follows:

$$[\mathbf{K}]\{\boldsymbol{u_d}\}^{t+\Delta t} - \beta_1[\mathbf{C}]_{\boldsymbol{p}}\{\boldsymbol{p_1}\}^{t+\Delta t} - \beta_2[\mathbf{C}]_{\boldsymbol{p}}\{\boldsymbol{p_2}\}^{t+\Delta t} - \frac{C_{Ts}}{C_f}[\mathbf{C}]_{\boldsymbol{T}}\{\boldsymbol{T_s}\}^{t+\Delta t} = \{\boldsymbol{R_d}\}^{t+\Delta t} \tag{5.26a}$$

$$
\begin{aligned}
&-\beta_1[\mathbf{C}]_{\boldsymbol{pT}}\{\boldsymbol{u}\}^{t+\Delta t}-\ \beta_{11}[\mathbf{M}]\{\boldsymbol{p_1}\}^{t+\Delta t}+\beta_{12}[\mathbf{M}]\{\boldsymbol{p_2}\}^{t+\Delta t}\\
&\quad+(\beta_1-\varphi_1)C_s[\mathbf{M}]\{\boldsymbol{T_s}\}^{t+\Delta t}-\beta\Delta t[\mathbf{H}]_{1p}\{\boldsymbol{p_1}\}^{t+\Delta t}\\
&\quad+\beta\Delta t\gamma[\mathbf{M}][\{\boldsymbol{p_2}\}^{t+\Delta t}-\{\boldsymbol{p_1}\}^{t+\Delta t}]\\
&\quad=-\beta_1[\mathbf{C}]_{\mathbf{pT}}\{\boldsymbol{u}\}^{t}-\ \beta_{11}[\mathbf{M}]\{\boldsymbol{p_1}\}^{t}+\beta_{12}[\mathbf{M}]\{\boldsymbol{p_2}\}^{t}\\
&\quad+(\beta_1-\varphi_1)C_s[\mathbf{M}]\{\boldsymbol{T_s}\}^{t}+(1-\beta)\Delta t[\mathbf{H}]_{1p}\{\boldsymbol{p_1}\}^{t}-(1\\
&\quad-\beta)\Delta t\gamma[\mathbf{M}][\{\boldsymbol{p_2}\}^{t+\Delta t}-\{\boldsymbol{p_1}\}^{t+\Delta t}]+\beta\Delta t\{\boldsymbol{W_1}\}^{t+\Delta t}+(1\\
&\quad-\beta)\Delta t\{\boldsymbol{W_1}\}^{t}
\end{aligned}
\tag{5.26b}
$$

$$
\begin{aligned}
&-\beta_2[\mathbf{C}]_{\boldsymbol{pT}}\{\boldsymbol{u}\}^{t+\Delta t}-\ \beta_{22}[\mathbf{M}]\{\boldsymbol{p_2}\}^{t+\Delta t}+\beta_{21}[\mathbf{M}]\{\boldsymbol{p_1}\}^{t+\Delta t}\\
&\quad+(\beta_2-\varphi_2)C_s[\mathbf{M}]\{\boldsymbol{T_s}\}^{t+\Delta t}-\beta\Delta t[\mathbf{H}]_{2p}\{\boldsymbol{p_2}\}^{t+\Delta t}\\
&\quad+\beta\Delta t\gamma[\mathbf{M}][\{\boldsymbol{p_1}\}^{t+\Delta t}-\{\boldsymbol{p_2}\}^{t+\Delta t}]\\
&\quad=-\beta_2[\mathbf{C}]_{\boldsymbol{pT}}\{\boldsymbol{u}\}^{t}-\ \beta_{22}[\mathbf{M}]\{\boldsymbol{p_2}\}^{t}+\beta_{21}[\mathbf{M}]\{\boldsymbol{p_2}\}^{t}\\
&\quad+(\beta_2-\varphi_2)C_s[\mathbf{M}]\{\boldsymbol{T_s}\}^{t}+(1-\beta)\Delta t[\mathbf{H}]_{2p}\{\boldsymbol{p_2}\}^{t}-(1\\
&\quad-\beta)\Delta t[\{\boldsymbol{p_1}\}^{t+\Delta t}-\{\boldsymbol{p_2}\}^{t+\Delta t}]+\beta\Delta t\{\boldsymbol{W_2}\}^{t+\Delta t}+(1\\
&\quad-\beta)\Delta t\{\boldsymbol{W_2}\}^{t}
\end{aligned}
\tag{5.26c}
$$

$$
\begin{aligned}
&-T_s\frac{C_s}{C_{fr}}[\mathbf{C}]_{\mathbf{Tu}}\{\boldsymbol{u}\}^{t+\Delta t}+T_s(\beta_1-\varphi_1)C_s[\mathbf{M}]\{\boldsymbol{p_1}\}^{t+\Delta t}+T_s(\beta_2\\
&\quad-\varphi_2)C_s[\mathbf{M}]\{\boldsymbol{p_2}\}^{t+\Delta t}-\rho^sC_{ps}[\mathbf{M}]\{\boldsymbol{T_s}\}^{t+\Delta t}\\
&\quad-\beta\Delta t[\mathbf{H}]_{\mathrm{Ts}}\{\boldsymbol{T_s}\}^{t+\Delta t}\\
&\quad=-T_s\frac{C_s}{C_{fr}}[\mathbf{C}]_{\mathbf{Tu}}\{\boldsymbol{u}\}^{t}+T_s(\beta_1-\varphi_1)C_s[\mathbf{M}]\{\boldsymbol{p_1}\}^{t}+T_s(\beta_2\\
&\quad-\varphi_2)C_s[\mathbf{M}]\{\boldsymbol{p_2}\}^{t}-\rho^sC_{ps}[\mathbf{M}]\{\boldsymbol{T_s}\}^{t}+(1\\
&\quad-\beta)\Delta t[\mathbf{H}]_{\mathrm{Ts}}\{\boldsymbol{T_s}\}^{t}-\beta\Delta t\{\boldsymbol{R_s}\}^{t+\Delta t}-(1-\beta)\Delta t\{\boldsymbol{R_s}\}^{t}
\end{aligned}
\tag{5.26d}
$$

Equation (5.26) is now converted in a simpler form using incremental nodal values for each time step, and this is the final implemented matrix equation in MATLAB:

$$[\mathbf{K}]\{\Delta\boldsymbol{u}\} - \beta_1[\mathbf{C}]_{\boldsymbol{p}}\{\Delta\boldsymbol{p_1}\} - \beta_2[\mathbf{C}]_{\boldsymbol{p}}\{\Delta\boldsymbol{p_2}\} - \frac{C_{Ts}}{C_f}[\mathbf{C}]_{\boldsymbol{T}}\{\Delta\boldsymbol{T_s}\} = \{\Delta\boldsymbol{R_d}\} + \frac{2\dot{D}\{\boldsymbol{u^e}\}[\mathbf{K}]}{(1-D)} = \{\Delta\boldsymbol{R}\} \tag{5.27a}$$

$$\begin{aligned} -\beta_1[\mathbf{C}]_{\boldsymbol{pT}}\{\Delta\boldsymbol{u}\} + \Big(-\beta_{11}[\mathbf{M}] - \beta\Delta t\big([\mathbf{H}]_{1p} + \gamma[\mathbf{M}]\big)\Big)\{\Delta\boldsymbol{p_1}\} + (\beta_{12}[\mathbf{M}] \\ + \beta\Delta t\gamma[\mathbf{M}])\{\Delta\boldsymbol{p_2}\} + (\beta_1 - \varphi_1)C_s[\mathbf{M}]\{\Delta\boldsymbol{T_s}\} \\ = \Delta t([\mathbf{H}]_{1p} + \gamma[\mathbf{M}])\{\boldsymbol{p_1}\}^t - \gamma[\mathbf{M}])\{\boldsymbol{p_2}\}^t + \beta\Delta t\{\boldsymbol{W_1}\}^{t+\Delta t} \\ + (1-\beta)\Delta t\{\boldsymbol{W_1}\}^t \end{aligned} \tag{5.27b}$$

$$\begin{aligned} -\beta_2[\mathbf{C}]_{\boldsymbol{pT}}\{\Delta\boldsymbol{u}\} + \Big(-\beta_{22}[\mathbf{M}] - \beta\Delta t\big([\mathbf{H}]_{1p} + \gamma[\mathbf{M}]\big)\Big)\{\Delta\boldsymbol{p_2}\} \\ + (\beta_2 - \varphi_2)C_s[\mathbf{M}]\{\Delta\boldsymbol{T_s}\} + (\beta_{21}[\mathbf{M}] + \beta\Delta t\gamma[\mathbf{M}])\{\Delta\boldsymbol{p_1}\} \\ = \Delta t([\mathbf{H}]_{2p} + \gamma[\mathbf{M}])\{\boldsymbol{p_2}\}^t - \gamma[\mathbf{M}])\{\boldsymbol{p_1}\}^t + \beta\Delta t\{\boldsymbol{W_2}\}^{t+\Delta t} \\ + (1-\beta)\Delta t\{\boldsymbol{W_2}\}^t \end{aligned} \tag{5.27c}$$

$$\begin{aligned} -T_s\frac{C_s}{C_{fr}}[\mathbf{C}]_{\boldsymbol{Tu}}\{\Delta\boldsymbol{u}\} + T_s(\beta_1 - \varphi_1)C_s[\mathbf{M}]\{\Delta\boldsymbol{p_1}\} \\ + T_s(\beta_2 - \varphi_2)C_s[\mathbf{M}]\{\Delta\boldsymbol{p_2}\} - \rho^s C_{ps}[\mathbf{M}]\{\Delta\boldsymbol{T_s}\} \\ - \beta\Delta t[\mathbf{H}]_{Ts}\{\Delta\boldsymbol{T_s}\} \\ = \Delta t[\mathbf{H}]_{Ts}\{\boldsymbol{T_s}\}^t - \beta\Delta t\{\mathbf{R_s}\}^{t+\Delta t} - (1-\beta)\Delta t\{\mathbf{R_s}\}^t \end{aligned} \tag{5.27d}$$

5.5 Global solving method

The separated element equilibrium equations were implemented into a set of global functions to set up the finite element equations. The single element equations are strongly non-linear and can only be defined in a rate form. Consequently, the global governing finite element equations are as follows:

$$\big[\boldsymbol{K_{global}}\big]^{\boldsymbol{i}}\{\Delta\boldsymbol{U}\}^i{}_{global} = \big\{\Delta\boldsymbol{R_{global}}\big\}^i \tag{5.28}$$

where $\left[\boldsymbol{K_{global}}\right]^{\boldsymbol{i}}$ is the incremental global stiffness matrix, $\{\Delta \boldsymbol{U}\}^{i}{}_{global}$ are the vectors of the incremental nodal displacements, pore and fracture pressures and temperature effects, $\left\{\Delta \boldsymbol{R_{global}}\right\}^{i}$ are the vectors of the incremental forces, fluid fluxes and energy exchange. The total incremental number is defined as i.

According to Ma (2014b), as the constitutive behaviour is non-linear, the global stiffness matrix is not constant and depends on the current stress state, damage, strain level and temperature. Using incremental displacements to calculate incremental forces produces unbalanced forces, considered an error in numerical implementation.

The global solution procedures used to solve non-linear continuum problems can be separated into iterative and incremental schemes. The iterative schemes use unbalanced forces to estimate the displacement increments, and this process is repeated until the remaining forces are smaller than a prescribed error tolerance. Well-known iterative approaches are the Newton-Raphson, the modified Newton Raphson, and the initial stress methods (Chun, 2005). Some significant advantages of the iterative schemes are the high accuracy, automatic achievement of equilibrium and low influence of the increment size. However, a major disadvantage is often the unsuccessful calculation of the load path error that can be an obstacle to estimating strongly non-linear equations (Sloan et al., 2001; Habte, 2006).

Incremental schemes are the most straightforward approach for a non-linear finite element solution. The governing differential equations are being treated as a system of ordinary differential equations by using fragments of linear approximations for the non-linear constitutive behaviour. This approach assumes that $\left[\boldsymbol{K_{global}}\right]^{\boldsymbol{i}}$, the incremental global stiffness matrix, is constant over each increment and is computed by the present stress state at the inception of each increment. Despite the sensitivity to increment size and the trend of the solutions to drift from the yield surface, it is a robust approach for highly non-linear and complex constitutive equations (Potts and Gens, 1985; Sloan et al., 2001).

This research uses the incremental scheme for the global solution. As the elastoplastic damage equations are non-linear, an explicit integration scheme is adopted with automatic sub-stepping and error control algorithms to correct the drift errors to improve the accuracy and robustness.

After solving the equations, the primary nodal variables are obtained to calculate the internal variables such as the stresses, strains, plastic hardening parameters and damage variable, temperature change and the permeability evolution due to different stresses and temperature change.

The solution of the global governing equation indicates the displacement, fluid pressures and temperatures at the element nodes. The nodal displacements are then reformed to estimate the strains at each node. Afterwards, the stresses and damage variables are calculated using the elastoplastic damage constitutive law.

5.6 Modified Euler's Forward Scheme with Automatic Sub-stepping

In Euler's forward scheme, the applied load is split into several increments, and the constitutive equations are integrated precisely using the elastoplastic matrix obtained at the previous stress state. This procedure is the first-order algorithm.

Specifically, a time step $\Delta\check{t}$ is used to calculate from any current effective stress $\sigma'_{\check{t}}$ and current damage variable $D_{\check{t}}$ the same variables at the next incremental step. Those are calculated as follows:

$$\sigma'_{\check{t}+\Delta\check{t}} = \sigma'_{\check{t}} + \Delta\sigma' \tag{5.29}$$

$$D_{\check{t}+\Delta\check{t}} = D_{\check{t}} + \Delta D \tag{5.30}$$

$\Delta\sigma'$the increment of effective stress and ΔD is the cumulative damage and is calculated as follows, respectively:

$$\begin{aligned}\Delta\sigma' &= \left\{\Delta\varepsilon - \frac{C_{Ts}}{C_f}\boldsymbol{\delta}\dot{T} - \left(\frac{2\dot{D}}{(1-D)}\right)\left(\boldsymbol{\varepsilon}^{el} - \frac{C_{Ts}}{C_f}\boldsymbol{\delta}\Delta T\right)\right\}\left(\frac{\boldsymbol{S}^e(D,T)h}{h + \boldsymbol{x}\boldsymbol{n}^T\boldsymbol{S}^e(D,T)}\right) \\ &= \Delta\varepsilon_{dam,T}\boldsymbol{S}^{epl}(D,T)\end{aligned} \tag{5.31}$$

$$\Delta D = \dot{D}_D(\sigma'_{\check{t}+\Delta\check{t}} + \Delta\sigma', D) \tag{5.32}$$

The plastic hardening parameters are now computed:

The effective pressure at a current initial time step can be calculated based on Figure 3.9, section 3.5.4 of Chapter 3.

$$p'_{c,\check{t}} = \breve{p}'_{cin} exp\left(\frac{N_{fin} - N_{in}}{\lambda - \kappa_D}\right) \tag{5.33}$$

In the next time step, the hardening parameter and effect stress can be calculated as follows:

$$p'_{c,\check{t}+\Delta\check{t}} = p'_{c,\check{t}} exp\left(\frac{v_{in\check{t}+\Delta\check{t}}\Delta\varepsilon_p^p}{\lambda - \kappa_D}\right) \tag{5.34}$$

$$h_p = -\frac{\partial f}{\partial \breve{p}'_c}\frac{\partial g}{\partial p'}\left(\frac{\partial \breve{p}'_c}{\partial \varepsilon_v^p} + \frac{\partial \breve{p}'_c}{\partial D}\frac{\dot{D}}{\dot{\varepsilon}_v^p}\right) \tag{5.35}$$

The main disadvantages of this approach are that it demands a minimal increment size to achieve a robust result, and yield and damage conditions may not be kept at the end of each increment. The modified Euler's forward scheme gives a more accurate solution by using second-order terms and the automatic sub-stepping of the imposed strain increment by controlling the error in incremental computational stresses and plastic hardening variables.

The procedure followed in the project is the modified Euler's algorithm. If the strain increment is determined based on the current stress state, another set of stress increments and plastic hardening parameters can be obtained for the next step using Euler's forward scheme. Then all these variables are updated. Afterwards, the modified Euler scheme is applied to compute another set of these variables by using now the updated values. An error for the given step is then determined, which is the difference between the second-order Euler's modified approach and the first-order Euler's solution. A user tolerance is proposed, and if the error is more prominent, the strain increment is subdivided into smaller steps using an expression for the primary error term. Otherwise, the stress state and plastic hardening variables are updated based on the modified Euler scheme. The size of each sub increment will vary according to the non-linearity of the constitutive equations through the iteration process.

Sloan et al. (2001) presented the modified Euler scheme with automatic sub-stepping. They expanded Sloan's (1987) research to cover critical state models that exhibit non-linear elastic behaviour inside the yield surface. Sloan et al. (2001) proved that the modified Euler's scheme

could control the integration error to be less than the prescribed for a specific load path. According to Sloan et al. (2001) and Habte (2006), a pseudo time sub increment is introduced ($0 < \Delta\bar{t}_w < 1$).

$$\Delta\bar{t}_w = \frac{\bar{t}_{w+1} - \bar{t}_w}{\Delta t} \tag{5.36}$$

$\Delta\bar{t}_w$ is the size of the w^{th} sub increment and Δt is the total time increment in which the incremental strain $\Delta\varepsilon$ is acting. The superscripts $w+1$ and w denote the quantities at the pseudotimes. Using now the explicit Euler's method at the end of the pseudo time step $\Delta\bar{t}_w$, the stress and the hardening and damage parameters can be determined as:

$$\begin{cases} \sigma'_{w+1} = \sigma'_w + \dfrac{1}{2}(\Delta\sigma'_I + \Delta\sigma'_{II}) \\ \breve{p}'_{c(w+1)} = \breve{p}'_{cw} + \dfrac{1}{2}(\Delta\breve{p}'_{cI} + \Delta\breve{p}'_{cII}) \\ D_{w+1} = D_w + \dfrac{1}{2}(\Delta D_I + \Delta D_{II}) \end{cases} \tag{5.37}$$

The values with the superscripts *I* and *II* are calculated by the explicit first-order Euler's scheme for the different time steps. Precisely, the $\Delta\sigma'_I$ and $\Delta\breve{p}'_{cI}$ are calculated using the values of $S_I^{epl}(D,T)$,$\Delta\lambda_I$,h_I,n_I,x_I and ε_{vI}^p computed at the stress state $\Delta\sigma'_w$ and plastic hardening parameter $\breve{p}'_{cw}$. The incremental damage ΔD_I is computed at the stress state $\sigma'_w + \Delta\sigma'_I$ and damage condition D_w.

$$\begin{cases} \Delta\sigma'_I = S_I^{epl}(D,T)\Delta\varepsilon_{dam.w} = [S^{epl}(D,T)(\sigma'_w)]\Delta\varepsilon_{dam.w} \\ \Delta\breve{p}'_{cI} = \breve{p}'_{cw}\exp\left(\dfrac{v\Delta\varepsilon_{vI}^p}{\lambda_{Dw} - \kappa_{Dw}}\right) - \breve{p}'_{cw} \\ \Delta D_I = f_D(\sigma'_w + \Delta\sigma'_I, D_w) \end{cases} \tag{5.38}$$

$\Delta\sigma'_{II}$ and $\Delta\breve{p}'_{cII}$ are the values evaluated using the values of $S_{II}^{epl}(D,T)$,$\Delta\lambda_{II}$,h_{II},n_{II},x_{II} and ε_{v2}^p at stress state $\sigma'_w + \Delta\sigma'_I$ and plastic hardening parameter $\breve{p}'_{cw} + \Delta\breve{p}'_{cI}$. The incremental damage ΔD_{II} is computed at the stress state $\sigma'_w + \Delta\sigma'_I + \Delta\sigma'_{II}$ and damage condition $D_w + \Delta D_I$.

$$\begin{cases} \Delta\sigma'_{II} = S_{II}^{epl}(D,T)\Delta\varepsilon_{dam.w} = [S^{epl}(D,T)(\sigma'_w + \Delta\sigma'_I)]\Delta\varepsilon_{dam.w} \\ \Delta\breve{p}'_{cII} = (\breve{p}'_{cw} + \Delta\breve{p}'_{cI})\exp\left(\dfrac{v\Delta\varepsilon^p_{vII}}{\lambda_{(D_w+\Delta D_I)} - \kappa_{(D_w+\Delta D_I)}}\right) - (\breve{p}'_{cw} + \Delta\breve{p}'_{cI}) \\ \Delta D_{II} = f_D(\sigma'_w + \Delta\sigma'_I + \Delta\sigma'_{II}, D_w + \Delta D_I) \end{cases} \tag{5.39}$$

The plastic volumetrics strains are computed as follows:

$$\begin{cases} \varepsilon^p_{vI} = \Delta\lambda_I \times x_{pI} = \dfrac{\boldsymbol{n}_I^T[\boldsymbol{S}^e(D_w)]\Delta\varepsilon_{dam,w}(D_w)}{h_I + \boldsymbol{n}_I^T[\boldsymbol{S}^e(D_w)]\boldsymbol{x_I}} \times x_{pI} \\ \varepsilon^p_{vII} = \Delta\lambda_{II} \times x_{pII} = \dfrac{\boldsymbol{n}_{II}^T[\boldsymbol{S}^e(D_w + \Delta D_I)]\Delta\varepsilon_{dam}(D_w + \Delta D_I)}{h_{II} + \boldsymbol{n}_{II}^T[\boldsymbol{S}^e(D_w + \Delta D_I)]\boldsymbol{x_{II}}} \times x_{pII} \end{cases} \tag{5.40}$$

where λ_I and λ_{II} are the plastic multipliers at each current state.

The strain is now calculated:

$$\Delta\varepsilon_{dam.w} = \Delta\bar{t}_w\Delta\varepsilon - \frac{2\dot{D}}{1-D}(\varepsilon^e - \varepsilon^T) \tag{5.41}$$

The local truncation error for the first order Euler method is $O(\Delta\bar{t}^2)$ and for the modified Euler scheme is $O(\Delta\bar{t}^3)$. The local error for the calculated values of σ'_{w+1} and $\breve{p}'_{c(w+1)}$ is determined as the difference between the second order modified Euler and the first order Euler scheme. Specifically:

$$\begin{cases} E_w(\sigma'_{w+1}) = \dfrac{1}{2}(\Delta\sigma'_{II} + \Delta\sigma'_I) \\ E_w\left(\breve{p}'_{c(w+1)}\right) = \dfrac{1}{2}(\Delta\breve{p}'_{cII} + \Delta\breve{p}'_{cI}) \\ E_w(D_{w+1}) = \dfrac{1}{2}(\Delta D_{II} + \Delta D_I) \end{cases} \tag{5.42}$$

The relative error of the modified Euler solution is obtained using the following form:

$$R_w = max\left(\frac{\|E_w(\sigma'_{w+1})\|}{\|\sigma'_{w+1}\|}, \frac{\left|E_w\left(\breve{p}'_{c(w+1)}\right)\right|}{\breve{p}'_{c(w+1)}}, \frac{|E_w(D_{w+1})|}{D_{w+1}}\right) \tag{5.43}$$

According to Ma (2014b) and Sloan et al. (2001), the global accuracy of the solution can be upgraded by reducing the local error and using it to examine the size of the following sub-step,

$\Delta\bar{T}_{w+1}$. If the relative error R_w is less than the prescribed tolerance $STOL$, the current strain sub increment is accepted. Otherwise, the size of the sub step is reduced and the solution process is repeated (Sloan et al., 2001). The next sub-step size despite, if the sub increment is accepted or rejected, will obtained using the following relation:

$$\Delta\bar{t}_{w+1} = \tilde{g}\Delta\bar{t}_w \tag{5.44}$$

where $\tilde{g}$ is a positive number that is selected to ensure that:

$$R_{w+1} \leq STOL \tag{5.45}$$

As the local truncation error for the first-order Euler method is in the order of $0(\Delta\bar{T}^2)$, then the local error for the next increment would be:

$$R_{w+1} \cong \tilde{g}^2 R_w \tag{5.46}$$

Consequently, the positive number $\tilde{g}$ is obtained as follows:

$$\tilde{g} = \sqrt{\frac{STOL}{R_w}} \tag{5.47}$$

Sloan et al. (2001) mentioned that this procedure for determining $\tilde{g}$ may become inaccurate for strongly non-linear constitutive equations. Based on numerical experiments on various plasticity problems, Sloan et al. (2001) suggested a conservative method for calculating $\tilde{g}$ that can minimize the number of rejected strain sub increments. Factor 0.9 is applied to the positive number.

$$\tilde{g} = 0.9\sqrt{\frac{STOL}{R_w}} \tag{5.48}$$

The suggested limits to improve the accuracy of the integration scheme and satisfy the error tolerance are:

$$0.1 \leq \tilde{g} \leq 1.1 \tag{5.49}$$

and

$$0.1\Delta\bar{t}_w \leq \Delta\bar{t}_{w+1} \leq 1.1\Delta\bar{t}_w \tag{5.50}$$

Therefore, acceptable sub increments sizes are calculated using the limits above and the following expression:

$$\Delta\bar{t}_{w+1} = 0.9\sqrt{\frac{STOL}{R_w}}\Delta\bar{t}_w \tag{5.51}$$

The importance of the coefficient 0.9 is that it is a safety factor to prevent the chosen sub-increment step from not reaching the target local error tolerance (Sloan et al., 2001). Other numbers can also be used and achieve the same effects. Based on Habte (2006), an absolute minimum step size $\Delta\bar{t}_{min}$ is imposed, two constraints are applied to this computation scheme and at least two step sizes of the same increment after failed approach. According to Sloan et al. (2001), the two applied constraints are used to improve the scheme's robustness. The constitutive law consists of gradient singularities, and the two step sizes are necessary in cases where the stress-strain path has a shape change in the curvature.

Summarizing all the critical aspects of the modified Euler method with automatic sub stepping, the following procedures are presented:

1. The first step is to set $= I$, $T = 0, \Delta\bar{t}_I = 1, \sigma'_w = \sigma'_t$,$\breve{p}'_{cw} = \breve{p}'_{ct}$, $D_w = D_t$ and $\Delta\varepsilon_I = \Delta\varepsilon$. No sub increments are required for this case.
2. Tentative stress increments, damage variable and plastic hardening parameters are calculated using Equation (5.37). The local error is then estimated from Equation (5.43).
3. Suppose the calculated local error is greater than the specified tolerance. In that case, the proposed solution is rejected, and the process is repeated using now a smaller sub-step size until a successful sub increment is achieved. Once the local error satisfies the limitation step 2 is updated.
4. Ignoring the sub increment's acceptance or rejection, the following sub step is computed by Equation (5.51).
5. The integration scheme is fully achieved when the total imposed strain increment is applied. This is determined by $\sum \Delta\bar{t}_w = \bar{t} = 1$ and the solution procedure is described by $\sigma'_{t+\Delta T} = \sigma'_{w+1}$, $\breve{p}'_{c(t+\Delta T)} = \breve{p}'_{c(w+1)}$, where $w + 1$ is the last sub increment.

5.7 Correction of the yield surface drift

In the conventional plasticity theory, the yield surface drift is the condition that the computed stresses at the end of each sub increment may not satisfy the yield condition. This yield surface drift depends on the integration scheme and the non-linearity of the constitutive equations. The main reason for this difference is that although elastoplastic stiffness varies with the stress state, damage, and plastic hardening parameters, it is assumed to be constant. The amount of discrepancy from the yield surface depends on the non-linearity of the constitutive relation. Imposing a yield surface correction at the end of each increment is essential for the complex constitutive model as the effects on the accuracy of the computation scheme is highly influenced when the growth of the stress point alternation from the yield surface is increasing.

According to Potts and Gens (1985), yield surface drift schemes include correcting the current stresses by projecting them back along with the plastic flow, the total strain increment direction, additional effective stress, normal to the yield surface and the consistency condition. The first three approaches may lead to substantial errors, and the correction back to normal ignores the plastic hardening parameter change. Consequently, the consistency condition is used as it considers stress and plastic hardening variation based on Habte (2006).

The current stress state always lies on the loading surface, while the equivalent image point is assumed to be on the bounding surface. With increasing stress, the loading surface reformed, and the stress state is now on the new loading surface. The new image point on the bounding surface during this increment will be constrained by the basic assumption of the bounding surface theory, the plastic hardening parameter, and the damage variable. This means that the new image point may not be located on the new bounding surface after the strain sub-increment. Drift correction is necessary to project the image point back to the bounding surface. According to Habte (2006), this correction is necessary to guarantee that the image point will not lie outside the bounding surface and that the loading surface will not cross.

In Figure 5.2 the current stress state is denoted as σ_t' on the loading surface and $\breve{\sigma}_t'$ on the bounding surface and the corresponding effective pressures of the two surfaces are $p_{c,t}'$ and $\breve{p}_{c,t}'$, respectively.

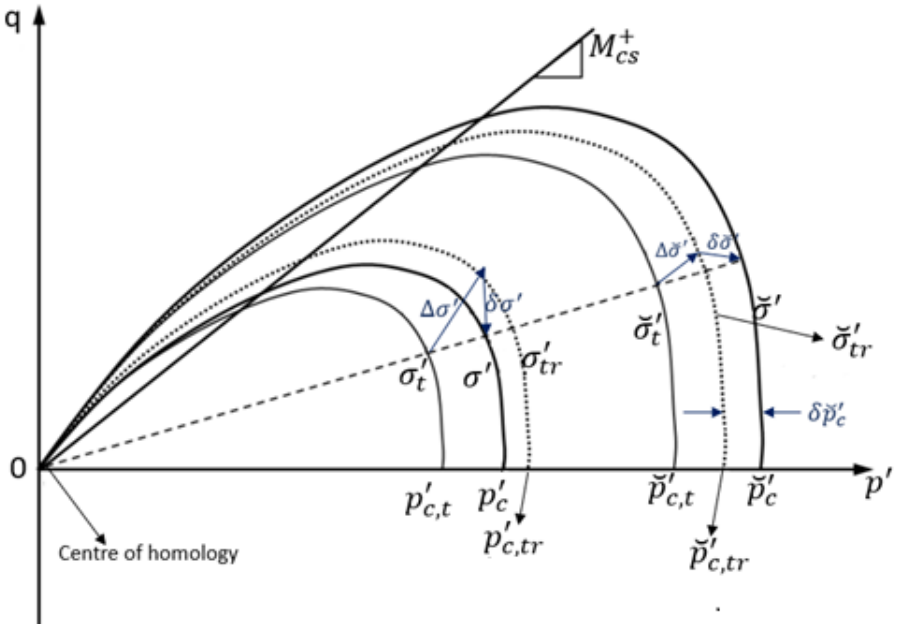

Figure 5. 2 Drift correction scheme for bounding surface plasticity (Habte, 2006)

A trial stress σ'_{tr} is computed at the end of a strain increment. The corresponding trial image point must satisfy the basic assumption of bounding surface theory and the consistency condition, $f = 0$, on the new bounding surface must be characterized by a trial hardening parameter $\breve{p}'_{c,tr}$. According to Habte (2006), the damage variable will be kept unchanged for simplicity. Even though the stress state and damage stress interact, the effect of the damage for a change in the stress and strain can be tackled by assuming that ΔD is approaching the consistency condition of the damage.

Using Equation (3.167) the relationship between the incremental trial stress and the incremental trial image stress is expressed as:

$$\frac{1}{h_b}\Delta\breve{\boldsymbol{\sigma}}' = \frac{1}{h}\Delta\boldsymbol{\sigma}' \tag{5.52}$$

The trial image point is calculated by:

$$\breve{\boldsymbol{\sigma}}'_{tr} = \breve{\boldsymbol{\sigma}}'_t + \Delta\breve{\boldsymbol{\sigma}}' = \breve{\boldsymbol{\sigma}}'_t + \frac{h_b}{h}\Delta\boldsymbol{\sigma}' \tag{5.53}$$

Drift correction may be applied when the trial image point $\breve{\sigma}'_{tr}$ is not satisfying the condition $f = 0$ at the corresponding bounding surface. The drift correction is expressed as:

$$\left|F\left(\breve{\boldsymbol{\sigma}}'_{tr}, \breve{p}'_{c,tr}\right)\right| \leq FTOL \tag{5.54}$$

Where $FTOL$ is the allowable tolerance on the yield condition. The drift correction aims to modify the computed stress $(\boldsymbol{\sigma}'_{tr})$ and the hardening parameter $\left(\breve{p}'_{c,tr}\right)$ to navigate the image point back to the bounding surface. The corrected image point must satisfy the condition on the bounding surface, which is expressed as:

$$\mathrm{F}\left(\breve{\boldsymbol{\sigma}}'_{tr} + \delta\breve{\boldsymbol{\sigma}}', \breve{p}'_{c,tr} + \delta\breve{p}'_{c}\right) = 0 \tag{5.55}$$

$\delta\breve{\boldsymbol{\sigma}}'$ and $\delta\breve{p}'_c$ are corrections to the image point stress and hardening parameter, respectively.

Ignoring second-order and above terms, using Taylor series expansion in Equation (5.55) a new equation can be created:

$$\begin{aligned}&\mathrm{F}\left(\breve{\boldsymbol{\sigma}}'_{tr} + \delta\breve{\boldsymbol{\sigma}}', \breve{p}'_{c,tr} + \delta\breve{p}'_{c}\right)\\ &\qquad = F\left(\breve{\boldsymbol{\sigma}}'_{tr}, \breve{p}'_{c,tr}\right) + \left(\frac{\partial F}{\partial \breve{\boldsymbol{\sigma}}'}\right)^{T} + \frac{\partial F}{\partial \breve{p}'_{c}}\left(\frac{\partial \breve{p}'_{c}}{\partial \varepsilon_v^p} + \frac{\partial \breve{p}'_{c}}{\partial D}\frac{\partial D}{\delta \varepsilon_v^p}\right)\delta\varepsilon_v^p = 0\end{aligned} \tag{5.56}$$

Based on Equation (3.167) and the basic assumption of the bounding surface, the corrections at the image point and stress point are expressed by:

$$\frac{1}{h_b}\delta\breve{\boldsymbol{\sigma}}' = \frac{1}{h}\delta\boldsymbol{\sigma}' \tag{5.57}$$

Assuming that there is no alternation in the strain increment during the correction process, the stress correction is connected to the elastic strain change. The thermal effects are also included in the elastic strain.

$$\delta\varepsilon^e = -\delta\varepsilon^p = [\boldsymbol{S}^e(D,T)]^{-1}\delta\boldsymbol{\sigma}' \tag{5.58}$$

The plastic strain increment correction is calculated as follows:

$$\delta\varepsilon^{p} = \delta\dot{\lambda}\boldsymbol{x} \tag{5.59}$$

where $\delta\dot{\lambda}$ is unknown scalar multiplier and $\boldsymbol{x}$ is the unit normal to the plastic potential at $\boldsymbol{\sigma}'_{tr}$.

According to Habte (2006) the correction for the plastic hardening parameter is determined as:

$$\delta\breve{p}'_{c} = \left(\frac{\partial\breve{p}'_{c}}{\partial\varepsilon_{v}^{p}} + \frac{\partial\breve{p}'_{c}}{\partial D}\frac{\partial D}{\delta\varepsilon_{v}^{p}}\right)\delta\varepsilon_{v}^{p} \tag{5.60}$$

where $\delta\varepsilon_{v}^{p}$ is the correction to the plastic volumetric strain which is expressed as:

$$\delta\varepsilon_{v}^{p} = \delta\dot{\lambda}\boldsymbol{x}_{p} \tag{5.61}$$

The correction to the plastic hardening parameter is:

$$\delta\breve{p}'_{c} = \left(\frac{\partial\breve{p}'_{c}}{\partial\varepsilon_{v}^{p}} + \frac{\partial D}{\delta\varepsilon_{v}^{p}}\right)\delta\dot{\lambda}\boldsymbol{x}_{p} \tag{5.62}$$

Substituting Equations (5.57) and (5.60) into Equation (5.56) yields:

$$\begin{aligned}\mathrm{F}\left(\breve{\boldsymbol{\sigma}}'_{tr} + \delta\breve{\boldsymbol{\sigma}}', \breve{p}'_{c,tr} + \delta\breve{p}'_{c}\right) &= F\left(\breve{\boldsymbol{\sigma}}'_{tr}, \breve{p}'_{c,tr}\right) - \delta\dot{\lambda}\left(\frac{h_b}{h}\right)\left(\frac{\partial F}{\partial\breve{\boldsymbol{\sigma}}'}\right)^{T}[\boldsymbol{S}^{e}(D,T)]\boldsymbol{x} \\ &+ \delta\dot{\lambda}\frac{\partial F}{\partial\breve{p}'_{c}}\left(\frac{\partial\breve{p}'_{c}}{\partial\varepsilon_{v}^{p}} + \frac{\partial\breve{p}'_{c}}{\partial D}\frac{\partial D}{\delta\varepsilon_{v}^{p}}\right)\boldsymbol{x}_{p} = 0\end{aligned} \tag{5.63}$$

Simplifying Equation (5.63) yields:

$$\mathrm{F}\left(\breve{\boldsymbol{\sigma}}'_{tr} + \delta\breve{\boldsymbol{\sigma}}', \breve{p}'_{c,tr} + \delta\breve{p}'_{c}\right) = \frac{F\left(\breve{\boldsymbol{\sigma}}'_{tr}, \breve{p}'_{c,tr}\right)}{\left\|\frac{\partial F}{\partial\breve{\boldsymbol{\sigma}}'}\right\|} - \delta\dot{\lambda}\left(\frac{h_b}{h}\right)\boldsymbol{n}^{T}[\boldsymbol{S}^{e}(D,T)]\boldsymbol{x} - \delta\lambda\dot{h}_{b} \tag{5.64}$$

The unknown plastic multiplier is:

$$\delta\dot{\lambda} = \frac{1}{h + \boldsymbol{n}^T[\boldsymbol{S}^e(D,T)]\boldsymbol{x}}\left(\frac{h_b}{h}\right)\frac{F\left(\breve{\boldsymbol{\sigma}}'_{tr}, \breve{p}'_{c,tr}\right)}{\left\|\frac{\partial F}{\partial \breve{\boldsymbol{\sigma}}'}\right\|} \tag{5.65}$$

The final updated stresses and plastic hardening parameters are calculated by:

$$\boldsymbol{\sigma}' = \boldsymbol{\sigma}'_{tr} + \delta\boldsymbol{\sigma}' \tag{5.66}$$

$$\breve{p}'_c = \breve{p}'_{c,tr} + \delta\breve{p}'_c \tag{5.67}$$

The above correction theory is applied repeatedly until the condition $\left|F\left(\breve{\boldsymbol{\sigma}}'_{tr}, \breve{p}'_{c,tr}\right)\right| \leq FTOL$ is reached.

According to Sloan et al. (2001), the above correction may result in a corrected stress further away from the yield surface. In these circumstances, Sloan et al. (2001) suggests replacing the one iteration with a correction scheme normal to the yield surface. In this scenario, keeping the plastic hardening parameter unchanged $\delta\breve{p}'_c = 0$ and applying the stress correction normal to the yield surface, the corrected stress can be expressed as:

$$\delta\boldsymbol{\sigma}' = -\delta\dot{\lambda}\boldsymbol{x} \tag{5.62}$$

The unknown plastic multiplier is now expressed as:

$$\delta\dot{\lambda} = \frac{1}{\boldsymbol{x}\boldsymbol{x}^T}\left(\frac{h_b}{h}\right)\frac{F\left(\breve{\boldsymbol{\sigma}}'_{tr}, \breve{p}'_{c,tr}\right)}{\left\|\frac{\partial F}{\partial \breve{\boldsymbol{\sigma}}'}\right\|} \tag{5.63}$$

The difference between the correction normal to the yield surface and the consistency correction scheme used before is that the first one keeps the hardening parameter unchanged $\breve{p}'_c = \breve{p}'_{c,tr}$ and only $\boldsymbol{\sigma}'$ is changing.

5.8 THM numerical validation using FEM

The above fully coupled THM model is implemented in MATLAB software and examples from literature are used to validate it. A unit thickness of the drawdown regime modelled by Ma and Zhao (2018), Kazemi (1969) and Gelet et al. (2012a) is considered and reproduced numerically in order to validate the constructed model.. A vertical wellbore of inner radius $r_w = 0.1\,m$ is considered, and a unit thickness of the wellbore is simulated, with the outer radius being set to 800 m to describe the boundary conditions at the far-field. Vertical deformation of the whole medium is assumed to be constrained. A vertical wellbore drilled in a thermo-elastoplastic fractured medium is considered with the active in-situ stresses presented in Figure 5.3a, while the boundary conditions are shown in Figure 5.3b. P_o is the initial pore and fissure pressure before drilling and T_{form} is the temperature of the formation before applying any pressure or thermal loading. The fully saturated formation is located at a depth of 1000m, and the subjected vertical gradients are presented in Figure 5.3b. An axisymmetric formulation is adopted, as the loading conditions display symmetry about the vertical axis. Distances of the horizontal grid points of the mesh (in m) from the centre of the wellbore are: [0.1, 0.101, 0.102, 0.105, 0.110, 0.115, 0.120, 0.125, 0.130, 0.140, 0.150, 0.20, 0.50, 1, 2, 5, 10, 20, 50, 100, 200, 500, 800].

Ignoring any damage effects the model was simplified to the elastic case in order to be validated against the numerical results of Gelet et al. (2012a), which are already validated against a single porosity case (McTigue, 1986). All the material moduli were set as an input, and they did not implement using critical state mechanics. The selected time for validation was t = 80s. An internal pressure P_i and temperature T_i is applied representing the constant mud pressure of Gelet et al (2012). The internal selected pressure is $P_i = 12$ MPa. The internal temperature was set equal to $T_i = +50℃,\ 0℃,\ -50℃$ to validate the case scenario of cooling or heating the fractured medium in the vicinity of the wellbore. The temperature of the formation was set to $T_{form} = 50℃$. The material parameters used for the validation are presented in Table 5.1. Figures 5.5, 5.7 and 5.9 represent the absolute values (a reminder that compression is negative, and tension is positive) and is validated against the Gelet's et al. (2012) outcomes.

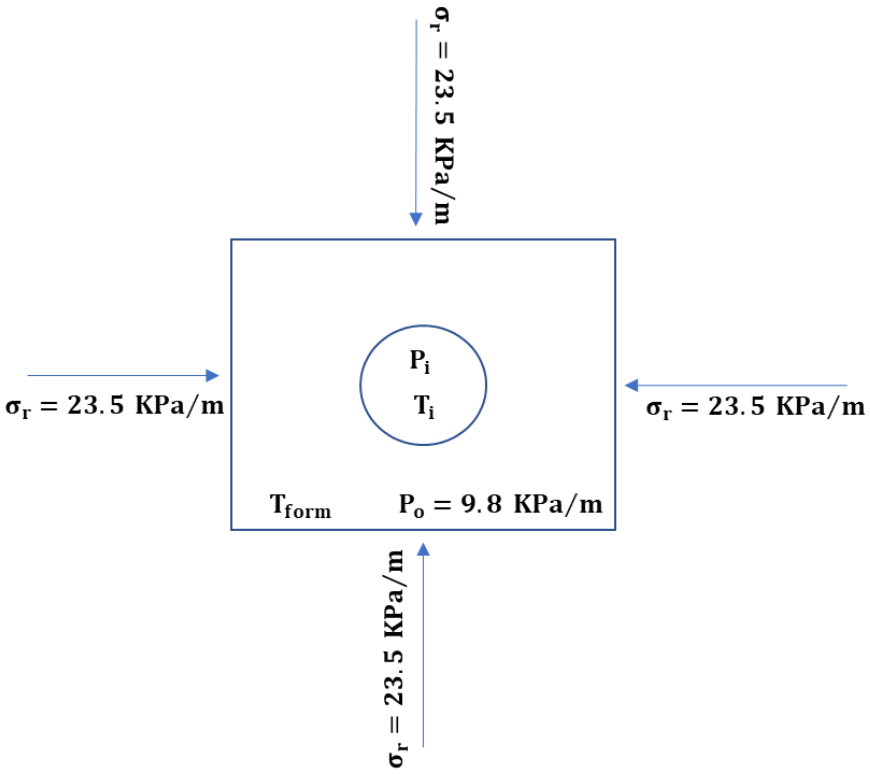

Figure 5.3a

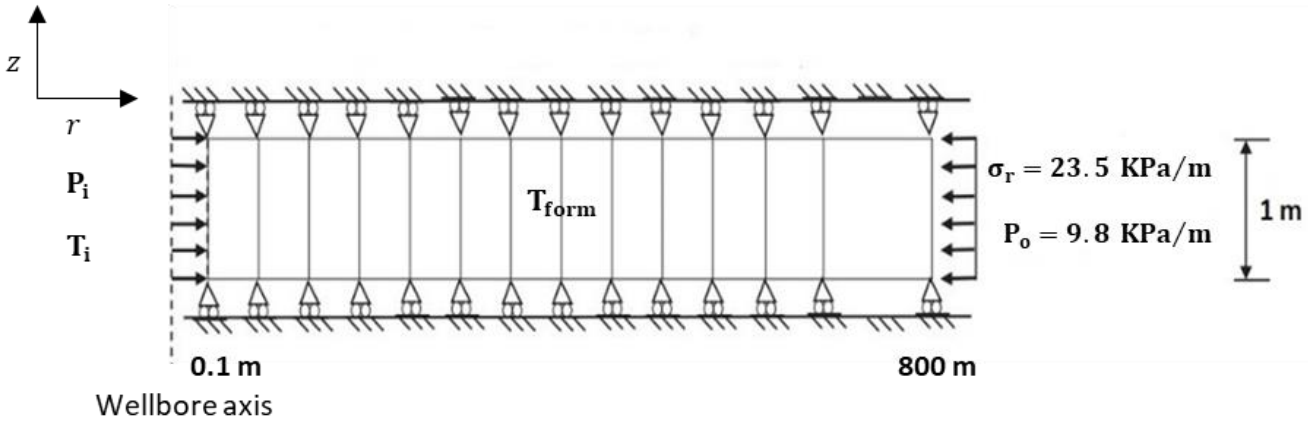

Figure 5.3b

Figure 5. 3 (a)Schematic illustration of the well-plan view, (b) Finite-element mesh and boundary conditions for axisymmetric problem (not to scale).

Table 5. 1 Material Parameters based on Gelet et al. (2012a) for the elastic problem.

Material Parameters (unit)	Value
Elastic modulus [E (GPa)]	9.5
Poisson's ratio [ν]	0.25
Storativity of the porous domain [β_{11} ($\mathrm{MPa^{-1}}$)]	7.23×10^{-09}
Storativity of fissure network [β_{22} ($\mathrm{MPa^{-1}}$)]	1.8×10^{-10}
Effective stress parameter [β_1]	0.27
Effective stress parameter [β_2]	0.1
Compressibility of the fluid [c_f ($\mathrm{MPa^{-1}}$)]	1.45×10^{-9}
Fluid viscosity [μ (MPa)]	10^{-9}
Porosity of porous domain (φ_1)	0.15
Porosity of fissure network (φ_2)	0.015
Permeability of porous block [k_1 ($\mathrm{m^2}$)]	5×10^{-20}
Permeability of fissure network [k_2 ($\mathrm{m^2}$)]	5×10^{-19}
Leakage parameter [γ ($1/\mathrm{P_a s}$)]	5.3×10^{-10}
Heat capacity of the porous domain [C_{ps} (J/kg℃)]	837
Thermal conductivity of the material [k_s (W/m℃)]	2.65
Volumetric thermal expansion coefficient of the porous domain [C_{Ts} (1/℃)]	1.8×10^{-5}
Volumetric thermal expansion coefficient of the fluid [C_{Tw} (1/℃)]	4.5×10^{-4}

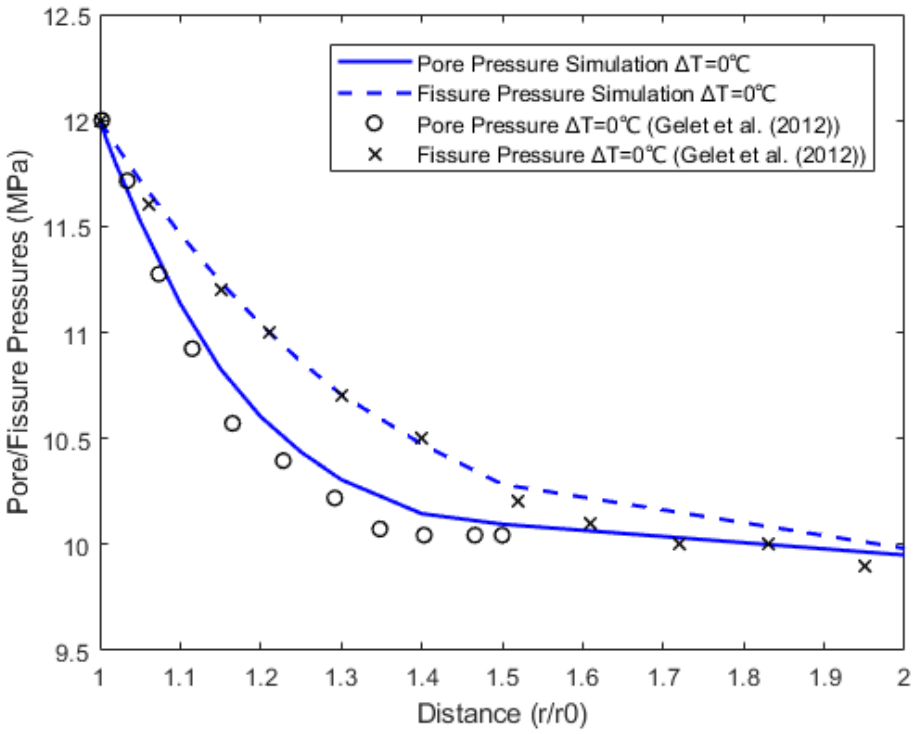

Figure 5. 4 Validation of pore and fissure pressure, at time 80 sec for 0 ℃ temperature change (Gelet et al., 2012a)

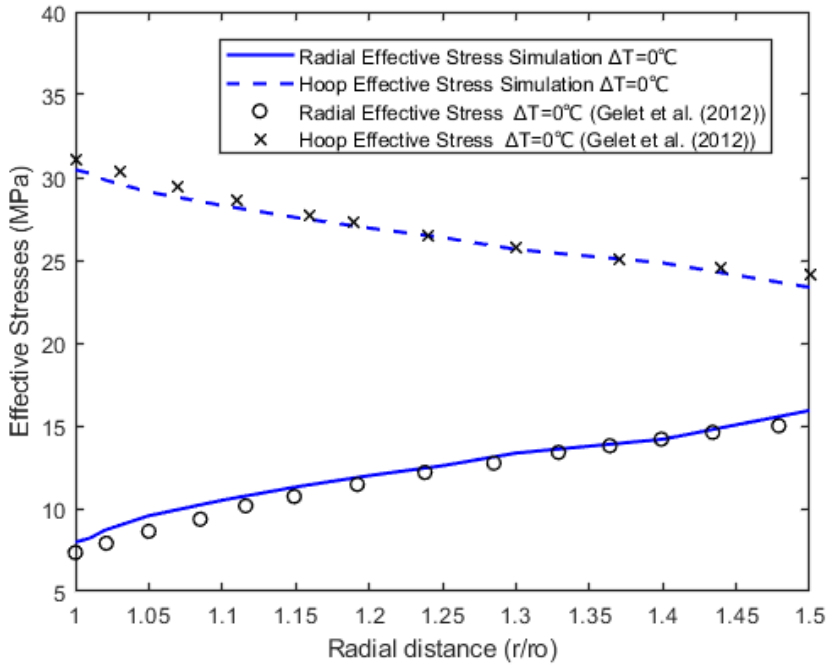

Figure 5. 5 Validation of the compressive Radial and Hoop effective stress, at time 80 sec for 0 ℃ temperature change (Gelet et al., 2012a)-absolute value presented

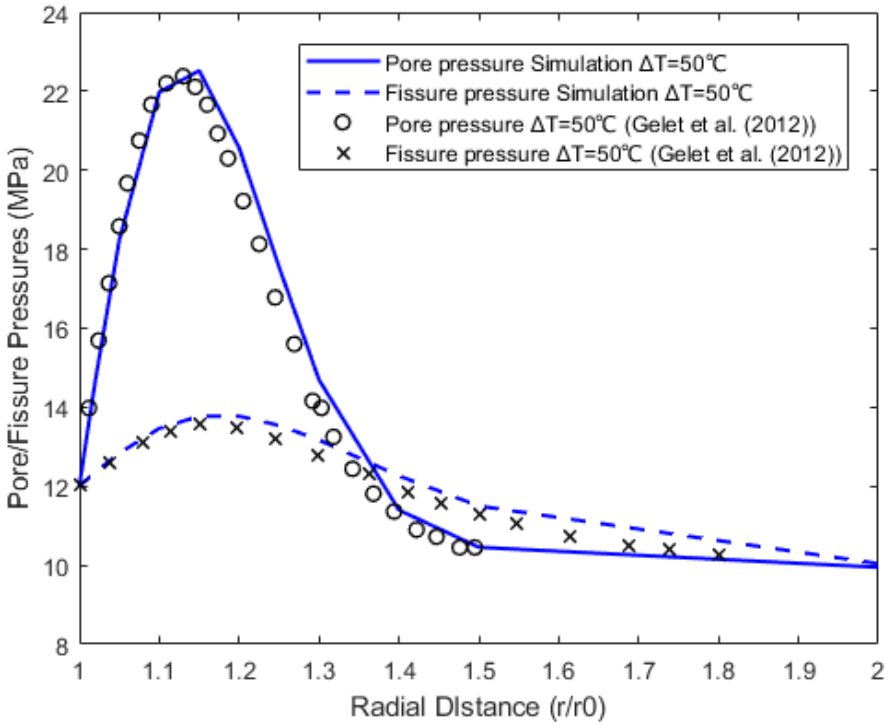

Figure 5. 6 Validation of pore and fissure pressure, at time 80 sec for +50 ℃ temperature change (Gelet et al., 2012a)

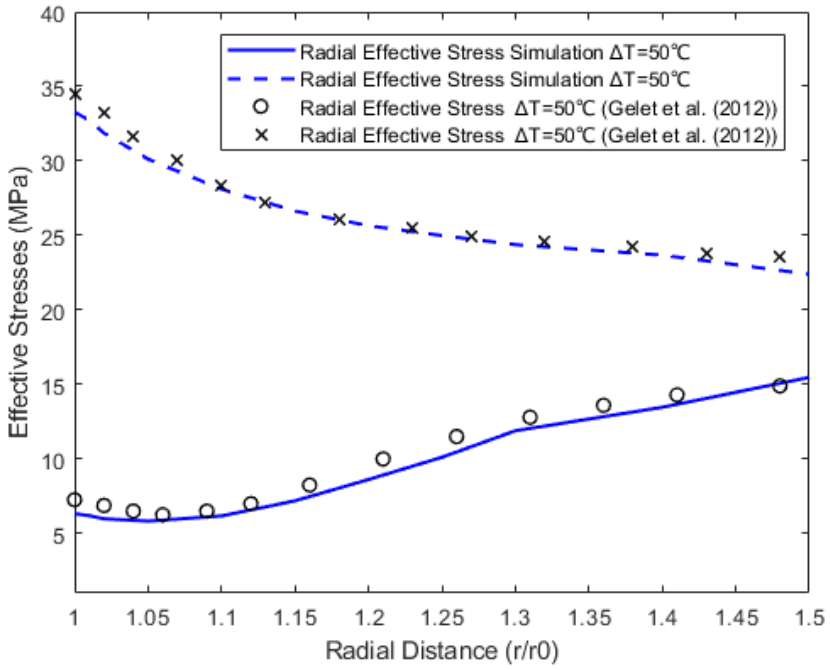

Figure 5. 7 Validation of the compressive Radial and Hoop effective stress, at time 80 sec for +50 ℃ temperature change (Gelet et al., 2012a)-absolute value presented

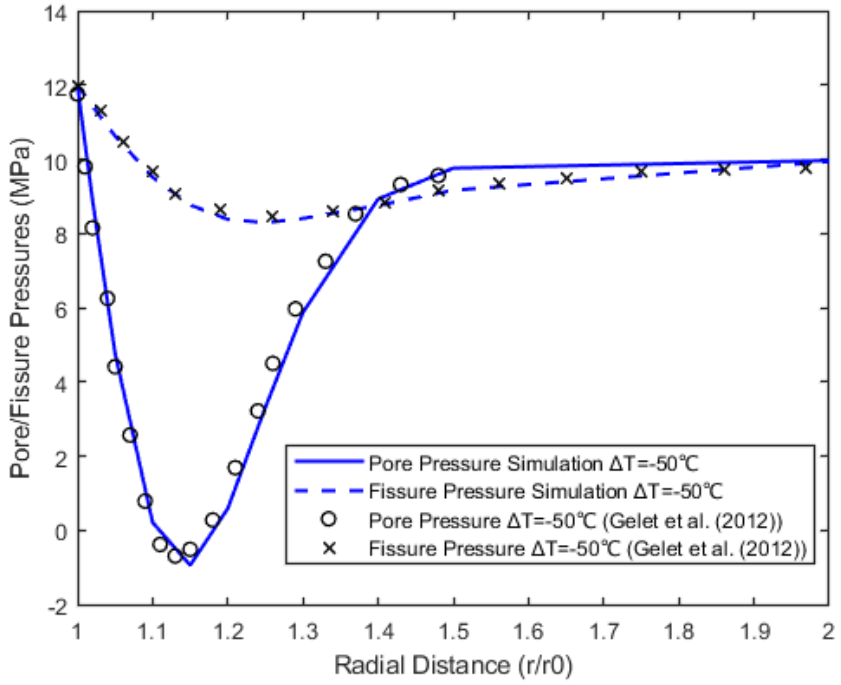

Figure 5. 8 Validation of pore and fissure pressure, at time 80 sec for -50 ℃ temperature change (Gelet et al., 2012a)

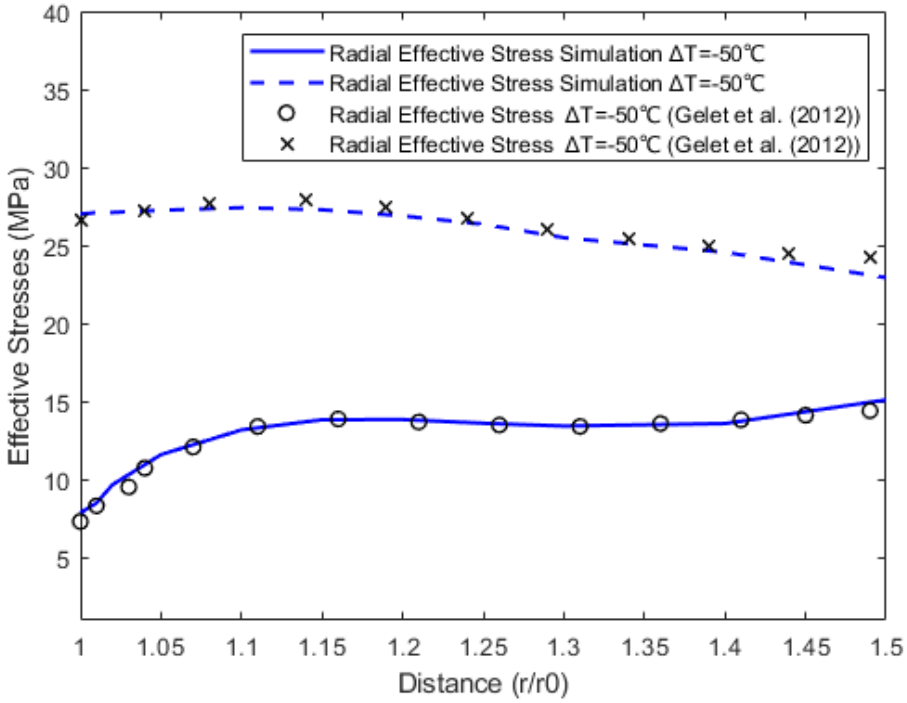

Figure 5. 9 Validation of the compressive Radial and Hoop effective stress, at 80 sec for -50 ℃ temperature change (Gelet et al., 2012a)-absolute value presented.

Based on Gelet's et al. (2012) research, the initial point of the radial stress is not influenced by changing the temperature while the hoop stress changes significantly. For this reason and adopting this assumption, the thermal expansion influence due to cooling or heating was applied only to the hoop stress as a boundary condition. Afterwards, solving the differential equations presented in Equation (5.27), using FEM in MATLAB, the influence on the non-linear behaviour due to temperature fluctuation to the effective stresses is presented. Figures 5.4 to 5.9 show that the model agrees with the results of Gelet et al. (2012a) and reasonably captures the behaviour of the rock in the vicinity of the wellbore. The model seems to remarkably agree with both the formation pressure and the effective stresses.

Plastic damage can influence the results of pore and fissure pressure, especially for less strong sandstone (Ma and Zhao, 2018). The damage evolution law presented in Chapter 3 and Section 3.4.3 is implemented inside the already validated model and further validated against the work of Ma and Zhao (2018), in which thermal effects are ignored and critical state mechanics are considered. The wellbore's internal pressure was set as 0, indicating a post-drilling scenario. The exact boundary conditions and mesh are shown in Figure 5.3. Based on Ma (2014b) and Kazemi (1969), the initial stress state for material with elastic modulus $E = 10$ GPa is $p_c' = 35.3$ MPa and $\breve{p}_c' = 63$ MPa. The material properties and critical state mechanics parameters based on Ma and Zhao (2018) are listed in Table 5.2 below:

Table 5. 2 Material parameters for the damage validation (Ma and Zhao, 2018)

Material Parameters (unit)	Value
Elastic modulus [E (GPa)]	10, 20, 100
Poisson's ratio [ν]	0.25
Storativity of the porous domain [β_{11} (MPa^{-1})]	7.23×10^{-09}
Storativity of fissure network [β_{22} (MPa^{-1})]	1.8×10^{-10}
Matrix coupling factor [$\beta_{12}=\beta_{21}$ (MPa^{-1})]	0
Effective stress parameter [β_1]	-0.99
Effective stress parameter [β_2]	-0.01
Compressibility of the fluid [c_f (MPa^{-1})]	1.45×10^{-9}
Fluid viscosity [μ (MPa)]	10^{-9}
Porosity of porous domain (φ_1)	0.04985
Porosity of fissure network (φ_2)	0.001243
Permeability of porous block [k_1 (m^2)]	5×10^{-20}
Permeability of fissure network [k_2 (m^2)]	5×10^{-19}
Leakage parameter [γ (1/P$_a$s)]	5.3×10^{-10}
Gradient of isotropic compression line (ICL) [λ]	0.1
Slope of the unloading- reloading line (URL) [κ]	0.031
Parameter controlling the shape of the bounding surface [M]	1.9
Material constant of the bounding surface [R]	2.45
Slope of the Critical State Line (CSL) [M_{cs}]	1.7
Hardening material constant [k_d]	1

The damage evolution law was adopted based on the principal tensile stress and Section 3.4.3.2. The damage variables used are presented as follows:

Table 5. 3 Damage material parameters

k_m	Y_{D0}	m_D	m	h_γ
0.45	0.001	0.0025	10	0.00015

According to Ma and Zhao (2018), different notation was used to the deformation model described by the Equation (5.27a). Consequently, the effective stress parameters were given the values $a1 = -0.99$ and $a2 = -0.01$, based on Johnson and Cleary (1991), to reproduce the results. The influence of the damage for a particular time step (t = 80s) is presented in Figure 5.10. The presented model captures the damaging effect of the general behaviour in the pore/fissure space. In Figure 5.11, the evolution of damage in time is also reproduced versus the radial distance, and the results fit satisfactory the outcome of Ma and Zhao (2018).

Finally, validating the thermal influence separately and the damage evolution, considering plasticity effects and the critical state concept, the model seems robust and accurately reproduces different scenarios. In Chapter 6, all of them are coupled together, different case scenarios are examined, and parametric studies are established.

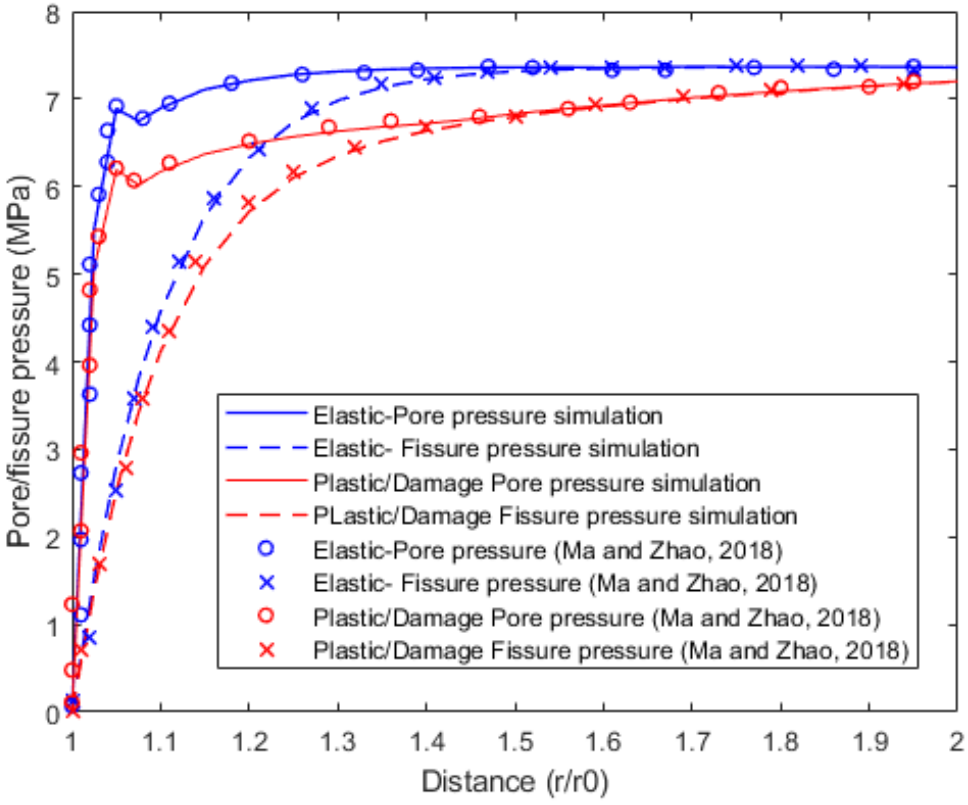

Figure 5. 10 Pore-Fissure pressure diagram with and without damage for a drilled borehole, validation for a material with E=10 GPa.

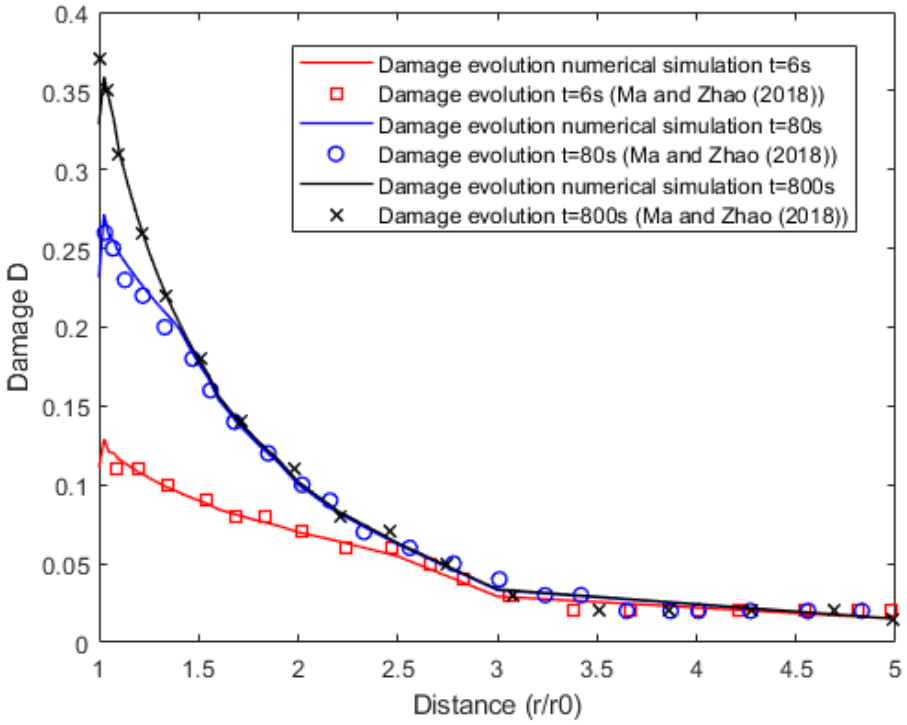

Figure 5. 11 Validation of damage evolution in different time steps for E=10 GPa (Ma and Zhao, 2018)

5.9 Bounding surface numerical validation and fitting parameter estimation

To reproduce the UCS and triaxial tests presented in Chapter 4 and estimate the critical state mechanic parameters, based on curve fitting to the experimental data, FEM was used again. The drift yield correction was also adopted. The model now, was created using an axially symmetric mesh. The mesh consisted of 64 four-node quadrilateral elements with 2 by 2 integration points. The quadrilateral elements were used, as according to Wirasaet et al. (2010), there are efficient and give robust results. One-half of the sample was analysed, and the boundary conditions are presented in Figure 5.12. The modified Euler with automatic sub-stepping was adopted as an integration procedure (discussed in Section 5.8) as the behaviour of rock due to elastoplastic considerations is significantly non-linear in both the deviatoric stress-axial strain and volumetric strain-axial strain spaces. Based on Ma (2014b), for strain increments smaller than 10^{-4}, the numbers of steps are sufficient to give a representative solution. Consequently, to reduce the computational time, the axial strain rate was set as 10^{-4}.

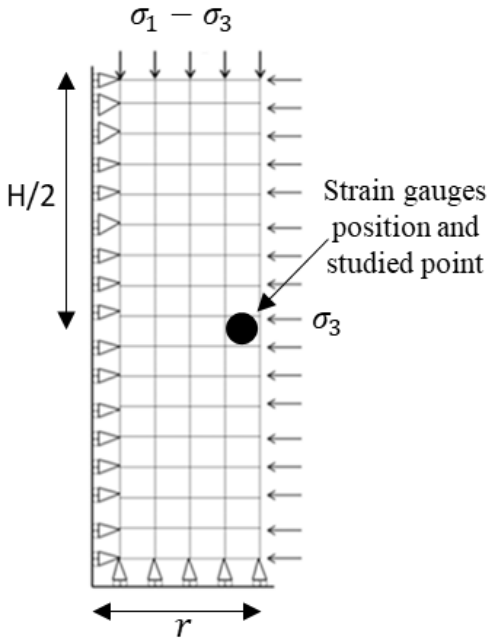

Figure 5. 12 The finite element mesh and boundary condition for the UCS and triaxial test simulation.

Using the experimental outcomes of Chapter 4 on Stainton Sandstone, Poisson's ratio could take different values according to the selected area and estimated Young's modulus (secant or tangent). Secant Poisson's ratio was used to reproduce the UCS tests (as mentioned in Chapter 4) due to the restriction of the high tangent value of Poisson's ratio, over the 0.5 limit, that could result in negative bulk modulus. To be consistent, the secant values of Poisson's ratio were used also for the triaxial tests. One interesting outcome is that the secant Poisson's ratio (from the beginning of the test to the 50% of the UCS test) can reproduce the results satisfactorily. At the start of the test, the slope of the deviatoric stress-axial strain curve is different and sharper, which indicates smaller Young's modulus at the beginning. Afterwards, Young's modulus is increasing as the material is tested. The Poisson's ratio is assumed to be constant for each temperature condition and expressed by the secant functions presented in Figure 4.22. Young's modulus can be captured by the critical state parameter equation as in Equation (5.6).

The peak height of the volumetric strain-axial strain plot is controlled by the slope of the unloading-reloading line κ, which also monitors the steepness of the slope of the deviatoric-axial strain curve in combination with the Poisson's ratio ν. Using the initial values of κ proposed in the research of Ma (2014b), a parametric study took place and the slope value was estimated for each test.

The hardening parameter m_p influences the numerical simulation for the strain conditions and deviatoric stress after the middle of the test. An increase in the m_p concludes with steeper volumetric-axial strain curves. It increases the deviatoric stress that the rock is exhibiting for the same axial strain, as seen in Figure 5.13.

The critical state line's slope M_{cs} numerically controls the maximum deviatoric stress, as seen in Figure 5.13. The M_{cs} was estimated in Chapter 4. Damage evolution parameters and initial damage are assumed to be constant in all the tests with $D_{initial} = 0.015$. The constitutive parameters used are presented in Table 5.4 to 5.6. The damage parameters are presented in Table 5.7. The void ratio was estimated based on the experimental tests as $e_0 = 0.38$.

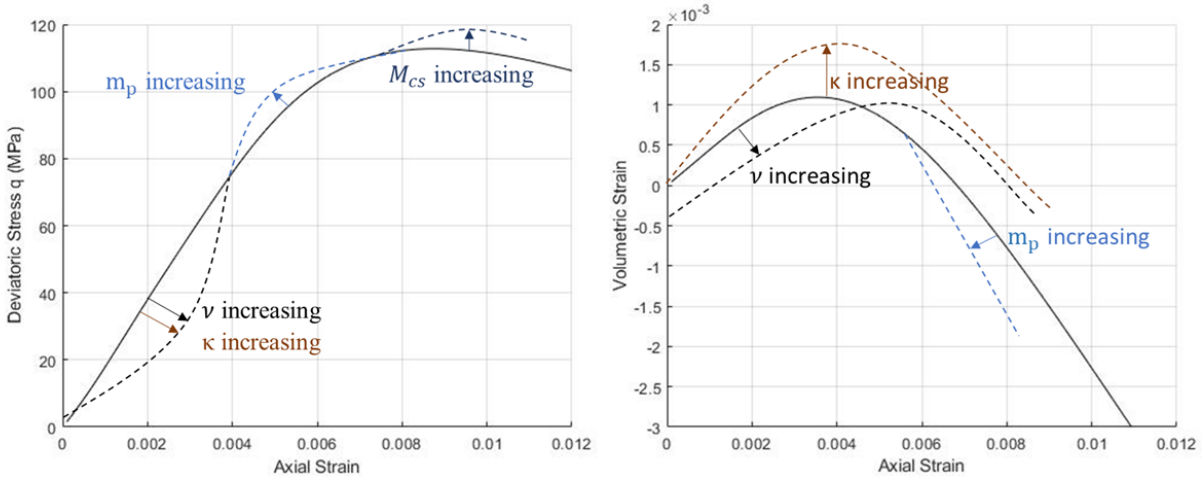

Figure 5. 13 Example of how the parameters is influencing the curves

Table 5. 4 Parameter values for UCS

	ν_{sec}	λ	κ	M_{cs}	m_p	k_d
15℃	0.26	0.1	0.00035	1.55	3	7
-5℃	0.15	0.1	0.00041	1.66	4	7
-10℃	0.17	0.1	0.00031	1.70	3	7

Table 5. 5. Parameter values for 12.5 MPa

	ν_{sec}	λ	κ	M_{cs}	m_p	k_d
15℃	0.26	0.1	0.00125	1.55	5	37
-5℃	0.15	0.1	0.00299	1.66	12	37
-10℃	0.17	0.1	0.00211	1.70	7	30

Table 5. 6 Parameter Values for 24 MPa.

	ν_{sec}	λ	κ	M_{cs}	m_p	k_d
15℃	0.18	0.1	0.00300	1.55	9	37
-5℃	0.16	0.1	0.00310	1.66	13	37
-10℃	0.16	0.1	0.00330	1.70	16	35

Table 5. 7 Damage parameters based on Ma (2014)

k_m	Y_{D0}	x_D	m	h_γ
0.0005	0.001	0.0025	10	0.0033

In Figures 5.14-5.19 the FEM numerical reproduction of the UCS experimental results is presented. The deviatoric-axial strain and volumetric-axial strain behaviour of rock is compared to the experimental data. However, as UCS is not designed for soils, expanding that critical state mechanics and bounding surface theory of Khalili's (2008) to rock material, is quite difficult to regenerate numerically the UCS experiments. For numerical purposes and as the confining pressure cannot be zero, for the UCS test 0.1 MPa confining pressure was assumed. This, however, is an obstacle in reproducing correctly the UCS tests, as the simulated samples is considered to be vertically constrained. Additionally, even at the experimental outcomes of UCS the results differ significantly, as the grain realignment of the particles of Sandstone may activate micro-fractures and induce different failure behaviour. The assumption of λ being 0.1, as in the triaxial tests and that the yield surface is of the same shape maybe another obstacle in perfectly reproducing the unconfined behaviour.

Figure 5.20 to 5.25 presents the numerical triaxial test simulation for the case of 12.5 MPa confining pressure and the three different temperatures. For the case of -10℃, only two experiments are presented, as in the third test, the strain gauges failed. Figure 5.26 to 5.31 present the numerical triaxial tests simulation compared to the experimental data for the 24 MPa confining pressure at three different conditions.

In all the experimental tests, the volumetric strain-axial strain graph varies significantly from sample to sample, indicating that each one may have slightly different behaviour in the transverse direction, even though they come from the same block. A robust representation of the experimental results for triaxial conditions can be seen in the deviatoric stress-axial strain curve. In contrast,

there is a good agreement for the volumetric strain-axial strain curve until reaching almost 6% axial strain. This is predominantly due to Poisson's ratio increases since the model cannot accept values of Poisson's ratio bigger than 0.5.

For the 12.5 MPa triaxial tests, the experimental increase in the deviatoric stress, the decrease of the Poisson's ratio (both Secant and Tangent) and the increase in the critical state line's slope, moving from 15℃ to -5℃, indicate an increase in κ by almost 9%. On the other hand, the slope of the unloading-reloading line increases 10% going from the -5℃ case to the -10℃ case. This can be explained as while the damage is increasing, the slope of the unloading-reloading line is becoming steeper (Zhang et al., 1990a; Zhang et al., 1990b).

For the 24 MPa confining pressure, in contrast to the 12.5 MPa conditions, the Poisson's ratio is not changing significantly for different temperature conditions and the M_{cs} is slightly influenced. However, cooling at higher confinement increases the hardening parameter. The Poisson's ratio remains the same, which means that the lateral-vertical strain ratio remains constant, more deviatoric stress for the same strain rate is achieved by the rock, and that material parameter k_d illustrates this.

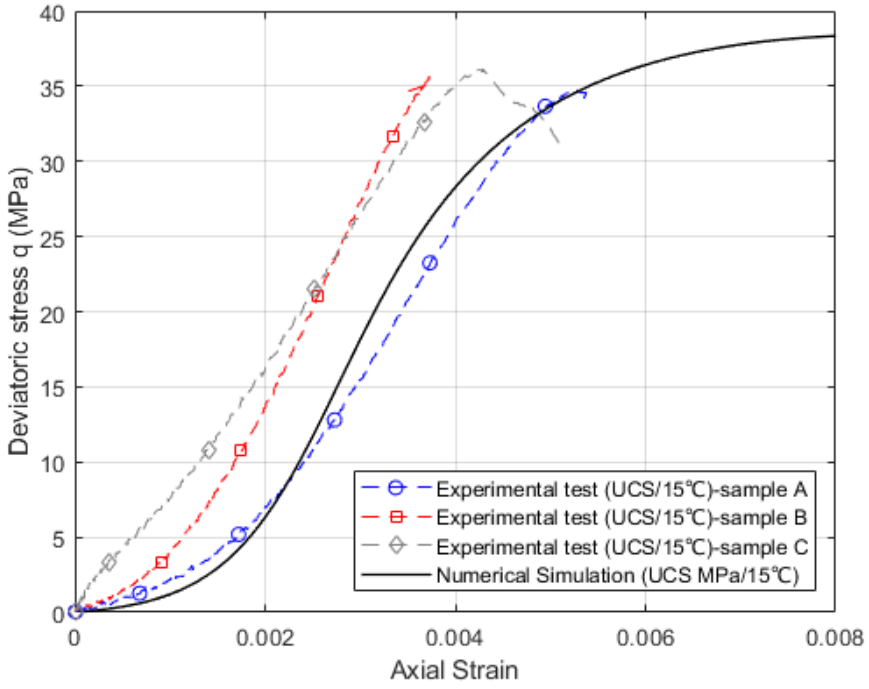

Figure 5. 14 Deviatoric stress-axial strain relationship for UCS test at 15℃. (Experimental tests and Numerical simulation)

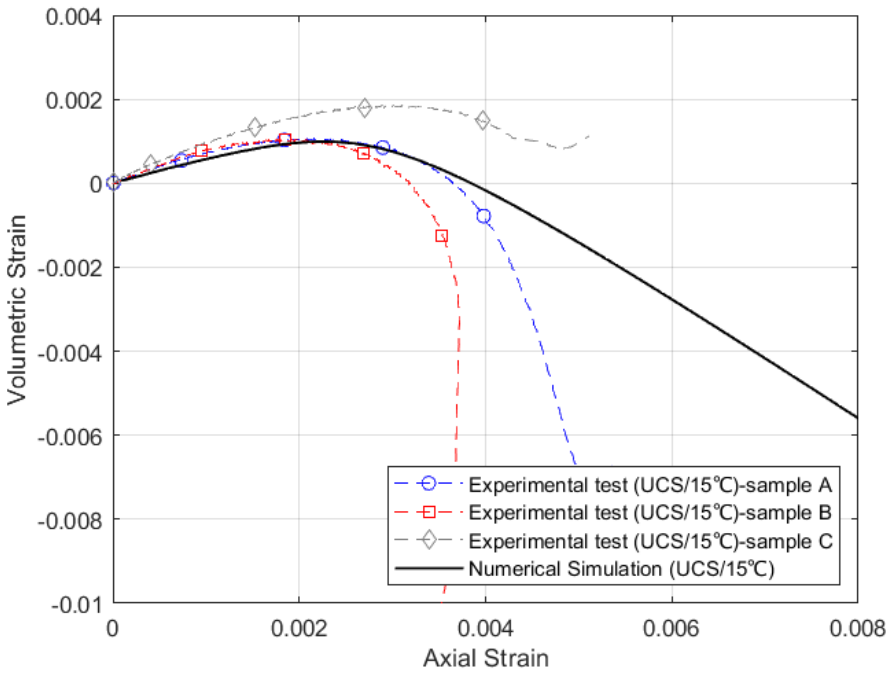

Figure 5. 15 Volumetric strain-axial strain relationship for UCS test at 15°C. (Experimental tests and Numerical simulation)

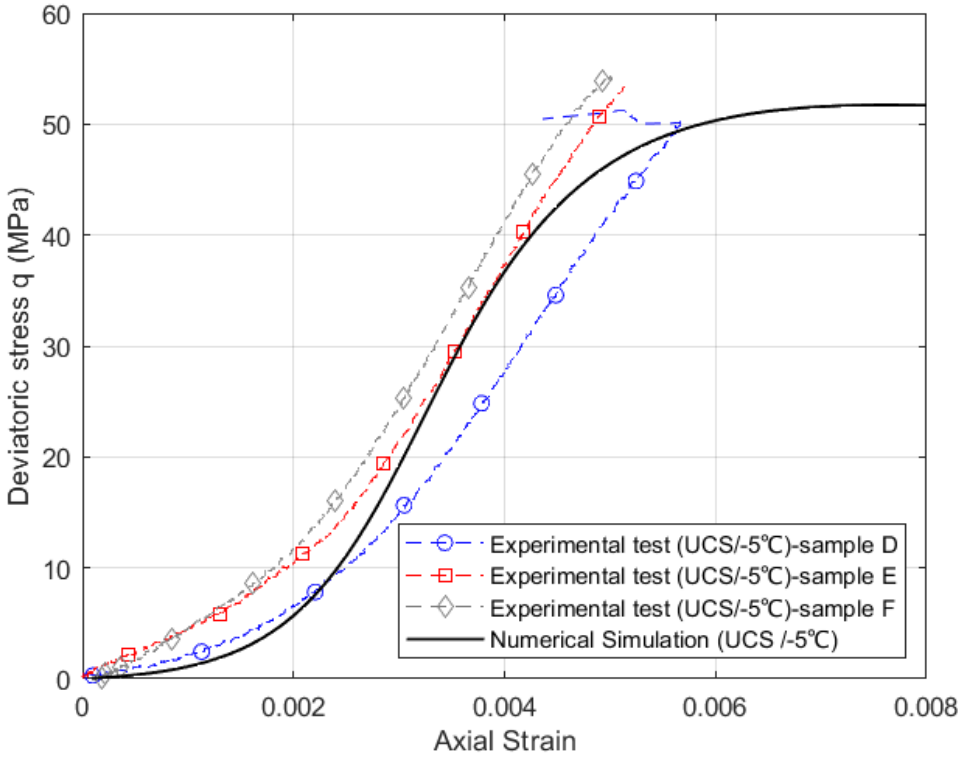

Figure 5. 16 Deviatoric stress-axial strain relationship for UCS test at -5°C. (Experimental tests and Numerical simulation)

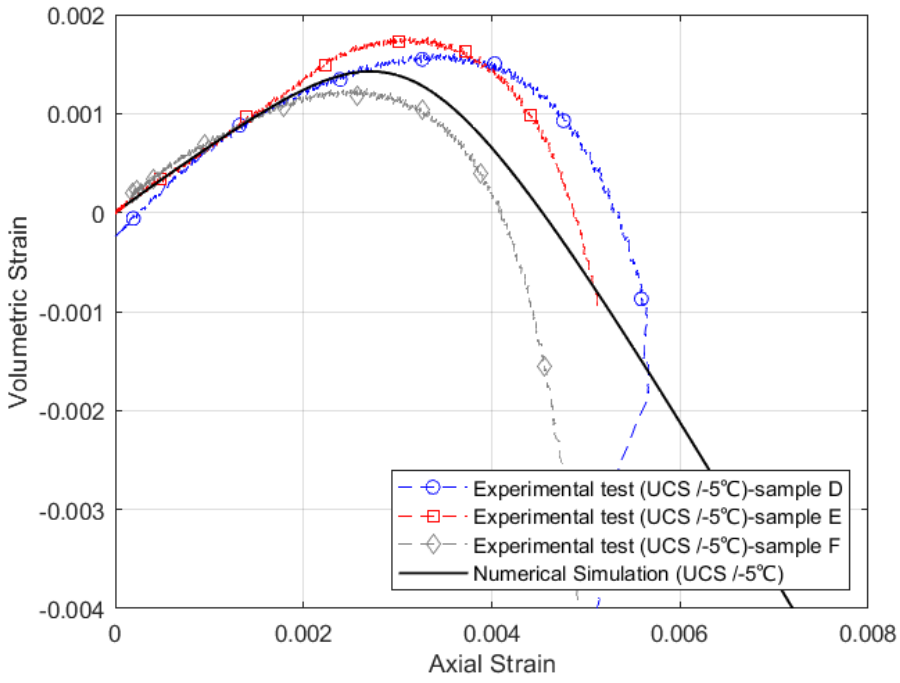

Figure 5. 17 Volumetric strain-axial strain relationship for UCS test at -5℃. (Experimental tests and Numerical simulation)

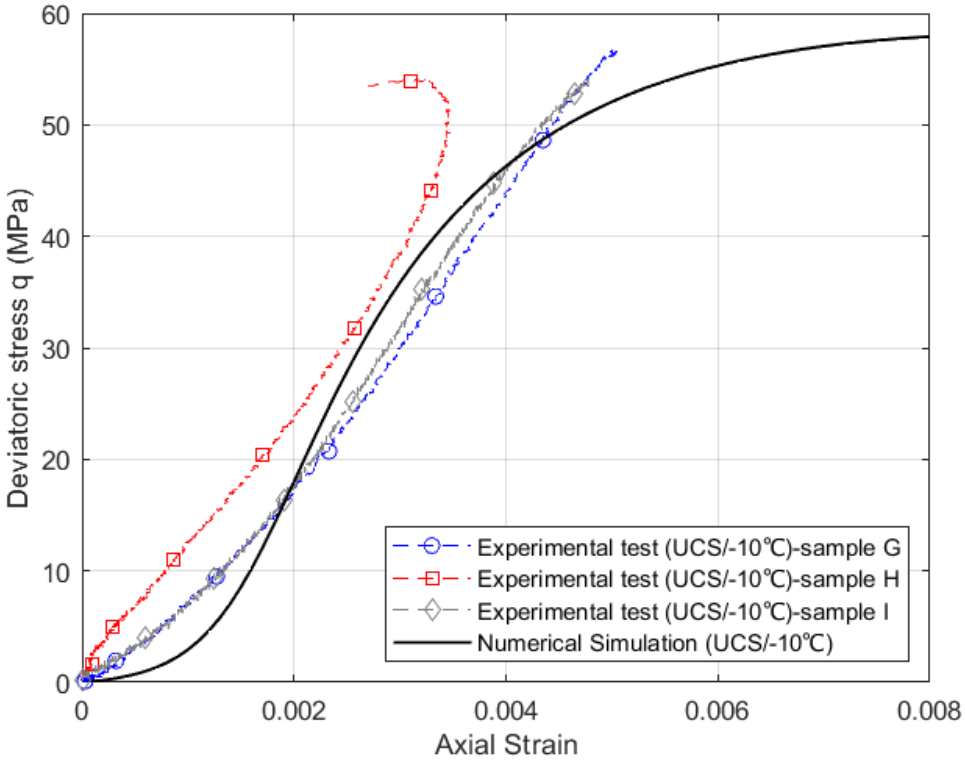

Figure 5. 18 Deviatoric stress-axial strain relationship for UCS test at -10℃. (Experimental tests and Numerical simulation)

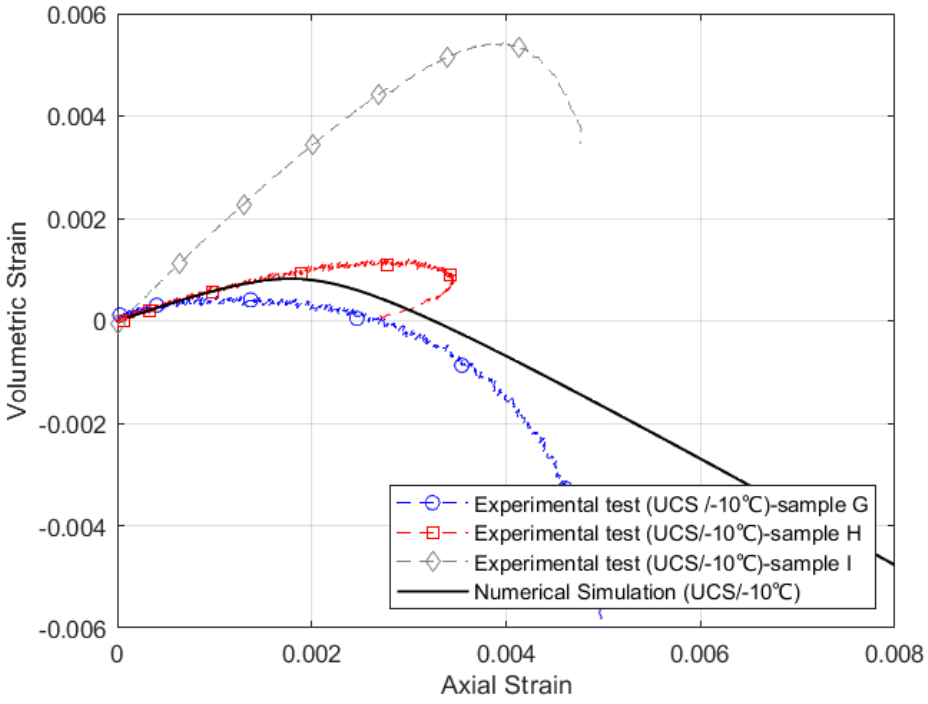

Figure 5. 19 Volumetric strain-axial strain relationship for UCS test at -10℃. (Experimental tests and Numerical simulation)

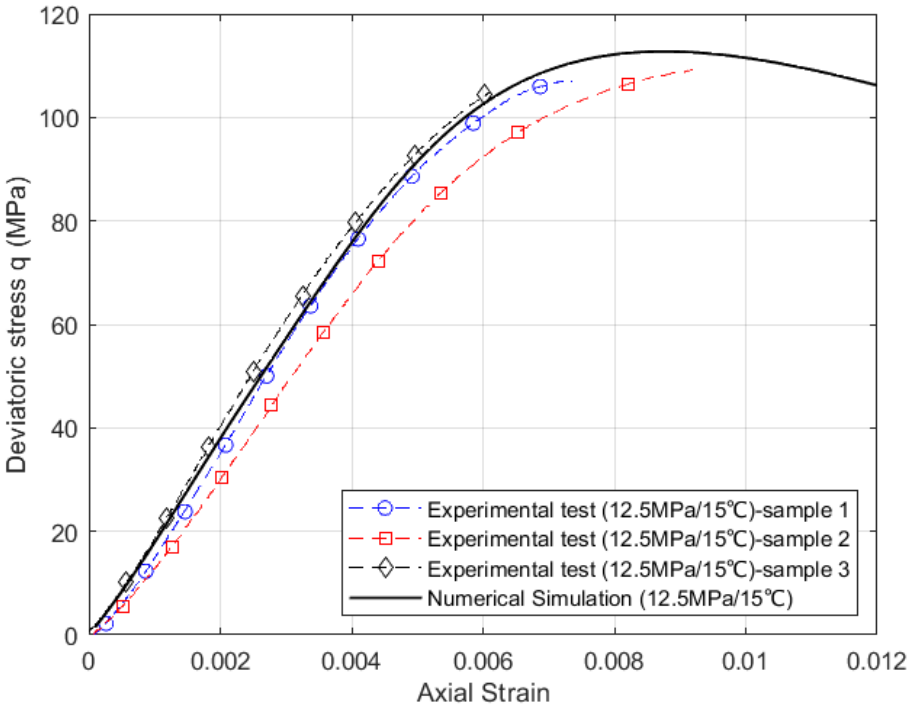

Figure 5.20 Deviatoric stress-axial strain relationship for triaxial 12.5 MPa test at 15℃. (Experimental tests and Numerical simulation)

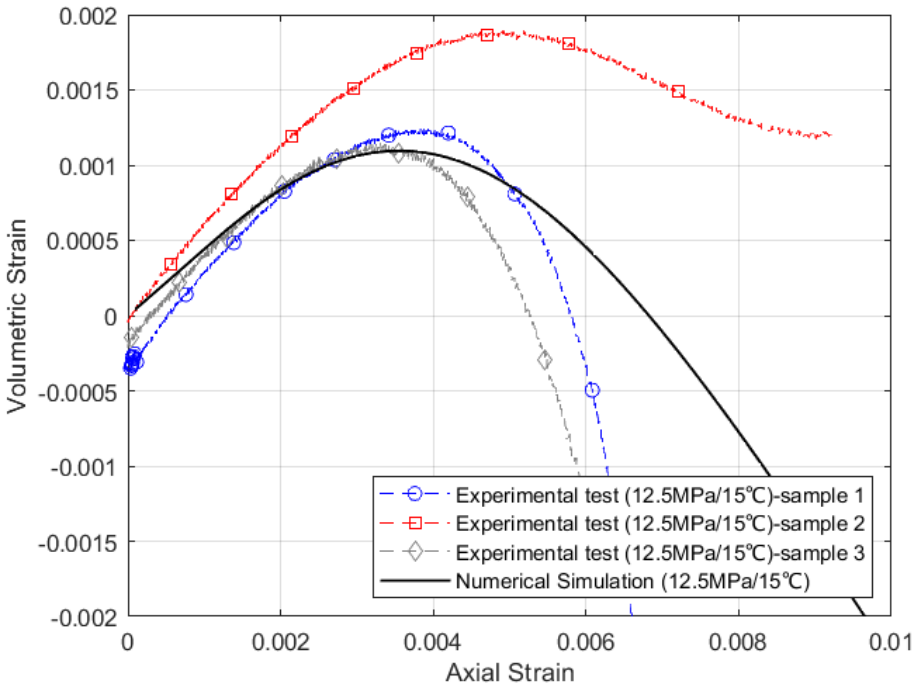

Figure 5. 21 Volumetric strain-axial strain relationship for triaxial 12.5 MPa test at 15℃. (Experimental tests and Numerical simulation)

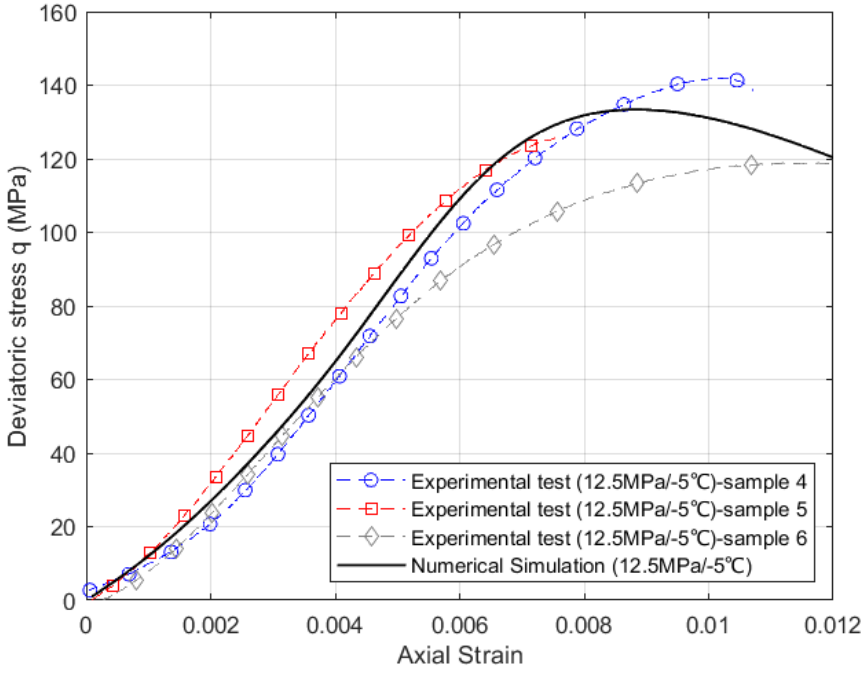

Figure 5. 22 Deviatoric stress-axial strain relationship for triaxial 12.5 MPa test at -5℃. (Experimental tests and Numerical simulation)

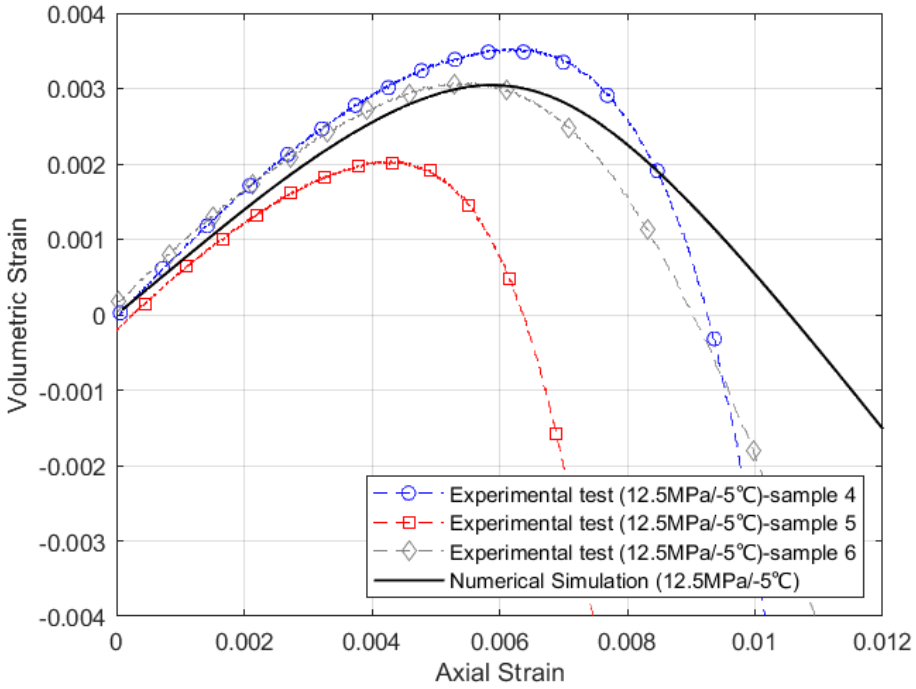

Figure 5. 23 Volumetric strain-axial strain relationship for triaxial 12.5 MPa test at -5℃. (Experimental tests and Numerical simulation)

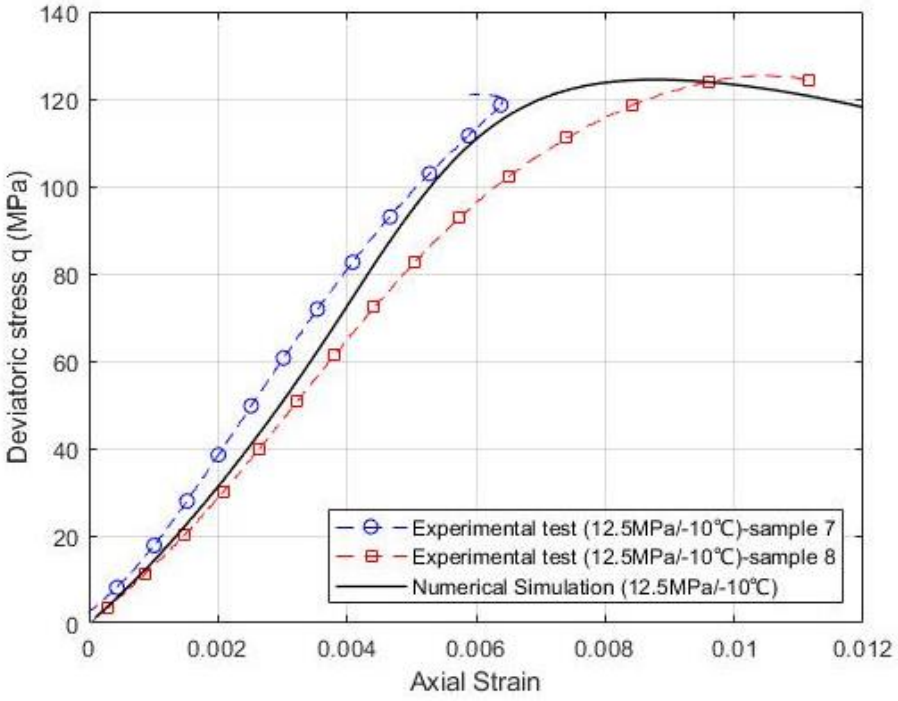

Figure 5. 24 Deviatoric stress-axial strain relationship for triaxial 12.5 MPa test at -10℃. (Experimental tests and Numerical simulation)

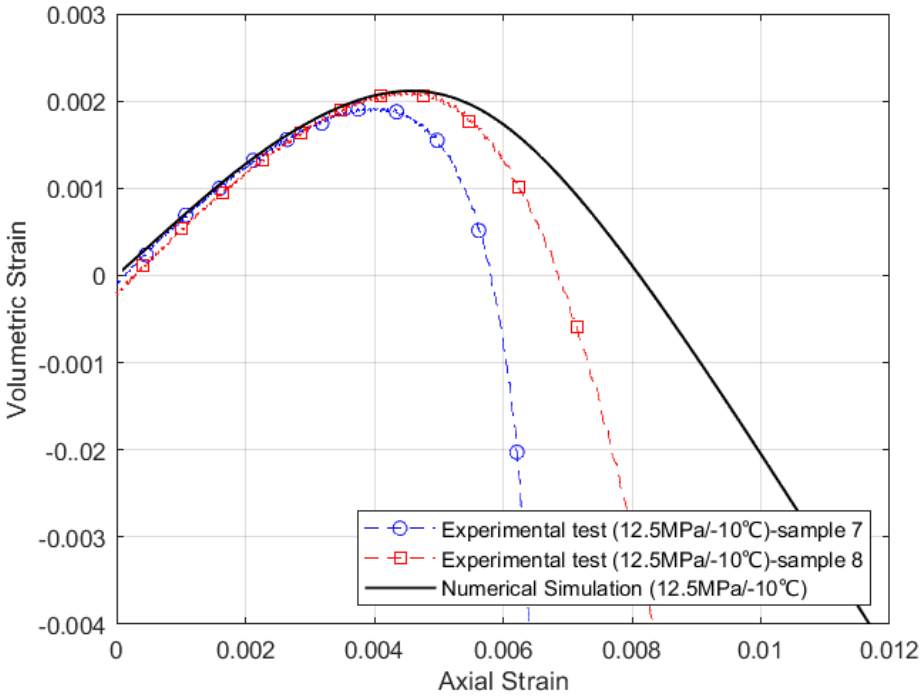

Figure 5. 25 Volumetric strain-axial strain relationship for triaxial 12.5 MPa test at -10°C. (Experimental tests and Numerical simulation

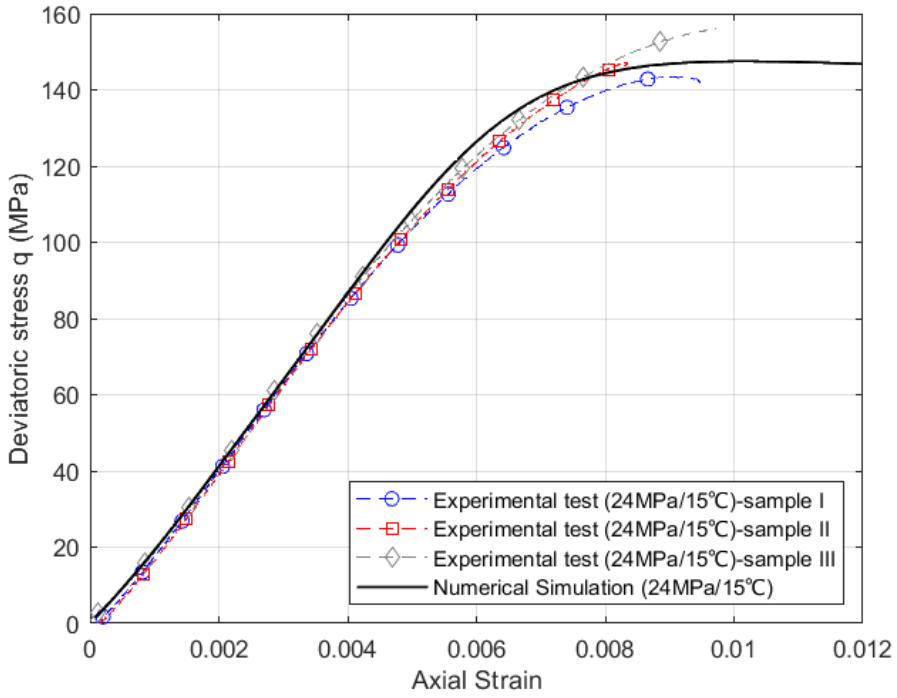

Figure 5. 26 Deviatoric stress-axial strain relationship for triaxial 24 MPa test at 15°C. (Experimental tests and Numerical simulation)

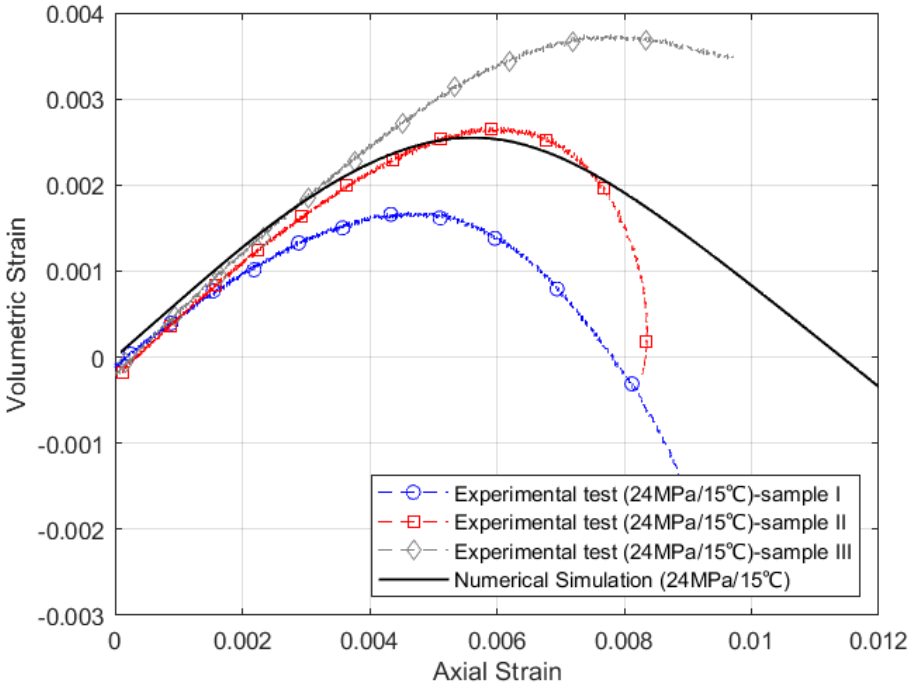

Figure 5. 27 Volumetric strain-axial strain relationship for triaxial 24 MPa test at 15°C. (Experimental tests and Numerical simulation)

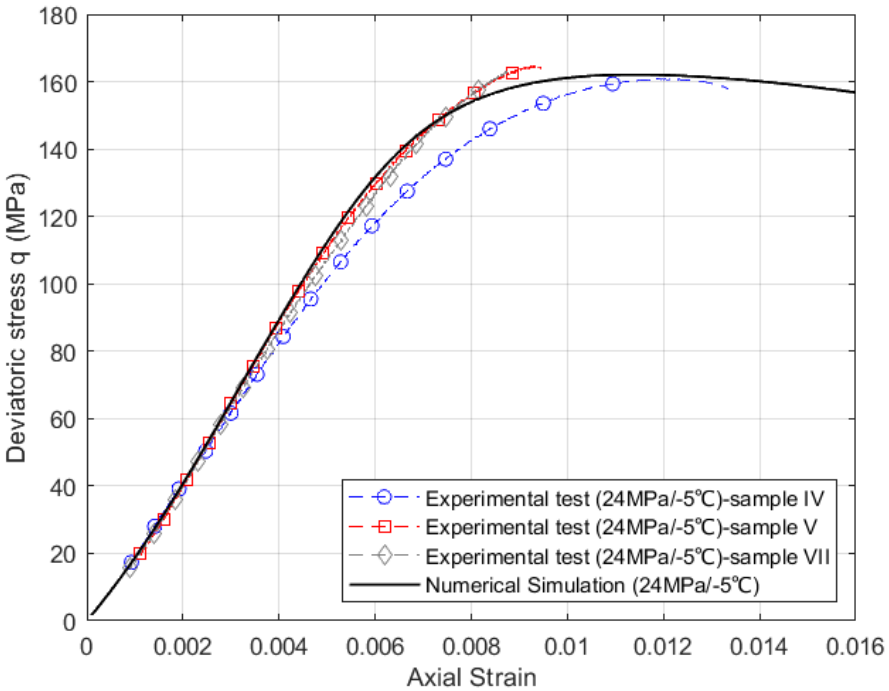

Figure 5. 28 Deviatoric stress-axial strain relationship for triaxial 24 MPa test at -5°C. (Experimental tests and Numerical simulation)

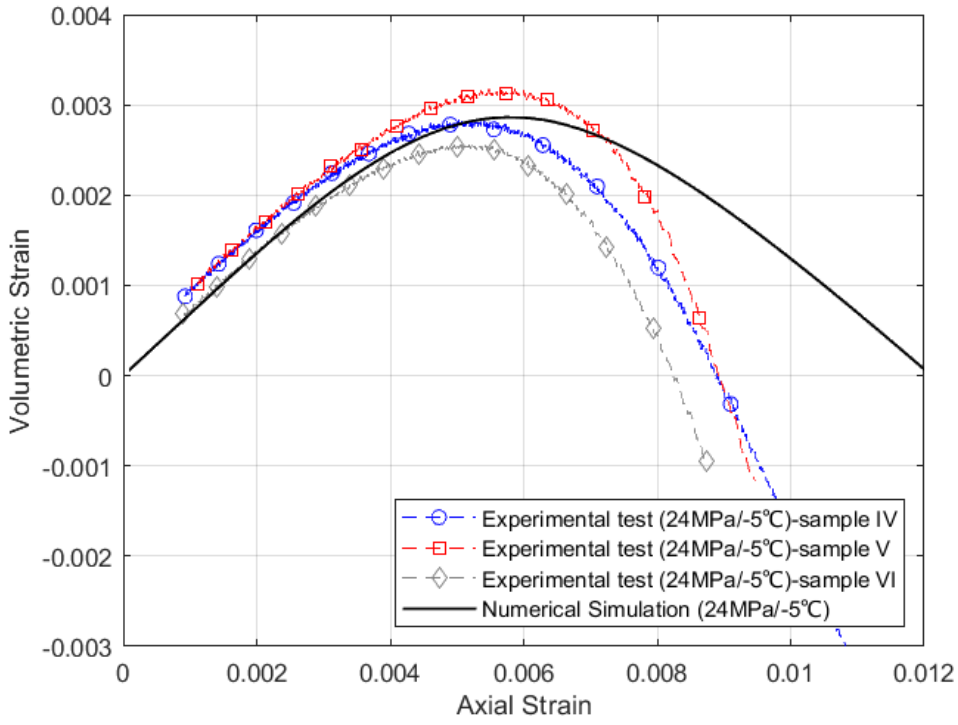

Figure 5. 29 Volumetric strain-axial strain relationship for triaxial 24 MPa test at -5℃. (Experimental tests and Numerical simulation)

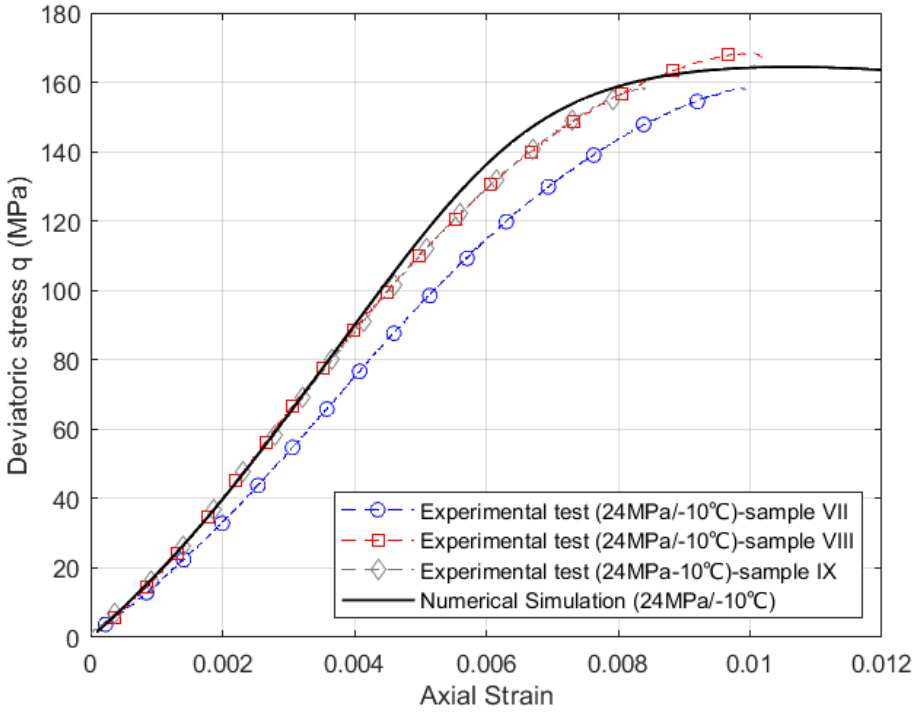

Figure 5. 30 Deviatoric stress-axial strain relationship for triaxial 24 MPa test at -10℃. (Experimental tests and Numerical simulation)

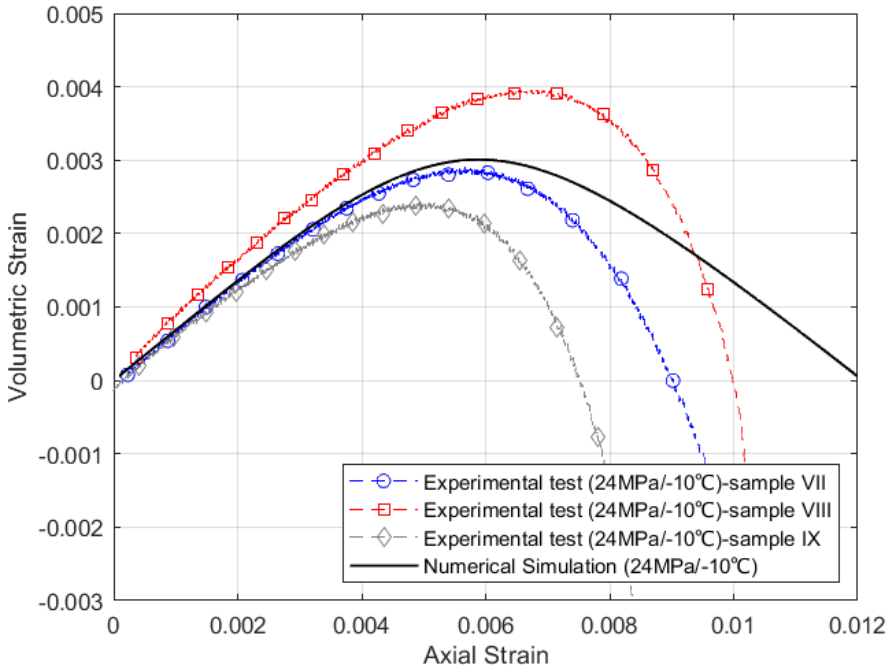

Figure 5. 31 Volumetric strain-axial strain relationship for triaxial 24 MPa test at -10°C. (Experimental tests and Numerical simulation)

Chapter 6. Representative scenarios and parametric studies

6.1 Introduction

This chapter shows different numerical simulations based on the governing equations presented in Chapter 3, the experimental results of Chapter 4 and the numerical implementation validation and parametric study of Chapter 5. Several THM problems are simulated to study the influence of the internal temperature and pressures produced by CO_2 injection on the surrounding wellbore rock. The assumptions made in FEM simulations are that the pressure and temperature of the CO_2 are taken as boundary conditions at the inner surface of the wellbore, the rock is fully saturated with saline water and consists of porous and fissure networks.

Different internal wellbore temperatures and pressures are simulated. These different values represent CO_2 injection conditions. Once a specific injection scenario is considered then the temperature and pressure will increase by increasing the studying depth of the wellbore (Vilarrasa et al., 2013). Pressure is influenced by the weight of the liquid CO_2 as it is moving deeper in the wellbore, while temperature of CO_2 increases, due to heat transfer from the warmer rock formation. It should be reminded that the temperature increases in relation to depth at a rate of 33°C/km. Material properties of rock that influence the results are also investigated, i.e., Young's modulus, leakage term and permeability. Finally, numerical simulations are presented using the Stainton Sandstone experimental results analysed in Chapter 4.

As mentioned in Chapter 3, we adopt the convention that compressive stresses and strains are negative, while tensile stresses and dilatancy are positive.

6.2 Different cases

In this section, the effects of internal wellbore pressures and temperatures, due to CO_2 injection, on the pore-fissure pressures, effective stresses and damage evolution of the surrounding rock are presented. A unit thickness of the drawdown regime modelled by Ma and Zhao (2018) and Kazemi (1969) is analysed in this chapter. A vertical wellbore of inner radius $r_w = 0.1\ m$ is considered and a unit thickness of the wellbore is simulated, with the outer radius being set to 800 m to describe the boundary conditions at the far-field. Vertical deformation of the whole medium is assumed to be constrained. Elastoplastic damage effects on the wellbore wall are considered and the isotropic material parameters for the parametric study were taken from Ma and Wang (2016), as shown in Table 6.1. The finite element mesh and boundary conditions of the problem can be seen in Figure 6.1. Since the loading displays symmetry about the vertical axis of the wellbore, an axisymmetric formulation is selected. Coordinates, measured in meters from the centre of the wellbore, of the horizontal grid points of the mesh are: [0.1, 0.1025, 0.105, 0.1075, 0.110, 0.115, 0.120, 0.125, 0.130, 0.135, 0.140, 0.145, 0.150, 0.155, 0.160, 0.17, 0.180, 0.190, 0.20, 0.22, 0.25, 0.30, 0.50, 1, 2, 5, 10, 20, 50, 100, 200, 400, 600, 800]. This demonstrates that more points are considered close to the wellbore, which is the area of interest, as mesh refinement technique. The results are presented at time $t = 80\ s$, and $t = 800s$. The time ($t = 80\ s$), corresponds to an early time response of the system, where the difference between the three temperatures is the largest.

Different scenarios are simulated to examine the behaviour of the rock during the injection of CO_2. The pressure of the CO_2 is considered as the internal pressure of the wellbore (P_i or P_{CO_2}) and the stress due to the weight of the formation as external radial stress (σ_r). The initial pore and fissure pressure, assuming the system to be in equilibrium, before injection, is equal to the hydrostatic pressure (P_0) and is influenced by effective stress parameters due to post drilling effects. The temperature of the formation (T_{form}) was selected according to the studied depth. It should be noted that the (P_0) and (T_{form}) are the pressure and temperature of the formation prior to any drilling. The internal temperature of the wellbore (T_i) was selected according to the injected temperature of the CO_2.

Table 6. 1 Material parameters used for the simulations based on [1] (Gelet et al., 2012a), [2] (Ma and Zhao, 2018), [3](Kazemi, 1969), [4] (Ma, 2014b)

Material Parameters (unit)	Value	References
$[E\ (\mathrm{GPa})]$	10, 20, 100	[2]
$[\nu]$	0.25	[1]
$[\beta_{11}\ (\mathrm{MPa^{-1}})]$	7.23×10^{-09}	[3]
$[\beta_{22}\ (\mathrm{MPa^{-1}})]$	1.8×10^{-10}	
$[\beta_{12}=\beta_{21}\ (\mathrm{MPa^{-1}})]$	0	
$[\beta_1]$	0.99	[2]
$[\beta_2]$	0.01	
$[c_f\ (\mathrm{MPa^{-1}})]$	1.45×10^{-9}	[3]
$[\mu\ (\mathrm{MPa})]$	10^{-9}	
(φ_1)	0.04985	
(φ_2)	0.001243	
$[k_1\ (\mathrm{m^2})]$	5×10^{-20}	[1]
$[k_2\ (\mathrm{m^2})]$	5×10^{-19}	
$[\gamma\ (/\mathrm{P_a s})]$	5.3×10^{-10}	
$[C_{ps}\ (\mathrm{J/kg^{\circ}C})]$	837	
$[\ k_s\ (\mathrm{W/m^{\circ}C})]$	2.65	
$[C_{Ts}\ (/\mathrm{K})]$	1.8×10^{-5}	
$[C_{Tw}\ (/\mathrm{K})]$	4.5×10^{-4}	
$[\ d_{sw}(\mathrm{kg/m^3})]$	1023	
(ICL) $[\lambda]$	0.1	[4]
(URL) $[\kappa]$	0.0033	
$[M]$	1.9	
$[R]$	2.45	
$[M_{cs}]$	1.7	
$[m_p]$	10	

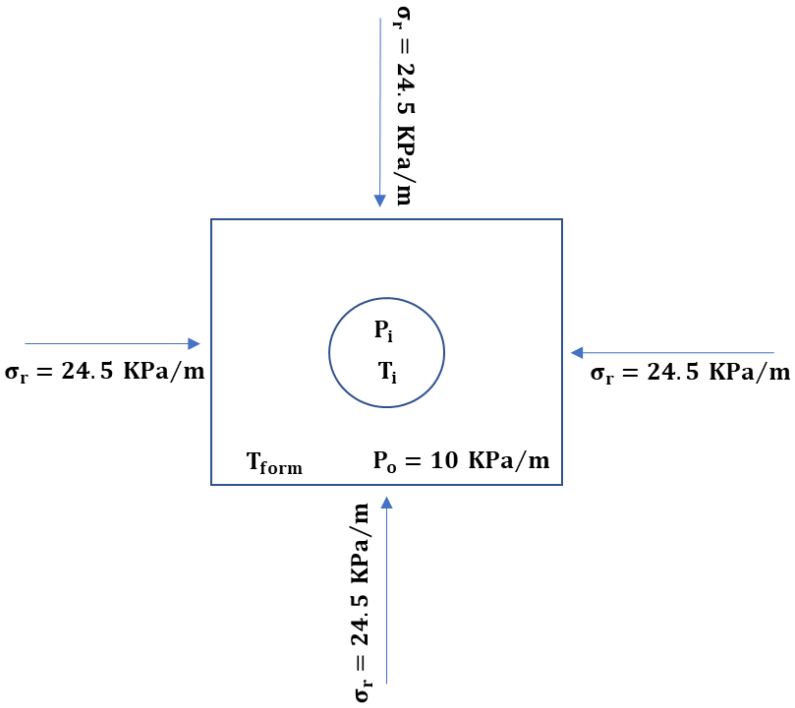

Figure 6.1a

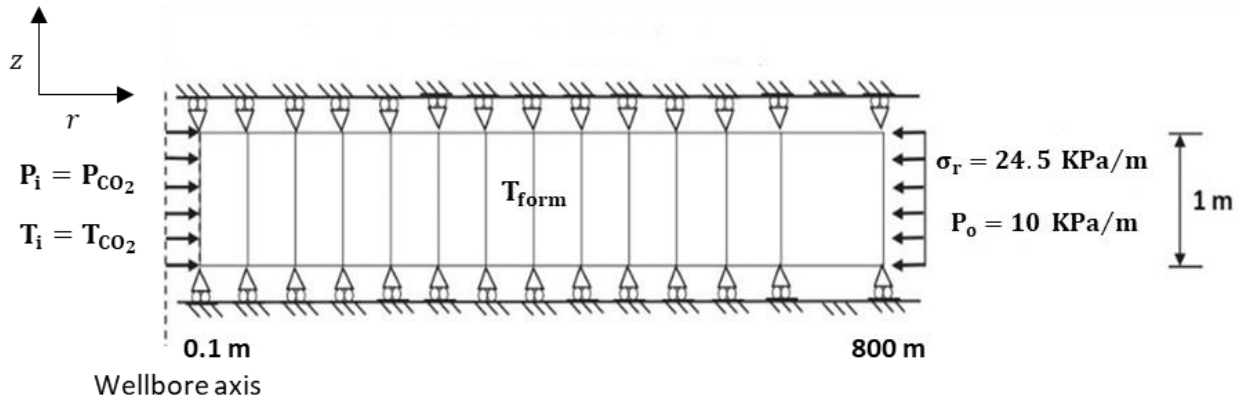

Figure 6.1b

Figure 6. 1 (a)Schematic illustration of the injection well-plan view, (b) finite-element mesh and boundary conditions for axisymmetric problem (not to scale).

The damage parameters for the damage evolution law which are based on the tensile principal stress are the same as those used in the validation of Ma's and Zhao (2018) results in Section 5.10.

During CO_2 injection, typically the pressure and temperature of the CO_2 will increase with depth of the wellbore (Vilarrasa et al., 2013). The phase of the CO_2 can change based on its pressure and temperature (see the phase diagram in Figure 2.1). In Sections 6.2.1, 6.2.2 and 6.2.3, three different

depths (three cases) are presented for the same internal wellbore temperatures. For 50 m, 500 m and 1000 m depth, 4.2 MPa, 8 MPa, and 12 MPa internal pressure and 5℃, 17℃ and 33℃ temperatures were selected respectively for the rock formation based on Vilarrasa et al. (2013) . Under these conditions, the CO_2 is in liquid phase.

The three different depths introduce three different case scenarios as presented in Table 6.2. According to the depth and based on Figure 6.1 the radial stress and hydrostatic pressure corresponding to each depth is presented in Table 6.2.

Table 6. 2 Studied Cases characteristics

	Temperature of the formation T_{form} (℃)	Internal wellbore pressure P_{int} (MPa)	Radial Stress of the formation σ_r (MPa)	Hydrostatic pressure P_0 (MPa)
Case 1 (50m depth)	5	4.2	1.2	1.5
Case 2 (500m depth)	17	8	12.5	6
Case 3 (1000m depth)	33	12	24.5	11

The simulated internal temperatures of the wellbore were -15℃, -10℃, -5℃, 0℃, 5℃. These temperatures were selected to identify the cooling effects on rock due to CO_2 injection and bridge the knowledge gap in literature. The range of them were based on the research of Vilarrasa et al. (2013).

The average density of the North Sea water is $1023\ \mathrm{kg/m^3}$ and consequently, the pore-fissure pressures will increase at a rate of $10\ \mathrm{MPa/km}$. A sea depth of 100 m is considered for all three cases. The selected saturated density of the rock is $2400\ \mathrm{kg/m^3}$ following (Gelet et al., 2012a), so at a certain depth the stress will increase by $23.5\ \mathrm{kPa/m}$ (Ma and Zhao, 2018) and the weight of the water due to the depth, which is $1023\ \mathrm{kg/m^3} \times 100\mathrm{m} = 102300\ \mathrm{kg/m^3} = 1\ \mathrm{kPa/m}$. The total increase of the radial stress according to the depth of the wellbore would be $24.5\ \mathrm{kPa/m}$.

Formation pressure presented at the results is calculated as follows:

$$Formation\ pressure = \beta_1 \overline{p_1} + \beta_2 \overline{p_2} \tag{6.1}$$

where $\overline{p_1}$ and $\overline{p_2}$ are the average values of the pore and fissure pressure for each element at a specific time step.

In Sections 6.2.1, 6.2.2 and 6.2.3, the model presented in Figure 6.1, is used as the input values of the three different cases to investigate the influence of internal pressure and temperature of the wellbore to the surrounding rock. This can reveal the THM effect of liquid CO_2 on the rock at the vicinity of the wellbore. These effects on the pore-fissure pressure distribution, formation pressures and effective stresses are also discussed.

6.2.1 Simulation of different internal temperatures at the wellbore head (Case 1)

The model mentioned in Figure 6.1 is used here. The pore-fissure pressures fluctuation diagram for the Case 1 and five different internal wellbore temperatures are presented in Figure 6.2. The formation pressures, expressed by Equation (6.1), for Case 1, are presented in Figure 6.3. The effective stresses in the vicinity of the wellbore are bestowed in Figure 6.4. Positive values of the hoop stress indicate the possibility of creating tensile fractures to the wellbore wall (Grandi et al., 2002). The studied times are $t = 80s$ and $t = 800$ s.

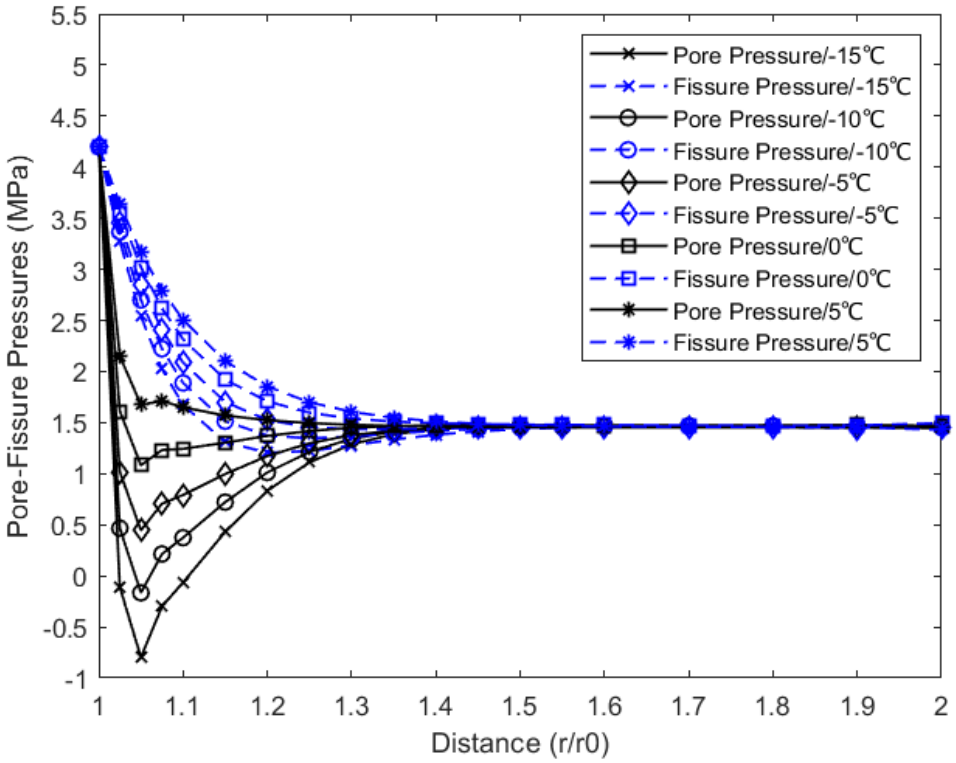

Figure 6.2a

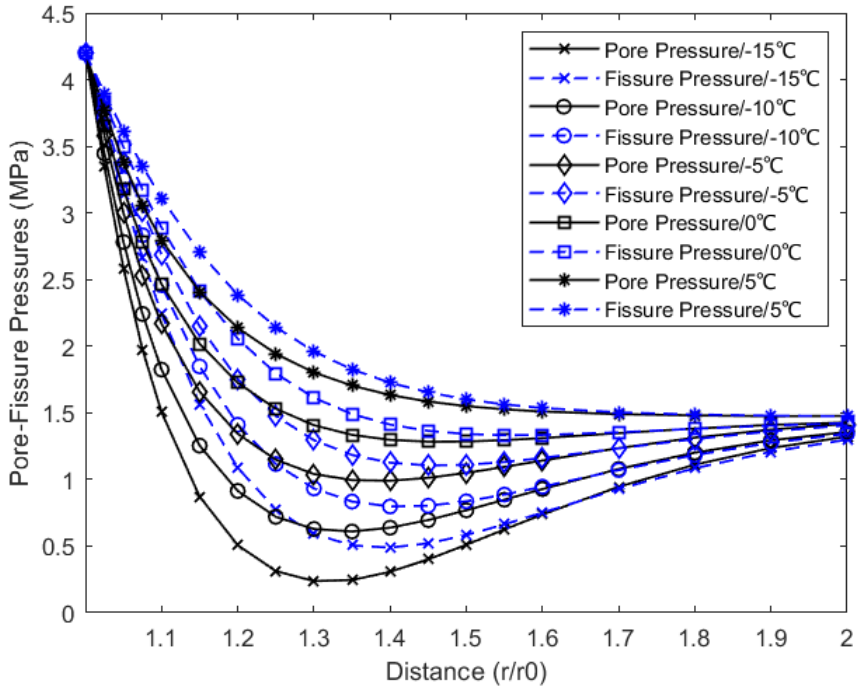

Figure 6.2b

Figure 6. 2 Pore-Fissure pressures profiles in a double-porosity system at a) t=80 s, b) t=800 s (Case 1)

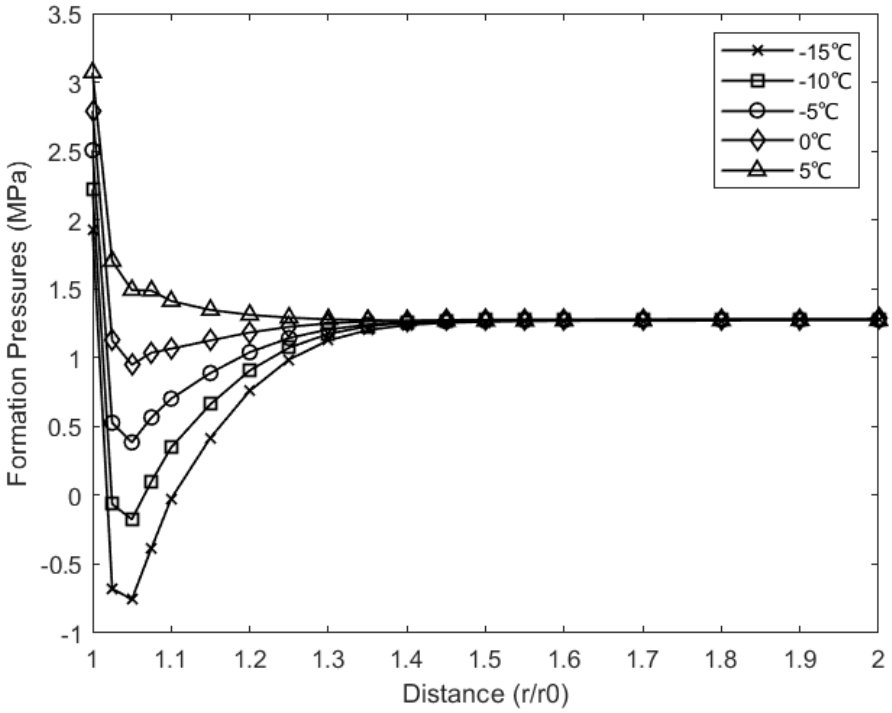

Figure 6.3a

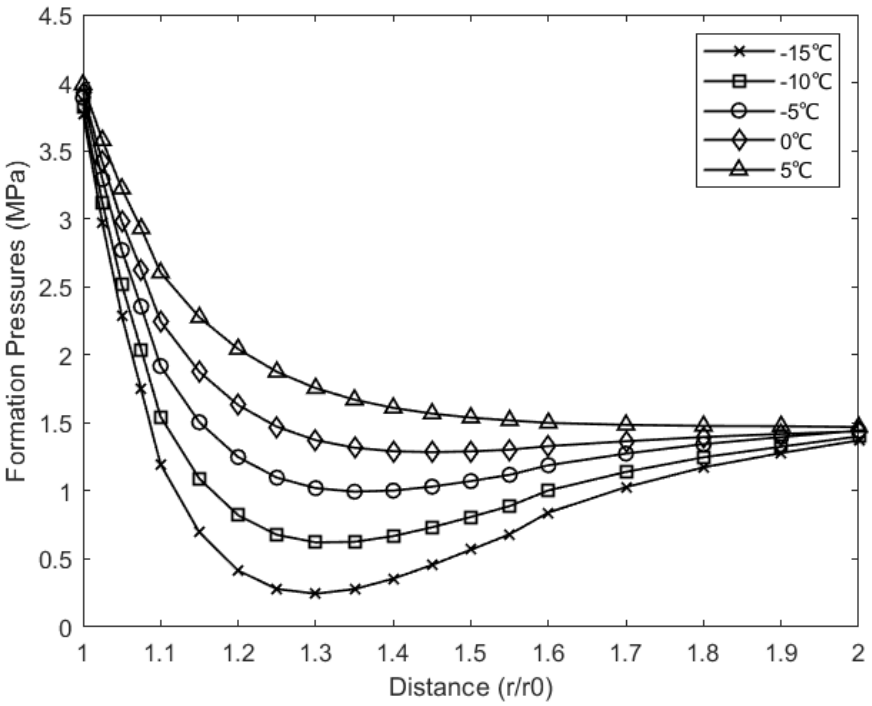

Figure 6.3b

Figure 6. 3 Formation pressures profiles in a double-porosity system at a) t=80 s, b) t=800 s (Case 1)

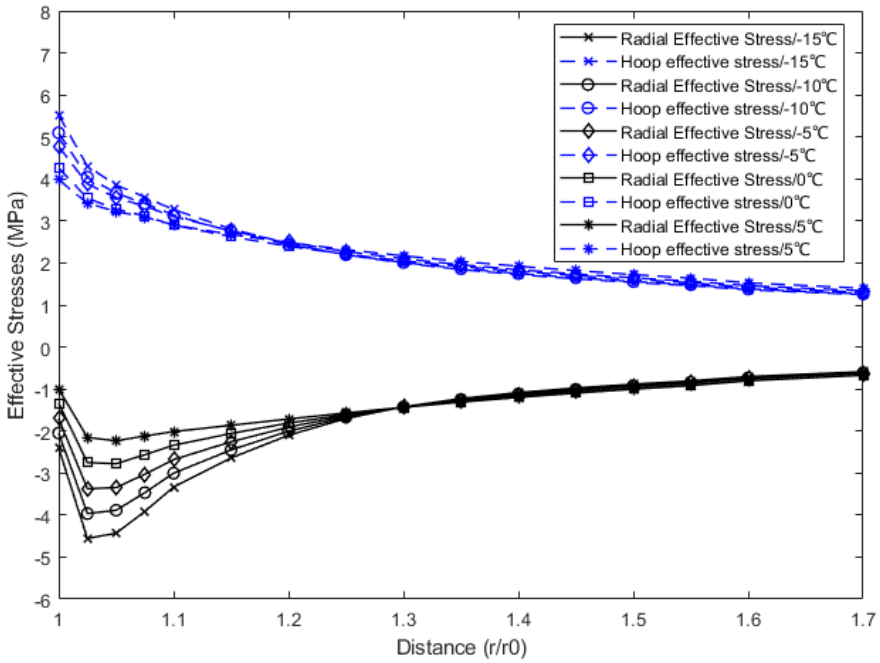

Figure 6.4a

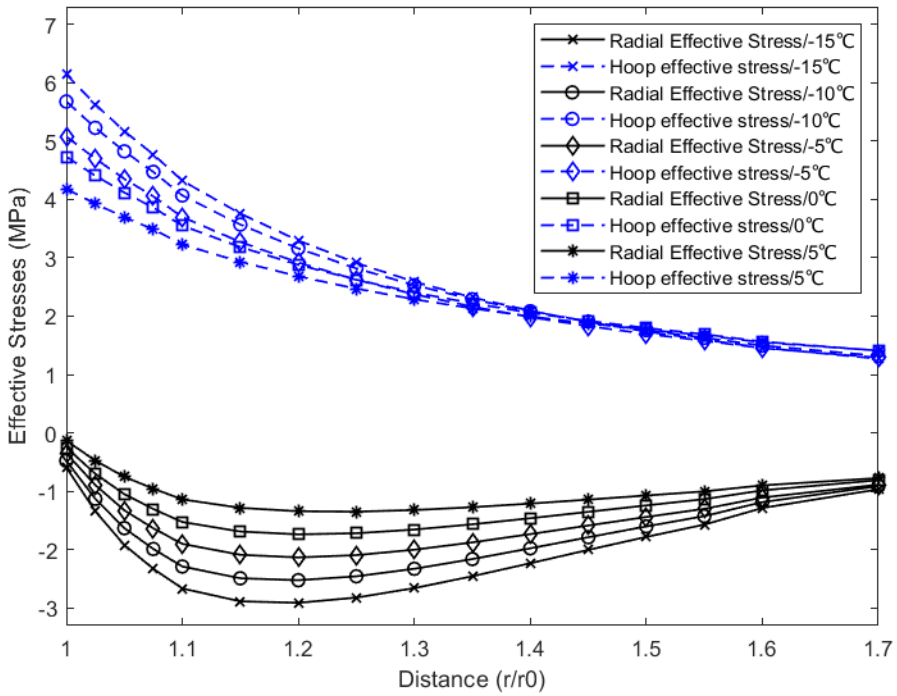

Figure 6.4b

Figure 6. 4 Radial and Hoop effective stresses profiles in a double-porosity system at a) t=80 s, b) t=800 s (Case 1)

Both figures (Figure 6.2 and 6.3), indicate a drop of pressure for an early response ($t = 80s$) and then the pore-fissure pressures and the total formation pressures increase at a later studied time ($t = 800s$). A negative value of pore pressure and formation pressure is outlined for $T_i = -15℃$. This indicates stress-relief, tensile behaviour of the rock formation and cavitation of water in pores, that can lead to fracturing (Khaledi et al., 2021). The tension of the rock to be more tensile when lower CO_2 temperatures are selected, can be seen in Figure 6.4. This tensile effect on the hoop stress increases with time, as seen in Figures 6.4a and 6.4b. In contrast, the radial effective stress at the vicinity of the wellbore wall becomes more compressive at an early simulation period ($t = 80s$). This compression effect decreases at the vicinity of the wellbore with time, while its radial expansion to the rock nearby increases, as seen in Figure 6.4b.

To avoid cavitation in pores and stress-relief, the tensile hoops stress needs to be reduced. One way to do that is by reducing the internal CO_2 pressure. As the CO_2 is selected to remain in the liquid phase, at -15℃, 2 MPa is the lowest pressure that can be applied in order for the CO_2 to not enter the gaseous phase following Figure 2.1.

Figures 6.5 and 6.6 present the effect of the internal pressure of the wellbore on the hoop effective stress and formation pressure, respectively. It is noted that the tensile hoop effective stress can be significantly reduced by selecting a lower internal pressure, as seen in Figure 6.5. Specifically, comparing the 6 MPa internal pressure to the 2 MPa for the same temperature condition (-15℃), the tensile hoop stress for 2 MPa injection pressure is nearly 2.5 times lower. As far as it concerns the formation pressure, lower internal pressure indicates a decrease in the tensile pressure, as seen in Figure 6.6. This can be explained as the hoop effective stress reduces, the pore-space increases in volume (stress-relief) and consequently the formation pressure of the medium tends to reduce.

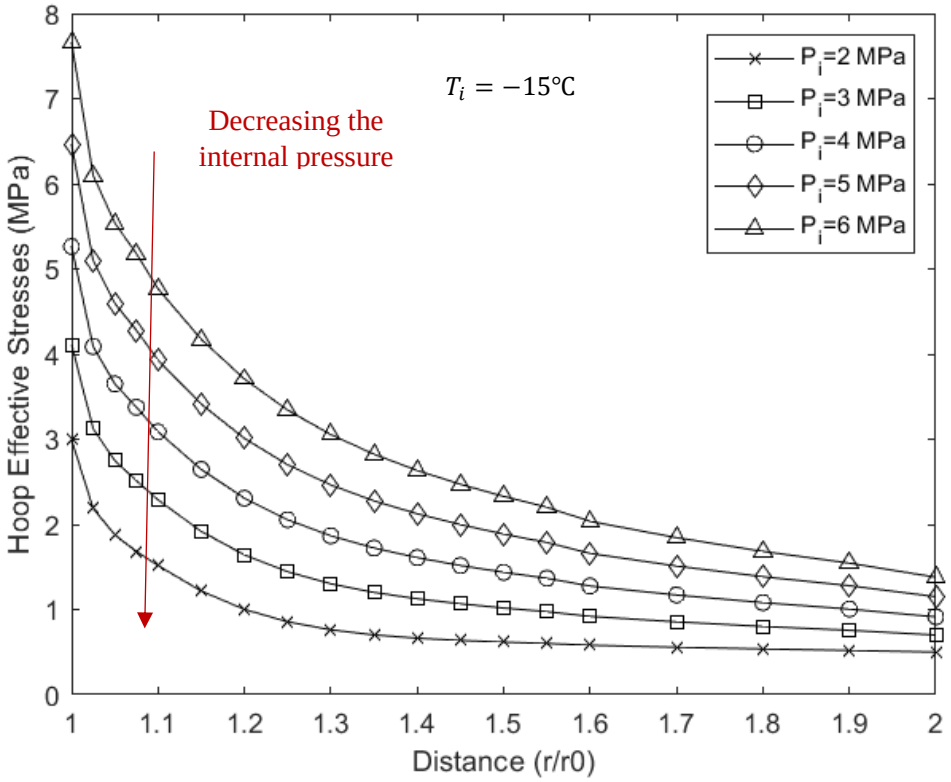

Figure 6. 5 Effect of decreasing the internal pressure to the hoop effective stress, t=80 s (Case 1)

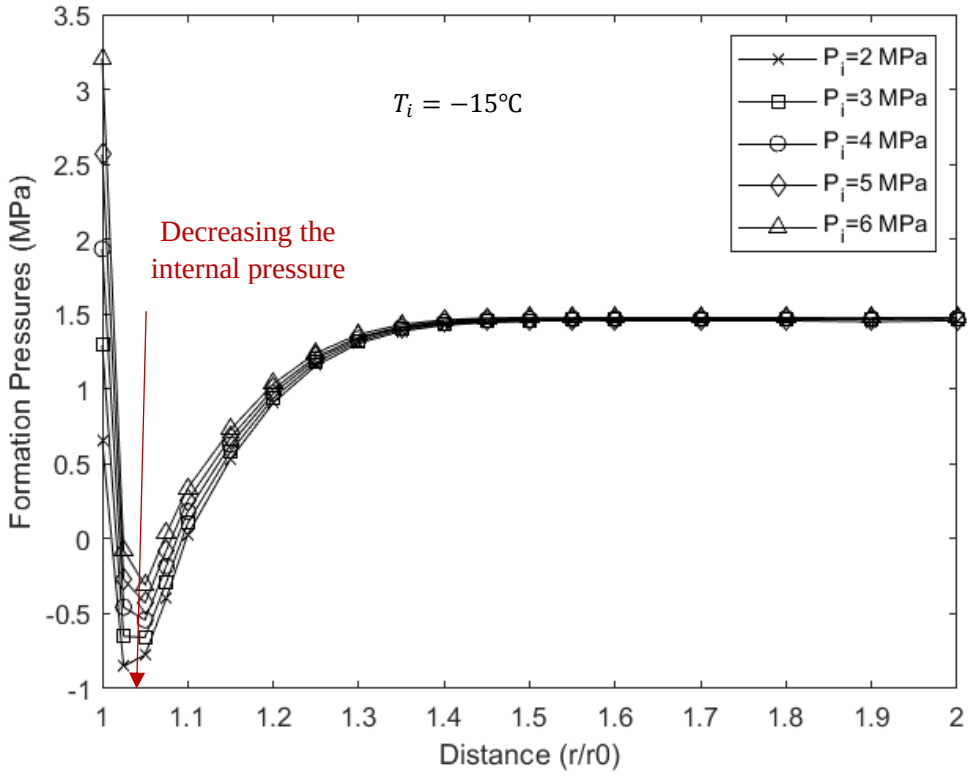

Figure 6. 6 Effect of decreasing the internal pressure to the formation Pressures, t=80 s (Case 1)

6.2.2 Simulation of different internal temperatures at 500 m depth of the wellbore (Case 2)

Case 2 is used to simulate the 500m depth conditions of the wellbore during CO_2 injection based on the model analysis of Figure 6.1. The pore-fissure pressures and the effective stresses are presented in Figure 6.7 and 6.8, respectively, for the Case 2. The same time response is selected, $t = 80s$ and $t = 800s$.

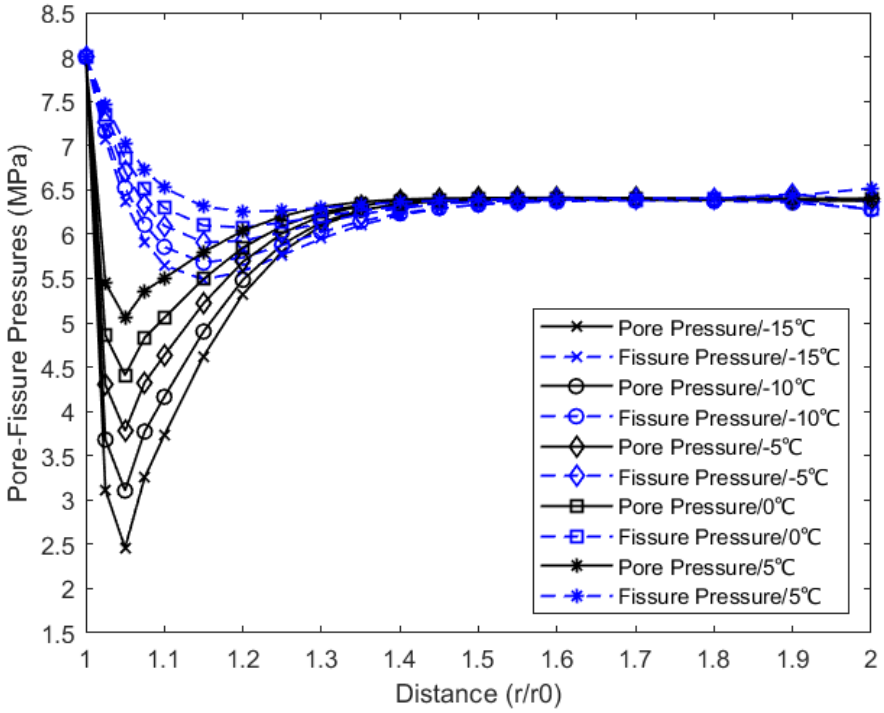

Figure 6.7a

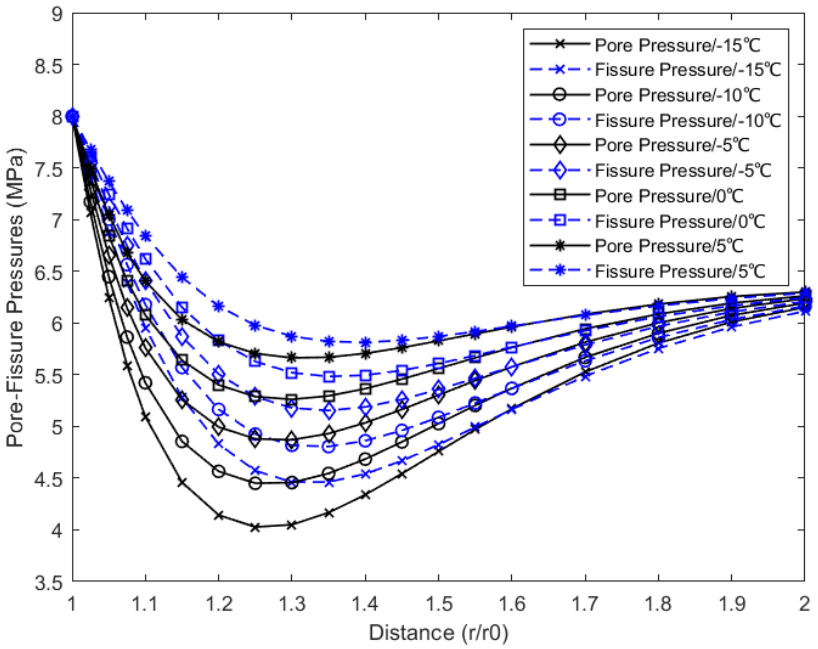

Figure 6.7b

Figure 6. 7 Pore-Fissure pressure profiles in a double-porosity system for different internal temperatures at a) t=80 s, b) t=800 s (Case 2)

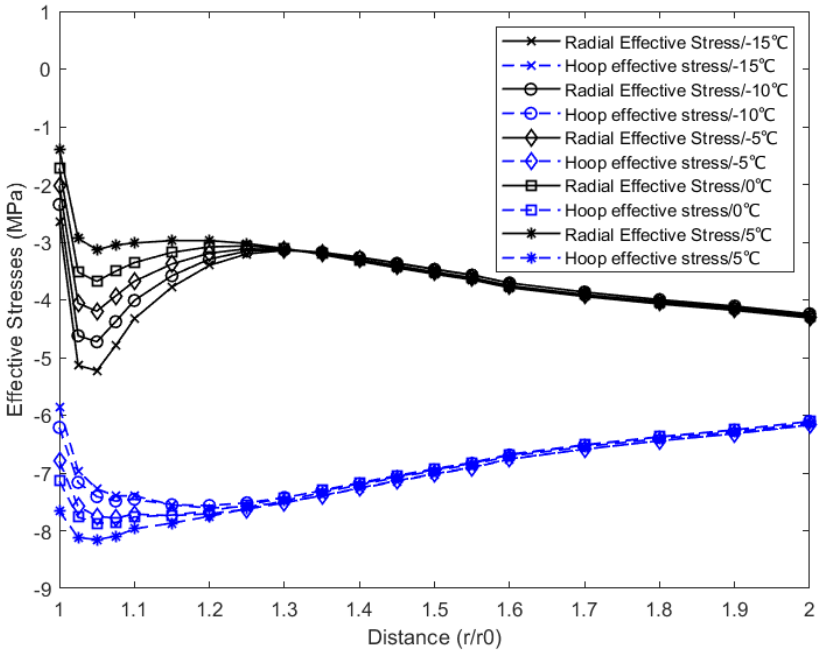

Figure 6.8a

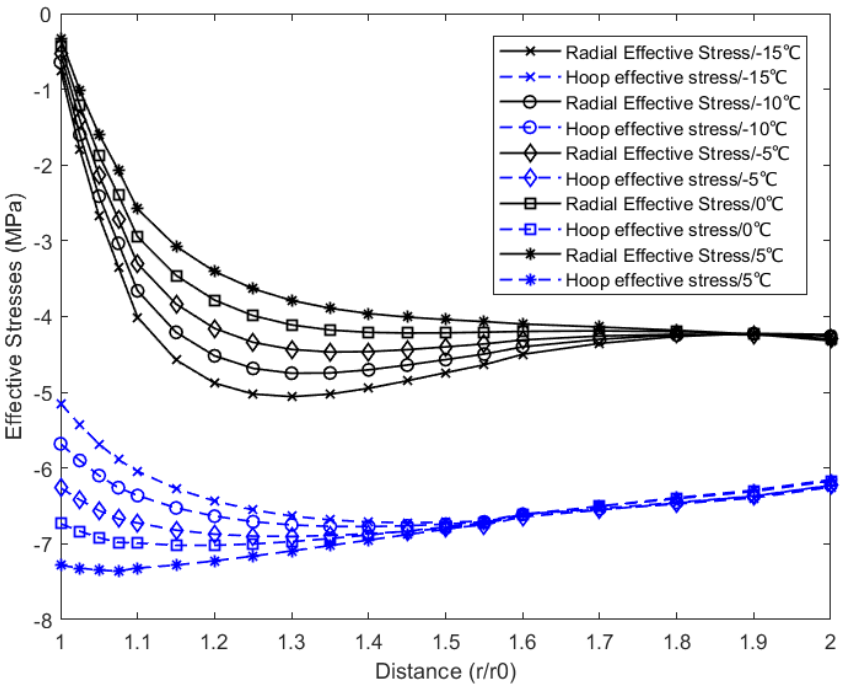

Figure 6.8b

Figure 6. 8 Radial and hoop effective stresses profiles in a dual-porosity system at a) t=80 s, b) t=800 s (Case 2)

As demonstrated in Figure 6.7, higher temperature difference between the wellbore wall and the injected CO_2 has a significant impact on the pore pressure drop and a remarkable effect on the fissure pressure reduction. At different time stages of simulation, and specifically for t=800 s, the pore and fissure pressure almost reach equilibrium. Both pore and fissure pressure values reduce, when the temperature difference between the rock formation and CO_2 temperature increases.

Furthermore, as temperature difference increases, so does the compressive hoop stress, while the compressive radial stress decreases, as seen in Figure 6.8a. At an early simulation time (*t=80 s*), different temperatures result to different hoop effective stress values in the vicinity of the wellbore; while, at a later simulation stage (t=800 s) hoop stress values in the vicinity of the wellbore are similar and independent from temperature. Additionally, hoop and radial effective stresses tend to be more tensile with time. Both radial and hoop effective stresses propagate in the rock formation and lead to compressive rock stress decrease. These above results were derived by comparing Figure 6.8a and 6.8b.

6.2.3 Injection pressures at 12 MPa and different temperatures for 1000m depth (Case 3).

Case 3 is now used in this section to simulate the 1000 m depth conditions of the wellbore during CO_2 injection based on the FEM model presented in Figure 6.1. The pore-fissure pressures and the effective stresses are presented in Figure 6.9 and 6.10, respectively, for the Case 3. The same time response is selected, $t = 80s$ and $t = 800s$.

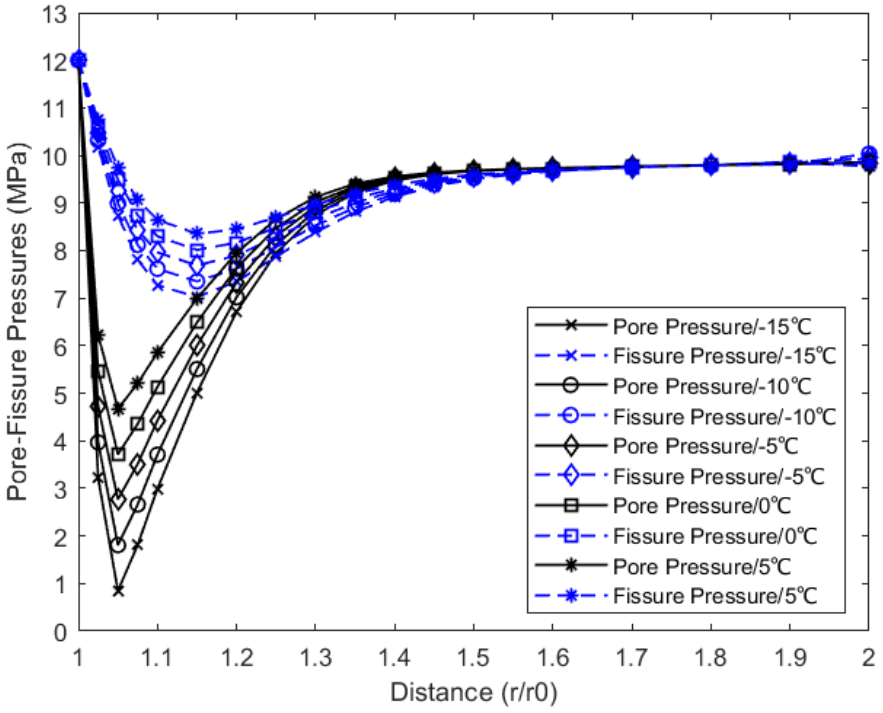

Figure 6.9a

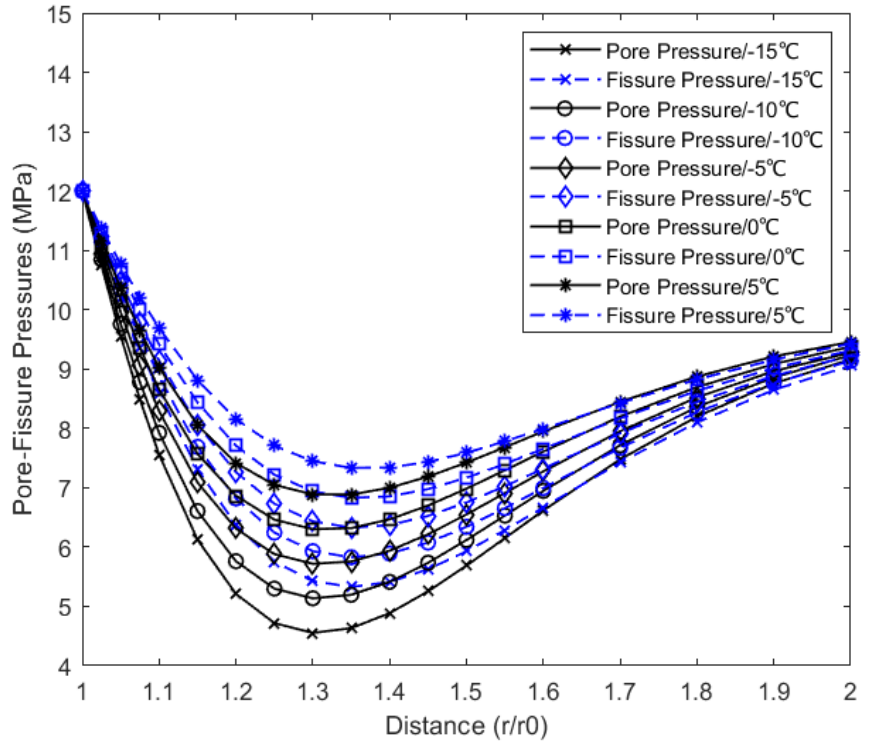

Figure 6.9b

Figure 6. 9 Pore-Fissure pressure profiles in a dual-porosity system at a) t=80 s, b) t=800 s (Case 3)

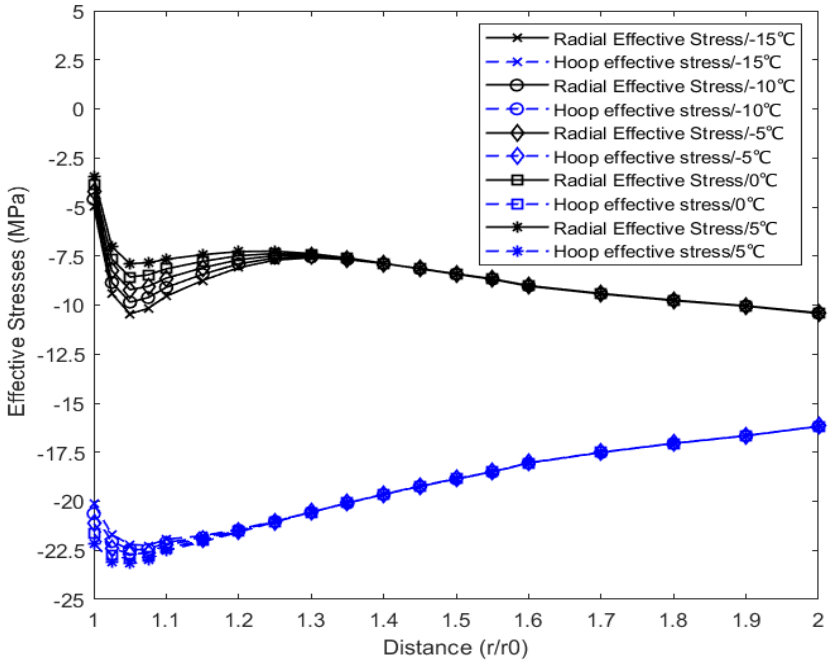

Figure 6.10a

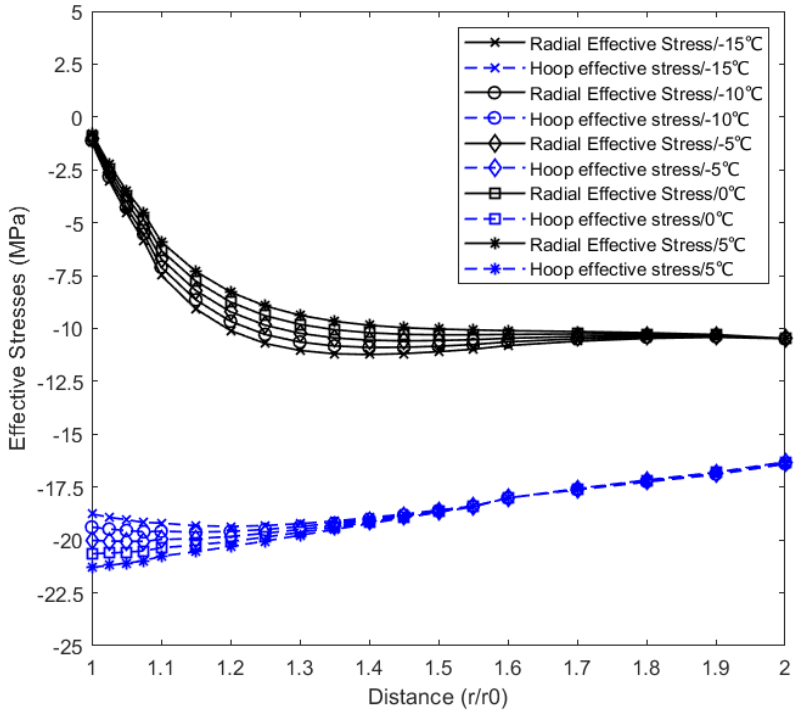

Figure 6.10b

Figure 6. 10 Radial and Hoop effective stresses profiles in a dual-porosity system at a) t=80 sec, b) t=800 s (Case 3)

For internal wellbore temperature of -15℃, there is a huge drop of the pore pressure at the early stage of the simulation (t=80s), from 12 MPa to almost 1 MPa compared to the temperature of 5℃ (Figure 6.9a). This can induce stress-relief and lead to rock fracturing (Khaledi et al., 2021). However, this pore pressure drop decreases as time passes and the pore and fissure pressure are trying to reach equilibrium. Additionally, for t=80 s, the compressive radial stress increases for higher temperature difference while the hoop stress decreases. For 800 s, this change in effective stresses becomes more apparent.

Studying different material parameters is also important, as mechanical parameters can influence the induced damage of the material. Additionally, different temperature conditions can also alter the effective and formation pressures of the rock. In Section 6.3, the influence of the Young's modulus, leakage term and permeability evolution are investigated. Young's modulus describes the elastic behaviour of the material, leakage term controls the flow between the porous and fissure domain and permeability indicates how quickly the saline water flows inside the fractured porous domain. All of them can influence the outcome of the deformation, flow, and heat transfer.

6.3 Parametric study of rock properties

6.3.1 Young's modulus (E) influence

For this parametric study two different depths were simulated, 50m and 1000 m depth of a wellbore, corresponding to the wellbore head and high depths conditions. These two depths were selected as hoop stress is in tension at the wellbore head and rock formation nearby the wellbore is in compression at higher depth. Based on the typical range of Young's modulus that a sandstone has (Małkowski et al., 2018), three different Young's modulus values used were 10 GPa, 20 GPa, and 30 GPa, to determine the influence of rock stiffness on the stresses and pressures of the formation near the wellbore when thermal loading is applied or not. The temperature of the formation is $T_{form} = 5℃$. The selected internal wellbore temperatures for the comparison are: -5℃, which induces thermal expansion and 5℃ which is the same as the formation. The -5℃ is selected as it does not create negative pore-pressures and consequently potential fracturing, as seen at the-10℃ and -15℃ internal wellbore temperatures.

The influence of Young's modulus on effective stresses and formation pressure can be seen in Figure 6.11 and Figure 6.12, respectively.

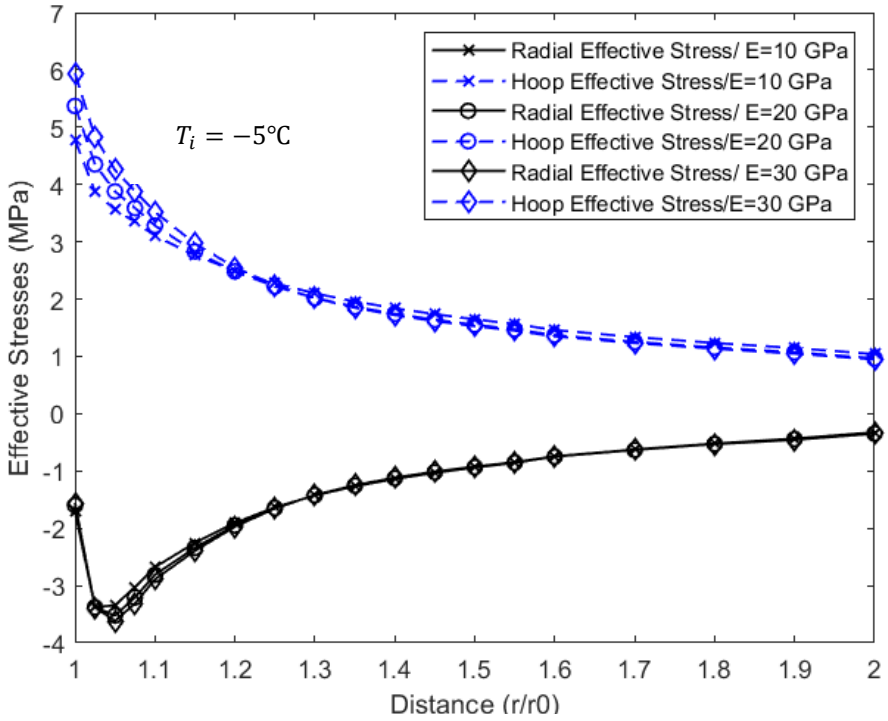

Figure 6.11a

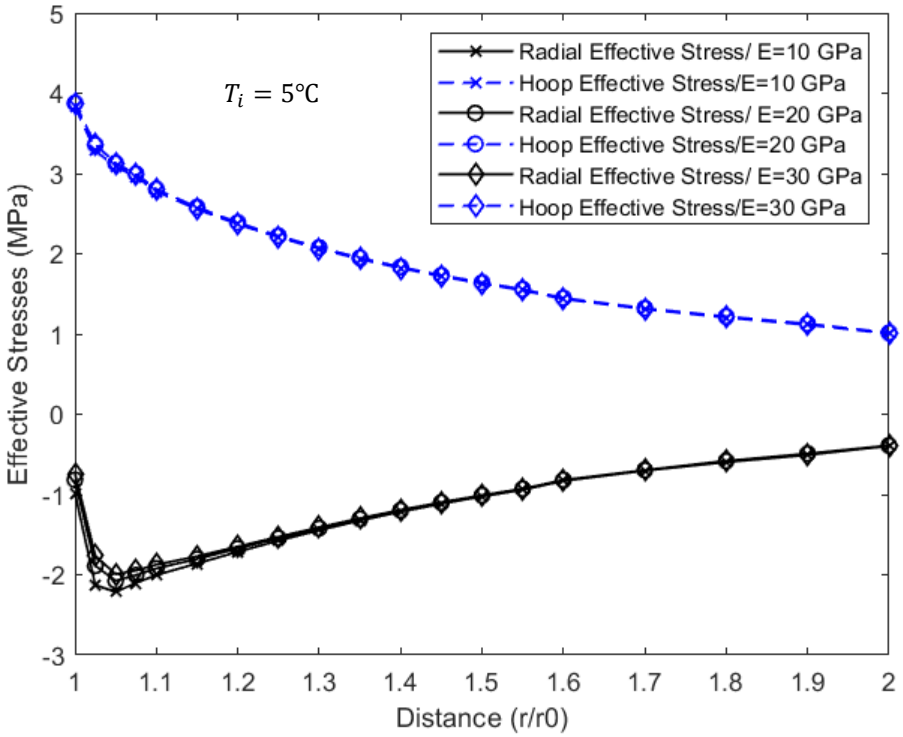

Figure 6.11b

Figure 6. 11 Influence of Young's modulus (E) on the effective stresses of the rock under different internal temperatures (Case 1, t=80 s)

For low injection temperature conditions, where the CO_2 is colder than the wellbore rock formation (as in Case 1 above), the hoop effective tensile stress increases, while Young's modulus increase. This agrees with the work of Kiran and Salehi (2017), who created a porous thermo-elastic model.

The higher the temperature difference is between the CO_2 inside the wellbore and the rock formation nearby the wellbore wall, the more apparent the drop of formation pressure is for stiffer materials, as seen in Figure 6.12.

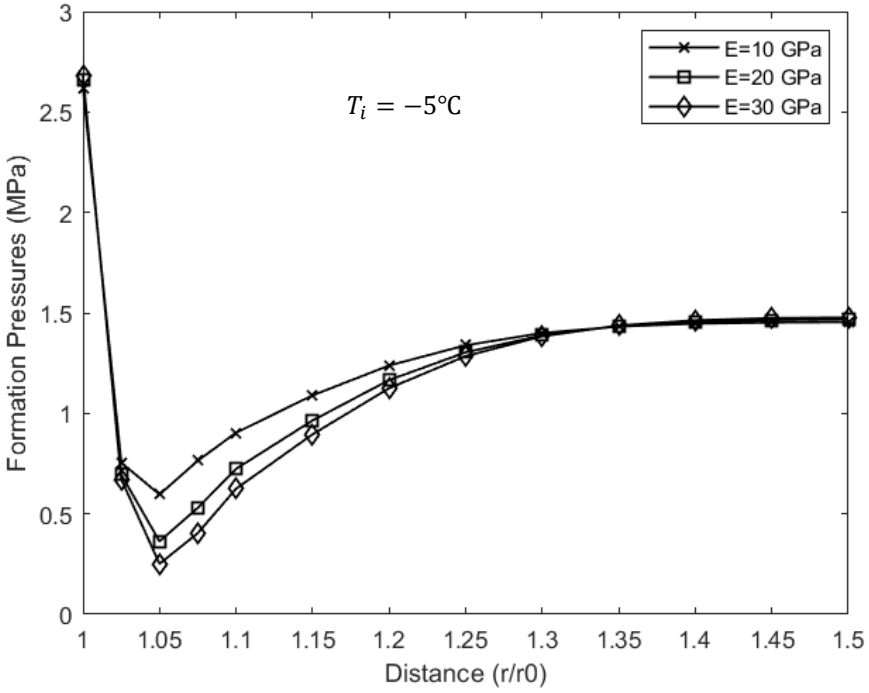

Figure 6.12a

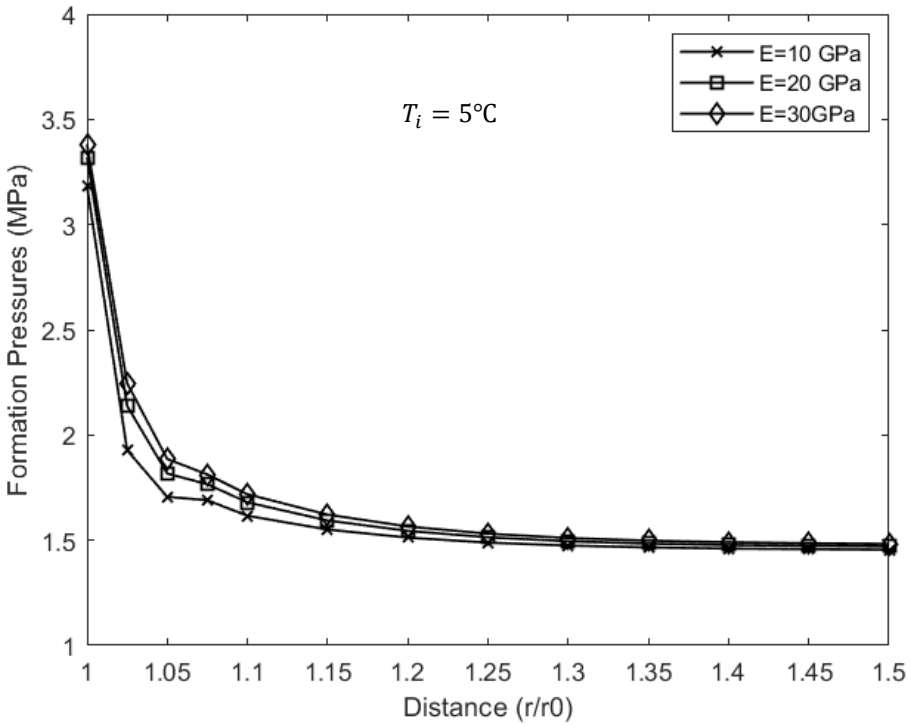

Figure 6.12b

Figure 6. 12 Influence of Young's modulus (E) on the formation pressure of the rock under different internal temperatures a)$T_i = -5℃$ and b) $T_i = 5℃$ for Case 1 conditions, t=80 s

Apart from effective stress and formation pressure, damage evolution is significantly influenced by the stiffness of the formation. It can be seen in Figure 6.13 that by increasing the stiffness less damage is produced. This is in agreement with Ma and Zhao (2018), who indicated after FEM numerical modelling that the biggest the Young's modulus of a material the less damage is being spotted at the vicinity of the wellbore. Increased temperature gradient between the wellbore wall and formation also increases the damage as seen by comparing Figure 6.13a and 6.13b.

For the wellbore, at higher depth (1000m) two different injection temperatures are used: 5℃ and 33℃. The temperature of the formation is $T_{form} = 33℃$, the same as in Case 3. These temperatures are selected to investigate if Young's modulus influence exist when there is a temperature difference between wellbore wall and formation. The Young's modulus influence to the effective stresses of the wellbore are presented in Figure 6.14.

In Figures 6.15 and 6.16 the influence of Young's modulus on formation pressure and damage evolution is presented, respectively.

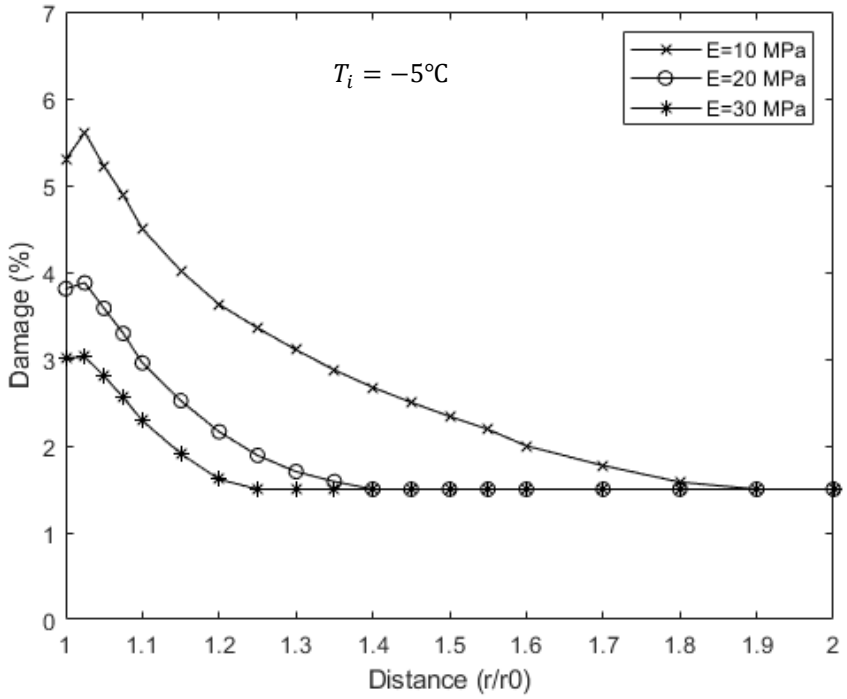

Figure 6.13a

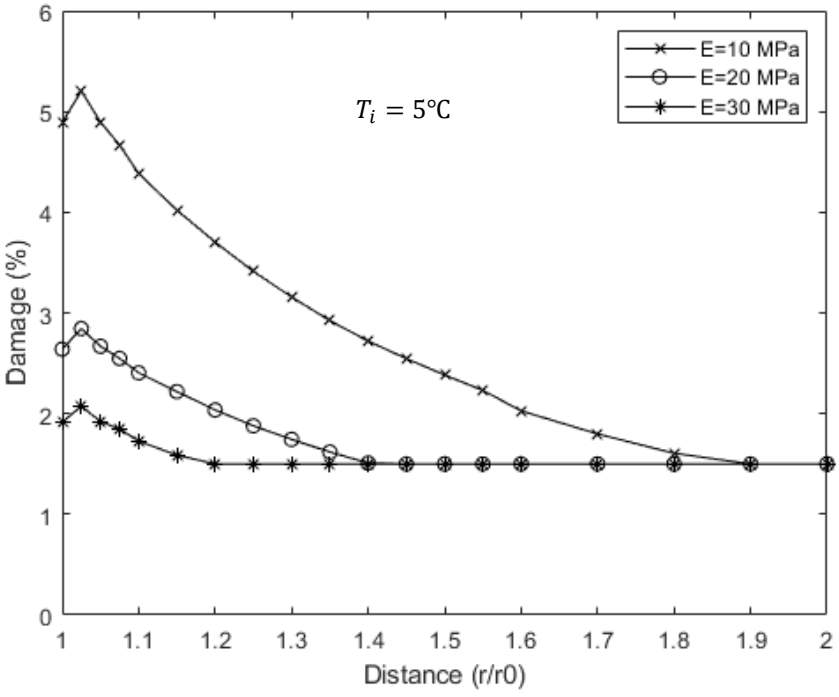

Figure 6.13b

Figure 6. 13 Influence of Young's modulus (E) on the damage of the rock under different internal temperatures a)$T_i = -5℃$ and b) $T_i = 5℃$ for Case 1 conditions, t=80 s

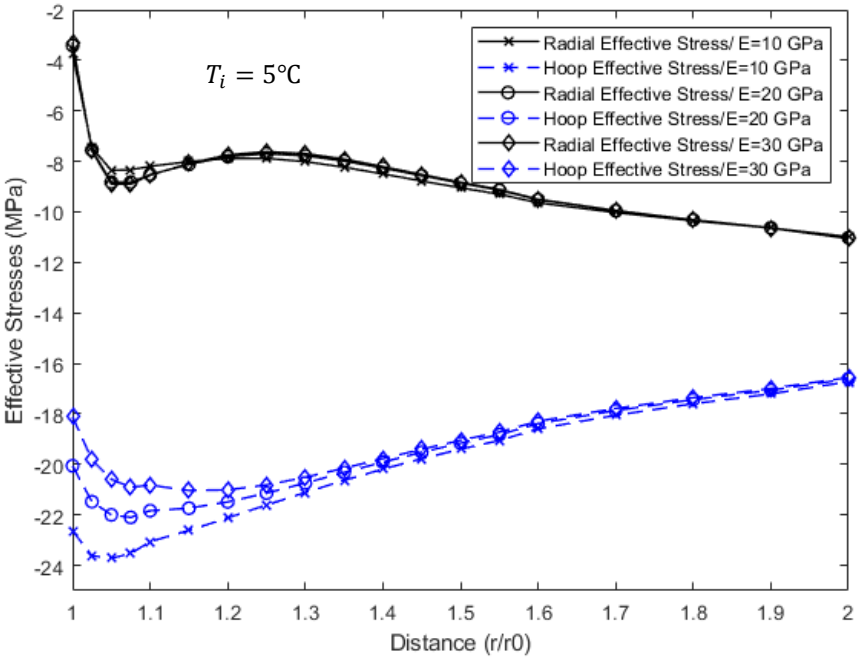

Figure 6.14a

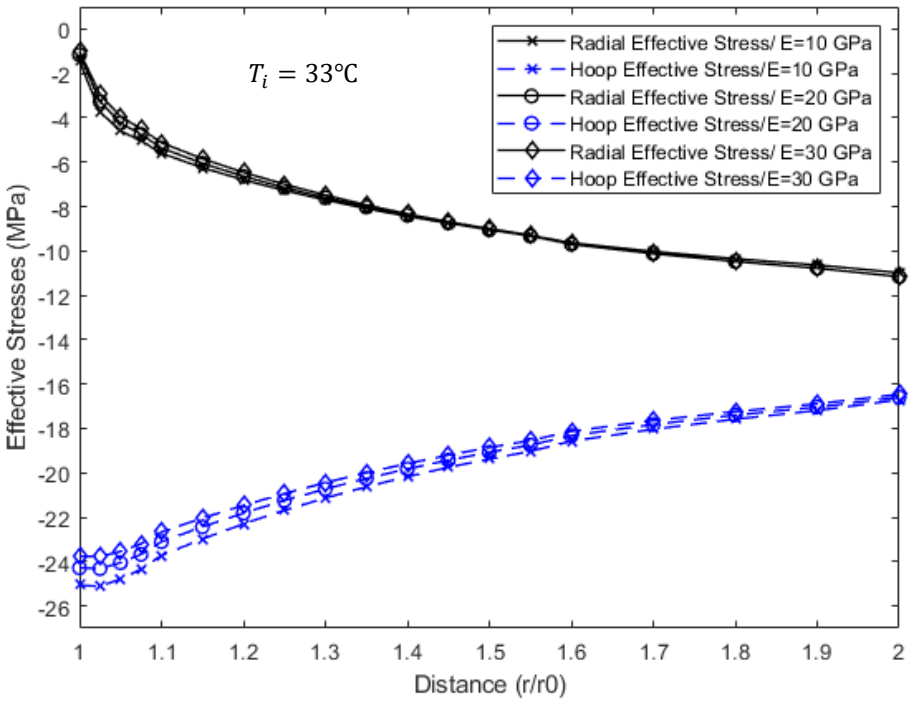

Figure 6.14b

Figure 6. 14 Influence of Young's modulus (E) on the effective stresses of the rock under different internal temperatures a)$T_i = 5$℃ and b) $T_i = 33$℃ for Case 3 conditions, t=80 s

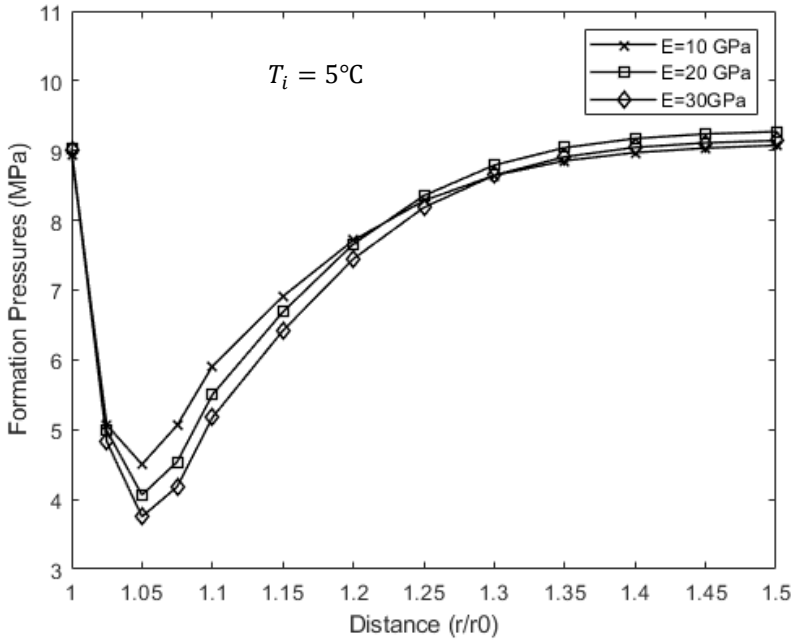

Figure 6.15a

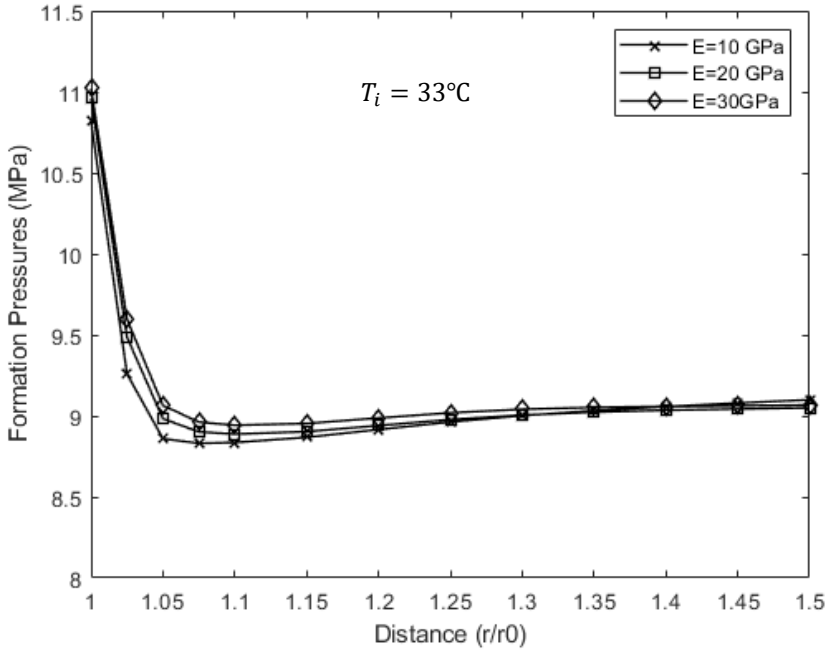

Figure 6.15b

Figure 6. 15 Influence of (E) on the formation pressure of the rock under different internal temperatures a)$T_i = 5℃$ and b) $T_i = 33℃$ for Case 3 conditions, t=80 s

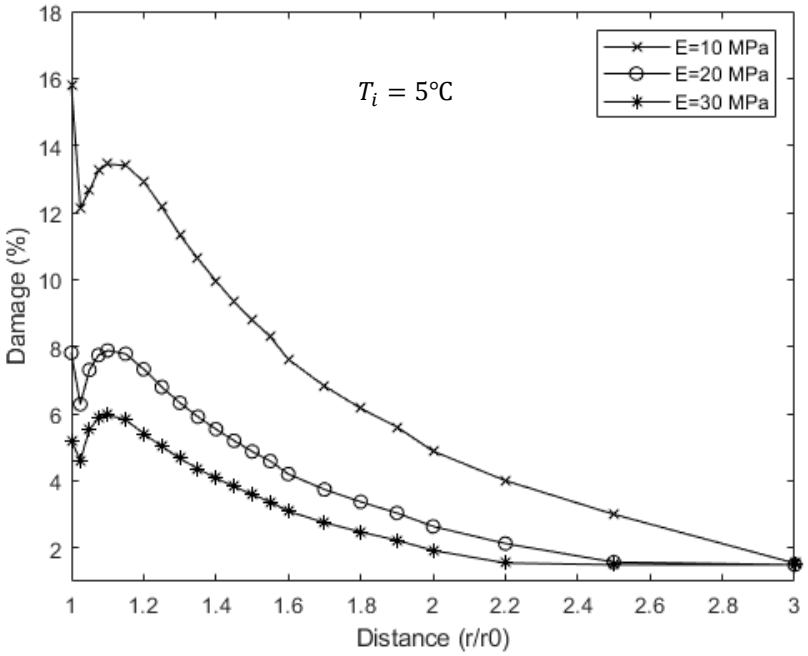

Figure 6.16a

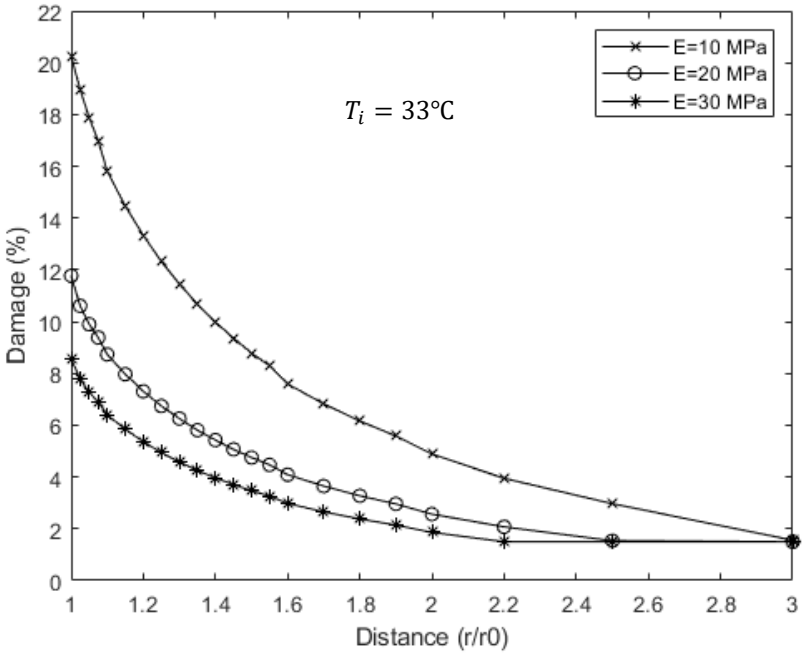

Figure 6.16b

Figure 6. 16 Influence of (E) on the damage of the rock under different internal temperatures a)$T_i = 5℃$ and b) $T_i = 33℃$ for Case 3 conditions, t=80 s

It was identified that at low internal temperatures and stiffer material, the hoop effective stress tends to induce higher tensile stress at the wellbore head (see Figure 6.11a), while reduces the compressive stress of wellbore wall at higher depth conditions (see Figure 6.14a).

Additionally, for the isothermal cases, where temperature of the formation is the same as the internal wellbore temperature, Young's modulus has an insignificant influence on the results (see Figure 6.11b, Figure 6.12b, Figure 6.13b, and Figure 6.14b). However, during thermal cooling, formation pressure decreased more for stiffer material, as seen in Figure 6.12a, and 6.15a.

6.3.2 Leakage term (γ) influence

The leakage parameter or aperture factor controls the transfer of mass between the porous block and the fissure domain in local thermal non-equilibrium. Values of the leakage term can vary from 5.3×10^{-11}/Pa·s to 10^{-7}/Pa·s (Kazemi, 1969; Gelet et al., 2012a). Three different values were used ($10^{-7}, 10^{-9}, 10^{-11}$) for Case 3 conditions to study the influence of the fluid leakage parameter on the results. The Case 3 condition, which describes a depth of 1000 m, was selected as an example to indicate the leakage aperture factor influence. The internal temperature for this parametric study is 5℃ corresponding to an injected temperature of -5℃ according to Vilarrasa and Laloui (2016). The same mesh, boundary conditions were used as described in Figure 6.1. Young's modulus was set equal to 10 GPa, to focus the parametric study to the leakage aperture factor. In Figure 6.17, the influence of the leakage term to the effective stresses of the wellbore is presented, while in Figure 6.18 and Figure 6.19 the effect of the leakage term to the pore-fissure rock pressures and damage is investigated, respectively.

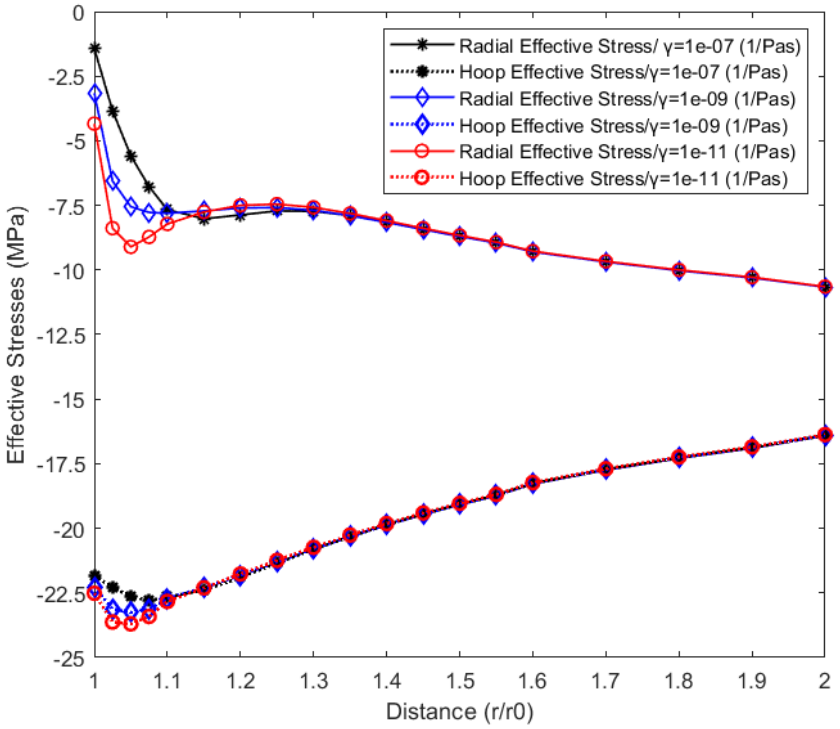

Figure 6.17 Leakage term influence on effective stress (Case 3, $T_i = 5$℃)

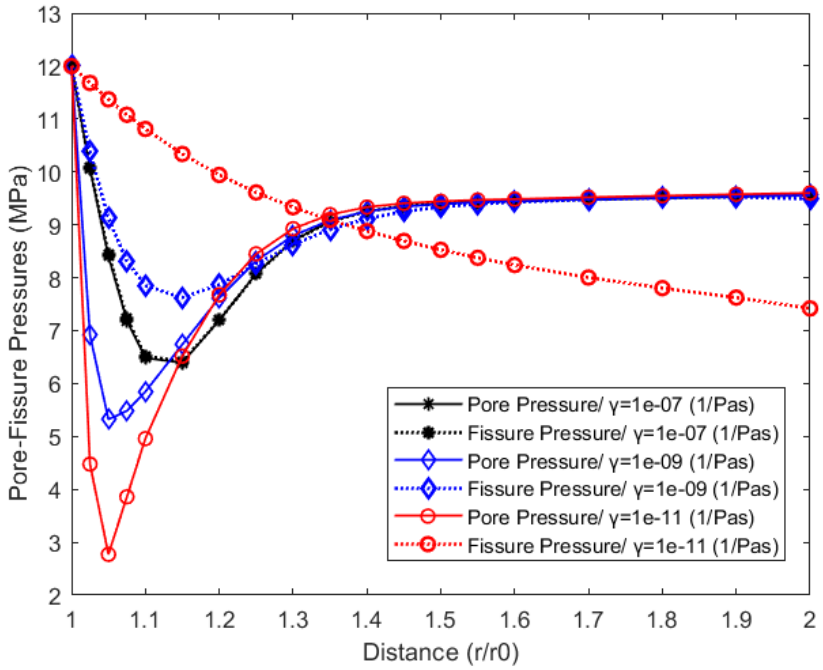

Figure 6. 18 Leakage term influence on pore-fissure pressure (Case 3, $T_i = 5$℃)

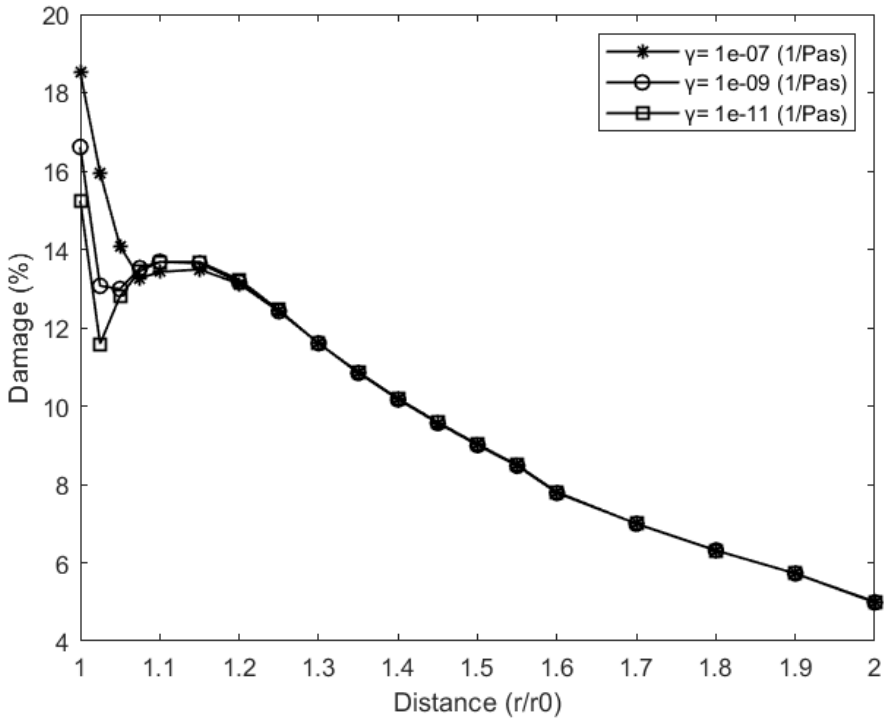

Figure 6. 19 Leakage term influence on damage (Case 3, $T_i = 5$℃)

From Figure 6.17, the radial effective stress becomes more compressive as the aperture factor decreases, while the hoop effective stress is slightly changing. Additionally, it can be seen from Figure 6.18 that lower leakage parameter induces higher pore pressure drop and increases the difference in pressure between the two phases. It can be outlined that rocks with low capability of mass transfer between the phases are vulnerable to potential fracturing due to stress relief and extreme pore pressure drop.

As far as it concerns the damage, the lower the leakage term is, the less damage appears in the vicinity of the wellbore at a specific timestep of injection, as seen in Figure 6.19. Once the mass transfer is achieved and the two domains are in equilibrium the damage will increase and the rock can then be considered as a single-phase medium.

6.3.3 Permeability influence

Changing the permeability of the rock can influence the dissipation speed of the fluid inside the domain. For the estimation of the permeability influence to the effective stresses and pore-fissure pressures, the permeability of the porous domain kept constant, while the permeability of the fissure network varied. The Case 3 conditions were selected, as there is no need to present any

other depth as the permeability influence would be identical. The internal wellbore temperature of 5℃ is used indicating the scenario of injecting CO_2 at -5℃. Figure 6.20 presents the permeability influence on the effective stresses, while Figure 6.21 the permeability influence on the pore and fissure pressures.

It can be seen in Figure 6.20 that the effective stresses are not influenced significantly by the permeability. However, changing the permeability, the difference between the pore and fissure network pressure can increase. Consequently, more time will be needed for them to achieve equilibrium (see Figure 6.21).

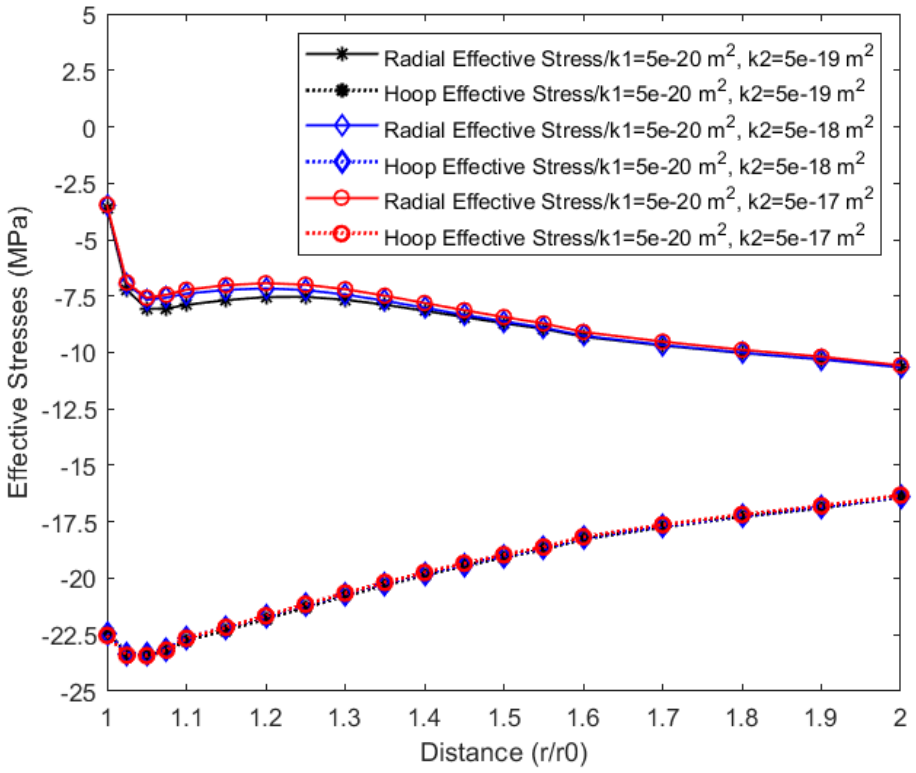

Figure 6. 20 Influence on the effective stress keeping the permeability of the porous domain constant and varying the permeability of the fissure network (Case 3, $T_i = 5$℃).

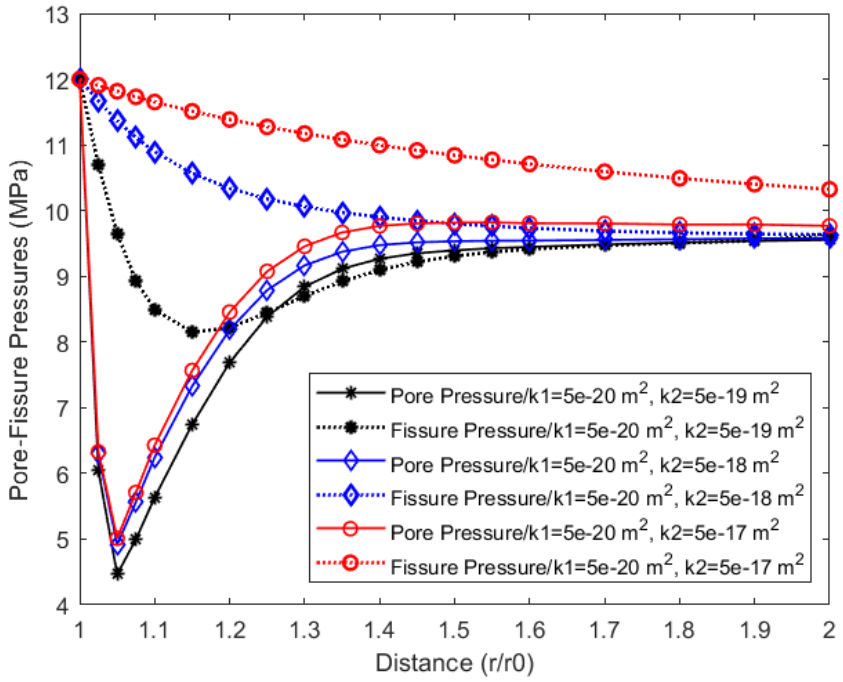

Figure 6. 21 Influence on the pore-fissure pressure keeping the permeability of the porous domain constant and varying the permeability of the fracture network (Case 3, $T_i = 5$℃).

6.4 Wellbore simulation results using Stainton sandstone as the hosting rock

In this section, the wellbore wall is simulated with rock characteristics derived from the experimental data in Chapter 4. The critical state concept is applied, and the boundary yield surface model's parameters used, are obtained by the parametric study achieved in Section 5.11. The mesh is the same as in Figure 6.1, with the inner radius being 0.1m and the outer radius 800m.

In Chapter 4, the Poisson's ratio, Young's modulus, shear, and bulk modulus were calculated, and it was identified that their values vary at different temperatures and confining pressures. Bulk modulus $K_{bulk}^{el}(D,T)$ was calculated based on Equation (3.161) and Young's modulus is expressed according to bulk modulus and Poisson' s ratio. Linear change with temperature for the critical state parameters is assumed. The secant Poisson's ratio is used for the analysis as the tangent value calculated by the experiments exceeds the elastic limit of 0.5 and the secant value better represents the triaxial tests (as discussed in Chapter 5). The critical state parameters used, are obtained from the numerical simulations of Section 5.11. All the parameters used, including mechanical and critical state parameters, are gathered in Table 6.3.

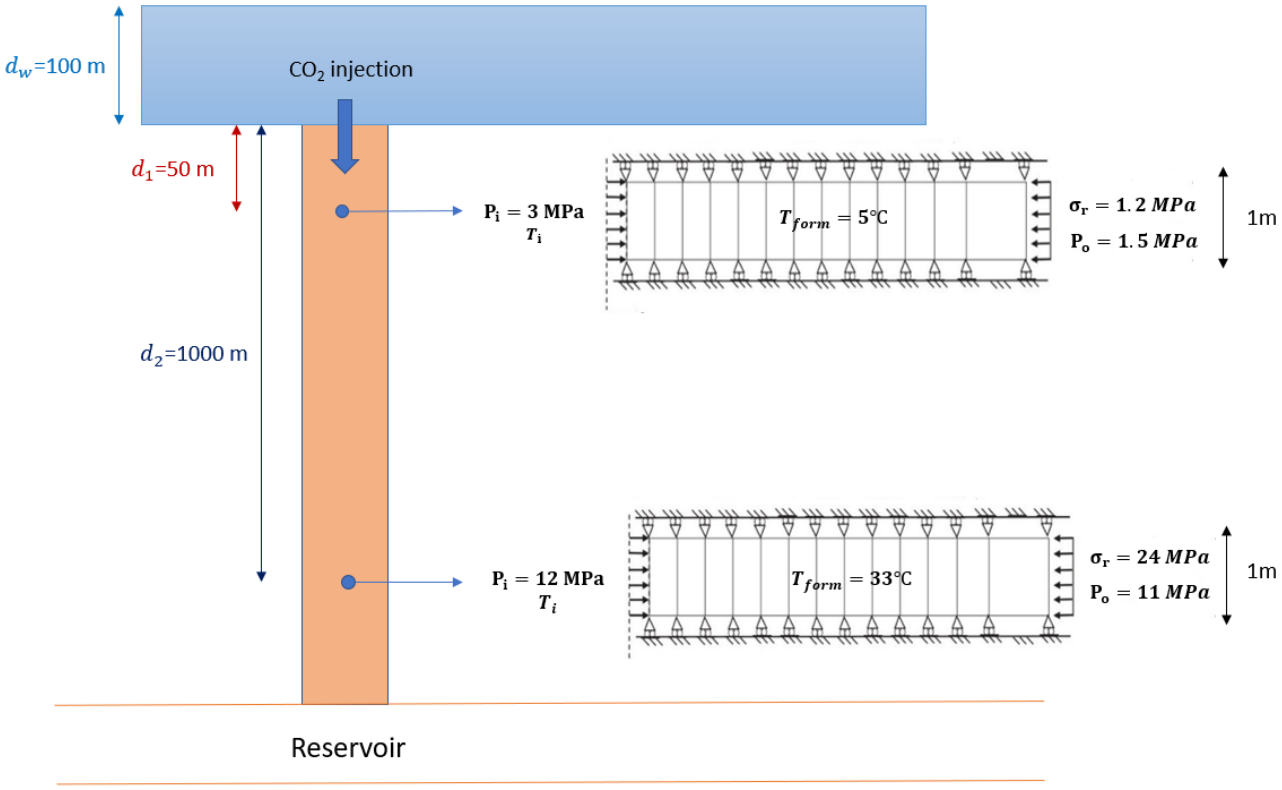

Figure 6. 22 Studied depths of a wellbore and loading conditions (d_w is the sea depth, d_1 is the 50 m depth of the wellbore, d_2 is the 1000 m depth of the wellbore)

As the fluid inside the porous and fissure network is saline water, the compressibility of it is considered to be 1.6× 10^{-9} GPa^{-1}, based on Fine and Millero (1973). The compressibility of the mixture is expressed based on Gelet et al. (2012a) as follows:

$$C_f = 3\frac{1-2\nu}{E} \tag{6.1}$$

The compressibility of the solid (C_s) is obtained by Ma and Zhao (2018) and is equal to 0.0364 GPa^{-1}. The compressibility of the porous medium is 0.9, based on Gelet et al. (2012a). The effective stress parameters based on equations presented in Section 3.1.2 were calculated as $\beta_1 = 0.66$ and $\beta_2 = 0.1$.

Table 6. 3 Stainton Sandstone parameters used for the simulation based on experimental results

Secant Poisson's ratio $[\nu]$ The presented equations are the experimental outcome of Section 4.4	**50m depth (UCS test)**:	$0.0025T + 0.277$ $-0.0086T + 0.222$	$T \geq -5℃$ $T < -5℃$
	1000m depth (24 MPa):	$0.0001T + 0.180$ $0.0026T + 0.192$	$T \geq -5℃$ $T < -5℃$
Porosity of porous domain (φ_1)	0.17		
Porosity of fissure network (φ_2)	0.017		
Gradient of isotropic compression line (ICL) $[\lambda]$	0.1		
Slope of the unloading-reloading line (URL) $[\kappa]$	**50m depth (UCS test)**:	$-9 \times 10^{-6}T + 0.0004$ $3 \times 10^{-5}T + 0.0006$	$T \geq -5℃$ $T < -5℃$
	1000m depth (24 MPa):	$-5 \times 10^{-6}T + 0.0031$ $-4 \times 10^{-5}T + 0.0029$	$T \geq -5℃$ $T < -5℃$
Parameter controlling the shape of the bounding surface $[M]$	1.9		
Material constant of the bounding surface $[R]$	2		
Average value of Slope of the Critical State Line (CSL) $[M_{cs}]$	$-0.008T + 1.62$ $-0.0055T + 1.63$	$T \geq -5℃$ $T < -5℃$	
Average value of hardening material constant $[m_p]$	**50m depth (UCS test)**: 3 **1000m depth (24 MPa)**: 13		
Material parameter $[k_d]$	**50m depth (UCS test)**: 7 **1000m depth (24 MPa)**: 37		

6.4.1 Simulation results for the wellbore head conditions (50 m wellbore depth case).

Four different internal temperatures of the wellbore due to CO_2 injection are simulated using the FEM model described in Figure 6.22 and input parameters of Table 6.3. The selected internal temperatures of the wellbore are -10℃, -5℃, 0℃ and 5℃. The injection pressure is assumed to be 3 MPa. For the 50m depth of the wellbore, the hydrostatic depth is considered 150m and consequently the applied pore-fissure pressures prior to injection are 1.5 MPa (as in Section 6.1). The pore-fissure pressures distribution for each internal temperature, for the first 80 s of injection, is presented in Figure 6.23. In Figure 6.24 and 6.25 the effective stress curves (both radial and hoop) and the damage evolution of the material, for each temperature scenario, is presented.

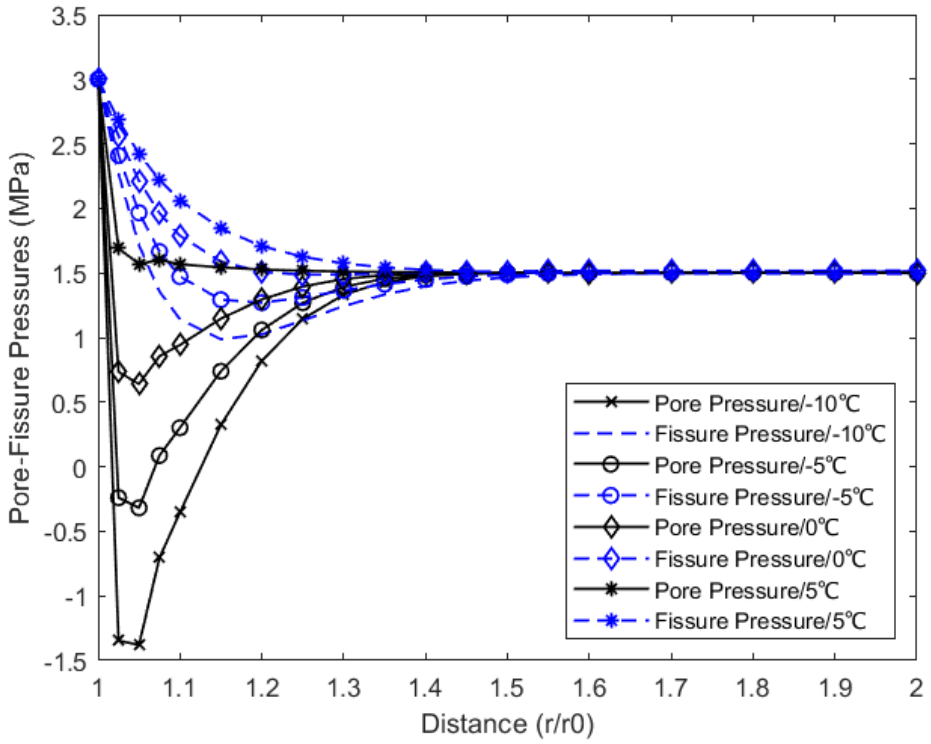

Figure 6. 23 Pore-fissure pressure profiles for Stainton sandstone for different injection temperatures at 80 s.

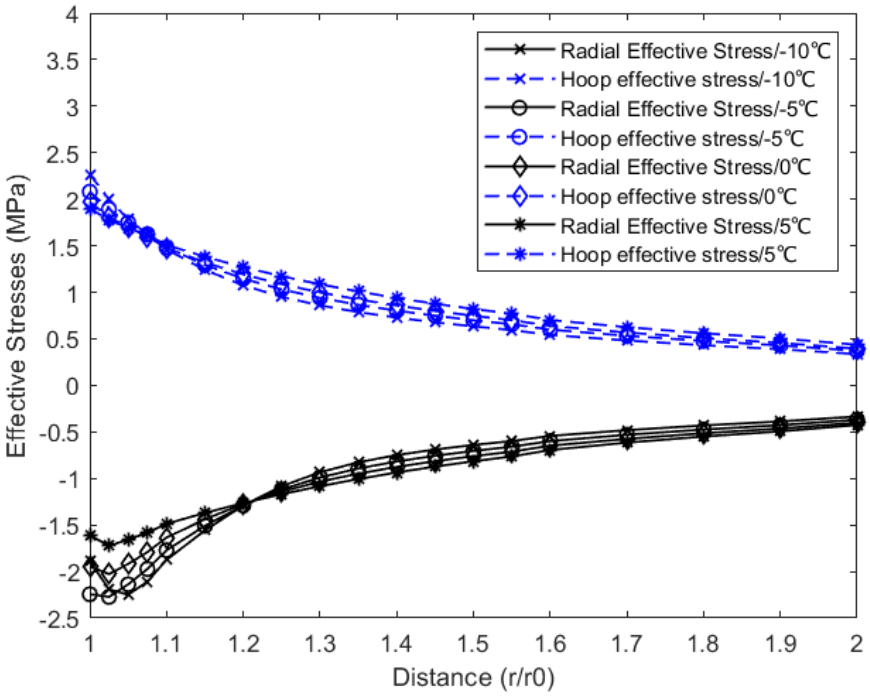

Figure 6. 24 Effective stress profiles for Stainton sandstone for different injection temperatures at 80 s.

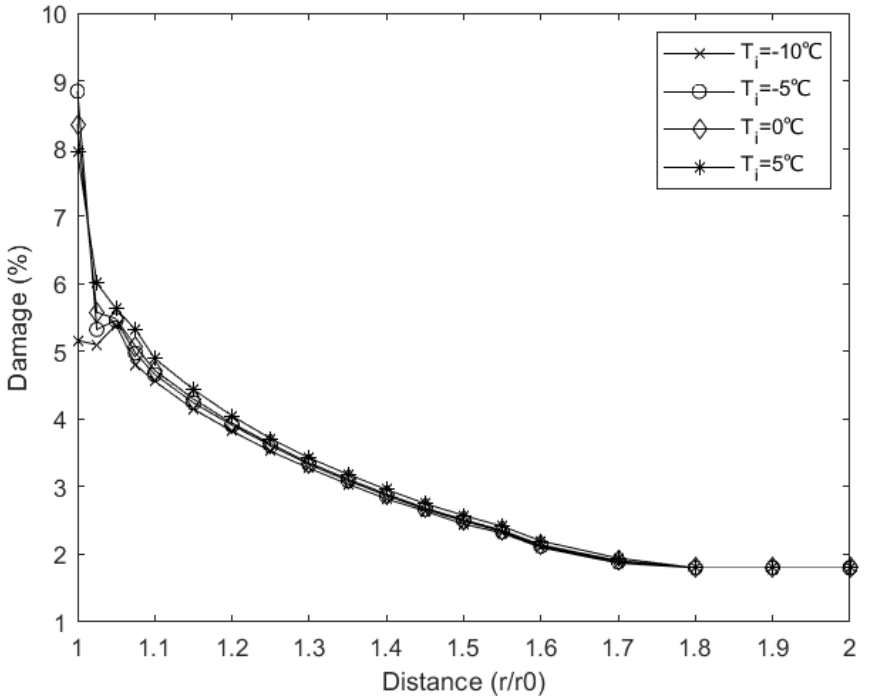

Figure 6. 25 Damage profile for Stainton sandstone for different internal temperatures at 80 s.

From Figure 6.25, at the wellbore head (the 50m depth case) damage decreases as the internal wellbore temperature is lower. This can be explained as pore pressure decreases significantly, while lower internal wellbore temperatures are selected (see Figure 6.23) and higher tensile stress is encountered, as seen in Figure 6.24. These results correspond to an early-stage response of the wellbore, for t=80s.

It should be also noted that Poisson's ratio significantly influences the results. Based on experimental outcomes of Section 4.4, the secant Poisson's ratio linear decrease from 15 ℃ to -5℃ stops, followed by an increase for further temperature drop, until reaching the -10℃. The huge drop of damage seen for the -10℃ can be explained by this change in trend for the Poisson's ratio.

Apart from the behaviour of the wellbore at an early stage of injection (t = 80s), profiles of fluid pressures, effective stresses, formation pressures and damage in the double porosity system describing the Stainton sandstone at different representative times for the wellbore head (50 m depth case) are presented for $T_i = -5℃$, as seen in Figures 6.26-6.31. The selected times correspond to an early (t = 80s), intermediate (t = 800s) and late response (t = 3200s). Immediately prior to the intermediate period, fluid leaks from the porous medium to the fractured network, and fluid pressures come into equilibrium.

Furthermore, at the early time of the simulation, as the fluid is firstly flowing in the fractured network, fissure pressure decreases, and the effective compressive hoop and radial stress increases (Figure 6.28-6.29). The formation tends to shrink, and permeability of the porous block may decrease due to compaction. The peak of pore pressure as seen in Figure 6.26 occurs due to low permeability of the pores. This pore pressure drop peak also reduces the effective radial stress at a small distance from the wellbore vicinity, which according to Ma and Zhao (2018) leads to tension cracking if pore pressure achieves a high level. Formation pressure (see Figure 6.30) drops significantly for early formation response, while afterwards formation pressure increases until stabilising. Damage increases with time reaching almost 15% of damage after 9 hours of injection (see Figure 6.31).

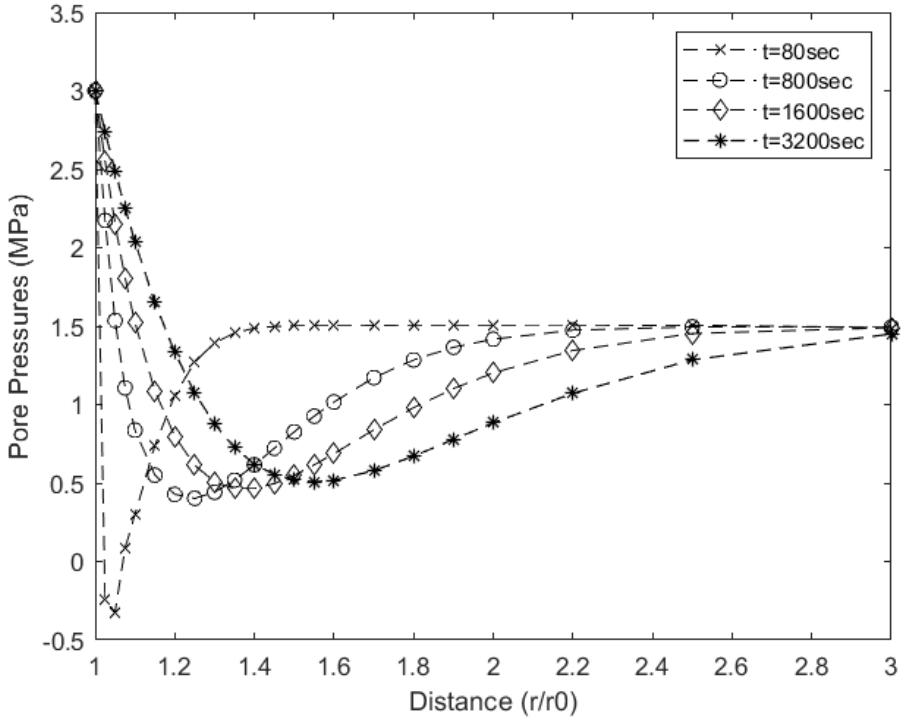

Figure 6. 26 Pore pressure evolution for the wellbore head – 50 m depth case.

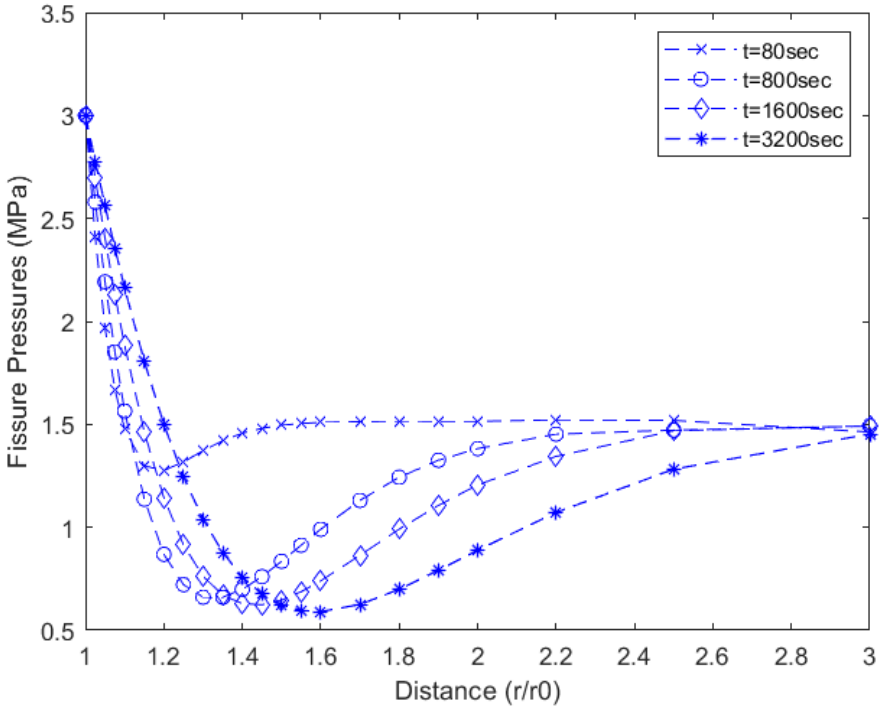

Figure 6. 27 Fissure pressure evolution for the wellbore head -50m depth case.

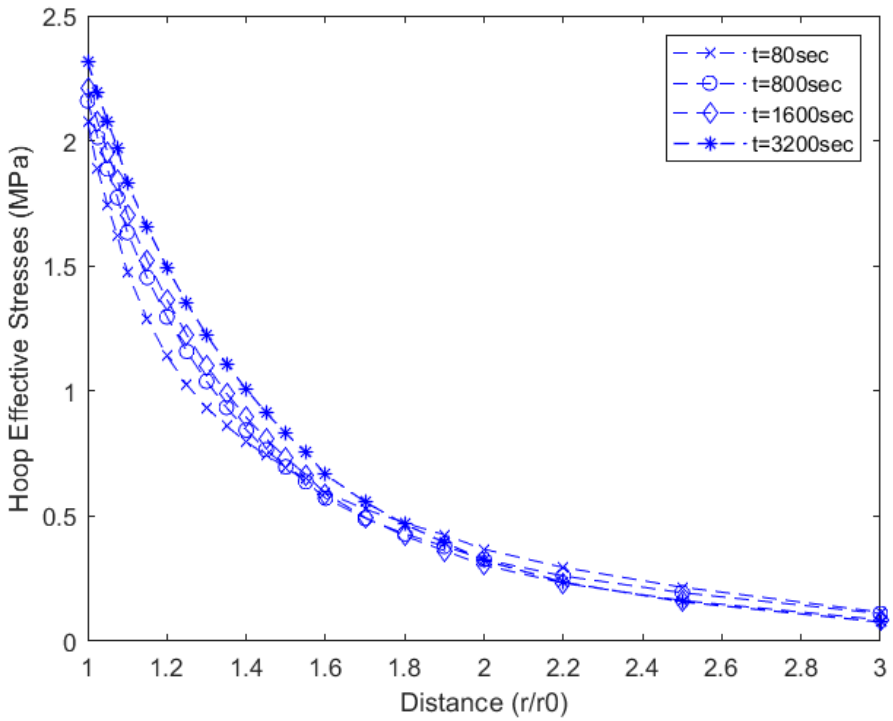

Figure 6. 28 Hoop effective stress evolution for the wellbore head – 50m depth case.

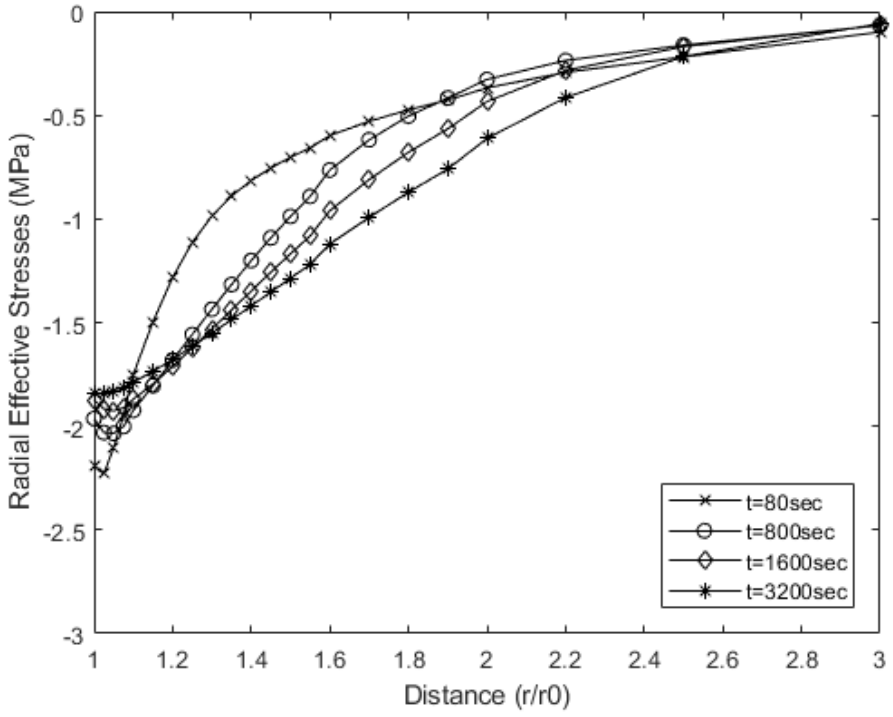

Figure 6. 29 Radial effective stress evolution for the wellbore head – 50m depth case.

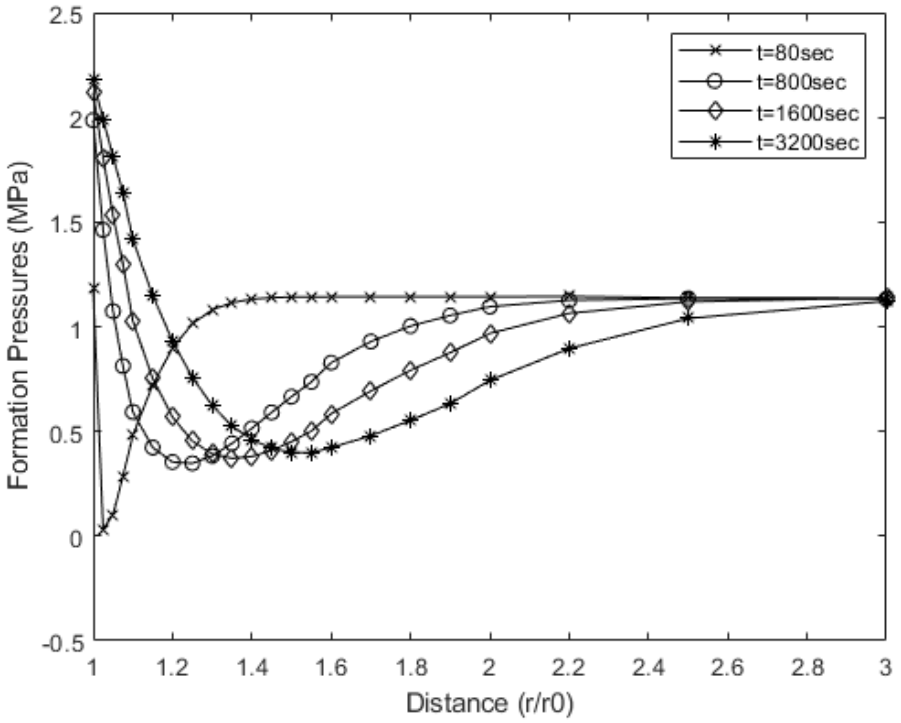

Figure 6.30 Wellbore pressure evolution for the wellbore head – 50m depth case.

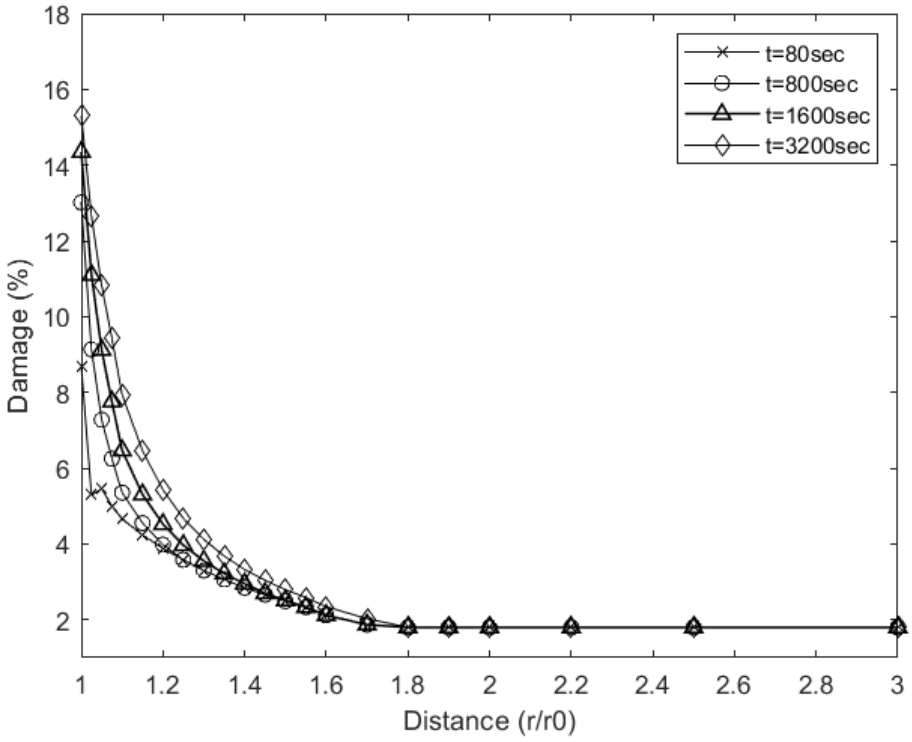

Figure 6.31 Damage evolution for the wellbore head – 50m depth case.

6.4.2 Results for 1000 m depth case.

Injecting CO_2 at various temperatures leads to a range of higher temperatures at higher depths (Lu and Connell, 2008; Lindeberg, 2011; Vilarrasa et al., 2013; Aursand et al., 2017). For an injection temperature of -10℃, at 1000 m depth temperature can increase and reach 0℃, while for an injection CO_2 temperature of 5℃, it can reach at 1000 m depth the temperature of 15℃ (Vilarrasa et al., 2013). Considering that the temperature of the Sandstone at 1000 m depth is $T_{form} = 33$℃, as seen in Figure 6.22, the lower the injected temperature, the higher the thermal loading applied. The effect of four different fluid temperatures, 0℃, 5℃, 10℃ and 15℃, on pore-fissure pressure, effective stress and damage are shown in Figures 6.32-6.34 respectively.

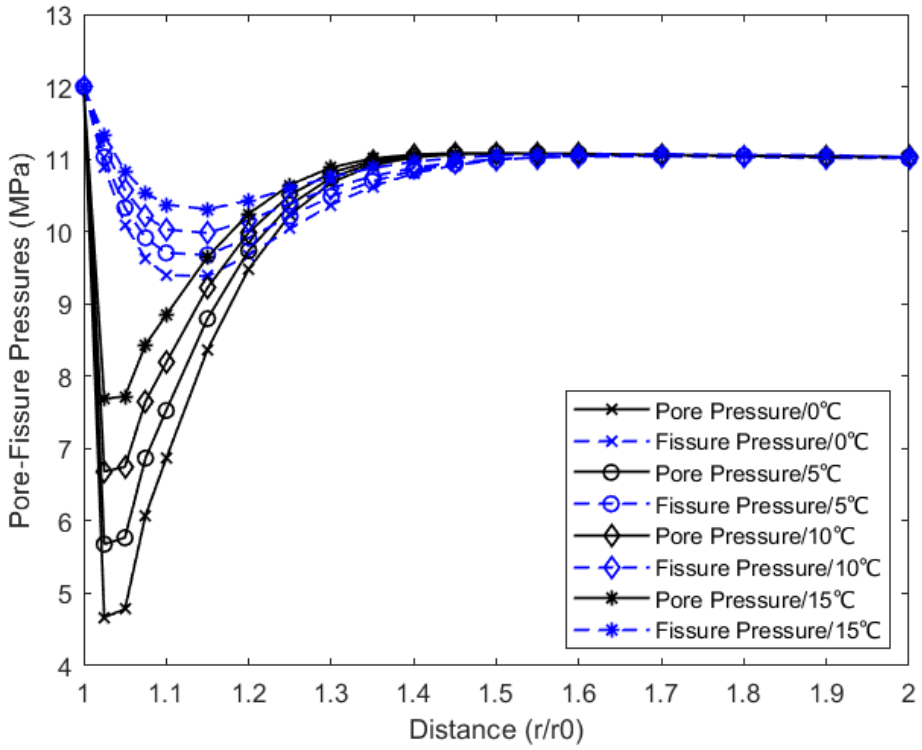

Figure 6. 32 Pore-fissure pressure profiles for Stainton sandstone for different internal temperatures at 80 s.

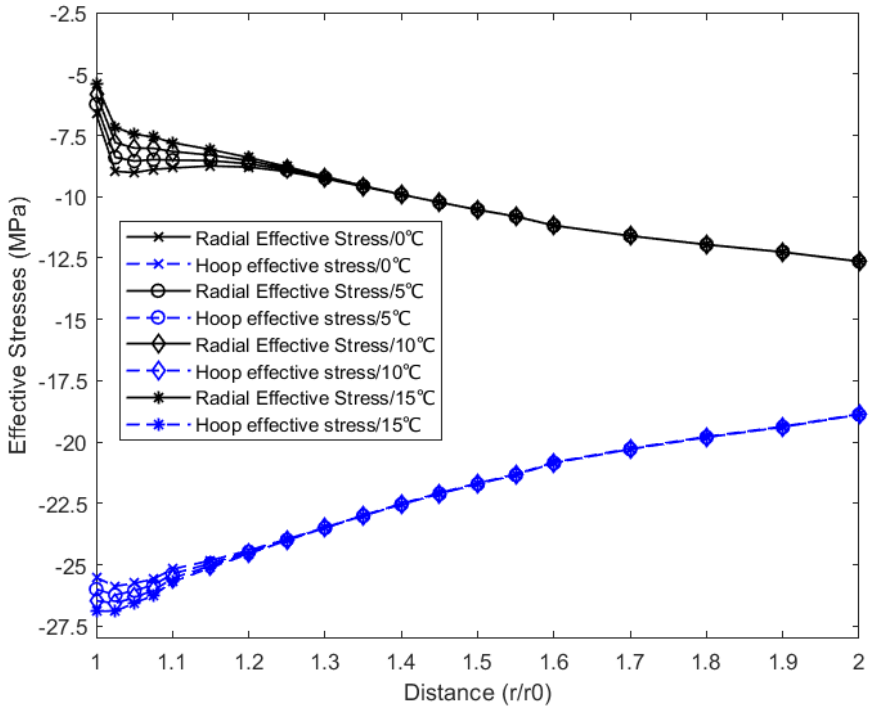

Figure 6. 33 Effective stresses profiles for Stainton Sandstone for different internal temperatures at 80 s.

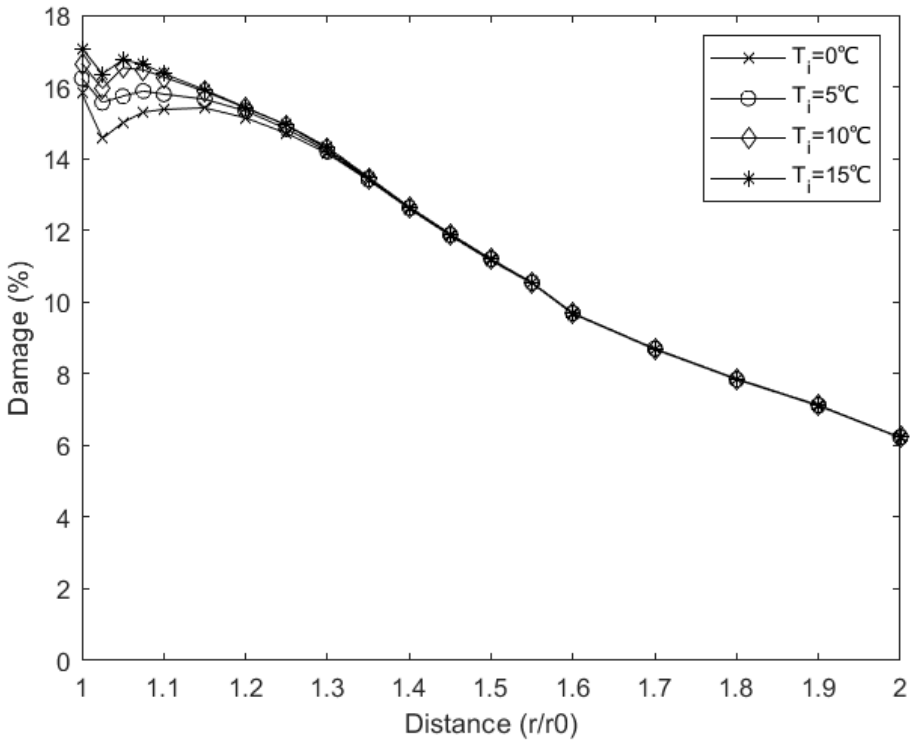

Figure 6. 34 Damage profile for Stainton sandstone for different internal temperatures at 80 sec.

Results indicate that cooling the rock in the vicinity of the wellbore significantly drops the pore pressure, while inducing more compression radially due to expansion and less compression in the hoop direction due to thermal expansion of the sandstone. Increasing the fluid temperature increases the formation pressure and radial compaction and decreases the hoop stress. Damage increases in the vicinity of the wellbore, while temperature difference between injected CO_2 and formation increases. This can be explained as thermal expansion decreases the damage as the compression hoop stress reduces and the radial effective stress increases.

Profiles of fluid pressures, effective stresses, and damage evolution at different representative times are presented in Figures 6.35-6.40 for the 1000m depth case. The selected fluid temperature is $T_i = 5℃$, corresponding to the scenario that CO_2 is injected at -5℃, with a mass flow rate of 1.5 kg/s and an overall heat transfer coefficient of 10 $Wm^{-2}K^{-1}$ (Vilarrasa et al. 2013).

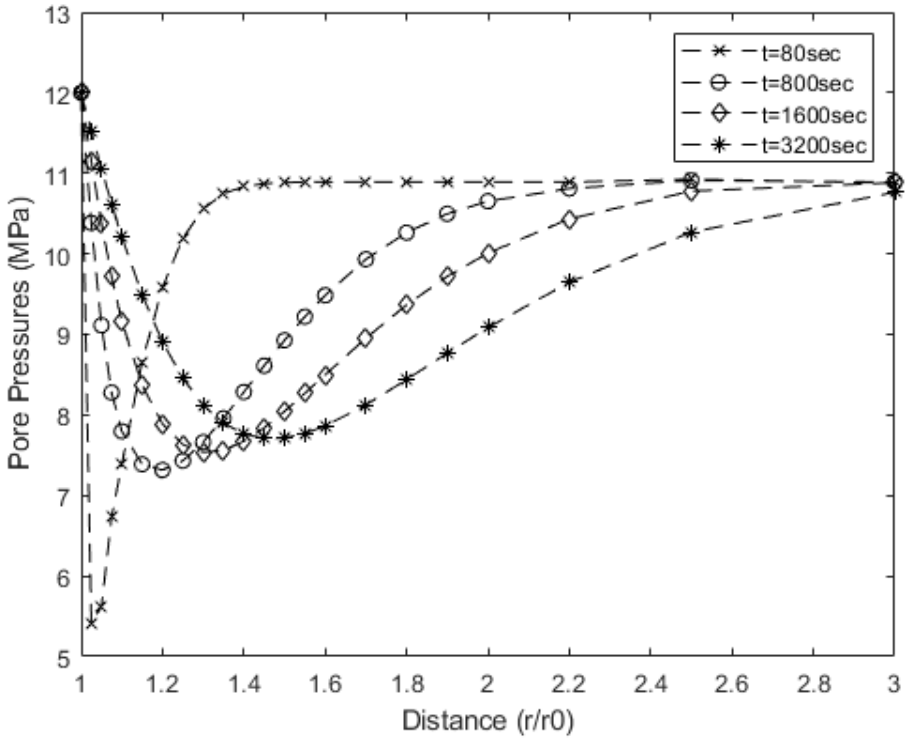

Figure 6. 35 Pore pressure evolution for the wellbore at 1000 m depth.

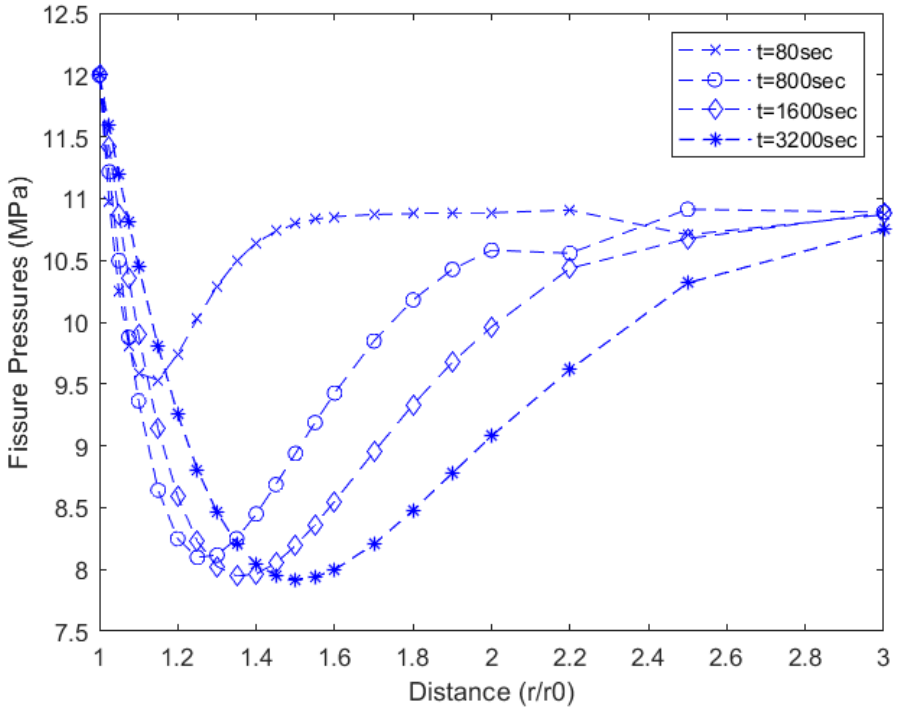

Figure 6. 36 Fissure pressure evolution for the wellbore at 1000 m depth

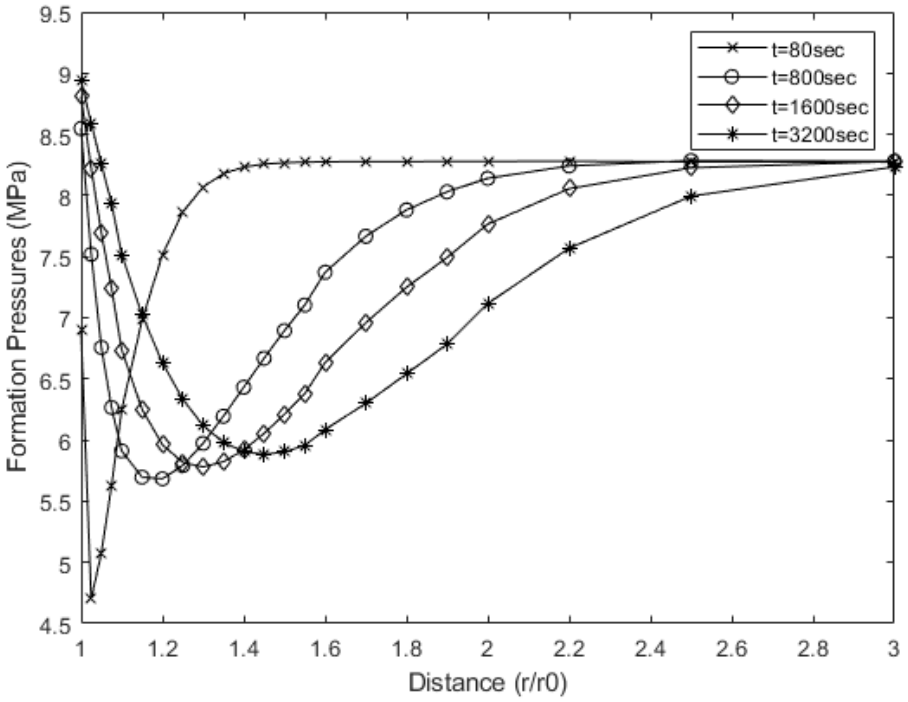

Figure 6. 37 Formation pressure evolution for the wellbore at 1000 m depth

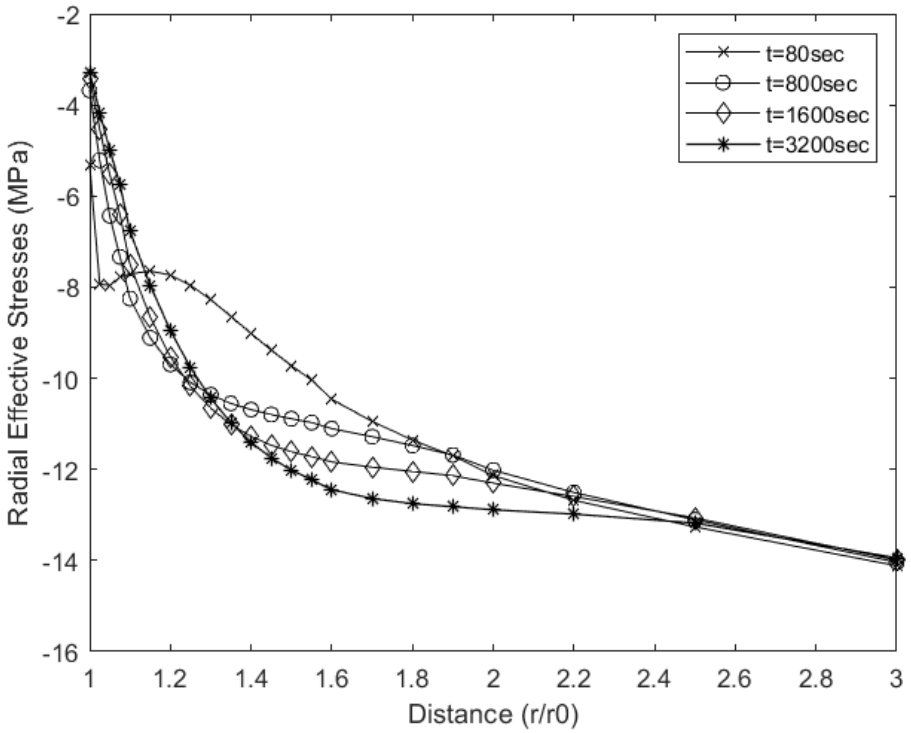

Figure 6. 38 Radial compressive effective stress evolution for the wellbore at 1000 m depth

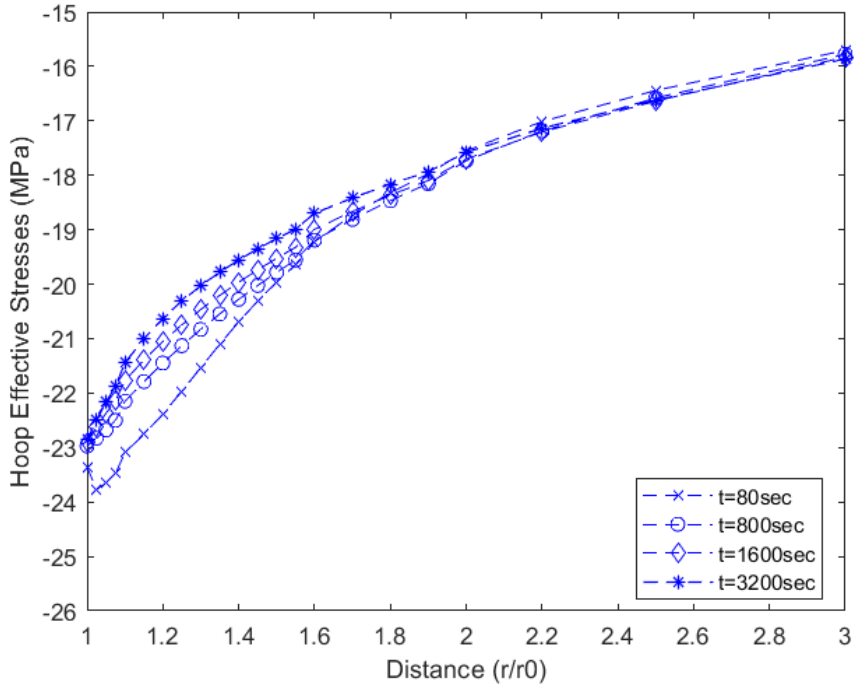

Figure 6. 39 Hoop effective compressive stress evolution for the wellbore at 1000 m depth

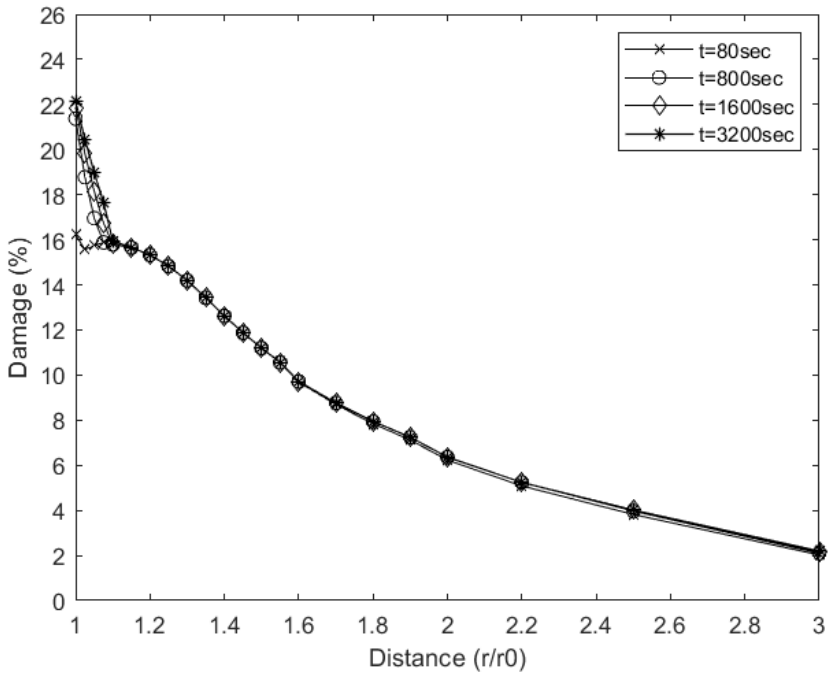

Figure 6. 40 Damage evolution for the wellbore at 1000 m depth

The behaviour of pore and fissure pressure distribution in the 1000 m depth case is similar to the wellbore head case, with significant decrease of pore pressure at early time period and quicker flow in the fissured network. At an early stage (t=80s), there is a slight increase in the compressive radial and hoop effective stress, as seen in Figure 6.38. As time passes, radial compressive stress continues to increase, while the hoop effective stress becomes more tensile, as seen in Figure 6.39. This indicates the possibility of fracture propagation in the hoop direction as stress-relief occurs. Additionally, damage variation with time, as seen in Figure 6.40 indicates that after a specific injection period, damage increases slightly reaching a peak of more than 20% at the wellbore.

6.5 Comparison of the experimental and numerical estimated Young's moduli

As mentioned in Section 6.1, Young's modulus was calculated based on Equation (5.6). The critical state mechanics concept was used to capture the change of the Young's modulus due to different loadings over time. For the two scenarios (50 m depth and 1000 m depth of wellbore) comparison between the experimental secant Young's modulus estimated from Section 4.4 and the numerical simulation's Young's modulus outcome using Equation (5.6) is achieved and presented in Table 6.4.

Table 6. 4 Comparing average Young's modulus values to numerical simulation outcomes.

Young's modulus (GPa)	15℃	-5℃	-10℃
UCS tests	6.3	7.2	9.78
Numerical simulation 50 m depth	6.6	8.2	10.4
Triaxial 24 MPa	21.8	21.5	20.8
Numerical simulation 1000 m depth	21.0	20.7	20.2

It can be outlined that numerical outcomes using Equation (5.6) are in good agreement with the experimental results presented in Section 4.4. In this way, using the linear functions of the critical state parameters and the function of secant Poisson's ratio over temperature, the behaviour of the wellbore can be simulated.

6.6 Influence of effective stress parameters

At this point it should be mentioned that the effective stress parameter greatly influences the results of the model, as they define the hydromechanical coupling. The effective stress parameter is hard to estimate as it depends on the compressibility of the grains. Selecting the 1000 m depth case as an example, the influence of the effectives stress parameters β_1 (for the porous domain) and β_2 (for the fracture domain) on the model is presented by keeping the one constant and changing the other. If one value is zero, this indicates that there is no contribution of fluid pressure from the certain phase (pores or fissures) to the effective stress of the medium. The values of effective stress parameters can vary from 0 to 1 according to (Bai, 2016b). For this parametric study, fluid temperature was selected equal to be 5℃.

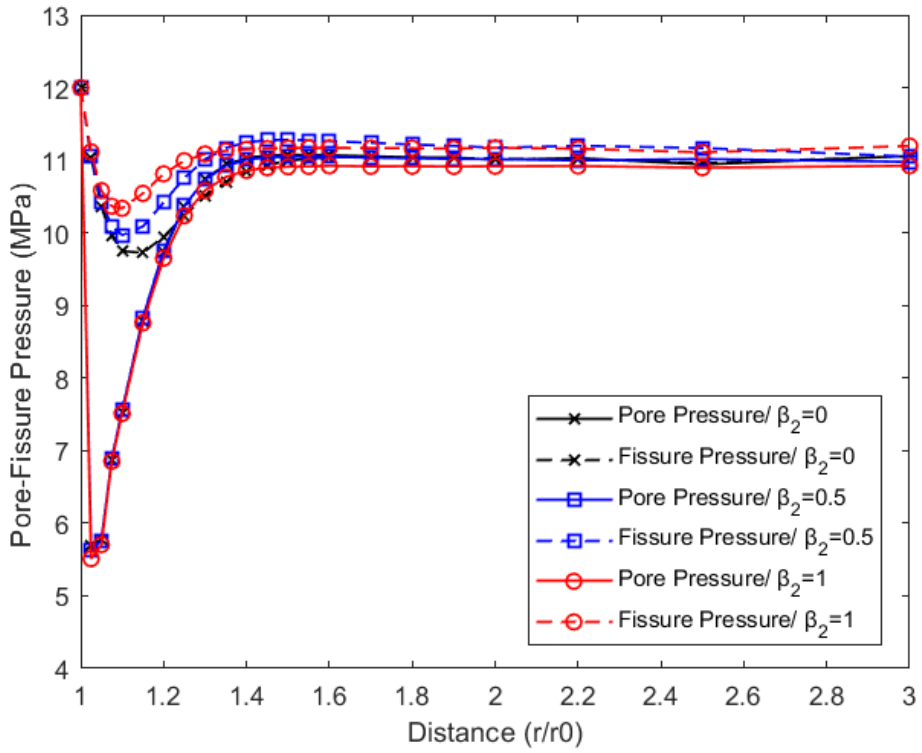

Figure 6. 41 Influence of β_2 with $\beta_1 = 0.66$ on pore-fissure pressures

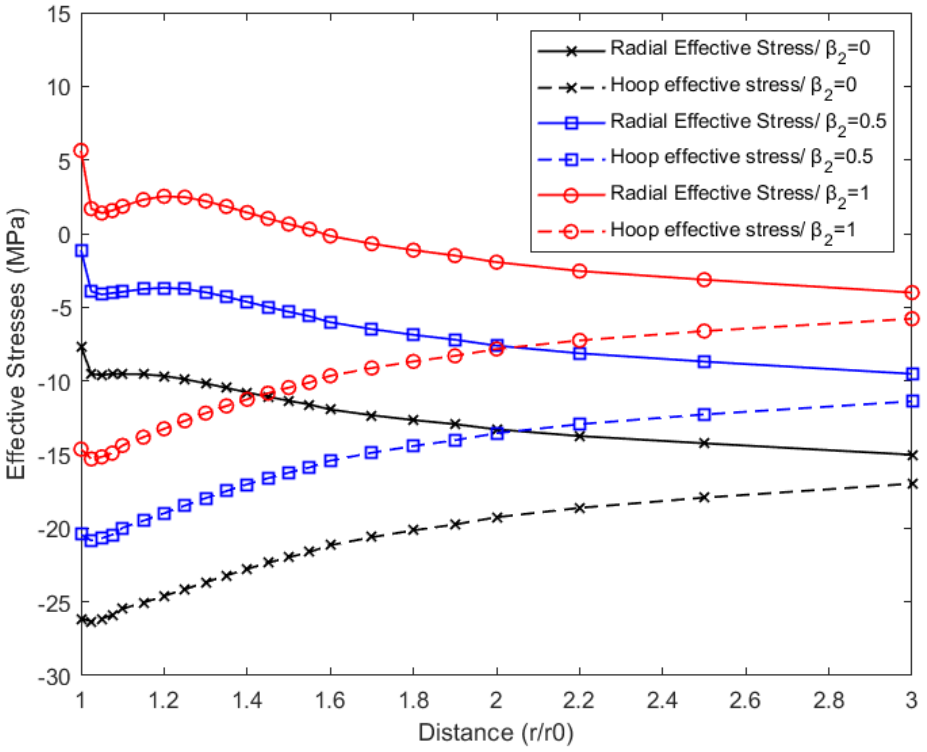

Figure 6. 42 Influence of β_2 with $\beta_1 = 0.66$ on the radial and hoop effective stresses.

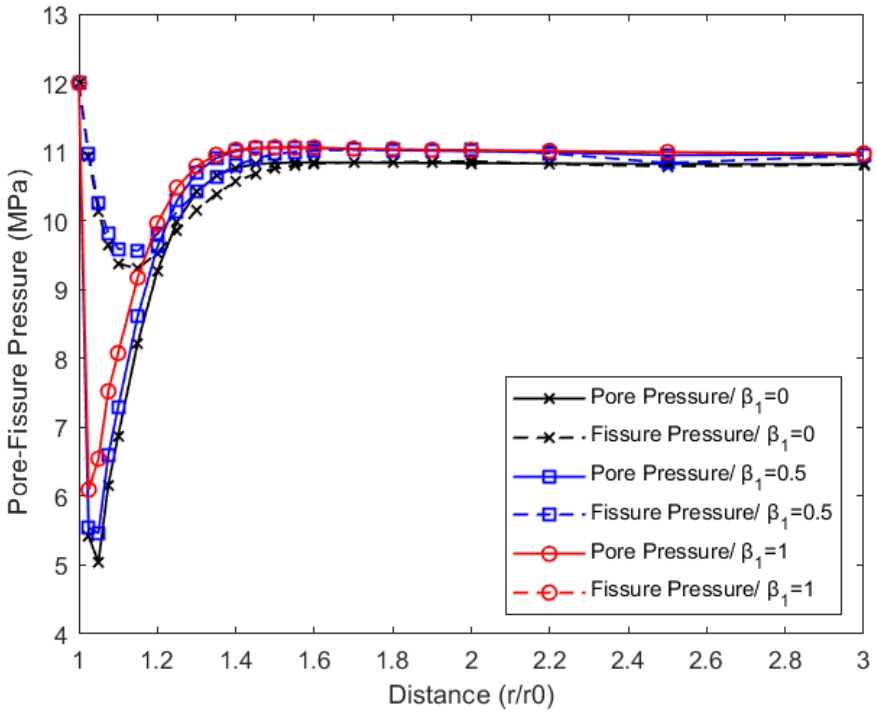

Figure 6. 43 Influence of β_1 with $\beta_2 = 0.1$ on the pore-fissure pressures.

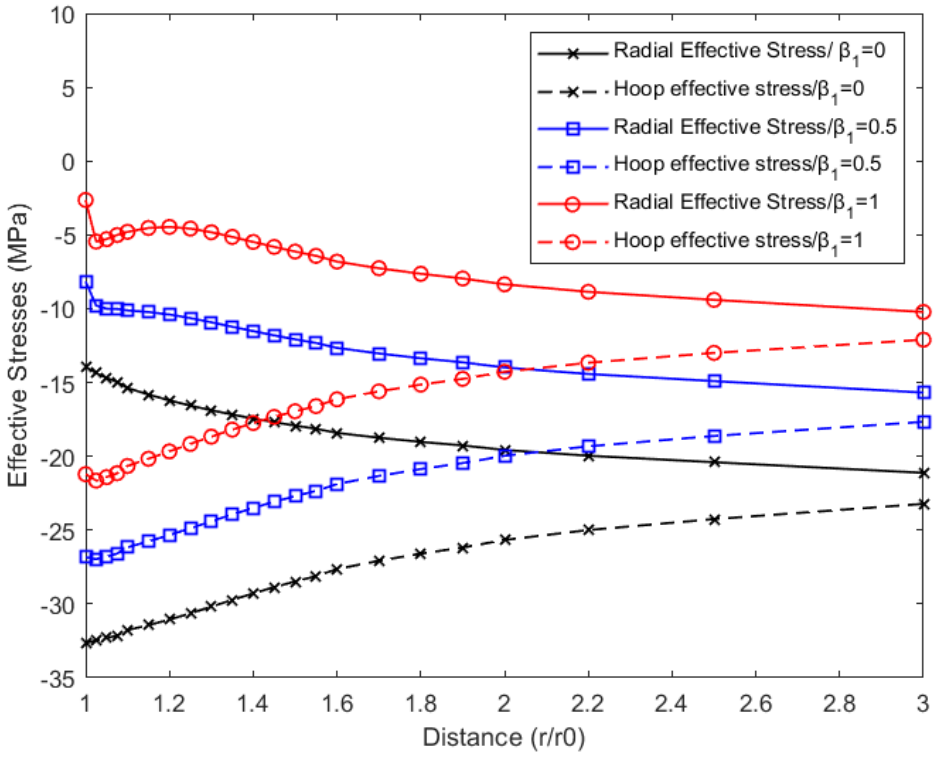

Figure 6. 44 Influence of β_1 with $\beta_2 = 0.1$ on the radial and hoop effective stresses.

It can be seen in Figures 6.41 and 6.42 that by increasing the value of β_2 and keeping $\beta_1 = 0.66$ constant, there is a tendency for the initial fissure pressure to drop in the far-field and for the tensile behaviour of both the hoop and radial stress to increase. If β_2 is held constant at 0.1 and then by increasing β_1, the same behaviour of the pore-fissure distribution and effective stress distribution over radial distance is achieved, as when β_2 increase and β_1 is constant (see Figure 6.43 and 6.44).

6.7 Discussions of numerical results

Three different case scenarios (wellbore representative depths) were studied to examine the behaviour of rock during injection of CO_2. The simulated internal temperatures and pressures were selected to describe wellbore wall case scenarios. Sub-zero conditions can appear due to the Joule-Thomson effect or low-temperature ship CO_2 injection that target to reduce energy spend for heating operations. Investigating the three different depths, it can be observed that at the vicinity of the wellbore, effective stresses increase with depth. Additionally, pore and fissure pressures fluctuate significantly with higher depths and internal pressures. In contrast to the wellbore head, at higher depths the effective hoop stresses are compressive (negative values).

Furthermore, results indicate that at an early stage of the applied internal pressures and temperatures, the pore pressure is influenced more, compared to the fissure pressure at the vicinity of the wellbore (see Figures 6.3, 6.7 and 6.9). Their difference is reduced as the radial distance increases. This happens due to lower permeability of the porous domain compared to the fractured network of the rock. This difference disappears as fluid dissipation occurs from one domain to the other at the far-field (Ma and Wang, 2016). Furthermore, cooling of the material indicates lower pore-fissure pressure for the three cases, in contrast to the radial effective stresses, which increase significantly.

Moreover, it should be mentioned that by decreasing the internal pressures and increasing the temperature difference between the wellbore wall and the injected CO_2, tensile stresses appear to the wellbore head. Specifically, tensile hoop stress forms at the vicinity of the wellbore head due to cooling, while radial effective stress tends to decrease (see Figure 6.4). This occurs due to thermal expansion of the material. For the same reason, at higher depths, the compressive hoop stress will decrease for lower internal temperatures (see Figures 6.7 and 6.10). Studying an early response of the wellbore rock, the identified increase in the tensile stress can cause damage or activate faults and fractures in the hoop area. As time passes, pore and fissure pressure reach

equilibrium. However, damage may have already formed. One way to reduce the hoop effective tensile stress is the reduction of the injected pressure. However, this can cause stress-relief and cavitation effects in the sandstone, concluding to negative formation pore water pressures.

The numerical mechanical parametric study indicated that the results are sensitive to the materials strength, leakage term, permeability, and effective stress parameters. At higher depths, less damage is seen for the same thermal and pressure loading. This is because rock is stronger and the higher Young's modulus is, the less damage is observed for the same thermo-mechanical loading. It should be outlined that higher levels of damage occurred for smaller Young's modulus (more deformable formations). Additionally, the stiffer the material is, the more apparent the tensile stress and the drop of the formation pressure is for higher temperature differences, between the injected CO_2 and the wellbore wall. Mass transfer between the phases or leakage term increases, at an early simulation stage results in reduction of the difference between pore and fissure pressures. At a certain value of $\gamma = 10^{-7}$/Pa·s, even at an early simulation period, the flow dissipation becomes the same for the two phases and damage increases as pore pressure rises quicker. Finally, the higher the permeability difference between the two phases is, more time is needed to achieve pressure equilibrium in the pore-fissure versus radial distance region.

The two scenarios simulated using the Stainton sandstone at 50 m depth and 1000 m depth of the wellbore, presented some interesting outcomes. The experimental results in Stainton sandstone indicated a different change of the Poisson's ratio, for temperatures lower than -5°C, which also influenced the effective stresses of the simulation and the initial damage of the material. It was mentioned that despite the Poisson's ratio reduction until -5°C, which means damage increases, freezing the rock further would enlarge the Poisson's ratio and result in a drop in damage at the vicinity of the wellbore. This outcome is also influenced by the critical state parameters, for both wellbore head conditions and for higher depths. Finally, the compressive hoop and radial stresses at the rock formation nearby the wellbore wall, highly depend on effective stress parameters. Compressibility of the grains needs to be calculated for proper estimation of these parameters.

Chapter 7. Conclusions

The main objective of this study was to develop a fully coupled analysis of heat flow, fluid flow and deformation in saturated double porous media considering elastoplastic and continuum damage effects. This way, the behaviour of rock adjacent to a wellbore wall loaded by pressure and temperature (as in a CO_2 injection scenario) can be investigated.

To achieve this aim, the accomplished tasks were:

- ✓ Formulation of the theoretical governing equations for the coupled THM model, describing the elastoplastic deformation, fluid flow and pressure evolution inside the double porous medium and heat transfer in the solid domain.
- ✓ Identification of the constitutive parameters and outline of the damage evolution model and boundary yield surface conditions including plasticity and hardening effects.
- ✓ Conduction of experimental UCS and triaxial tests (at 12.5 MPa and 24 MPa confining pressure) at 15℃, -5℃ and -10℃. Results of the experiments are presented in terms of deviatoric stress and strains. Linear change of the mechanical parameters over temperature is assumed to be used to numerical models. Micromechanical analysis was undertaken to verify the low Poisson's ratio. The critical state line slope was also estimated from the experimental results and used as input for the numerical simulations.
- ✓ Numerical implementation of the governing equations into a finite element code using MATLAB software. Key techniques for the numerical implementation of the coupled flow deformation model are Galerkin's method for spatial discretization and the finite difference technique for temporal discretisation. The global solution provides the displacements, pore-fissure pressures, and temperature of the domain for the local solution, which is calculated by implementing strain increments in the constitutive equations. Non-linearity of the elastoplastic damage equation is addressed by an explicit integration approach. A modified Euler's method with an automatic sub stepping scheme is used in the explicit scheme. A yield surface drift correction is implemented to increase the accuracy and robustness of the results.
- ✓ Validation of the numerical model achieved using results from literature for both THM effects on elastic material and hydro-mechanical effects on elastoplastic material.

- ✓ Numerical representation of the experimental tests that achieved using critical state mechanics. Each critical state parameter influenced a different part of the deviatoric stress-strain curve, making it possible to estimate the values from curve fitting.
- ✓ The final model, after a parametric analysis was used to estimate the effect of various injection scenarios on rock surrounding the wellbore. Temperature effects on pore-fissure pressure distribution, hoop and radial effective stress and damage evolution are presented.

7.1 Summary of main findings

Expanding the experimental results of the UCS and triaxial conditions to CCS applications, it can be observed that freezing the sandstone can increase the Young's, shear and bulk modulus of the rock, especially at the wellhead, which is represented by the UCS test. Freezing during thermal loading can increase the strength of the rock. However, a sub-zero temperature can decrease Poisson's ratio, making the rock vulnerable to fracturing and consequently potential damage. Confining pressure also significantly influences the sensitivity of the mechanical parameters in relation to temperature. It was identified that the less confinement there is, the less temperature affects the rock parameters.

The numerical model, critical state mechanics and bounding yield surface model satisfactorily reproduced the UCS and triaxial experimental results. The secant Poisson's ratio performed better during the parametric fitting procedure to the experimental data compared to the tangent Poisson's ratio. Additionally, critical state parameters (e.g., unloading-reloading line slope and hardening parameters) were influenced significantly by the saline water temperature. As critical state mechanics theory is mainly applied to soils, there was a difficulty in reproducing the curve of the UCS experimental results and the assumption of an extremely low confinement (0.1 MPa) was necessary. FEM implemented in MATLAB is suggested, as a robust and precise way to reproduce triaxial test data and estimate critical state parameters.

Results of pore-fissure pressure, formation pressure, effective stress and damage evolution with time were presented for certain depths. It should be outlined that injection at lower temperature than the formation, reduces the pore and fissure pressures from its initial pre-injection values. In terms of effective stresses, and injection at sub-zero temperatures, tensile hoop stress slightly propagates at a radial distance from the wellbore and increases with time, while the radial stress

becomes more compressive. At high depths, the compressive hoop stress decreases (tendency to become more tensile), and the radial stress becomes more compressive, propagating more and more radially in time. The decrease of the formation pressure with time for the certain depths, starting from an initial high value and the decrease of the compressive stresses due to thermal expansion result in increase of the damage with time, especially in the vicinity of the wellbore, where huge fluctuations occur. This damage may be crucial after certain injection period.

7.2 Recommendations for further research

In line with the work presented in this PhD thesis, the following topics are suggested for further work:

- A sensitivity analysis of the mechanical critical state mechanics parameters for the elastoplastic damage model is required for sub-zero temperatures. A large set of experimental data: triaxial, poly-axial and temperature tests is required to identify mechanical and critical state parameters evolution with temperature and characterise different rock parameters, such as heat capacity, thermal conductivity, and the thermal expansion coefficient.
- Extension of this model to consider multiphase flow and heat transfer between the porosities (pores and fractures). A fully coupled THM model with thermo-plasticity considerations could be developed for multi-phase flow for a fractured porous media. Existence of water, air and ice at sub-zero temperatures can be considered, to also explain the change of the mechanical properties at freezing conditions.
- Simulation of well-barrier materials that protect the existed rock close to the wellbore and estimation of their contribution to the absorption of thermal loading and pressure can be analysed.

References

Abdulagatova, Z., Abdulagatov, I. & Emirov, V. 2009. Effect of temperature and pressure on the thermal conductivity of sandstone. *International Journal of Rock Mechanics and Mining Sciences,* 46**,** 1055-1071.

Agada, S., Jackson, S., Kolster, C., Dowell, N. M., Williams, G., Vosper, H., Williams, J. & Krevor, S. 2017. The impact of energy systems demands on pressure limited CO2 storage in the Bunter Sandstone of the UK Southern North Sea. *International Journal of Greenhouse Gas Control,* 65**,** 128-136.

Aifantis, E. 1980. On the problem of diffusion in solids. *Acta Mechanica,* 37**,** 265-296.

Aifantis, E. C. & Beskos, D. 1980. Heat extraction from hot dry rocks. *Mechanics Research Communications,* 7**,** 165-170.

Al-Ameri, W. A., Abdulraheem, A. & Mahmoud, M. 2016. Long-term effects of CO2 sequestration on rock mechanical properties. *Journal of Energy Resources Technology,* 138.

Alejano, L. R. & Bobet, A. 2012. Drucker–prager criterion. *The ISRM Suggested Methods for Rock Characterization, Testing and Monitoring: 2007-2014.* Springer.

Andersen, O. & Nilsen, H. M. 2018. Investigating simplified modeling choices for numerical simulation of CO2 storage with thermal effects. *International Journal of Greenhouse Gas Control,* 72**,** 49-64.

Armitage, P., Faulkner, D., Worden, R., Aplin, A., Butcher, A. & Iliffe, J. 2011. Experimental measurement of, and controls on, permeability and permeability anisotropy of caprocks from the CO2 storage project at the Krechba Field, Algeria. *Journal of Geophysical Research: Solid Earth,* 116.

Arslan, G. 2007. Sensitivity study of the Drucker–Prager modeling parameters in the prediction of the nonlinear response of reinforced concrete structures. *Materials & design,* 28**,** 2596-2603.

Assayag, N., Matter, J., Ader, M., Goldberg, D. & Agrinier, P. 2009. Water–rock interactions during a CO2 injection field-test: implications on host rock dissolution and alteration effects. *Chemical geology,* 265**,** 227-235.

Aursand, P., Hammer, M., Lavrov, A., Lund, H., Munkejord, S. T. & Torsæter, M. 2017. Well integrity for CO2 injection from ships: Simulation of the effect of flow and material parameters on thermal stresses. *International Journal of Greenhouse Gas Control,* 62**,** 130-141.

Azin, R., Mehrabi, N., Osfouri, S. & Asgari, M. 2015. Experimental Study of CO2 – Saline Aquifer-Carbonate Rock Interaction during CO2 Sequestration. *Procedia Earth and Planetary Science,* 15**,** 413-420.

Bachu, S. & Adams, J. J. 2003. Sequestration of CO2 in geological media in response to climate change: capacity of deep saline aquifers to sequester CO2 in solution. *Energy Conversion and management,* 44**,** 3151-3175.

Bachu, S. & Stewart, S. 2002. Geological sequestration of anthropogenic carbon dioxide in the Western Canada sedimentary basin: suitability analysis. *Journal of Canadian Petroleum Technology,* 41.

Bai, M., Meng, F., Elsworth, D., Abousleiman, Y. & Roegiers, J. C. 1999. Numerical modelling of coupled flow and deformation in fractured rock specimens. *International journal for numerical and analytical methods in geomechanics,* 23**,** 141-160.

Bai, Y. 2016a. *Coupled thermo-hydro-mechanical (THM) model for multiphase flow through deformable porous media with double porosity.* Doctor of Philosophy, The University of New South Wales.

Bai, Y. 2016b. Coupled thermo-hydro-mechanical (THM) model for multiphase flow through deformable porous media with double porosity.

Barenblatt, G. I., Zheltov, I. P. & Kochina, I. 1960. Basic concepts in the theory of seepage of homogeneous liquids in fissured rocks [strata]. *Journal of applied mathematics and mechanics,* 24**,** 1286-1303.

Barrio, M., Aspelund, A., Weydahl, T., Sandvik, T. E., Wongraven, L. R., Krogstad, H., Henningsen, R., Mølnvik, M. & Eide, S. I. 2005. - Ship-based transport of CO2. *In:* RUBIN, E. S., KEITH, D. W., GILBOY, C. F., WILSON, M., MORRIS, T., GALE, J. & THAMBIMUTHU, K. (eds.) *Greenhouse Gas Control Technologies 7.* Oxford: Elsevier Science Ltd.

Bathe, K.-J. 2006. *Finite element procedures,* Klaus-Jurgen Bathe.

Baud, P., Zhu, W. & Wong, T. F. 2000. Failure mode and weakening effect of water on sandstone. *Journal of Geophysical Research: Solid Earth,* 105**,** 16371-16389.

Bear, J. & Corapcioglu, M. 1981. A mathematical model for consolidation in a thermoelastic aquifer due to hot water injection or pumping. *Water Resources Research,* 17**,** 723-736.

Benson, S. M. & Surles, T. 2006. Carbon dioxide capture and storage: An overview with emphasis on capture and storage in deep geological formations. *Proceedings of the IEEE,* 94**,** 1795-1805.

Bentham, M., Mallows, T., Lowndes, J. & Green, A. 2014. CO2 STORage Evaluation Database (CO2 Stored). The UK's online storage atlas. *Energy Procedia,* 63**,** 5103-5113.

Bernabé, Y., Li, M. & Maineult, A. 2010. Permeability and pore connectivity: A new model based on network simulations. *Journal of Geophysical Research: Solid Earth,* 115.

Bigoni, D. & Piccolroaz, A. 2004. Yield criteria for quasibrittle and frictional materials. *International journal of solids and structures,* 41**,** 2855-2878.

Biot, M. A. 1941. General theory of three-dimensional consolidation. *Journal of applied physics,* 12**,** 155-164.

Bjørlykke, K. & Høeg, K. 1997. Effects of burial diagenesis on stresses, compaction and fluid flow in sedimentary basins. *Marine and Petroleum Geology,* 14**,** 267-276.

Bowen, R. & Garcia, D. 1970. On the thermodynamics of mixtures with several temperatures. *International Journal of Engineering Science,* 8**,** 63-83.

Bowen, R. M. 1982. Compressible porous media models by use of the theory of mixtures. *International Journal of Engineering Science,* 20**,** 697-735.

Bower, K. M. & Zyvoloski, G. 1997. A numerical model for thermo-hydro-mechanical coupling in fractured rock. *International Journal of Rock Mechanics and Mining Sciences,* 34**,** 1201-1211.

Bragg, R. A. & Andersland, O. B. 1981. Strain rate, temperature, and sample size effects on compression and tensile properties of frozen sand. *Engineering Geology,* 18**,** 35-46.

Brignoli, M. & Sartori, L. Incremental constitutive relations for the study of wellbore failure. The 34th US Symposium on Rock Mechanics (USRMS), 1993. OnePetro.

Brook, M., Shaw, K., Vincent, C. & Holloway, S. 2003. Gestco case study 2a-1: Storage potential of the Bunter Sandstone in the UK sector of the southern North Sea and the adjacent onshore area of Eastern England.

Burlion, N., Gatuingt, F., Pijaudier-Cabot, G. & Daudeville, L. 2000. Compaction and tensile damage in concrete: constitutive modelling and application to dynamics. *Computer methods in applied mechanics and engineering,* 183**,** 291-308.

Busch, B., Hilgers, C., Gronen, L. & Adelmann, D. 2017. Cementation and structural diagenesis of fluvio-aeolian Rotliegend sandstones, northern England. *Journal of the Geological Society,* 174**,** 855-868.

Cappa, F., Guglielmi, Y. & De Barros, L. 2022. Transient evolution of permeability and friction in a slowly slipping fault activated by fluid pressurization. *Nature communications,* 13**,** 3039.

Cappa, F. & Rutqvist, J. 2011. Modeling of coupled deformation and permeability evolution during fault reactivation induced by deep underground injection of CO2. *International Journal of Greenhouse Gas Control,* 5**,** 336-346.

Carey, J. W., Lei, Z., Rougier, E., Mori, H. & Viswanathan, H. 2015. Fracture-permeability behavior of shale. *Journal of Unconventional Oil and Gas Resources,* 11**,** 27-43.

Carrera, J., Silva, O., Rötting, T., Carbonell, R., Vilarrasa, V., Pérez-Estaún, A. & Group, C. S. R. 2011. Characterization and working programme of Hontomín CO2 injection site (Spain). Monitoring, hydrogeochemical characterization and injection tests.

Carter, J. P. & Liu, M. D. 2005. Review of the structured cam clay model. *Soil constitutive models: Evaluation, selection, and calibration.*

Celia, M. A., Bachu, S., Nordbotten, J. M. & Bandilla, K. W. 2015. Status of CO2 storage in deep saline aquifers with emphasis on modeling approaches and practical simulations. *Water Resources Research,* 51**,** 6846-6892.

Chadwick, R., Zweigel, P., Gregersen, U., Kirby, G., Holloway, S. & Johannessen, P. 2004. Geological reservoir characterization of a CO2 storage site: The Utsira Sand, Sleipner, northern North Sea. *Energy,* 29**,** 1371-1381.

Charlez, P. A. 1997. Rock Mechanics. Volume 2. Petroleum Applications.

Chen, L., Shao, J.-F. & Huang, H. 2010. Coupled elastoplastic damage modeling of anisotropic rocks. *Computers and Geotechnics,* 37**,** 187-194.

Chen, Z., Tham, L., Yeung, M. & Xie, H. 2006. Confinement effects for damage and failure of brittle rocks. *International Journal of Rock Mechanics and Mining Sciences,* 43**,** 1262-1269.

Cheng, A.-D., Abousleiman, Y. & Roegiers, J.-C. Review of some poroelastic effects in rock mechanics. International journal of rock mechanics and mining sciences & geomechanics abstracts, 1993. Elsevier, 1119-1126.

Chun, C. 2005. Iterative methods improving Newton's method by the decomposition method. *Computers & Mathematics with Applications,* 50**,** 1559-1568.

Couling, N. & Hein, C. Viscosity. Volumetric Society forum. Society and Space, 2019.

Cui, L., Kaliakin, V. N., Abousleiman, Y. & Cheng, A. H. D. 1997. Finite element formulation and application of poroelastic generalized plane strain problems. *International Journal of Rock Mechanics and Mining Sciences,* 34**,** 953-962.

Cuss, R., Rutter, E. & Holloway, R. 2003. The application of critical state soil mechanics to the mechanical behaviour of porous sandstones. *International Journal of Rock Mechanics and Mining Sciences,* 40**,** 847-862.

Dafalias, Y. & Popov, E. 1975. A model of nonlinearly hardening materials for complex loading. *Acta mechanica,* 21**,** 173-192.

Dafalias, Y. F. & Herrmann, L. R. 1986. Bounding surface plasticity. II: Application to isotropic cohesive soils. *Journal of Engineering Mechanics,* 112**,** 1263-1291.

David, C., Wong, T.-F., Zhu, W. & Zhang, J. 1994. Laboratory measurement of compaction-induced permeability change in porous rocks: Implications for the generation and maintenance of pore pressure excess in the crust. *Pure and Applied Geophysics,* 143**,** 425-456.

De Andrade, J., Torsæter, M., Todorovic, J., Opedal, N., Stroisz, A. & Vrålstad, T. Influence of casing centralization on cement sheath integrity during thermal cycling. IADC/SPE Drilling Conference and Exhibition, 2014. OnePetro.

De La Cruz, V. & Spanos, T. 1989. Thermomechanical coupling during seismic wave propagation in a porous medium. *Journal of Geophysical Research: Solid Earth,* 94**,** 637-642.

Delage, P., Sultan, N. & Cui, Y. J. 2000. On the thermal consolidation of Boom clay. *Canadian Geotechnical Journal,* 37**,** 343-354.

Detournay, E. & Cheng, A.-D. Poroelastic response of a borehole in a non-hydrostatic stress field. International Journal of Rock Mechanics and Mining Sciences & Geomechanics Abstracts, 1988. Elsevier, 171-182.

Dixon, J., Bell, K. & Brush, S. 2022. Which way to net zero? a comparative analysis of seven UK 2050 decarbonisation pathways. *Renewable and Sustainable Energy Transition,* 2**,** 100016.

Dolarevic, S. & Ibrahimbegovic, A. 2007. A modified three-surface elasto-plastic cap model and its numerical implementation. *Computers & structures,* 85**,** 419-430.

Dong, L., Xu, H., Fan, P. & Wu, Z. 2021. On the Experimental Determination of Poisson's Ratio for Intact Rocks and Its Variation as Deformation Develops. *Advances in Civil Engineering,* 2021.

Dougill, J. 1976. Mechanics in engineering. *ASCE EMD,* 333-355.

Dragoni, M. 1993. The brittle-ductile transition in tectonic boundary zones.

Duarte, C. A. & Kim, D.-J. 2008. Analysis and applications of a generalized finite element method with global–local enrichment functions. *Computer methods in applied mechanics and engineering,* 197**,** 487-504.

Ducrotoy, J.-P., Elliott, M. & De Jonge, V. N. 2000. The north sea. *Marine pollution bulletin,* 41**,** 5-23.

Duguid, J. O. & Lee, P. 1977. Flow in fractured porous media. *Water Resources Research,* 13**,** 558-566.

Eiken, O., Ringrose, P., Hermanrud, C., Nazarian, B., Torp, T. A. & Høier, L. 2011. Lessons learned from 14 years of CCS operations: Sleipner, In Salah and Snøhvit. *Energy procedia,* 4**,** 5541-5548.

Eshiet, K. & Sheng, Y. 2014. Investigation of geomechanical responses of reservoirs induced by carbon dioxide storage. *Environmental Earth Sciences,* 71**,** 3999-4020.

Everall, T. J. & Sanislav, I. V. 2018. The Influence of Pre-Existing Deformation and Alteration Textures on Rock Strength, Failure Modes and Shear Strength Parameters. *Geosciences,* 8**,** 124.

Fahrenthold, E. 1991. A continuum damage model for fracture of brittle solids under dynamic loading.

Fan, L., Xu, C. & Wu, Z. 2020. Effects of cyclic freezing and thawing on the mechanical behavior of dried and saturated sandstone. *Bulletin of Engineering Geology and the Environment,* 79**,** 755-765.

Fang, X., Xu, J. & Wang, P. 2018. Compressive failure characteristics of yellow sandstone subjected to the coupling effects of chemical corrosion and repeated freezing and thawing. *Engineering Geology,* 233**,** 160-171.

Fang, Z. & Harrison, J. 2002a. Application of a local degradation model to the analysis of brittle fracture of laboratory scale rock specimens under triaxial conditions. *International Journal of Rock Mechanics and Mining Sciences,* 39**,** 459-476.

Fang, Z. & Harrison, J. 2002b. Development of a local degradation approach to the modelling of brittle fracture in heterogeneous rocks. *International Journal of Rock Mechanics and Mining Sciences,* 39**,** 443-457.

Fardis, M. N., Alibe, B. & Tassoulas, J. L. 1983. Monotonic and cyclic constitutive law for concrete. *Journal of engineering mechanics,* 109**,** 516-536.

Fardis, M. N. & Chen, E.-S. 1986. A cyclic multiaxial model for concrete. *Computational mechanics,* 1**,** 301-315.

Feng, G., Kang, Y., Meng, T., Hu, Y.-Q. & Li, X.-H. 2017. The influence of temperature on mode I fracture toughness and fracture characteristics of sandstone. *Rock Mechanics and Rock Engineering,* 50**,** 2007-2019.

Fernandez, E. S., Naylor, M., Lucquiaud, M., Wetenhall, B., Aghajani, H., Race, J. & Chalmers, H. 2016. Impacts of geological store uncertainties on the design and operation of flexible CCS offshore pipeline infrastructure. *International Journal of Greenhouse Gas Control,* 52**,** 139-154.

Ferronato, M., Gambolati, G., Janna, C. & Teatini, P. 2010. Geomechanical issues of anthropogenic CO2 sequestration in exploited gas fields. *Energy Convers. Manage.,* 51**,** 1918.

Figueiredo, B., Tsang, C.-F., Rutqvist, J. & Niemi, A. 2015. A study of changes in deep fractured rock permeability due to coupled hydro-mechanical effects. *International Journal of Rock Mechanics and Mining Sciences,* 79**,** 70-85.

Fine, R. A. & Millero, F. J. 1973. Compressibility of water as a function of temperature and pressure. *The Journal of Chemical Physics,* 59**,** 5529-5536.

Fisher, Q. J., Casey, M., Clennell, M. B. & Knipe, R. J. 1999. Mechanical compaction of deeply buried sandstones of the North Sea. *Marine and Petroleum Geology,* 16**,** 605-618.

Fossum, A. F. & Fredrich, J. T. Cap plasticity models and compactive and dilatant pre-failure deformation. 4th North American Rock Mechanics Symposium, 2000. OnePetro.

Frash, L. P., Carey, J. W., Ickes, T. & Viswanathan, H. S. 2017. Caprock integrity susceptibility to permeable fracture creation. *International Journal of Greenhouse Gas Control,* 64**,** 60-72.

Frash, L. P., Carey, J. W., Lei, Z., Rougier, E., Ickes, T. & Viswanathan, H. S. 2016. High-stress triaxial direct-shear fracturing of Utica shale and in situ X-ray microtomography with permeability measurement. *Journal of Geophysical Research: Solid Earth,* 121**,** 5493-5508.

Fredrich, J. T., Evans, B. & Wong, T. F. 1989. Micromechanics of the brittle to plastic transition in Carrara marble. *Journal of Geophysical Research: Solid Earth,* 94**,** 4129-4145.

Gajo, A. 2002. A non-linear analysis of non-isothermal wave propagation in linear-elastic fluid-saturated porous media. *International Journal of Plasticity,* 18**,** 313-344.

Gajo, A. & Bigoni, D. 2015. Elastoplastic coupling for thermo-elasto-plasticity at high temperature. *Geomechanics for Energy and the Environment,* 4.

Gajo, A. & Wood, M. 1999. Severn–Trent sand: a kinematic-hardening constitutive model: the q–p formulation. *Géotechnique,* 49**,** 595-614.

Gelet, R. 2011. *Thermo-hydro-mechanical study of deformable porous media with double porosity in local thermal non-equilibrium.* Université de Grenoble; University of New South Wales.

Gelet, R., Loret, B. & Khalili, N. 2012a. Borehole stability analysis in a thermoporoelastic dual-porosity medium. *International Journal of Rock Mechanics and Mining Sciences,* 50**,** 65-76.

Gelet, R., Loret, B. & Khalili, N. 2012b. A thermo-hydro-mechanical coupled model in local thermal non-equilibrium for fractured HDR reservoir with double porosity. *Journal of Geophysical Research: Solid Earth,* 117.

Gerogiannopoulos, N. & Brown, E. The critical state concept applied to rock. International Journal of Rock Mechanics and Mining Sciences & Geomechanics Abstracts, 1978. Elsevier, 1-10.

Gessner, K. 2009. Coupled Models of Brittle-plastic Deformation and Fluid Flow: Approaches, Methods, and Application to Mesoproterozoic Mineralisation at Mount Isa, Australia. *Surveys in Geophysics,* 30**,** 211.

Gholami, R. & Raza, A. 2022. CO2 sequestration in sandstone reservoirs: How does reactive flow alter trapping mechanisms? *Fuel,* 324**,** 124781.

Gluyas, J. G. & Bagudu, U. 2020. The Endurance CO2 storage site, Blocks 42/25 and 43/21, UK North Sea. *Geological Society, London, Memoirs,* 52**,** 163-171.

Goodarzi, S., Settari, A., Zoback, M. & Keith, D. 2015. Optimization of a CO2 storage project based on thermal, geomechanical and induced fracturing effects. *Journal of Petroleum Science and Engineering,* 134**,** 49-59.

Goodman, M. & Cowin, S. 1972. A continuum theory for granular materials. *Archive for Rational Mechanics and Analysis,* 44**,** 249-266.

Goodman, R. E. 1989. *Introduction to rock mechanics,* Wiley New York.

Gor, G. Y. & Prévost, J. H. 2013. Effect of CO2 Injection Temperature on Caprock Stability. *Energy Procedia,* 37**,** 3727-3732.

Grandi, S., Rao, R. V. & Toksoz, M. N. 2002. Geomechanical modeling of in-situ stresses around a borehole. Massachusetts Institute of Technology. Earth Resources Laboratory.

Greenwood, N., Parker, E., Fernand, L., Sivyer, D., Weston, K., Painting, S., Kröger, S., Forster, R., Lees, H. & Mills, D. 2010. Detection of low bottom water oxygen concentrations in the North Sea; implications for monitoring and assessment of ecosystem health. *Biogeosciences,* 7**,** 1357-1373.

Guo, P. & Wan, R. 1998. Modelling the cyclic behaviour of brittle materials using a bounding surface plasticity-damage model. *International Journal of Rock Mechanics and Mining Sciences,* 4**,** 437-438.

Habte, M. A. 2006. *Numerical and constitutive modelling of monotonic and cyclic loading in variably saturated soils,* University of New South Wales.

Haimson, B. & Chang, C. 2000. A new true triaxial cell for testing mechanical properties of rock, and its use to determine rock strength and deformability of Westerly granite. *International Journal of Rock Mechanics and Mining Sciences,* 37**,** 285-296.

Han, D. & Chen, W.-F. 1985. A nonuniform hardening plasticity model for concrete materials. *Mechanics of materials,* 4**,** 283-302.

Han, G. 2003. Rock stability under different fluid flow conditions.

Han, Y., Jia, H., Wang, T., Wang, L., Li, Q. & Wang, Y. 2022. Fracture toughness and cracking behavior of frozen sandstone at different freezing temperatures. *Engineering Fracture Mechanics,* 271**,** 108664.

Hangx, S., Van Der Linden, A., Marcelis, F. & Bauer, A. 2013. The effect of CO2 on the mechanical properties of the Captain Sandstone: Geological storage of CO2 at the Goldeneye field (UK). *International Journal of Greenhouse Gas Control,* 19**,** 609-619.

Hansen, O., Gilding, D., Nazarian, B., Osdal, B., Ringrose, P., Kristoffersen, J.-B., Eiken, O. & Hansen, H. 2013. Snøhvit: The history of injecting and storing 1 Mt CO2 in the fluvial Tubåen Fm. *Energy Procedia,* 37**,** 3565-3573.

Haszeldine, R. S. 2009. Carbon capture and storage: how green can black be? *Science,* 325**,** 1647-1652.

Hawkins, A. 1998. Aspects of rock strength. *Bulletin of Engineering Geology and the Environment,* 57**,** 17-30.

Hawkins, P. 1978. Relationship between diagenesis, porosity reduction, and oil emplacement in late Carboniferous sandstone reservoirs, Bothamsall Oilfield, E Midlands. *Journal of the Geological Society,* 135**,** 7-24.

Heinemann, N., Wilkinson, M., Pickup, G. E., Haszeldine, R. S. & Cutler, N. A. 2012. CO2 storage in the offshore UK Bunter Sandstone Formation. *International Journal of Greenhouse Gas Control,* 6**,** 210-219.

Herzog, H. & Golomb, D. 2004. Carbon capture and storage from fossil fuel use. *Encyclopedia of energy,* 1**,** 277-287.

Hills, T., Florin, N. & Fennell, P. S. 2016. Decarbonising the cement sector: a bottom-up model for optimising carbon capture application in the UK. *Journal of cleaner production,* 139**,** 1351-1361.

Horseman, S. & Mcewen, T. 1996. Thermal constraints on disposal of heat-emitting waste in argillaceous rocks. *Engineering Geology,* 41**,** 5-16.

Hou, C., Jin, X., He, J. & Li, H. 2022. Experimental studies on the pore structure and mechanical properties of anhydrite rock under freeze-thaw cycles. *Journal of Rock Mechanics and Geotechnical Engineering,* 14**,** 781-797.

Hsu, C. 1999. A closure model for transient heat conduction in porous media.

Hu, K., Zhu, Q.-Z., Chen, L., Shao, J.-F. & Liu, J. 2018. A micromechanics-based elastoplastic damage model for rocks with a brittle–ductile transition in mechanical response. *Rock Mechanics and Rock Engineering,* 51**,** 1729-1737.

Huang, L., Liang, J., Ma, J. & Chen, W. 2022. A dynamic bounding surface plasticity damage model for rocks subjected to high strain rates and confinements. *International Journal of Impact Engineering,* 168**,** 104306.

Huang, S., Liu, Q., Liu, Y., Ye, Z. & Cheng, A. 2018. Freezing Strain Model for Estimating the Unfrozen Water Content of Saturated Rock under Low Temperature. *International Journal of Geomechanics,* 18**,** 04017137.

Ishii, E., Sanada, H., Funaki, H., Sugita, Y. & Kurikami, H. 2011. The relationships among brittleness, deformation behavior, and transport properties in mudstones: An example from the Horonobe Underground Research Laboratory, Japan. *Journal of Geophysical Research: Solid Earth,* 116.

Jagota, V., Sethi, A. P. S. & Kumar, K. 2013. Finite element method: an overview. *Walailak Journal of Science and Technology (WJST),* 10**,** 1-8.

Jasinge, D., Ranjith, P. G. & Choi, S. K. 2011. Effects of effective stress changes on permeability of latrobe valley brown coal. *Fuel,* 90**,** 1292-1300.
Jen, C.-P., Li, C. & Zhang, K. 2017. Effects of Injection Pressure on Geological CO2 Storage in the Northwest Taiwan Basin. *Aerosol and Air Quality Research,* 17**,** 1033-1042.
Jia, H. L., Han, L., Zhao, T., Sun, Q. & Tan, X. J. 2022. Strength and the cracking behavior of frozen sandstone containing ice-filled flaws under uniaxial compression. *Permafrost and Periglacial Processes,* 33**,** 160-175.
Jiang, P., Li, X., Xu, R., Wang, Y., Chen, M., Wang, H. & Ruan, B. 2014. Thermal modeling of CO2 in the injection well and reservoir at the Ordos CCS demonstration project, China. *International journal of greenhouse gas control,* 23**,** 135-146.
Jianjun, -. Z., Mingli, -. X., Jianle, -. Y. & Weihua, -. Z. 2019. - EXPERIMENTAL STUDY ON MECHANICAL PROPERTIES AND DAMAGE EVOLUTION OF FRACTURED ROCK UNDER FREEZING-THAWING ACTION. - *JOURNAL OF ENGINEERING GEOLOGY,* - 27**,** - 1199.
Jie, B., Zhijie, X. & Yilin, F. 2016. A coupled thermal-hydro-mechanical simulation for carbon dioxide sequestration. *Environmental Geotechnics,* 3**,** 312-324.
Jin, M., Pickup, G., Mackay, E., Todd, A., Sohrabi, M., Monaghan, A. & Naylor, M. 2012. Static and Dynamic Estimates of CO2-Storage Capacity in Two Saline Formations in the UK. *SPE Journal,* 17**,** 1108-1118.
Jing, L., Tsang, C. F. & Stephansson, O. 1995. DECOVALEX—An international co-operative research project on mathematical models of coupled THM processes for safety analysis of radioactive waste repositories. *International Journal of Rock Mechanics and Mining Sciences & Geomechanics Abstracts,* 32**,** 389-398.
Johnson, E. & Cleary, M. P. Implications of recent laboratory experimental results for hydraulic fractures. Low permeability reservoirs symposium, 1991. OnePetro.
Ju, J. W. 1989. On energy-based coupled elastoplastic damage theories: Constitutive modeling and computational aspects. *International Journal of Solids and Structures,* 25**,** 803-833.
Kachanov, L. 1980. Crack and damage growth in creep—a combined approach. *International Journal of Fracture,* 16**,** R179-R181.
Kang, X. & Liao, H. 2019. Bounding surface plasticity model for jointed soft rocks considering overconsolidation and structural decay. *Computers and Geotechnics,* 108**,** 295-307.
Kazemi, H. 1969. Pressure transient analysis of naturally fractured reservoirs with uniform fracture distribution. *Society of petroleum engineers Journal,* 9**,** 451-462.
Khaled, M., Beskos, D. & Aifantis, E. 1984. On the theory of consolidation with double porosity—III A finite element formulation. *International journal for numerical and analytical methods in geomechanics,* 8**,** 101-123.
Khaledi, K., Hamdi, P., Winhausen, L., Jalali, M., Jaeggi, D. & Amann, F. 2021. Unloading induced absolute negative pore pressures in a low permeable clay shale. *Engineering Geology,* 295**,** 106451.
Khalili-Naghadeh, N. & Valliappan, S. 1991. Flow through fissured porous media with deformable matrix: implicit formulation. *Water Resources Research,* 27**,** 1703-1709.
Khalili, N. 2008. Two-phase fluid flow through fractured porous media with deformable matrix. *Water Resources Research,* 44.
Khalili, N., Habte, M. & Valliappan, S. 2005. A bounding surface plasticity model for cyclic loading of granular soils. *International journal for numerical methods in engineering,* 63**,** 1939-1960.

Khalili, N., Habte, M. A. & Zargarbashi, S. 2008. A fully coupled flow deformation model for cyclic analysis of unsaturated soils including hydraulic and mechanical hystereses. *Computers and Geotechnics,* 35**,** 872-889.

Khalili, N. & Selvadurai, A. 2003a. A fully coupled constitutive model for thermo-hydro-mechanical analysis in elastic media with double porosity. *Geophysical Research Letters,* 30.

Khalili, N. & Selvadurai, P. 2003b. A fully coupled constitutive model for thermo-hydro-mechanical analysis in elastic media with double porosity. *Geophysical Research Letters - GEOPHYS RES LETT,* 30.

Khalili, N., Uchaipichat, A. & Javadi, A. A. 2010. Skeletal thermal expansion coefficient and thermo-hydro-mechanical constitutive relations for saturated homogeneous porous media. *Mechanics of Materials,* 42**,** 593-598.

Khalili, N. & Valliappan, S. 1996. Unified theory of flow and deformation in double porous media. *European Journal of Mechanics, A/Solids,* 15**,** 321-336.

Khan, A. S., Xiang, Y. & Huang, S. 1991. Behavior of Berea sandstone under confining pressure part I: Yield and failure surfaces, and nonlinear elastic response. *International Journal of Plasticity,* 7**,** 607-624.

Khoei, A., Azami, A. & Haeri, S. 2004. Implementation of plasticity based models in dynamic analysis of earth and rockfill dams: A comparison of Pastor–Zienkiewicz and cap models. *Computers and Geotechnics,* 31**,** 384-409.

Khurshid, I. & Fujii, Y. 2021. Geomechanical analysis of formation deformation and permeability enhancement due to low-temperature CO 2 injection in subsurface oil reservoirs. *Journal of Petroleum Exploration and Production,* 11**,** 1915-1923.

Kiefer, B., Waffenschmidt, T., Sprave, L. & Menzel, A. 2017. A gradient-enhanced damage model coupled to plasticity—multi-surface formulation and algorithmic concepts. *International Journal of Damage Mechanics,* 27**,** 253-295.

Kiran, R. & Salehi, S. 2017. Thermoporoelastic modeling of time-dependent wellbore strengthening and casing smear. *Journal of Energy Resources Technology,* 139.

Kodama, J., Goto, T., Fujii, Y. & Hagan, P. 2013. The effects of water content, temperature and loading rate on strength and failure process of frozen rocks. *International Journal of Rock Mechanics and Mining Sciences,* 62**,** 1-13.

Kong, B., Wang, E., Li, Z., Wang, X., Liu, X., Li, N. & Yang, Y. 2016. Electromagnetic radiation characteristics and mechanical properties of deformed and fractured sandstone after high temperature treatment. *Engineering Geology,* 209**,** 82-92.

Krajcinovic, D. 1989. Damage mechanics. *Mechanics of materials,* 8**,** 117-197.

Krogh, E., Nilsen, R. & Henningsen, R. 2012. Liquefied CO2 injection modelling. *Energy Procedia,* 23**,** 527-555.

Kwon, Y. W. & Bang, H. 2018. *The finite element method using MATLAB,* CRC press.

Laguros, J. G. 1969. Effect of temperature on some engineering properties of clay soils. *Highway Research Board Special Report.*

Leary, P. 1991. Deep borehole log evidence for fractal distribution of fractures in crystalline rock. *Geophysical Journal International,* 107**,** 615-627.

Lemaitre, J. Evaluation of dissipation and damage in metals. Proc. ICM Kyoto, 1971.

Lemaitre, J. 1984. How to use damage mechanics. *Nuclear Engineering and Design,* 80**,** 233-245.

Lemaitre, J. 1985a. A continuous damage mechanics model for ductile fracture.

Lemaitre, J. 1985b. A Continuous Damage Mechanics Model for Ductile Fracture. *Journal of Engineering Materials and Technology,* 107**,** 83-89.
Lemaitre, J. & Chaboche, J. 1975. A non-linear model of creep-fatigue damage cumulation and interaction(for hot metallic structures). *Mechanics of visco-elastic media and bodies***,** 1975.
Lervik, K., Spencer, A. & Warrington, G. 1989. Outline of Triassic stratigraphy and structure in the central and northern North Sea. *Correlation in hydrocarbon exploration.* Springer.
Li, J. 2022. Accelerate the offshore CCUS to carbon-neutral China. *Fundamental Research.*
Li, S. & Zhang, D. 2018. How Effective Is Carbon Dioxide as an Alternative Fracturing Fluid? *SPE Journal*.
Li, X., Xu, R., Wei, L. & Jiang, P. 2015. Modeling of wellbore dynamics of a CO2 injector during transient well shut-in and start-up operations. *International Journal of Greenhouse Gas Control,* 42**,** 602-614.
Li, Y., Li, Y.-H., Wang, F.-A. & Ren, B.-Z. 2013. Densities and viscosities of cefodizime sodium in water and normal saline from (278.15 to 313.15) K. *Thermochimica Acta,* 568**,** 189-195.
Lindeberg, E. 2011. Modelling pressure and temperature profile in a CO2 injection well. *Energy Procedia,* 4**,** 3935-3941.
Liping, W., Ning, L., Jilin, Q., Yanzhe, T. & Shuanhai, X. 2019. A study on the physical index change and triaxial compression test of intact hard rock subjected to freeze-thaw cycles. *Cold Regions Science and Technology,* 160**,** 39-47.
Liu, S., Yang, G., Dong, X., Shen, Y. & Liu, H. 2021. Mechanical Characteristics of Frozen Sandstone under Lateral Unloading: An Experimental Study. *Advances in Civil Engineering,* 2021**,** 6653294.
Liu, Z. & Yu, X. 2011. Coupled thermo-hydro-mechanical model for porous materials under frost action: theory and implementation. *Acta Geotechnica,* 6**,** 51-65.
Lu, M. & Connell, L. D. 2008. Non-isothermal flow of carbon dioxide in injection wells during geological storage. *International journal of greenhouse gas control,* 2**,** 248-258.
Lü, P., Li, Q. & Song, Y. 2004. Damage constitutive of concrete under uniaxial alternate tension–compression fatigue loading based on double bounding surfaces. *International journal of solids and structures,* 41**,** 3151-3166.
Luo, X., Wang, M., Oko, E. & Okezue, C. 2014. Simulation-based techno-economic evaluation for optimal design of CO2 transport pipeline network. *Applied Energy,* 132**,** 610-620.
Luo, Z. & Bryant, S. 2011. Influence of thermo-elastic stress on fracture initiation during CO2 injection and storage. *Energy Procedia,* 4**,** 3714-3721.
Ma, J. 2014a. *Coupled flow deformation analysis of fractured porous media subject to elasto-plastic damage.* PhD thesis, The University of New South Wales.
Ma, J. 2014b. *Coupled flow deformation analysis of fractured porous media subject to elasto-plastic damage.* Ph. D Thesis, The University of New South Wales, Australia.
Ma, J. 2016. An elastoplastic model for partially saturated collapsible rocks. *Rock Mechanics and Rock Engineering,* 49**,** 455-465.
Ma, J., Chen, J., Chen, W. & Huang, L. 2022. A coupled thermal-elastic-plastic-damage model for concrete subjected to dynamic loading. *International Journal of Plasticity,* 153**,** 103279.
Ma, J. & Wang, J. 2016. A stress-induced permeability evolution model for fissured porous media. *Rock mechanics and rock engineering,* 49**,** 477-485.
Ma, J. & Zhao, G.-F. 2018. Borehole Stability Analysis in Fractured Porous Media Associated with Elastoplastic Damage Response. *International Journal of Geomechanics,* 18**,** 04018022.

Ma, J., Zhao, G. & Khalili, N. 2016. A fully coupled flow deformation model for elasto-plastic damage analysis in saturated fractured porous media. *International Journal of Plasticity,* 76**,** 29-50.

Majid Hassanizadeh, S. 1986. Derivation of basic equations of mass transport in porous media, Part 1. Macroscopic balance laws. *Advances in Water Resources,* 9**,** 196-206.

Małkowski, P., Ostrowski, Ł. & Brodny, J. 2018. Analysis of Young's modulus for Carboniferous sedimentary rocks and its relationship with uniaxial compressive strength using different methods of modulus determination. *Journal of Sustainable Mining,* 17**,** 145-157.

Marshall, J. D., Tucker, O. D. & Lovelock, C. E. 2016. Goldeneye: modelling a depleted field for carbon capture–how much uncertainty is left?

Martin-Roberts, E., Scott, V., Flude, S., Johnson, G., Haszeldine, R. S. & Gilfillan, S. 2021. Carbon capture and storage at the end of a lost decade. *One Earth,* 4**,** 1569-1584.

Mashayekhi, M., Ziaei-Rad, S., Parvizian, J., Nikbin, K. & Hadavinia, H. 2005. Numerical analysis of damage evolution in ductile solids. *Structural Durability & Health Monitoring,* 1**,** 67.

Masoumi, H., Douglas, K. J. & Russell, A. R. 2016. A bounding surface plasticity model for intact rock exhibiting size-dependent behaviour. *Rock Mechanics and Rock Engineering,* 49**,** 47-62.

Masri, M., Sibai, M., Shao, J.-F. & Mainguy, M. 2014. Experimental investigation of the effect of temperature on the mechanical behavior of Tournemire shale. *International Journal of Rock Mechanics and Mining Sciences,* 70**,** 185-191.

Masters, I., Pao, W. K. & Lewis, R. 2000. Coupling temperature to a double-porosity model of deformable porous media. *International Journal for Numerical Methods in Engineering,* 49**,** 421-438.

Mathias, S. A., Hardisty, P. E., Trudell, M. R. & Zimmerman, R. W. 2009. Screening and selection of sites for CO2 sequestration based on pressure buildup. *International Journal of Greenhouse gas control,* 3**,** 577-585.

Matter, J. M., Takahashi, T. & Goldberg, D. 2007. Experimental evaluation of in situ CO2-water-rock reactions during CO2 injection in basaltic rocks: Implications for geological CO2 sequestration. *Geochemistry, Geophysics, Geosystems,* 8.

Mctigue, D. F. 1986. Thermoelastic response of fluid-saturated porous rock. *Journal of Geophysical Research: Solid Earth,* 91**,** 9533-9542.

Menéndez, B., Zhu, W. & Wong, T.-F. 1996. Micromechanics of brittle faulting and cataclastic flow in Berea sandstone. *Journal of structural geology,* 18**,** 1-16.

Meng, F., Wong, L. N. Y. & Zhou, H. 2021. Rock brittleness indices and their applications to different fields of rock engineering: A review. *Journal of Rock Mechanics and Geotechnical Engineering,* 13**,** 221-247.

Metz, B., Davidson, O., De Coninck, H., Loos, M. & Meyer, L. 2005. *IPCC special report on carbon dioxide capture and storage*, Cambridge: Cambridge University Press.

Mitchell, T. & Faulkner, D. 2008. Experimental measurements of permeability evolution during triaxial compression of initially intact crystalline rocks and implications for fluid flow in fault zones. *Journal of Geophysical Research: Solid Earth,* 113.

Mogi, K. 1971. Fracture and flow of rocks under high triaxial compression. *Journal of Geophysical Research (1896-1977),* 76**,** 1255-1269.

Mohamad-Hussein, A. & Shao, J. 2007. An elastoplastic damage model for semi-brittle rocks. *Geomechanics and Geoengineering: An International Journal,* 2**,** 253-267.

Mohamed, I. M. & Nasr-El-Din, H. A. Formation Damage Due to CO2 Sequestration in Deep Saline Carbonate Aquifers. SPE International Symposium and Exhibition on Formation Damage Control, 2012. SPE-151142-MS.

Morris, J. P., Lomov, I. N. & Glenn, L. A. 2003. A constitutive model for stress-induced permeability and porosity evolution of Berea sandstone. *Journal of Geophysical Research: Solid Earth,* 108.

Morrow, C., Shi, L. & Byerlee, J. 1984. Permeability of fault gouge under confining pressure and shear stress. *Journal of Geophysical Research: Solid Earth,* 89**,** 3193-3200.

Mortara, G. 2009. A hierarchical single yield surface for frictional materials. *Computers and Geotechnics,* 36**,** 960-967.

Mukherjee, H. & Brill, J. P. 1999. Multiphase flow in wells. *Memorial Fund of AIME, Society of Petroleum Engineers Inc.: Richardson, TX, USA.*

Nair, R., Abousleiman, Y. & Zaman, M. 2004. A finite element porothermoelastic model for dual-porosity media. *International Journal for Numerical and Analytical Methods in Geomechanics,* 28**,** 875-898.

Neaupane, K. M., Yamabe, T. & Yoshinaka, R. 1999. Simulation of a fully coupled thermo–hydro–mechanical system in freezing and thawing rock. *International Journal of Rock Mechanics and Mining Sciences,* 36**,** 563-580.

Nevicato, D. 2022. CCS projects underway at TotalEnergies. *Responsabilite et Environnement***,** 43-49.

Nishimura, S., Gens, A., Olivella, S. & Jardine, R. 2009. THM-coupled finite element analysis of frozen soil: formulation and application. *Géotechnique,* 59**,** 159-171.

Noorishad, J., Tsang, C. F. & Witherspoon, P. A. 1992. Theoretical and field studies of coupled hydromechanical behaviour of fractured rocks—1. Development and verification of a numerical simulator. *International Journal of Rock Mechanics and Mining Sciences & Geomechanics Abstracts,* 29**,** 401-409.

Noy, D. J., Holloway, S., Chadwick, R. A., Williams, J. D. O., Hannis, S. A. & Lahann, R. W. 2012. Modelling large-scale carbon dioxide injection into the Bunter Sandstone in the UK Southern North Sea. *International Journal of Greenhouse Gas Control,* 9**,** 220-233.

Ofoegbu, G. & Curran, J. 1991. Yielding and damage of intact rock. *Canadian Geotechnical Journal,* 28**,** 503-516.

Oldenburg, C. M. 2007. Joule-Thomson cooling due to CO2 injection into natural gas reservoirs. *Energy Conversion and Management,* 48**,** 1808-1815.

Olivella, S., Carrera, J., Gens, A. & Alonso, E. E. 1994. Nonisothermal multiphase flow of brine and gas through saline media. *Transport in Porous Media,* 15**,** 271-293.

Page, B., Turan, G., Zapantis, A., Burrows, J., Consoli, C., Erikson, J., Havercroft, I., Kearns, D., Liu, H. & Rassool, D. 2020. The global status of CCS 2020: vital to achieve net zero.

Painter, S. L. & Karra, S. 2014. Constitutive Model for Unfrozen Water Content in Subfreezing Unsaturated Soils. *Vadose Zone Journal,* 13**,** vzj2013.04.0071.

Pan, J.-B., Lee, C.-C., Lee, C.-H., Yeh, H.-F. & Lin, H.-I. 2010. Application of fracture network model with crack permeability tensor on flow and transport in fractured rock. *Engineering Geology,* 116**,** 166-177.

Pao, W. K., Lewis, R. W. & Masters, I. 2001. A fully coupled hydro-thermo-poro-mechanical model for black oil reservoir simulation. *International journal for numerical and analytical methods in geomechanics,* 25**,** 1229-1256.

Papanastasiou, P. 1997. The influence of plasticity in hydraulic fracturing. *International Journal of Fracture,* 84**,** 61-79.

Parfomak, P. W., Folger, P. & Vann, A. Carbon dioxide (CO2) pipelines for carbon sequestration: emerging policy issues. 2007. Congressional Research Service, Library of Congress Washington, DC.

Park, C., Synn, J. H., Shin, H. S., Cheon, D. S., Lim, H. D. & Jeon, S. W. 2004. Experimental study on the thermal characteristics of rock at low temperatures. *International Journal of Rock Mechanics and Mining Sciences,* 41**,** 81-86.

Paterson, L., Ennis-King, J. & Sharma, S. Observations of thermal and pressure transients in carbon dioxide wells. SPE Annual Technical Conference and Exhibition, 2010. OnePetro.

Pecker, C. & Deresiewicz, H. 1973. Thermal effects on wave propagation in liquid-filled porous media. *Acta Mechanica,* 16**,** 45-64.

Pensee, V. & Kondo, D. 2003. Micromechanics of anisotropic brittle damage: comparative analysis between a stress based and a strain based formulation. *Mechanics of materials,* 35**,** 747-761.

Petersen, H. & Hertle, M. 2018. A review of the coaly source rocks and generated petroleums in the Danish North Sea: an underexplored Middle Jurassic petroleum system? *Journal of Petroleum Geology,* 41**,** 135-154.

Potts, D. & Gens, A. 1985. A critical assessment of methods of correcting for drift from the yield surface in elasto-plastic finite element analysis. *International Journal for Numerical and Analytical Methods in Geomechanics,* 9**,** 149-159.

Pruess, K. & Garcia, J. 2002. Multiphase flow dynamics during CO2 disposal into saline aquifers. *Environmental Geology,* 42**,** 282-295.

Pruess, K., Oldenburg, C. M. & Moridis, G. J. 1999. TOUGH2 User's Guide Version 2. United States.

Pye, S., Li, F. G., Price, J. & Fais, B. 2017. Achieving net-zero emissions through the reframing of UK national targets in the post-Paris Agreement era. *Nature energy,* 2**,** 1-7.

Qasem, N. A., Generous, M. M., Qureshi, B. A. & Zubair, S. M. 2021. A comprehensive review of saline water correlations and data: part II—thermophysical properties. *Arabian Journal for Science and Engineering,* 46**,** 1941-1979.

Quirk, D. G., Underhill, J. R., Gluyas, J. G., Howe, M. J., Wilson, H. A. & Anderson, S. 2022. A low-carbon future for The North Sea Basin. *Geological Society, London, Special Publications,* 494**,** 197-213.

Rao, Q.-H., Wang, Z., Xie, H.-F. & Xie, Q. 2007. Experimental study of mechanical properties of sandstone at high temperature. *Journal of Central South University of Technology,* 14**,** 478-483.

Rathnaweera, T. D., Ranjith, P. G., Perera, M. S. A. & De Silva, V. R. S. 2017. Development of a laboratory-scale numerical model to simulate the mechanical behaviour of deep saline reservoir rocks under varying salinity conditions in uniaxial and triaxial test environments. *Measurement,* 101**,** 126-137.

Rayward-Smith, W. & Woods, A. W. 2011. Some implications of cold CO2 injection into deep saline aquifers. *Geophysical Research Letters,* 38.

Rice, J. R. & Cleary, M. P. 1976. Some basic stress diffusion solutions for fluid-saturated elastic porous media with compressible constituents. *Reviews of Geophysics,* 14**,** 227-241.

Robertson, E. C. 1988. Thermal properties of rocks.

Romana, M. & Vásárhelyi, B. A discussion on the decrease of unconfined compressive strength between saturated and dry rock samples. 11th ISRM Congress, 2007. International Society for Rock Mechanics and Rock Engineering.

Roussanaly, S., Bureau-Cauchois, G. & Husebye, J. 2013. Costs benchmark of CO2 transport technologies for a group of various size industries. *International Journal of Greenhouse Gas Control,* 12**,** 341-350.

Rowe, P. W. & Taylor, G. I. 1962. The stress-dilatancy relation for static equilibrium of an assembly of particles in contact. *Proceedings of the Royal Society of London. Series A. Mathematical and Physical Sciences,* 269**,** 500-527.

Roy, P., Morris, J. P., Walsh, S. D., Iyer, J. & Carroll, S. 2018. Effect of thermal stress on wellbore integrity during CO2 injection. *International Journal of Greenhouse Gas Control,* 77**,** 14-26.

Rudnicki , J. 2001. Coupled deformation-diffusion effects in the mechanics of faulting and failure of geomaterials. *Applied Mechanics Reviews,* 54**,** 483-502.

Rutqvist, J. 2011. *Status of the TOUGH-FLAC simulator and recent applications related to coupled fluid flow and crustal deformations*.

Rutqvist, J. 2012. The geomechanics of CO2 storage in deep sedimentary formations. *Geotechnical and Geological Engineering,* 30**,** 525-551.

Rutqvist, J., Birkholzer, J., Cappa, F. & Tsang, C. F. 2007. Estimating maximum sustainable injection pressure during geological sequestration of CO2 using coupled fluid flow and geomechanical fault-slip analysis. *Energy Convers. Manage.,* 48**,** 1798.

Rutqvist, J., Vasco, D. W. & Myer, L. 2009. Coupled reservoir–geomechanical analysis of CO2 injection at In Salah, Algeria. *Energy Procedia,* 1**,** 1847.

Rutqvist, J., Wu, Y. S., Tsang, C. F. & Bodvarsson, G. 2002. A modeling approach for analysis of coupled multiphase fluid flow, heat transfer, and deformation in fractured porous rock. *International Journal of Rock Mechanics and Mining Sciences,* 39**,** 429-442.

Rutter, E. 1986. On the nomenclature of mode of failure transitions in rocks. *Tectonophysics,* 122**,** 381-387.

Rutter, E. & Glover, C. 2012. The deformation of porous sandstones; are Byerlee friction and the critical state line equivalent? *Journal of Structural Geology,* 44**,** 129-140.

Salari, M., Saeb, S. A., Willam, K., Patchet, S. & Carrasco, R. 2004. A coupled elastoplastic damage model for geomaterials. *Computer methods in applied mechanics and engineering,* 193**,** 2625-2643.

Savvidou, C. & Booker, J. 1989. Consolidation around a heat source buried deep in a porous thermoelastic medium with anisotropic flow properties. *International Journal for Numerical and Analytical Methods in Geomechanics,* 13**,** 75-90.

Schiffmann, R. 1971. A thermoelastic theory of consolidation. *Environmental and geophysical heat transfer*.

Schultz, R. A., Okubo, C. H. & Fossen, H. 2010. Porosity and grain size controls on compaction band formation in Jurassic Navajo Sandstone. *Geophysical Research Letters,* 37.

Segall, P. & Fitzgerald, S. D. 1998. A note on induced stress changes in hydrocarbon and geothermal reservoirs. *Tectonophysics,* 289**,** 117-128.

Shah, K. R. 1997. An elasto-plastic constitutive model for brittle-ductile transition in porous rocks. *International Journal of Rock Mechanics and Mining Sciences,* 34**,** 283. e1-283. e13.

Shao, J.-F., Jia, Y., Kondo, D. & Chiarelli, A.-S. 2006a. A coupled elastoplastic damage model for semi-brittle materials and extension to unsaturated conditions. *Mechanics of materials,* 38**,** 218-232.

Shao, J. F., Jia, Y., Kondo, D. & Chiarelli, A. S. 2006b. A coupled elastoplastic damage model for semi-brittle materials and extension to unsaturated conditions. *Mechanics of Materials,* 38**,** 218-232.

Shao, J. F. & Rudnicki, J. W. 2000. A microcrack-based continuous damage model for brittle geomaterials. *Mechanics of Materials,* 32**,** 607-619.

Shen, B., Shi, J. & Barton, N. 2018. An approximate nonlinear modified Mohr-Coulomb shear strength criterion with critical state for intact rocks. *Journal of Rock Mechanics and Geotechnical Engineering,* 10**,** 645-652.

Sheng, D., Sloan, S. & Yu, H. 2000. Aspects of finite element implementation of critical state models. *Computational mechanics,* 26**,** 185-196.

Sheorey, P. R. 1997. *Empirical rock failure criteria,* AA Balkema.

Shi, Y. & Wang, C. Y. 1986. Pore pressure generation in sedimentary basins: overloading versus aquathermal. *Journal of Geophysical Research: Solid Earth,* 91**,** 2153-2162.

Shimada, M. 2000. *Mechanical behaviour of rocks under high pressure conditions,* CRC Press.

Silva, O. 2015. *Non-Isothermal Flow of CO2 in Injection Wells: Evaluation of Different Injection Modes*.

Silva, O., Carrera, J. & Vilarrasa, V. 2011. An efficient injection concept for CO2 geological storage.

Singh, M., Singh, B. & Shankar, D. 2005. Critical State Mechanics in Non-Linear Failure Criterion for Rocks. *Journal of Rock Mechanics and Tunnelling Technology,* 11**,** 13-24.

Sloan, S. W., Abbo, A. J. & Sheng, D. 2001. Refined explicit integration of elastoplastic models with automatic error control. *Engineering Computations*.

Sovacool, B. K., Iskandarova, M. & Geels, F. W. 2023. "Bigger than government": Exploring the social construction and contestation of net-zero industrial megaprojects in England. *Technological Forecasting and Social Change,* 188**,** 122332.

Spetzler, H. A., Sobolev, G. A., Sondergeld, C. H., Salov, B. G., Getting, I. C. & Koltsov, A. 1981. Surface deformation, crack formation, and acoustic velocity changes in pyrophyllite under polyaxial loading. *Journal of Geophysical Research: Solid Earth,* 86**,** 1070-1080.

Sun, Q., Geng, J. & Zhao, F. 2020. Experiment study of physical and mechanical properties of sandstone after variable thermal cycles. *Bulletin of Engineering Geology and the Environment,* 79**,** 3771-3784.

Sündermann, J. & Pohlmann, T. 2011. A brief analysis of North Sea physics. *Oceanologia,* 53**,** 663-689.

Sutherland, F., Duffy, L., Ashby, D., Legrand, P., Jones, G. & Jude, E. Net Zero Teesside: Subsurface Evaluation of Endurance. 1st Geoscience & Engineering in Energy Transition Conference, 2020. EAGE Publications BV, 1-5.

Svensson, R., Odenberger, M., Johnsson, F. & Strömberg, L. 2004. Transportation systems for CO2—application to carbon capture and storage. *Energy Conversion and Management,* 45**,** 2343-2353.

Tan, X., Chen, W., Tian, H. & Cao, J. 2011. Water flow and heat transport including ice/water phase change in porous media: Numerical simulation and application. *Cold Regions Science and Technology,* 68**,** 74-84.

Tao, Q. & Ghassemi, A. 2010. Poro-thermoelastic borehole stress analysis for determination of the in situ stress and rock strength. *Geothermics,* 39**,** 250-259.
Taylor, T. R., Kittridge, M. G., Winefield, P., Bryndzia, L. T. & Bonnell, L. M. 2015. Reservoir quality and rock properties modeling – Triassic and Jurassic sandstones, greater Shearwater area, UK Central North Sea. *Marine and Petroleum Geology,* 65**,** 1-21.
Tenma, N., Yamaguchi, T. & Zyvoloski, G. 2008. The Hijiori Hot Dry Rock test site, Japan: Evaluation and optimization of heat extraction from a two-layered reservoir. *Geothermics,* 37**,** 19-52.
Torsæter, M., Todorovic, J., Lavrov, A., Gawel, K., Lund, H., Roy, P. & Carroll, S. 2017. Avoiding damage of CO2 injection wells caused by temperature variations. *Energy Procedia,* 114**,** 5275-5286.
Ulusay, R. 2014. *The ISRM suggested methods for rock characterization, testing and monitoring: 2007-2014,* Springer.
Valliappan, S., Murti, V. & Wohua, Z. 1990. Finite element analysis of anisotropic damage mechanics problems. *Engineering Fracture Mechanics,* 35**,** 1061-1071.
Vilarrasa, V. 2016. The role of the stress regime on microseismicity induced by overpressure and cooling in geologic carbon storage. *Geofluids,* 16**,** 941-953.
Vilarrasa, V., Bloster, D., Olivella, S. & Carrera, J. 2010. Coupled hydromechanical modeling of CO2 sequestration in deep saline aquifers. *Int. J. Greenhouse Gas Control,* 4**,** 910.
Vilarrasa, V. & Laloui, L. 2016. Impacts of Thermally Induced Stresses on Fracture Stability During Geological Storage of CO2. *Energy Procedia,* 86**,** 411-419.
Vilarrasa, V. & Rutqvist, J. 2017. Thermal effects on geologic carbon storage. *Earth-Science Reviews,* 165**,** 245-256.
Vilarrasa, V., Silva, O., Carrera, J. & Olivella, S. 2013. Liquid CO2 injection for geological storage in deep saline aquifers. *International Journal of Greenhouse Gas Control,* 14**,** 84-96.
Von Terzaghi, K. 1923. Die Berechnug der Durchlassigkeit des Tones aus dem Verlauf der hydromechanischen Spannungserscheinungen. *Sitzungsber. Akad. Wiss.(Wien). Math.-Naturwiss. Kl., Abt. Iia,* 132**,** 125-138.
Voyiadjis, G. Z. & Abu-Lebdeh, T. M. 1993. Damage model for concrete using bounding surface concept. *Journal of engineering mechanics,* 119**,** 1865-1885.
Voyiadjis, G. Z., Abu Al-Rub, R. K. & Palazotto, A. N. 2004. Thermodynamic framework for coupling of non-local viscoplasticity and non-local anisotropic viscodamage for dynamic localization problems using gradient theory. *International Journal of Plasticity,* 20**,** 981-1038.
Voyiadjis, G. Z. & Kattan, P. I. 2005. *Damage mechanics,* CRC Press.
Walker, R. J., Holdsworth, R. E., Armitage, P. J. & Faulkner, D. R. 2013. Fault zone permeability structure evolution in basalts. *Geology,* 41**,** 59-62.
Wang, C., Li, S., Zhang, T. & You, Z. 2019a. Experimental study on mechanical characteristics and fracture patterns of unfrozen/freezing saturated coal and sandstone. *Materials,* 12**,** 992.
Wang, C., Li, S., Zhang, T. & You, Z. 2019b. Experimental Study on Mechanical Characteristics and Fracture Patterns of Unfrozen/Freezing Saturated Coal and Sandstone. *Materials (Basel, Switzerland),* 12**,** 992.
Wang, H.-Y. & Zhang, Q. 2021. Mechanical Behavior of Frozen Porous Sandstone under Uniaxial Compression. *Geofluids,* 2021**,** 1872065.
Wang, H., Wang, J., Wang, X., Dou, F. & Hu, B. 2019c. Coupled hydro-thermal-mechanical analysis for cold CO2 injection into a deep saline aquifer. *Thermal Science,* 23**,** 917-925.

Wang, Z.-L., Dafalias, Y. F. & Shen, C.-K. 1990. Bounding surface hypoplasticity model for sand. *Journal of engineering mechanics,* 116**,** 983-1001.
Waples, D. & Waples, J. 2004. A Review and Evaluation of Specific Heat Capacities of Rocks, Minerals, and Subsurface Fluids. Part 1: Minerals and Nonporous Rocks. *Natural Resources Research,* 13**,** 97-122.
Warren, J. & Root, P. J. 1963. The behavior of naturally fractured reservoirs. *Society of Petroleum Engineers Journal,* 3**,** 245-255.
Watanabe, K. & Osada, Y. 2017. Simultaneous measurement of unfrozen water content and hydraulic conductivity of partially frozen soil near 0°C. *Cold Regions Science and Technology,* 142**,** 79-84.
Wilson, R. & Aifantis, E. C. 1982. On the theory of consolidation with double porosity. *International Journal of Engineering Science,* 20**,** 1009-1035.
Wirasaet, D., Tanaka, S., Kubatko, E., Westerink, J. & Dawson, C. 2010. A performance comparison of nodal discontinuous Galerkin methods on triangles and quadrilaterals. *International Journal for Numerical Methods in Fluids,* 64**,** 1336-1362.
Wohua, Z. & Valliappan, S. 1998. Continuum Damage Mechanics Theory and Application-Part I: Theory. *International Journal of Damage Mechanics,* 7**,** 250-273.
Wong, T.-F., David, C. & Zhu, W. 1997a. The transition from brittle faulting to cataclastic flow in porous sandstones: Mechanical deformation. *Journal of Geophysical Research: Solid Earth,* 102**,** 3009-3025.
Wong, T. & Baud, P. 1999. Mechanical compaction of porous sandstone. *Oil & Gas Science and Technology,* 54**,** 715-727.
Wong, T. F., David, C. & Zhu, W. 1997b. The transition from brittle faulting to cataclastic flow in porous sandstones: Mechanical deformation. *Journal of Geophysical Research: Solid Earth,* 102**,** 3009-3025.
Wood, D. M. 1990. *Soil behaviour and critical state soil mechanics,* Cambridge university press.
Wood, D. M. 1991. *Soil Behaviour and Critical State Soil Mechanics,* Cambridge, Cambridge University Press.
Worden, R. H. & Burley, S. 2003. Sandstone diagenesis: the evolution of sand to stone. *Sandstone diagenesis: Recent and ancient,* 4**,** 3-44.
Wu, G., Wang, Y., Swift, G. & Chen, J. 2013. Laboratory Investigation of the Effects of Temperature on the Mechanical Properties of Sandstone. *Geotechnical and Geological Engineering,* 31.
Xiao, F., Jiang, D., Wu, F., Zou, Q., Chen, J., Chen, B. & Sun, Z. 2021. Effects of high temperature on the mechanical behaviors of sandstone under true-triaxial unloading conditions. *Bulletin of Engineering Geology and the Environment,* 80**,** 4587-4601.
Xu, T., Tang, C.-A., Zhao, J., Li, L. & Heap, M. J. 2012. Modelling the time-dependent rheological behaviour of heterogeneous brittle rocks. *Geophysical Journal International,* 189**,** 1781-1796.
Yale, D. P. Coupled Geomechanics-Fluid Flow Modeling: Effects of Plasticity and Permeability Alteration. SPE/ISRM Rock Mechanics Conference, 2002. SPE-78202-MS.
Yang, S.-Q., Huang, Y.-H. & Tian, W.-L. 2021. Influence of Water Saturation and Real-Time Testing Temperature on Mechanical Behavior of Sandstone Under Conventional Triaxial Compression. *Rock Mechanics and Rock Engineering,* 54**,** 4355-4367.

Yang, S.-Q., Xu, P., Li, Y.-B. & Huang, Y.-H. 2017. Experimental investigation on triaxial mechanical and permeability behavior of sandstone after exposure to different high temperature treatments. *Geothermics,* 69**,** 93-109.

Yazdchi, M., Valliappan, S. & Zhang, W. 1996. A continuum model for dynamic damage evolution of anisotropic brittle materials. *International journal for numerical methods in engineering,* 39**,** 1555-1583.

Youssef, M. Temperature changes and their effects on some physical properties of soils. Proc. 5th ICSMFE, 1961. 419-421.

Yu, H. S. 1998. CASM: a unified state parameter model for clay and sand. *International Journal for Numerical and Analytical Methods in Geomechanics,* 22**,** 621-653.

Yuan, S. & Harrison, J. 2006. A review of the state of the art in modelling progressive mechanical breakdown and associated fluid flow in intact heterogeneous rocks. *International Journal of Rock Mechanics and Mining Sciences,* 43**,** 1001-1022.

Yugui, Y., Feng, G., Hongmei, C. & Peng, H. 2016. Energy dissipation and failure criterion of artificial frozen soil. *Cold Regions Science and Technology,* 129**,** 137-144.

Zang, A., Stephansson, O., Stenberg, L., Plenkers, K., Specht, S., Milkereit, C., Schill, E., Kwiatek, G., Dresen, G., Zimmermann, G., Dahm, T. & Weber, M. 2017. Hydraulic fracture monitoring in hard rock at 410 m depth with an advanced fluid-injection protocol and extensive sensor array. *Geophysical Journal International,* 208**,** 790-813.

Zhang, G., Liu, E., Chen, S., Zhang, D., Liu, X., Yin, X. & Song, B. 2019. Effects of uniaxial and triaxial compression tests on the frozen sandstone combining with CT scanning. *International Journal of Physical Modelling in Geotechnics,* 19**,** 261-274.

Zhang, J., Wong, T.-F. & Davis, D. M. 1990a. Micromechanics of pressure-induced grain crushing in porous rocks. *Journal of Geophysical Research: Solid Earth,* 95**,** 341-352.

Zhang, J., Wong, T.-F., Yanagidani, T. & Davis, D. M. 1990b. Pressure-induced microcracking and grain crushing in Berea and Boise sandstones: acoustic emission and quantitative microscopy measurements. *Mechanics of Materials,* 9**,** 1-15.

Zhang, X.-B., Zhao, G.-M. & Meng, X.-R. 2013. Elastoplastic analysis of surrounding rock on circular roadway based on Drucker Prager yield criterion. *Journal of China Coal Society,* 38**,** 30-37.

Zhang, Z., Wang, G., Massarotto, P. & Rudolph, V. 2006. Optimization of pipeline transport for CO2 sequestration. *Energy Conversion and Management,* 47**,** 702-715.

Zhao, Y., Zhou, H., Zhong, J. & Liu, D. 2019. Study on the relation between damage and permeability of sandstone at depth under cyclic loading. *International Journal of Coal Science & Technology,* 6**,** 479-492.

Zhou, C. & Zhu, F. 2010. An elasto-plastic damage constitutive model with double yield surfaces for saturated soft rock. *International Journal of Rock Mechanics and Mining Sciences,* 47**,** 385-395.

Zhu, Q., Li, D. & Wang, W. 2021. Mechanical behavior and permeability evolution of sandstone with confining pressure after dynamic loading. *Geomechanics and Geophysics for Geo-Energy and Geo-Resources,* 7**,** 1-20.

Zhu, T., Jing, H., Su, H., Yin, Q., Du, M. & Han, G. 2016. Physical and mechanical properties of sandstone containing a single fissure after exposure to high temperatures. *International Journal of Mining Science and Technology,* 26**,** 319-325.

Zhu, W., Montési, L. G. J. & Wong, T.-F. 2007. A probabilistic damage model of stress-induced permeability anisotropy during cataclastic flow. *Journal of Geophysical Research: Solid Earth,* 112.

Zhu, W. & Wong, T.-F. 1996. Permeability reduction in a dilating rock: Network modeling of damage and tortuosity. *Geophysical Research Letters,* 23**,** 3099-3102.

Zhu, W. & Wong, T.-F. 1997. The transition from brittle faulting to cataclastic flow: Permeability evolution. *Journal of Geophysical Research: Solid Earth,* 102**,** 3027-3041.

Ziabakhsh-Ganji, Z. & Kooi, H. 2014. Sensitivity of Joule–Thomson cooling to impure CO2 injection in depleted gas reservoirs. *Applied energy,* 113**,** 434-451.

Zienkiewicz, O. C., Taylor, R. L. & Zhu, J. Z. 2005. *The finite element method: its basis and fundamentals*, Elsevier.

Zimmerman, R. 2000. Coupling in poroelasticity and thermoelasticity. *International Journal of Rock Mechanics and Mining Sciences,* 37**,** 79-87.

Zoback, M. D. & Byerlee, J. 1975. Permeability and effective stress. *AAPG Bulletin,* 59**,** 154-158.

Zoback, M. D. & Zoback, M. L. 2002. Stress in the Earth's lithosphere. *Encyclopedia of physical science and technology,* 16**,** 143-154.